DOCTORAL DISSERTATION

in the discipline:

Automation, Electronics, Electrical Engineering and Space Technologies

Measurement uncertainty of quantity modelled with non-integer order differ-integral equations

Author: **Faisal Saleem**, M.Sc., Eng.

Supervisor: **Józef Wiora**, Ph.D., D.Sc., Eng.

Co-supervisor: **Alicja Wiora**, Ph.D., Eng.

Department of Measurements and Control Systems

Faculty of Automatic Control, Electronics and Computer Science

Silesian University of Technology

Gliwice, June 2026

Dedication

To my parents
Mr. & Mrs. Saleem

Author Declaration

I declare that the doctoral dissertation entitled, **"Measurement uncertainty of quantity modelled with non-integer order differ-integral equations"** is consistent with the doctoral dissertation prepared and submitted as part of education at the doctoral school run by the Silesian University of Technology.

Faisal Saleem,
Department of Measurements and Control Systems,
Faculty of Automatic Control, Electronics and Computer Science,
Silesian University of Technology, Gliwice, Poland

Use of Artificial Intelligence (AI) Tools

The author acknowledges the use of **Microsoft 365 Copilot** for improving the linguistic quality of the dissertation, including grammar, spelling, punctuation, sentence structure, clarity, and readability. The registered version of Microsoft 365 Copilot used for language editing was provided by the **Silesian University of Technology, Poland**. The prompt employed for language editing and revision is provided in Appendix A.

No AI tools were used for the generation of research content, development of scientific results, data analysis, modeling, interpretation of results, or formulation of conclusions. The author takes full responsibility for the integrity, accuracy, and originality of the work.

Faisal Saleem,
Department of Measurements and Control Systems,
Faculty of Automatic Control, Electronics and Computer Science,
Silesian University of Technology, Gliwice, Poland

Acknowledgements

I wish to express my deepest gratitude to my PhD supervisor, **Józef Wiora**, and my co-supervisor, **Alicja Wiora**, for their unwavering guidance, patience, and intellectual support throughout this research. Their critical insights, high standards, and continuous encouragement have been indispensable to the successful completion of this dissertation.

I am profoundly grateful to the Rector of the Silesian University of Technology, **Marek Pawełczyk**, for promoting a multidisciplinary research environment that supports international collaboration among doctoral students. His commitment to academic excellence has enabled diverse learning opportunities through conferences, workshops, and international research visits, which have significantly enriched this research.

I also extend my sincere thanks to the **Department of Measurements and Control Systems** for fostering a stimulating and supportive academic environment. I am especially thankful to the professors, faculty members, and doctoral students whose constructive feedback and insightful remarks during faculty presentations consistently contributed to improving the quality and relevance of this research.

I would like to express my sincere appreciation to **Muhammad Wasim** (Department of Aeronautics and Astronautics Engineering, Institute of Space Technology, Islamabad, Pakistan) for his constructive discussions and valuable remarks on the research findings throughout the course of this work. I would also like to express gratitude to my fellow doctoral student **Abu Feyo Bantu** and **Atif Mehmood** for proof reading the dissertation and providing valuable remarks.

I also wish to acknowledge **Ahsan Ali** (University of Engineering & Technology, Taxila, Pakistan), **Delfim F. M. Torres** (University of Aveiro, Portugal), and **Guido Maione and Paolo Lino** (Polytechnic University of Bari, Italy) for hosting me during my international research visits. The time spent at the **Advanced Control Laboratory** (University of Engineering & Technology) in September 2024, at **Center for Research and Development in Mathematics and Applications** (University of Aveiro) in November 2024 and July 2025, as well as at the **Department of Electrical & Information Engineering** (Polytechnic University of Bari) in February 2025, provided an inspiring and collaborative research environment that significantly supported the development of this work.

I gratefully acknowledge the support of the **International Mobility Office** and the **Joint Doctoral School** at the Silesian University of Technology in facilitating these international mobilities. I also acknowledge the financial support provided by **NAWA** and the **Erasmus**$^+$ programmes, and the **Young Scientist Research Grant**.

Finally, I wish to express my deepest gratitude to my **wife** for her unwavering support and patience throughout this demanding journey. Her understanding and constant motivation have been a source of strength at every stage of this work. I also sincerely thank my **family and friends** for their continued support and belief in me.

Abstract

Real-time systems require controlled operation to maintain the desired performance, typically ensured by feedback controllers. Control design algorithms rely on accurate modeling techniques that describe the dynamic behavior of physical systems. The developed measurement models capture system dynamics based on the observed input-output data.

Dynamic measurement systems often exhibit distributed dynamics and nonlinear behavior. Sensory measurements capture the transient and steady-state responses in such systems. These dynamic properties arise from different physical phenomena and distinct uncertainty sources. These factors influence both modeling accuracy and controller performance.

Classical methods address uncertainty in static measurements and Integer-Order (IO) dynamic models. However, methods for non-integer-order differ-integral equations remain insufficiently developed. This gap limits the application of Fractional-Order (FO) modelling in metrology, despite its proven capability to represent complex physical dynamics with high accuracy.

This dissertation examines uncertainty in quantities described by FO dynamic equations. It integrates metrology, model identification, fractional calculus, and control theory. The work establishes a framework for uncertainty evaluation in systems exhibiting FO behavior.

The principal contribution of this dissertation is the evaluation of uncertainty propagated through the identified parameters of FO models. It develops a direct uncertainty propagation framework based on time-dependent sensitivity coefficients derived analytically from FO differ-integral equations. The proposed method incorporates the covariance of the identified parameters and applies the law of propagation of uncertainty to quantify the uncertainty associated with the identified parameters. Experimental data from several measurement passes indicate that the estimated parameters follow normal probability distributions, which enables a probabilistic description. The resulting uncertainty intervals calculated from the time-dependent sensitivity coefficients and the covariance matrix of the the normally distributed parameters enclose the measured data. This experimental analysis confirms the validity of the proposed method. Comparison with digital filtering methods indicates that the proposed approach yields conservative uncertainty estimates and avoids information loss associated with signal transformation.

The methodology subsequently extends the uncertainty evaluation to closed-loop systems. It derives sensitivity coefficients of the closed-loop FO model and utilizes these coefficients to assess uncertainty propagated through controlled dynamics. Finally, it conducts a comparative analysis of uncertainty propagation in the closed-loop response using GrünwaldLetnikov, Riemann-Liouville, and Caputo implementations of FO operators. The experimental results demonstrate that the FO differential integral equations can be integrated into a rigorous metrological framework for dynamic uncertainty evaluation.

Streszczenie

Systemy czasu rzeczywistego wymagają pracy regulowanej w celu zapewnienia zadanej jakości działania, co zazwyczaj jest realizowane za pomocą regulatorów ze sprzężeniem zwrotnym. Algorytmy projektowania układów regulacji opierają się na dokładnych metodach modelowania, które opisują dynamiczne zachowanie układów fizycznych. Opracowane modele pomiarowe odwzorowują dynamikę systemu na podstawie obserwowanych danych wejściowo-wyjściowych.

Dynamiczne systemy pomiarowe często wykazują dynamikę rozproszoną oraz zachowania nieliniowe. Pomiary realizowane przez czujniki rejestrują odpowiedzi przejściowe oraz stany ustalone takich systemów. Właściwości dynamiczne wynikają z różnych zjawisk fizycznych oraz odmiennych źródeł niepewności. Czynniki te wpływają zarówno na dokładność modelowania, jak i na jakość działania układów regulacji.

Klasyczne metody dotyczą oceny niepewności w pomiarach statycznych oraz w modelach dynamicznych całkowitego rzędu (Integer-Order, IO). Jednakże metody przeznaczone dla równań różniczkowo-całkowych niecałkowitego rzędu pozostają niewystarczająco rozwinięte. Luka ta ogranicza zastosowanie modelowania ułamkowego (Fractional-Order, FO) w metrologii, pomimo jego udowodnionej zdolności do dokładnego odwzorowania złożonych zjawisk fizycznych.

Niniejsza rozprawa doktorska dotyczy analizy niepewności wielkości opisywanych dynamicznymi równaniami ułamkowymi. Praca integruje metrologię, identyfikację modeli, rachunek ułamkowy oraz teorię sterowania. W jej ramach opracowano podejście do oceny niepewności w systemach wykazujących właściwości ułamkowego rzędu.

Główny wkład rozprawy koncentruje się na ocenie niepewności propagowanej przez parametry modeli ułamkowego rzędu wyznaczone w procesie identyfikacji. Opracowano bezpośrednie podejście do propagacji niepewności oparte na czasowo zależnych współczynnikach czułości, wyprowadzonych analitycznie z równań różniczkowo-całkowych ułamkowego rzędu. Zaproponowana metoda uwzględnia macierz kowariancji estymowanych parametrów oraz wykorzystuje prawo propagacji niepewności do kwantyfikacji niepewności związanej z tymi parametrami. Dane eksperymentalne, uzyskane na podstawie wielokrotnych realizacji pomiarów, wskazują, że estymowane parametry podlegają rozkładom normalnym, co umożliwia ich probabilistyczny opis. Wyznaczone przedziały niepewności, obliczone na podstawie czasowo zależnych współczynników czułości oraz macierzy kowariancji parametrów o rozkładzie normalnym, obejmują dane pomiarowe. Analiza eksperymentalna potwierdza tym samym poprawność zaproponowanej metody. Porównanie z metodami filtracji cyfrowej wskazuje, że zaproponowane podejście prowadzi do bardziej zachowawczych oszacowań niepewności oraz eliminuje utratę informacji związaną z transformacją sygnału.

Opracowana metodyka została następnie rozszerzona na układy zamknięte. Wyprowadzono współczynniki czułości dla modeli ułamkowego rzędu w strukturze pętli regulacji i

wykorzystano je do oceny niepewności propagowanej w dynamice regulowanej. W końcowym etapie przeprowadzono analizę porównawczą propagacji niepewności w odpowiedzi układu zamkniętego przy zastosowaniu operatorów ułamkowych w ujęciu Grünwalda–Letnikowa, Riemanna–Liouville'a oraz Caputo.

Wyniki badań eksperymentalnych wskazują, że równania różniczkowo-całkowe ułamkowego rzędu mogą zostać włączone do rygorystycznego aparatu metrologicznego oceny niepewności w systemach dynamicznych.

Translated with Microsoft 365 Copilot.

List of publications

Research conducted within this dissertation topic and prior collaborative work resulted in the following scientific publications.

Publications within the dissertation topic

Journal articles

1. **Faisal Saleem**, Józef Wiora, and Delfim F.M. Torres. Fractional-order modeling of a flow rate measurement system utilizing Grünwald–Letnikov based optimization. *Measurement*. pp. 120692 (2026). DOI: 10.1016/j.measurement.2026.120692
   Impact factor: 5.6 **Ministry points:** 200
2. **Faisal Saleem**, Alicja Wiora, and Józef Wiora. Configuration and reduced-order modeling of a flow system based on experimental data. *Scientific Reports*, 15(1): 35294 (2025).
   DOI: 10.1038/s41598-025-19211-3
   Impact factor: 3.9 **Ministry points:** 140
3. Karol Marciniak, **Faisal Saleem**, and Józef Wiora. Influence of models approximating the fractional-order differential equations on the calculation accuracy. *Communications In Nonlinear Science And Numerical Simulation*. **131** pp. 107807 (2024).
   DOI: 10.1016/j.cnsns.2023.107807
   Impact factor: 3.8 **Ministry points:** 100

Conference proceedings

1. **Faisal Saleem**, Delfim F.M. Torres, and Józef Wiora. Propagation of Measurement Uncertainty Associated with Parameter Identification in Fractional-Order Dynamic Systems. *Conference On Automation*. (2026). Automation
   Presented: May 2026.
2. **Faisal Saleem**, Józef Wiora, Guido Maione, and Paolo Lino. Impact of approximation methods on the performance of fractional-order PI controllers designed in frequency domain. *2025 Signal Processing: Algorithms, Architectures, Arrangements, And Applications (SPA)*. pp. 34-39 (2025). DOI: 10.23919/SPA65537.2025.11215137
3. Józef Wiora, Alicja Wiora, and **Faisal Saleem**. Barriers to Implementing Digital Twin Technologies in Industrial Settings. *2025 IMEKO TC-6 International Conference on Metrology and Digital Transformation*. DOI: 10.21014/tc6-2025.037
4. **Faisal Saleem** and Józef Wiora. Applicability of Fractional-Order PID Controllers for Twin Rotor Aerodynamic System Objects. *Conference On Automation*. pp. 39-48 (2024). DOI: 10.1007/978-3-031-78266-4_4

Original work published as abstract

- **Faisal Saleem** and Józef Wiora, Kernelized PCA-based reduced-order linear parameter varying (LPV) modeling of twin rotor aerodynamic system. In: Materiały i technologie XXI wieku. XXV Międzynarodowa studencka konferencja naukowa, 16 maj 2024, Katowice. Materiały konferencyjne. Książka abstraktów / Maciąg Tomasz (eds.), 2024, pp.57-57, ISBN 978-83-7880-961-6

Publications outside of the dissertation topic

Journal articles

1. Muhammad Wasim, Ahsan Ali, **Faisal Saleem**, Inam Ul Hasan Shaikh, and Jamshed Iqbal. Robust adaptive control with lumped model uncertainty and wind disturbance estimation for airship trajectory tracking. *PLoS One*. **20**, e0335392 (2025).
   DOI: 10.1371/journal.pone.0335392
   Impact factor: 2.6 **Ministry points:** 100
2. Muhammad Wasim, Ahsan Ali, Mohammad Ahmad Choudhry, Inam Ul Hasan Shaikh, and **Faisal Saleem**. Robust design of sliding mode control for airship trajectory tracking with uncertainty and disturbance estimation. *Journal Of Systems Engineering And Electronics*. **35**, 242-258 (2024).
   DOI: 10.23919/JSEE.2024.000017
   Impact factor: 2.1 **Ministry points:** 40
3. Muhammad Ijaz, Rabia Nazir, Musaed Alhussein, Jameel Ahmad, Khursheed Aurangzeb, and **Faisal Saleem**. Digital resonant control of power converters under variable grid frequency conditions. *Frontiers In Energy Research*. **11** pp. 1272329 (2023). DOI: 10.3389/fenrg.2023.1272329
   Impact factor: 2.4 **Ministry points:** 100
4. Muhammad Jamshed Abbass, Robert Lis, and **Faisal Saleem**. The maximum power point tracking (MPPT) of a partially shaded PV array for optimization using the antlion algorithm. *Energies*. **16**, 2380 (2023). DOI: https://doi.org/10.3390/en16052380
   Impact factor: 3.2 **Ministry points:** 140
5. **Faisal Saleem**, Ahsan Ali, Inam Ul Hasan Shaikh, and Muhammad Wasim. Application and comparison of kernel functions for linear parameter varying model approximation of nonlinear systems. *Applied Mathematics-A Journal Of Chinese Universities*. **38**, 58-77 (2023). DOI: 10.1007/s11766-023-3965-8
   Impact factor: 1.3 **Ministry points:** 20

Contents

List of Figures

List of Tables

Listings

Acronyms

ABSC	Adaptive Backstepping Controller	67
AMPL	A Mathematical Programming Language	12
AS	Active Set	62
CA	Charef Approximation Method	17
CFE	Continued Fraction Expansion	1
CM	Carlson Method	15
CT	Computation Time	117
DC	Direct Current	31
DE	Differential Equation	3
DFT	Discrete Fourier Transform	23
DIE	Differ-Integral Equation	2
DISI	Dual Inertia Servo Inverter	29
DM	Dynamic Metrology	9
DOF	Degree of Freedom	90
FI	Flow Indicator	34
FO	Fractional-Order	1
FOMCON	Fractional-Order Modeling and Control	10
FT-T1	Turbine Flow Meter	34
FT-V	Vortex Flow Meter	34
GL	Grünwald-Letnikov	1
GUM	Guide to the Expression of Uncertainty in Measurement	1
IDE	Integrated Development Environment	43
IO	Integer-Order	1
IOD	Input-Output Data	34
IOFOD	Integer Order Approximation for Fractional Order Derivative	16
IP	Interior Point	62
IPOPT	Interior Point Optimizer	93
ISE	Integral Square Error	46
K-S	Kolmogorov-Smirnov	143

LPV	Linear Parameter Varying	5
LTI	Linear Time Invariant	26
M-SBL	Improved Stability Boundary Locus	15
MAE	Mean Absolute Error	71
MAPE	Mean Absolute Percentage Error	112
MIMO	Multi-Input Multi-Output	29
MM	Matsuda Method	14
NEOS-server	State-of-the-Art Solvers for Numerical Optimization	43
NFO	Nominal Fractional-Order	105
OM	Oustaloup Method	17
P	Water Pump	34
P&ID	Piping and Instrumentation Diagram	36
PCA	Principal Component Analysis	19
PDF	Probability Density Function	143
PDV	Preprocessed Data Variation	103
PI	Proportional Integral	3
PID	Proportional Integral Derivative	25
PMSM	Permanent Magnet Synchronous Motor	29
PRV	Preprocessed Residual Variation	110
Q-Q	Quantile-Quantile	143
RL	Riemann-Liouville	1
RO	Refined Oustaloup	17
SISO	Single-Input Single-Out	29
SIT	System Identification Toolbox	19
SQP	Sequential Quadratic Programming	72
SQPL	Sequential Quadratic Programming Legacy	62
SVD	Singular Value Decomposition	73
TF	Transfer Function	10
TO	Truncation Order	4, 5
TRAS	Twin Rotor Aerodynamic System	5
TRR	Trust Region Reflective	62
UDV	Unprocessed Data Variation	104

URV	Unprocessed Residual Variation	110
VFD	Variable Frequency Drive	34
XO	Xue Oustaloup	17

List of Symbols

Latin Symbols

Symbol	Units	Description	
h	–	Current sampling instant	74
K	–	Static gain of the system	17
k	–	Coverage factor for evaluation of expanded uncertainty	9
l	–	Current measurement pass	39
m	–	Truncation order of the Grünwald–Letnikov implementation	12
N	–	Number of independent measured values	8
n	–	Number of quantities influencing the measurand	8
$\hat{\mathbf{P}}$	–	Matrix of reduced parameters, $\hat{\mathbf{P}} \in \mathbb{R}^{n_r \times Q}$	73
$\mathbf{P}$	–	Parameter matrix, $\mathbf{P} \in \mathbb{R}^{p_n \times Q}$	73
$\tilde{\mathbf{P}}$	–	Matrix of the reconstructed parameters, $\tilde{\mathbf{P}} \in \mathbb{R}^{p_n \times Q}$	73
Q	–	Total number of frequency steps in one pass	39
q	–	Current index of the input steps	39
$\mathbf{S}$	–	Matrix of singular values, $\mathbf{S} \in \mathbb{R}^{p_n \times p_n}$	73
$\mathbf{\Sigma}_{\mathrm{p}}$	–	Positive-definite covariance matrix, $\mathbf{\Sigma}_{\mathrm{p}} \in \mathbb{R}^{p_n \times p_n}$	145
T	–	Generalized time constant of fractional order inertia	30
U	–	Expanded uncertainty	9
u	Hz	Input frequency for the flow rate measurement system	91
$\mathbf{U}$	–	Matrix of singular vectors, $\mathbf{U} \in \mathbb{R}^{n_r \times p_n}$	73
V	V	Input voltage to the electric motor in fractional-order inertia	29
w	–	Smallest integer greater than the fractional order α	12
$\bar{x}$	–	Estimate of the mean of the measured quantity	8
Y	–	Measurand	8

Greek Symbols

Symbol	Units	Description

Operators & Special Symbols

$f(\cdot)$	–	Measurement function mapping the measurand	8
$f(t)$	–	Time-dependent continuously differentiable function	10
$\Gamma(\cdot)$	–	Euler's gamma function	11
$G_{\mathrm{cl}}(s)$	–	Transfer function of the closed-loop system	62
$\hat{G}(s)$	–	Transfer function of the reduced-order model	73
$G_p(s)$	–	Transfer function of the pitch angle of TRAS	33
$G(s)$	–	Transfer function of the plant	15
$G_y(s)$	–	Transfer function of the yaw angle of TRAS	33
$\Im(G)$	–	Imaginary part of the transfer function	46
$\mathscr{J}^{\beta}$	–	Fractional integral of order β, $\beta > 0$	11
$\mathscr{D}^{\beta}_{\mathrm{RL}}$	–	Riemann–Liouville fractional-order integral	12
$\mathscr{L}$	–	Laplace transform	10
$L(s)$	–	Transfer function of the open-loop system	128
$\Re(G)$	–	Real part of the transfer function	46
$s(x)$	–	Estimate of the standard deviation of the quantity x	144
$u_A(x)$	–	Standard uncertainty evaluated by Type A methods	8
$u_c(y)$	–	Combined standard uncertainty	9
$u_D(y_{\mathrm{e}}(t))$	$\mathrm{m^3\,h^{-1}}$	Time-dependent uncertainty component in the estimated dynamic response by the fractional-order model	147

Symbols with subscripts

Symbol	Units	Description	
c_i	–	Sensitivity coefficients	9
E_{ISE}	–	Integral square error	46
E_{m}	$\mathrm{m^3/h}$	Mean absolute error using estimated and measured flow rate	85
E_{MAPE}	%	Mean absolute percentage error using the reference and estimated flow rates	112
e_{r}	$\mathrm{m^3/h}$	Root mean square error between the reference and estimated flow rates	112
f_{in}	Hz	Input frequency of the voltage operating the water pump	38
g^{α}_{m}	–	Grünwald coefficients of the fractional-order derivative	11

CHAPTER 1

Introduction

For every measurement, a measurement uncertainty should be reported together with the estimate of the measurand [1]. The uncertainty quantifies the quality of the measurement and reflects the inadequacy of knowledge about the measurand. The information deficiency about the measurand may arise from the calibration errors, sensor limitations, stochastic variability, environmental effects, etc. Consequently, the true value of measurand is unattainable [2, 3].

An estimate of the measurand can be obtained from the average of the measured quantity. The correctness of the estimate relies on the possibility of performing virtually infinite measurements under the same experimental conditions. As a result, the average value acquired from limited measurements is considered as an estimate of the average value. Owing to the challenges in attaining the accurate estimate of the measurand, the measurement results are reported as the measured quantity and the associated uncertainty component [2].

The "Guide to the Expression of Uncertainty in Measurement (GUM)" presents a foundational framework to evaluate the uncertainty [4]. The standardized framework by GUM is widely applied to numerous science and engineering applications. However, the classical GUM methods of uncertainty assessment, and their Monte Carlo extension are well suited for the stationary measurements. Several real-time applications, i.e., robots, drones, electric motors, flow system, etc., exhibit time-dependent responses.

Hence, the uncertainty becomes time-dependent, and its variation also depends on the system dynamics, including transients, long-memory effects, and bandwidth limitations [1, 5]. In such cases, model mismatch, parameter uncertainty, and numerical approximations become active sources of uncertainty propagation. Consequently, these effects distort key dynamic performance indices, including rise time, overshoot, and settling time. They also produce inconsistent probabilities when reported as bands around time-dependent trajectories. Hence, the accurate measurement models are also crucial to evaluating the dynamic uncertainty.

The Fractional-Order (FO) models have proven effective in numerous applications including diffusive and viscoelastic phenomena [6], fluid flow [7], robotics [8], and the systems whose behavior differs from the classical Integer-Order (IO) dynamics [9]. The FO model employ non-integer differ-integral operators – such as the Grünwald-Letnikov (GL), Caputo, Riemann-Liouville (RL) definitions – to implement non-integer order derivatives and integrals [10, 11]. These methods can accurately model the dynamics of the systems exhibiting memory effects and actuator lags [12]. Furthermore, IO approximations of FO derivatives used in practice, such as Oustaloup filters, Continued Fraction Expansion (CFE), Charef, and Matsuda methods, introduce approximation errors [13]. These errors influence the evaluation of dynamic uncertainty.

1.1 Problem statement

The FO approaches have become increasingly popular for modeling dynamic systems in many applications. However, there is still a lack of widely accepted or experimentally validated method for assessing time-dependent uncertainty in the outputs of these models. This gap becomes critical when:

1. models are developed by identifying parameters from noisy data,
2. the acquired data exhibits variable sampling time, or
3. FO Differ-Integral Equation (DIE) is implemented using numerical approximations.

The classical GUM based methods focus on the stationary measurements. The others, such as digital filtering, rely on parameter-space transformations. These transformations can reduce covariance of the parameters. Moreover, they make the results more difficult to interpret and implement. This dissertation addresses the problem of developing a direct, time-domain method for propagating parameter uncertainty through FO models. The considered models are identified from measured data that exhibits noise and variable sampling intervals. Additional, unmeasured effects such as temperature, humidity, friction, hysteresis, electromagnetic interference, etc., also contribute to modeling inaccuracies.

1.2 Motivation

Sensory measurements in dynamic systems capture response in transient and steady-state regions. These dynamic attributes arise from different physical mechanisms and distinct sources of uncertainty. Relying only on steady-state uncertainty can create a false sense of confidence. Such descriptions ignore amplification effects, rapid variations, and cross-interactions during the transient response. Many systems present transient responses that dominate the overall dynamic performance. These responses influence the modeling accuracy and controller performance in closed-loop systems. Therefore, a complete uncertainty assessment must consider a time-dependent evaluation.

The need for time-dependent uncertainty analysis becomes even more pronounced when modeling systems which exhibit FO dynamics. The FO models offer enhanced flexibility, memory-like characteristics, and improved accuracy for systems with distributed parameters or non-local behavior. These advantages make FO models effective to estimate transient and steady-state behaviors alike. However, despite their modeling potential, the analysis of measurement uncertainty within FO frameworks remains underdeveloped. Existing studies often emphasize nominal model accuracy or controller tuning, which offers a limited insight into uncertainty propagation through FO models. Furthermore, the influence of IO approximation methods on uncertainty propagation through FO models is worth analyzing. This gap is critical, because each of these factors directly influences the reliability of the estimated system behavior.

This dissertation addresses the aforementioned challenges by developing a unified framework to analyze the uncertainty propagation in FO models. It examines the influence of measurement noise and parameter variability on the accuracy and robustness of the modeled response. It also provides the tuning rules for FO Proportional Integral (PI) controller and analyzes the impact of IO approximation methods on the closed-loop performance. Because the practical implementations rely on such approximations, their effects on control accuracy, robustness, and long-term behavior require systematic assessment. The dissertation therefore integrates model identification, analysis of IO approximations, and propagation of measurement uncertainty into a coherent and comprehensive framework.

1.3 Objectives

The dissertation addresses the problem of measurement uncertainty in non-integer-order differ-integral systems. Such systems appear widely in control engineering, fluid dynamics, and sensor-driven processes. Their modeling remains challenging due to nonlinear behavior, noisy measurements, and fractional-operator approximations.

This work presents IO and FO modeling approaches derived from experimental data and introduces tuning rules for the FO-PI controller. It analyses the influence of IO approximation methods for fractional operators and examines their impact on FO-based controller performance. The studies show that the selected approximation model, controller structure, and estimation method strongly affect the dynamic response. By combining theoretical analysis, numerical simulations, and laboratory tests, the dissertation develops a unified framework for quantifying measurement uncertainty in FO dynamic systems. The dissertation verifies these approaches through numerical simulations and experimental data for specific case studies. Building on these foundations, the dissertation pursues the following research objectives.

Obj.1 Analyze the influence of models approximating the FO Differential Equation (DE).

Obj.2 Develop a mathematical modeling approach to estimate the dynamic response of a laboratory flow rate measurement system for a broad operating range.

Obj.3 Conceptualize FO modeling as an optimization problem with GL-based FO-DIE and construction of a nominal FO model for a laboratory flow rate measurement system.

Obj.4 Analyze the robustness and performance accuracy of the FO model for a laboratory flow rate measurement system and its comparison with the classical IO models.

Obj.5 Propose tuning rules for FO-PI controller and analyze the impact of approximation methods on the closed-loop performance for specific case studies.

Obj.6 Develop a dynamic uncertainty propagation framework for FO models using time-dependent sensitivity coefficients.

1.4 Hypothesis

Modern control engineering increasingly employs FO modeling to capture complex dynamical behaviors. Fractional operators offer enhanced flexibility and describe processes with memory, hereditary effects, or distributed dynamics. Reliable FO models require careful attention to modeling assumptions, numerical implementations, and uncertainty sources. The following hypotheses provide the theoretical basis for analyzing these aspects within the proposed identification and uncertainty-quantification framework. The hypotheses of this work are listed as:

H.1 The FO methods can accurately model the complex nonlinear systems with fewer parameters compared to classical IO approaches.

H.2 For FO models constructed via GL operators, finite-memory and discretization choices (e.g., Truncation Order (TO) of GL coefficients) introduce predictable contributions to the model accuracy and consequently to the measurement uncertainty. The TO can be tuned to construct a robust FO model with increased accuracy.

H.3 The uncertainty component attributable to identified parameters can be isolated and quantified in the output space without requiring intermediate transformations. Thus, it yields a simpler analysis and clear interpretability.

1.5 Contributions

The development of robust FO modeling and control strategies demands clear methodological advances supported by rigorous analysis and experimental evidence. Recent progress in identification techniques, controller design, and uncertainty evaluation highlights the need for an integrated framework that unifies these elements within a coherent engineering workflow. This dissertation addresses these challenges and presents contributions that strengthen the theoretical foundations and practical applicability of FO methods in modeling, control, and metrology. The key contributions of the dissertation are:

C.1 Conceptualization of FO modeling as an optimization problem that constructs an FO model incorporating measurement uncertainty, along with experimental validation for accuracy analysis.

C.2 Tuning rules for designing FO-PI controllers using the classical frequency-domain approach, along with their validation for two case studies.

C.3 A conceptual framework for assessing the uncertainty propagated by the identified parameters in the dynamic response of FO-DIE-based measurement models.

C.4 Practical guidelines for researchers and metrologists on integrating FO modeling with uncertainty evaluation.

C.5 Analysis of the uncertainty components propagated by the identified parameters under different implementations of the FO-DEs.

1.6 Organization of the thesis

The contents of the dissertation are organized as follows.

Chapter 2 provides a brief review of metrological foundations. It presents definitions of FO operators and discusses relevant approximation methods to realize FO operators. Finally, the chapter reviews related studies reported in the literature.

Chapter 3 presents the case studies used as application examples to validate the proposed approaches. The case studies include FO inertia without delay, Twin Rotor Aerodynamic System (TRAS), and a laboratory flow rate measurement system. The chapter also describes the laboratory hardware configuration. It presents data acquisition algorithms. Furthermore, it discusses data sets used for modeling the flow rate measurement system.

Chapter 4 presents accuracy analysis of the approximation methods listed in Chapter 2 for realizing FO operators. The analysis uses MATLAB simulations for TRAS and FO inertia model without delay from Chapter 3.

Chapter 5 presents Linear Parameter Varying (LPV) approach to model the laboratory flow rate measurement system. The chapter uses the experimental data from a laboratory hardware setup presented in Chapter 3. Furthermore, it compares the results of the proposed approach with classical IO models.

Chapter 6 addresses the limitations of the modeling approach presented in Chapter 5. It proposes a FO modeling approach for the flow system presented in Chapter 3. The approach uses a constant input instead of the full operating range and investigates the applicability of FO modeling to accurately represent the dynamics of a complex nonlinear system. This chapter implements the GL formulation of the FO operators. It evaluates model robustness by introducing bounded parameter perturbations and analyzing their influence on the estimated response. It further examines the influence of the TO of GL coefficients and solver selection on modeling accuracy.

Chapter 7 presents tuning rules for designing FO-PI controllers. It develops a control design approach using TRAS. It also analyzes the influence of the approximation methods in Chapter 4 on the closed-loop response. This method enables evaluation of uncertainty propagation in the closed-loop response, as presented in Chapter 8.

Chapter 8 builds on the conclusions presented in Chapter 6. It develops a FO time-delay model for the flow system in Chapter 3 under a constant input. For the identified FO model, it proposes a framework to analyze the propagation of measurement uncertainty associated with the estimated parameters. It then applies the tuning rules from Chapter 7 to design a FO-PI controller for the flow system. Using the closed-loop structure, it evaluates the uncertainty propagated in the dynamic response. It further analyzes the influence of different implementations of FO operators on uncertainty assessment.

Finally, Chapter 9 summarizes the findings, contributions, and limitations of the methods presented in each chapter of the dissertation. It also proposes future research directions to address the identified limitations. Table 1.1 summarizes chapter-wise traceability of research outcomes across the dissertation.

Table 1.1: Traceability of research objectives, methodologies, validation approaches, outcomes, and contributions.

Chapter	Research objective	Methodology	Validation Approach	Outcome	Contribution
Chapter 4	**Obj.1**	Accuracy analysis	Simulations	Achieved	–
Chapter 5	**Obj.2**	Reduced-order modeling	Experiments	Achieved	–
Chapter 6	**Obj.3**; **Obj.4**	FO modeling framework	Experiments & simulations	Achieved; **H.1** and **H.2** (100 % verified)	**C.1**
Chapter 7	**Obj.5**	Tuning rules for FO controller	Simulations	Achieved	**C.2**
Chapter 8	**Obj.6**	Dynamic uncertainty propagation framework	Experiments	Achieved; **H.3** (100 % verified)	**C.3**; **C.4**; **C.5**

CHAPTER 2

Background and Literature Review

This chapter presents the background knowledge and key definitions related to metrology and FO calculus. It also defines popular approximation methods used for practical realization of FO operators. Furthermore, it discusses several studies from the literature related to the objectives of the dissertation.

2.1 Foundations of metrology

The experimental process to obtain one or more values of the clearly specified quantity using a defined method, a calibrated system, and documented procedure under controlled actions is defined as the measurement [4]. The clearly specified quantity intended to be measured is known as the measurand. Since the measurement is related to real systems, the imperfect instruments and incomplete models result in an estimate rather than the exact value [2, 14]. Consequently, measurement results should be presented by a complete report containing the measured quantity and the associated uncertainty. The uncertainty associated with the measurement result characterizes the quality of the measurement [2, 4]. Therefore, a measurement result consists of the value attributed to the measurand together with the associated measurement uncertainty. Other pertinent information, such as applied corrections and environmental conditions, forms part of the measurement report.

Measurement uncertainty has several defining characteristics that distinguish it fundamentally from measurement error. Measurement uncertainty is a "non-negative parameter that characterizes the dispersion of the quantity values that could reasonably be attributed to the measurand" [15]. It includes contributions from all recognized sources, such as incomplete definition of the measurand, environmental influences, finite resolution of the measuring instrument, and other relevant effects [4]. It quantifies the dispersion of the values that could reasonably be attributed to the measurand, after all recognized influence quantities and corrections have been taken into account. By contrast, measurement error is the difference between a measured value (or indication) and a reference value; the reference may be a conventional true value or a calibrated value with stated uncertainty [15].

In metrology, error is commonly decomposed into random error, arising from unpredictable variations in influence quantities, and systematic error, arising from persistent or predictable effects. After applying known corrections, a residual systematic error may remain [4]. Although corrections can be applied to account for systematic effects, a residual systematic error may remain unknown because the true value is not available. These characteristics imply that measurement error and measurement uncertainty are distinct concepts and must be treated separately; they should not be conflated [4, 15].

A set of devices combined with a mathematical structure which maps the input to the measured signal through a defined transformation is known as the measurement system [4, 15]. The output of a measurement system may represent either a time-independent quantity or a time-dependent quantity. Consequently, the associated measurement uncertainty may also be time-independent or time-dependent [5]. The time-dependent component of the uncertainty is commonly referred to as dynamic uncertainty [1].

2.1.1 Measurement uncertainty

The GUM provides a standardized framework for uncertainty assessment in measurements of stationary quantities characterized by constant parameters. Considering a measurand Y is dependent on the n other quantities $X_1, X_2, ..., X_n$, the measurand is mapped by a function $f(\cdot)$:

$$Y = f(X_1, X_2, ..., X_n). \tag{2.1}$$

The unavailability of the measurands X_i, $i \in \{1, 2, ..., n\}$ enforces the use of the respective estimates x_i, $i \in \{1, 2, ..., n\}$ [4]. The uncertainty component are evaluated as Type A and Type B. The Type A is the component evaluated by statistical analysis of the repeated observations whereas Type B uses the scientific judgments from well defined information, i.e., calibration certificates, manufacturer specifications, or other published data [4].

Standard uncertainty

Type A standard uncertainty requires the mean, standard deviation, and standard deviation of the mean. However, the inability to perform infinite measurements limits enforces the use of estimate of the mean $\bar{x}$ of the measured quantity x [2]:

$$\bar{x} = \frac{1}{N} \sum_{i=1}^{N} x_i \tag{2.2}$$

where N denotes the number of independent measured values of the estimate x of measurand X. The estimate of the arithmetic mean is used to calculate the experimental standard deviation:

$$s(x) = \sqrt{\frac{1}{N-1} \sum_{i=1}^{N} (x_i - \bar{x})^2}, \tag{2.3}$$

which leads to the standard uncertainty $u_A(x)$:

$$u_A(x) = \frac{s(x)}{\sqrt{N}}. \tag{2.4}$$

Combined uncertainty

The combined standard uncertainty $u_c(y)$ is obtained by applying the law of propagation of uncertainty to the input quantities in the measurement model. The law of propagation when the input quantities are correlated is [4]:

$$u_c^2(y) = \sum_{i=1}^{N} c_i^2 u^2(x_i) + 2 \sum_{i=1}^{N-1} \sum_{j=i+1}^{N} c_i c_j v(x_i, x_j), \tag{2.5}$$

where c_i are the sensitivity coefficients defined by:

$$c_i = \left. \frac{\partial f}{\partial x_i} \right|_{x_1,\ldots,x_N}. \tag{2.6}$$

Moreover, $u(x_i)$ and $v(x_i, x_j)$ denote the standard uncertainty of input X_i, and the covariance between the estimates of X_i and X_j, respectively. The variables x_i and x_j denote the estimates of the inputs X_i and X_j. The combined uncertainty, when the input quantities are uncorrelated, is [2]:

$$u_c(y) = \sqrt{\sum_{i=1}^{N} (c_i u(x_i))^2}. \tag{2.7}$$

Expanded uncertainty

The GUM standardizes reporting the uncertainty by forming the expanded uncertainty U [4]:

$$U = k\, u_c(y) \tag{2.8}$$

where k denotes the coverage factor. The coverage factor defines the level of confidence. A common choice sets $k = 2$, which yields a coverage probability of about 95 % for measurement processes whose output quantity follows a normal distribution.

2.1.2 Dynamic metrology

Many measurement results exhibit non-stationary characteristics and therefore cannot be described using quantities that remain constant in time [1]. As a result, the associated measurement uncertainty cannot be expressed as a time-independent quantity. To address this, traditional GUM-based metrology has been extended to the domain of Dynamic Metrology (DM) in order to incorporate metrological principles for time-dependent measured values and their associated uncertainties [5, 16, 17].

Unlike the traditional metrology which assumes stable measurands, the DM considers the measurand as a time-dependent function. The measurand is reconstructed from the system output which has been distorted from the dynamic characteristics of the measurement system. Therefore, the dynamic model describing the time-dependent response of the measurement system holds a key importance in DM.

The sensors, actuators, and the associated hardware of the measurement system exhibit a dynamic response. This dynamic response is typically characterized by an impulse response function in the Laplace domain, known as Transfer Function (TF). The time-dependent dynamic behavior of the measurement systems can also be described by DIEs in time domain. Since both the measurand and the system response vary with time, the associated uncertainty and dynamic errors are also time-dependent. The errors include instantaneous difference between the measured and reference values, while the uncertainty can be described by the time-dependent functions [16].

2.2 Fractional-order calculus

FO calculus has gained popularity for modeling and control of physical phenomena in recent years [18, 19]. The FO-DIEs capture the dynamic behavior of real-time systems [20], chemical and biological processes [21, 22], materials [9], and wave propagation [23]. These capabilities reinforce the role of FO calculus in modeling. The Fractional-Order Modeling and Control (FOMCON) toolbox [24] further supports this role by enabling efficient implementation of modeling, identification, and control design for real-time applications.

The fractional differentiation of α order of a continuous function $f(t)$, denoted by $\mathcal{D}^\alpha f(t)$ can be given as [10]:

$$\mathcal{D}^\alpha f(t) = \begin{cases} \frac{d^\alpha}{dt^\alpha} f(t) & \text{if } \alpha > 0, \\ f(t) & \text{if } \alpha = 0, \\ \int f(\tau)(d\tau)^{-\alpha} & \text{if } \alpha < 0, \end{cases} \tag{2.9}$$

where $\alpha \in \mathbb{R}$ is a real number. The operators $\frac{d^\alpha}{dt^\alpha} f(t)$ and $\int f(\tau)(d\tau)^{-\alpha}$ denote the FO derivative and integral, respectively, of order α of the function $f(t)$.

The FO operator $\mathcal{D}^\alpha$ can be considered a FO derivative when $\alpha > 0$ and a FO integral when $\alpha < 0$. The Laplace transforms $\mathscr{L}$ of the FO derivative and integral by assuming zero initial conditions for $\alpha > 0$ are [25]

$$\mathscr{L}\{\mathcal{D}^\alpha f(t)\} = s^\alpha F(s) \tag{2.10}$$

and

$$\mathscr{L}\{\mathcal{D}^{-\alpha} f(t)\} = s^{-\alpha} F(s), \tag{2.11}$$

respectively.

2.2.1 Definitions of FO derivatives and integrals

Several ways to define the FO differ-integral equations have been proposed in the literature. The classical definitions of FO operators include GL, RL, and Caputo [26–29]. Literature also presents numerous alternative definitions of FO derivatives, i.e., Weyl [30], Marchaud [30, 31], Riesz [32], Hadamard [33], etc. Several variants of the FO operators combining properties of different operators are also available. For example, the Hilfer derivative combines RL and Caputo derivatives by introducing a type parameter for continuous transition between RL and Caputo [34]. Many additional definitions using Mittag-Leffler kernels such as Atangana–Baleanu [35] and Atangana–Baleanu Caputo [36], etc., are also available to choose from the literature.

However, selecting a FO definition to implement the FO operator depends on the application under consideration. Because this study compares the performance of the GL, RL, and Caputo, it presents definitions only for these operators.

To distinguish from the notations in Eq. (2.9), separate variables are introduced – α denotes the order of FO derivative and β denotes the order of FO integral. Furthermore, the FO derivative and integral are denoted by $\mathscr{D}^\alpha$ and $\mathscr{I}^\beta$, respectively. These notations assume positive values for α and β.

Grünwald-Letnikov FO derivative and integral

The GL derivative and integral of a function $f(t)$ are [11]:

$$\mathscr{D}^\alpha f(t) = \lim_{M\to\infty} \frac{1}{\Delta t^\alpha} \sum_{m=0}^{M} g_m^\alpha \cdot f(t - m \cdot \Delta t), \tag{2.12}$$

and

$$\mathscr{I}^\beta f(t) = \lim_{M\to\infty} \Delta t^\beta \sum_{m=1}^{M} g_m^\beta \cdot f(t - m \cdot \Delta t), \tag{2.13}$$

where g_m^α and g_m^β denote the Grünwald coefficients of FO derivative and FO integral, respectively. Moreover, Δt denotes the sampling interval for computing the numerical differentiation and integration. The GL coefficients are calculated as [37]:

$$g_m^\alpha = \frac{\Gamma(\alpha+1)}{\Gamma(m+1)\cdot\Gamma(\alpha-m+1)} \tag{2.14}$$

and

$$g_m^\beta = \frac{\Gamma(\beta+m)}{\Gamma(\beta)\cdot\Gamma(m+1)} \tag{2.15}$$

where $\Gamma(\cdot)$ represents the Euler's gamma function, which is defined as [38]:

$$\Gamma(w) = \int_0^\infty t^{w-1} e^{-t}\, dt, \tag{2.16}$$

where $w \in \mathbb{R}$. The variable w is a general representation, which can take notations of α for the FO derivative and β for the FO integral. The recursive computation of the Grünwald coefficients provides a practical workaround for software such as A Mathematical Programming Language (AMPL) which are unable to directly evaluate $\Gamma(\cdot)$ [14]. The recursive computations for g_m^α and g_m^β are [39]:

$$g_m^\alpha[m] = \begin{cases} 1 & \text{if } m = 0, \\ (-1) \cdot \frac{\alpha_0 - m + 1}{m} \cdot g_m^\alpha[m-1] & \text{if } m > 0 \end{cases} \tag{2.17}$$

and

$$g_m^\beta[m] = \begin{cases} 1 & \text{if } m = 0, \\ \frac{\beta_0 + m - 1}{m} \cdot g_m^\beta[m-1] & \text{if } m > 0 \end{cases} \tag{2.18}$$

where m is the TO of the GL implementation. The order m influences the implementation error and computation time in numerical solution of the GL-based DIEs [14, 40].

Riemann–Liouville FO derivative and integral

The RL derivative of order α, $\mathscr{D}_{\mathrm{RL}}^\alpha$ and integral of order β, $\mathscr{D}_{\mathrm{RL}}^\beta$ are given by [41, 42]:

$$\mathscr{D}_{\mathrm{RL}}^\alpha f(t) = \frac{d^w}{dt^w}\left[\frac{1}{\Gamma(w-\alpha)}\int_0^t (t-\tau)^{w-\alpha-1} f(\tau)\, d\tau\right] \qquad \text{for } w-1 < \alpha < w \tag{2.19}$$

and

$$\mathscr{I}_{\mathrm{RL}}^\beta f(t) = \frac{1}{\Gamma(\beta)}\int_0^t (t-\tau)^{\beta-1} f(\tau)\, d\tau \qquad \text{for } \beta > 0, \tag{2.20}$$

respectively. Moreover, w is the smallest integer greater than α defined as $w = \lceil \alpha \rceil$.

Caputo FO derivative

Definition of Caputo FO derivative of order α, $\mathscr{D}_{\mathrm{C}}^\alpha$ is [43]:

$$\mathscr{D}_{\mathrm{C}}^\alpha f(t) = \frac{1}{\Gamma(w-\alpha)}\int_0^t (t-\tau)^{w-\alpha-1} \frac{d^w f(\tau)}{d\tau^w}\, d\tau \qquad \text{for } w-1 < \alpha < w \tag{2.21}$$

The Caputo derivative is defined by modifying the order of operations, not by introducing a new fractional integral operator. The relation between $\mathscr{D}_{\mathrm{C}}^\alpha$ and $\mathscr{D}_{\mathrm{RL}}^\alpha$ of a function $f(t)$ are given by [41]:

$$\mathscr{D}_{\mathrm{RL}}^\alpha f(t) = \frac{d^w}{dt^w}\left(\mathscr{I}_{\mathrm{RL}}^{w-\alpha} f(t)\right) \qquad \text{for } w-1 < \alpha < w \tag{2.22}$$

and

$$\mathscr{D}_{\mathrm{C}}^{\alpha} f(t) = \mathscr{I}_{\mathrm{RL}}^{w-\alpha}\left(\frac{d^{w}}{dt^{w}} f(t)\right) \qquad \text{for } w-1<\alpha<w, \tag{2.23}$$

respectively. Moreover, the implementation of Caputo FO integral is identical to Eq. (2.20). The FO integral operator in both frameworks are same in the sense that:

- The RL fractional integral serves as the foundation,
- The Caputo derivative is defined by first taking the IO derivative, then applying the RL fractional integral [44].

2.2.2 Approximation methods for FO operators

In the Laplace domain, the operation $\mathscr{D}^{\alpha} f(t)$,assuming zero initial conditions, is equivalent to $s^{\alpha} F(s)$. The below-presented methods aim to approximate the FO-DE with classical integration and/or differentiation.

Continued fraction expansions approximation method

The CFE method replaces the fractional order of the Laplace operator s with a continued fraction to obtain a rational function [45]. CFE uses a mathematical tool known as continued fractions, which are based on recursion. To begin with, CFE uses the following substitution [46, 47]:

$$s^{\alpha} = (1+v)^{\alpha}. \tag{2.24}$$

The expansion of $(1+v)^{\alpha}$ is as follows:

$$(1+v)^{\alpha} = 1+\cfrac{\alpha v}{1+\cfrac{(1-\alpha)v}{2+\cfrac{(1+\alpha)v}{3+\cfrac{(2-\alpha)v}{2+\cfrac{(2+\alpha)v}{5+\cfrac{(3-\alpha)v}{2+\cfrac{(3+\alpha)v}{7+\ldots}}}}}}} = b_0+\cfrac{a_1}{b_1+\cfrac{a_2}{b_2+\cfrac{a_3}{b_3+\cfrac{a_4}{b_4+\cfrac{a_5}{b_5+\cfrac{a_6}{b_6+\cfrac{a_7}{b_7+\ldots}}}}}}}. \tag{2.25}$$

This continued fraction can also be written using the line notation as

$$(1+v)^{\alpha} = b_0+\frac{a_1}{b_1+}\,\frac{a_2}{b_2+}\,\frac{a_3}{b_3+\ldots}. \tag{2.26}$$

where $b_0 = 1$, $b_j = 2$, and $b_{j+1} = j+1$ for $j = 2N_{\mathrm{F}}$, $N_{\mathrm{F}} \geq 1$, and $a_1 = \alpha v$, $a_j = (N_{\mathrm{F}}-\alpha)v$, $a_{j+1} = (N_{\mathrm{F}}+\alpha)v$ for $j = 2N_{\mathrm{F}}$, $N_{\mathrm{F}} \geq 1$. In the next step, the value of s^{α} is obtained by substituting $v = s-1$. Only one parameter, the order of approximation N_{F}, is available to select in this model. CFE performs well for low frequencies and does not require specifying the frequency range of operation [46]. Increasing the order of the model results in a better fit and a wider frequency range. However, a significant increase in the order of the model does not lead to a proportionally significant increase in the usable frequency range [46]. The main limitation of this model is that only one parameter, N_{F}, can be adjusted.

Matsuda approximation model

Being an extension of the CFE approach, the Matsuda approximation method produces a recursive model [13]. The model is constructed to fit points that are uniformly distributed in the frequency domain over a specified range [48]. The Matsuda method allows to select the frequency band $\omega = [\omega_b, \omega_h]$, where ω_b and ω_h denote the lower and upper frequency limits, respectively. For the chosen band, the Matsuda Method (MM) first computes the frequencies as follows:

$$\omega_k = \left\{ \begin{array}{ll} \omega_b \left(\frac{\omega_h}{\omega_b}\right)^{\frac{k-1}{N_F-1}} & \text{if } N_{\mathrm{F}} > 1 \\ \omega_h & \text{if } N_{\mathrm{F}} = 1 \end{array} \right\}. \tag{2.27}$$

where N_{F} is the order of approximation.

Next, it evaluates the gains corresponding to these frequencies as [49]:

$$d_{N_{\mathrm{F}}}(\omega_k) = \begin{cases} |G(j\omega_k)| & \text{if } N_{\mathrm{F}} = 0 \\ \frac{\omega_k - \omega_{N_{\mathrm{F}}-1}}{d_{N_{\mathrm{F}}-1}(\omega_k) - d_{N_{\mathrm{F}}-1}(\omega_{N_{\mathrm{F}}-1})} & \text{if } N_{\mathrm{F}} = 1, 2, 3, ..., N_{\mathrm{F}} \end{cases} \tag{2.28}$$

Solving the above expressions yields an upper triangular matrix of dimension $(2N_{\mathrm{F}} + 1) \times (2N_{\mathrm{F}} + 1)$:

$$D = \begin{bmatrix} d_0(\omega_0) & d_0(\omega_1) & \dots & d_0(\omega_{N_{\mathrm{F}}}) \\ 0 & d_1(\omega_1) & \dots & d_1(\omega_{N_{\mathrm{F}}}) \\ 0 & 0 & \ddots & \vdots \\ 0 & 0 & \dots & d_{N_F}(\omega_{N_{\mathrm{F}}}) \end{bmatrix}. \tag{2.29}$$

The coefficients contained in D are subsequently used to construct the continued fraction expansion in the form

$$s^\alpha = D_{11} + \frac{s - \omega_0}{D_{22} + \frac{s-\omega_1}{D_{33} + \frac{s-\omega_2}{D_{44}+\dots}}} = D_{11} + \frac{s - \omega_0}{D_{22}+} \, \frac{s - \omega_1}{D_{33}+} + \dots. \tag{2.30}$$

Increasing the model order within the selected frequency range enhances the accuracy of the Matsuda approximation. This provides an advantage over the conventional CFE method, which does not permit the selection of a frequency range.

Carlson approximation methods

The approximation method introduced by Carlson is derived from the classical Newton iteration process [49]. This method relies on the following relation [49]:

$$H(s)^{1/\alpha} - G(s) = 0 \tag{2.31}$$

Rearranging this yields:

$$H(s) = (G(s))^{\alpha} \tag{2.32}$$

The Carlson Method (CM) starts with the initial condition $H_0(s) = 1$ [49, 50]. Subsequent values of $H_i(s)$ are then computed recursively. Two formulations of $H_i(s)$ exist in the literature. The first expression is given in [49, 51]:

$$H_i(s) = H_{i-1}(s)\frac{(q-m)H_{i-1}^2(s) + (q+m)G(s)}{(q+m)H_{i-1}^2(s) + (q-m)G(s)} \qquad \text{for } i = 1, \ldots, N_F \tag{2.33}$$

where $q = \frac{1}{\alpha}$ and $m = \frac{q}{2}$.

The second formulation is provided in [50]:

$$H_i(s) = H_{i-1}(s)\frac{\left(\frac{1}{\alpha}-1\right)H_{i-1}^{1/\alpha}(s) + \left(\frac{1}{\alpha}+1\right)s}{\left(\frac{1}{\alpha}+1\right)H_{i-1}^{1/\alpha}(s) + \left(\frac{1}{\alpha}-1\right)s} \qquad \text{for } i = 1, \ldots, N_F \tag{2.34}$$

Equation (2.34) can be applied directly only when $\frac{1}{\alpha}$ is an integer, that is, when $\frac{1}{\alpha} \in \{\pm 2, \pm 3, \ldots\}$. In such cases, non-integer values of $\frac{1}{\alpha}$ are represented as products of elementary operators.

Consequently, the resulting order of the TF may differ even for models intended to approximate the same operator. For instance, for a first-order construction, the TF order is one for $s^{0.1}$, two for $s^{0.3} = s^{0.2} \times s^{0.1}$, and three for $s^{0.4} = s^{0.1} \times s^{0.3}$. For many other exponents, the resulting order can be even higher.

Improved stability boundary locus fitting method

Improved Stability Boundary Locus (M-SBL) works in a similar manner as curve fitting. It operates by fitting the stability boundary locus of (s^{α}) and its approximation model [46]. This method finds the model parameters which provide the best fitting to the sample points selected in the frequency domain. The M-SBL solves the system of equations for real and imaginary parts together. This results in a linear system of equations. As in the Matsuda method, the points are equally spaced on the logarithmic scale of frequency. This method bases on the implementation of a closed-loop control system consisting of an object and a PI controller. The characteristic equation of the closed-loop TF can be

$$D(s) = 1 + C(s)G(s) \tag{2.35}$$

where $G(s)$ and $C(s)$ are the TF of the plant and PI controller, respectively. Here,

$G(s) = s^\alpha$ and $C(s) = k_\mathrm{P} + \frac{k_\mathrm{I}}{s}$. As a result, the following equation is obtained.

$$D(s) = 1 + \left(k_\mathrm{P} + \frac{k_\mathrm{I}}{s}\right) s^\alpha = 0 \tag{2.36}$$

Assuming $s = j\omega$, where $j = \sqrt{-1}$, and $s^\alpha = (j\omega)^\alpha = \omega^\alpha[\cos(\frac{\pi}{2}\alpha) + j\sin(\frac{\pi}{2}\alpha)]$, a system of equations is solved. The approximated model obtained for s^α is

$$G_{N_\mathrm{F}}(s) = \frac{a_0 s^{N_\mathrm{F}} + a_1 s^{N_\mathrm{F}-1} + \ldots + a_{N_\mathrm{F}-1}s + a_{N_\mathrm{F}}s^0}{a_{N_\mathrm{F}} s^{N_\mathrm{F}} + a_{N_\mathrm{F}-1} s^{N_\mathrm{F}-1} + \ldots + a_1 s + a_0 s^0}, \tag{2.37}$$

where $a_{N_\mathrm{F}} = 1$ and N_F is the order of approximation. The characteristic equation for this plant and the PI controller becomes [46]:

$$\Delta_{N_\mathrm{F}}(j\omega) = 1 + C(s)G_{N_\mathrm{F}}(s). \tag{2.38}$$

The frequency domain expression of this equation is [46]:

$$\Delta_{N_\mathrm{F}}(j\omega) = \sum_{r=0}^{N_\mathrm{F}} \left[(j\omega)^{r+1} - (j\omega)^{N_\mathrm{F}-r+1}\frac{\cos\left(\frac{\pi}{2}\alpha\right)}{\omega^\alpha} - (j\omega)^{N_\mathrm{F}-r}\frac{\sin\left(\frac{\pi}{2}\alpha\right)}{\omega^{\alpha-1}}\right] a_r = 0, \tag{2.39}$$

assuming $\chi_r = (j\omega)^{r+1} - (j\omega)^{N_\mathrm{F}-r+1}\frac{\cos(\frac{\pi}{2}\alpha)}{\omega^\alpha} - (j\omega)^{N_\mathrm{F}-r}\frac{\sin(\frac{\pi}{2}\alpha)}{\omega^{\alpha-1}}$. The simpler form of the above equation is

$$\Delta_{N_\mathrm{F}}(j\omega) = \sum_{r=0}^{N_\mathrm{F}} \chi_r a_r = 0, \tag{2.40}$$

or

$$\sum_{k=1}^{N_\mathrm{F}} \sum_{r=0}^{N_\mathrm{F}-1} \chi_{rk} a_r = -\sum_{k=1}^{N_\mathrm{F}} \chi_{N_\mathrm{F}k}\, a_{N_\mathrm{F}}, \tag{2.41}$$

which results in the following system of equations [46]:

$$[\chi_{rk}][a_0 \quad a_1 \quad \ldots \quad a_{N_\mathrm{F}-1}]^T = [-\chi_{N_\mathrm{F}1} \quad -\chi_{N_\mathrm{F}2} \quad \ldots \quad -\chi_{N_\mathrm{F}N_\mathrm{F}}]^T. \tag{2.42}$$

The values of χ_{rk} and $\chi_{N_F k}$ can be calculated as:

$$\chi_{rk} = (j\omega_k)^{r+1} - (j\omega_k)^{N_\mathrm{F}-r+1}\frac{\cos\left(\frac{\pi}{2}\alpha\right)}{\omega_k^\alpha} - (j\omega_k)^{N_\mathrm{F}-r}\frac{\sin\left(\frac{\pi}{2}\alpha\right)}{\omega_k^{\alpha-1}}, \tag{2.43}$$

$$\chi_{N_\mathrm{F}k} = (j\omega_k)^{N_\mathrm{F}+1} - j\omega_k\frac{\cos\left(\frac{\pi}{2}\alpha\right)}{\omega_k^\alpha} - \frac{\sin\left(\frac{\pi}{2}\alpha\right)}{\omega_k^{\alpha-1}}. \tag{2.44}$$

This method allows modification of three parameters: N_F, ω_b, and ω_h. A built-in function `M_SBL()` facilitates the implementation of M-SBL in `MATLAB`. This function is available in the Integer Order Approximation for Fractional Order Derivative (IOFOD) toolbox [52].

Oustaloup approximation method

The IO approximation of the term $G(s) = s^\alpha$ over the frequency band $[\omega_b, \omega_h]$ with Oustaloup Method (OM) is given by [53]:

$$G(s) = K \prod_{i=1}^{N_\mathrm{F}} \frac{s + z_i}{s + p_i} \qquad \text{for } 0 < \alpha < 1, \tag{2.45}$$

where $z_i = K\,\omega_b \omega_u^{(2i-1+\alpha)/N_\mathrm{F}}$ and $p_i = \omega_b \omega_u^{(2i-1+\alpha)/N_\mathrm{F}}$ – z_i and p_i denote the locations of zeros and poles, respectively. The parameter K denotes the static gain of the system. For OM, it is calculated by $K = \omega_h^\alpha$. Furthermore, $\omega_u = \sqrt{\omega_h/\omega_b}$ and N_F is the approximation order. Its implementation within the FOMCON toolbox is described in [10]. Refined Oustaloup (RO) and Xue Oustaloup (XO) approximations are given as [10]:

$$s^\alpha \approx \left(\frac{d}{b}\omega_h\right)^\alpha \frac{ds^2 + b\omega_h s}{d(1-\alpha)s^2 + b\omega_h s + d\alpha} \prod_{k=-N_\mathrm{F}}^{N_\mathrm{F}} \frac{s + p_\mathrm{F}}{s + z_\mathrm{F}}, \tag{2.46}$$

and

$$s^\alpha \approx \left(\frac{d}{b}\omega_h\right)^\alpha \left(\prod_{k=-N_\mathrm{F}}^{N_\mathrm{F}} \frac{z_\mathrm{X}}{p_\mathrm{X}}\right) \frac{ds^2 + b\omega_h s}{d(1-\alpha)s^2 + b\omega_h s + d\alpha} \prod_{k=-N_\mathrm{F}}^{N_\mathrm{F}} \frac{s + p_\mathrm{X}}{s + z_\mathrm{X}}, \tag{2.47}$$

respectively, where

$$p_\mathrm{F} = \omega_b \omega_u^{(k+N_\mathrm{F}+\frac{1}{2}-\frac{1}{2}\alpha)/(2N_\mathrm{F}+1)},$$

$$z_\mathrm{F} = \omega_b \omega_u^{(k+N_\mathrm{F}+\frac{1}{2}+\frac{1}{2}\alpha)/(2N_\mathrm{F}+1)},$$

$$p_\mathrm{X} = \left(\frac{d}{b}\omega_h\right)^{(\alpha-2k)/(2N_\mathrm{F}+1)},$$

$$z_\mathrm{X} = \left(\frac{b}{d}\omega_h\right)^{(\alpha+2k)/(2N_\mathrm{F}+1)}.$$

Charef approximation method

The Charef Approximation Method (CA) provides an IO approximation by minimizing the magnitude error, expressed in decibels, between the FO operator and its IO approximation. This technique identifies a continuous sequence of recursive pole-zero pairs using the "singularity function method" [54]. For a finite frequency interval truncated to N_F frequency points, the Charef approximation is given by [54, 55]:

$$G_{\mathrm{ch}}(s) = \frac{\prod_{i=0}^{N_{\mathrm{F}}-1}\left(1+\frac{s}{z_i}\right)}{\prod_{i=0}^{N_{\mathrm{F}}}\left(1+\frac{s}{p_i}\right)}, \tag{2.48}$$

where z_i, p_i, and N_{F} denote the i-th zero, the i-th pole, and the approximation order, respectively. In Charef model, the approximation order is same as the total number of pole-zero pairs. The first pole and zero are defined as

$$\begin{aligned} p_0 &= \omega_{\mathrm{c}} \cdot 10^{x_e/20} \\ z_0 &= p_0 \cdot 10^{x_e/10} \end{aligned} \tag{2.49}$$

where ω_{c} is the corner frequency and x_e represents the specified magnitude error between the actual and approximated characteristics in dB. The remaining poles and zeros are computed recursively as

$$\begin{aligned} p_i &= (a \cdot b)^i \cdot p_0, \qquad & i = 1, 2, 3, \ldots \\ z_i &= (a \cdot b)^i \cdot a \cdot p_0, \qquad & i = 1, 2, 3, \ldots \end{aligned} \tag{2.50}$$

where a and b determine the ratios of each zero to its preceding pole and each pole to its preceding zero, respectively. These ratios are computed as:

$$\begin{aligned} a &= \frac{z_0}{p_0} = \cdots = \frac{z_{N_{\mathrm{F}}-1}}{p_{N_{\mathrm{F}}-1}}, \\ b &= \frac{p_1}{z_0} = \cdots = \frac{p_{N_{\mathrm{F}}}}{z_{N_{\mathrm{F}}-1}}. \end{aligned}$$

2.3 Related studies

Mathematical models offer a structured way to describe the dynamic behavior of physical systems. Modeling approaches transform measured or observed responses into mathematical expressions. This enables a systematic analysis of the real-time systems and supports application of control design algorithms to achieve the desired objectives. Therefore, mathematical modeling remains essential in engineering applications.

Several real-world applications display strong nonlinear, multiscale, and dynamic effects. Memory, coupling, and dynamic variations often appear together in numerous processes challenging the accurate modeling phenomenon. To overcome these challenges, a vast number of modeling techniques have been proposed and applied to real-time systems.

2.3.1 Modeling approaches

The literature presents several complementary modeling approaches relevant to dynamic systems. Physics-based differential equations describe spatio-temporal behavior of several systems such as those operating in clinical and biomedical contexts, including cardiac electromechanics and cardiovascular flow simulators [56]. Nonlinear system identification provides experimental-driven structures that organize excitation design, model class selection, cost specification, and validation [57]. Established choices for nonlinear modeling modeling include Wiener and Wiener–Hammerstein blocks [58], polynomial expansions [59], nonlinear state-space forms [60], and the best linear approximation [61]. Koopman-operator based linear models employ extended dynamic mode decomposition to construct linear predictors of nonlinear dynamics [62]. Such models enable real-time model predictive control of soft robotic arms during trajectory-tracking tasks [63].

Integer-order modeling

Machine-learning-driven modeling augments these approaches with physics-informed neural networks, Gaussian processes, and deep architectures [64]. Principal Component Analysis (PCA) based LPV is applied to construct reduced-ordered control-oriented models suitable for a single controller across the operating range [65]. Standard model identification approaches supported by System Identification Toolbox (SIT) [66, 67], Galerkin-type reductions [68], diffusion and kinematic wave approximations [69], LPV identification of irrigation canals [70], multi-model LPV for reactors [71], support-vector approaches [72], and distributed-parameter fluid lines [73].

Minkina [74] adopted a combined theoretical and experimental system identification approach to characterize nonlinear thermocouple dynamics under unit step excitation. The author established that temperature-dependent properties of the thermocouple shield affect system behavior. Conventional linear first-order models become insufficient for temperature increments above $(20–30)$ K. Heat transfer characteristics identified from unit step response measurements in air indicate nonlinear dependence. Nonlinearity analysis of the identified model indicated parabolic or exponential dependence of the time constant on temperature. The study validated the proposed model using experimental data. Another study by Minkina [75] presented similar findings to the preceding article. The author proved nonlinear temperature sensor dynamics using the Stone–Weierstrass theorem for uniform approximation of continuous functions. The proposed models adequately describe sensor dynamics over an extended measurement range. Consequently, the derived exponential models allow representation as both linear and nonlinear models. Furthermore, experimental tests supporting the theoretical contributions confirm the reported findings.

Fraction-order modeling

FO has also gained wide adoption for modeling and control of physical phenomena in recent years [76, 77]. FO derivatives compactly capture the dynamics of real-time systems [20], chemical and biological processes [21, 22], disease progression [78], materials [9], and wave propagation [23], which motivates their use in mathematical modeling. This development has been supported by the FOMCON toolbox [24], which streamlines implementation of modeling, identification, and control algorithms in practical applications. The effectiveness of FO operators and supporting tools has motivated researchers to investigate their applicability to diverse real-time applications.

Oprzędkiewicz [79] proposed discrete TF models for FO inertia. The study developed TF models dedicated to implementation on PLC platforms. The digital representation of these models ensures suitability for industrial applications. The author employed the Charef approximation for practical realization of the proposed models [54]. Lino et al. [7] developed a FO model to improve air–fuel mixture metering accuracy. They compared the performance of the proposed model with classical IO models. Simulation and experimental results indicated that the FO model outperforms the IO models and accurately matches the real injector performance across various operating conditions. Their findings indicate that the FO model supports mechanical optimization of the injector which can lead to reduced pollutant emissions and fuel consumption.

Caponetto et al. [80] constructed an enhanced FO model of a heating process for non-composite materials. They employed Nelder-Mead simplex algorithm on the experimental data collected from a finite beam length filled with air, styrofoam, and metal buckshots. Their findings suggest the FO nature of the heating processes for the case when diffusion occurs in non-continuous composite materials. Tang et al. [37] proposed a GL integral–differential equation-based modeling approach for water flow. The authors used a swarm intelligence algorithm inspired by water flow patterns to identify the FO model. They also analyzed solver behavior, parameter sensitivity, and TO trade-offs that guide implementation under timing constraints.

Russillo et al. [81] derived the exact analytical dispersion relation for an unbounded one-dimensional space-fractional elastic body by seeking plane wave harmonic solutions. The authors enforced matching conditions on frequency and group velocity at the boundary of the first Irreducible Brillouin zone. They identified FO model parameters that reproduce the wave dispersion of a monoatomic Lagrange lattice. The results demonstrate that the space-fractional continuum model accurately captures the dispersion curve and group velocity. The findings indicate that the identified parameters homogenize the discrete lattice microstructure. Quantitative error analysis further confirms that the non-local space-fractional model replicates the dispersive behavior of the monoatomic chain.

Kari [82] proposed a FO visco-elastic model of tough, doubly cross-linked, single-network polyvinyl alcohol. The author employed a Mittag-Leffler relaxation function of order 0.5 to construct the model using three parameters. The parameters include the frequency of maximum loss modulus, the equilibrium elastic modulus, and the relaxation intensity. The results demonstrate that the FO model covers the full frequency range and accurately fits the measured data. Fang et al. [83] proposed nonlocal visco-elastic models within the frameworks of Eringen's nonlocal theory and gradient elasticity theory. They introduced new mechanical elements that enable time–space fractional constitutive models such as the FO Kelvin–Voigt and FO Maxwell models. Their findings indicate that the proposed FO nonlocal models can support ultrasonic nondestructive testing.

San-Millan et al. [84] constructed a two-input, two-output FO model of a laboratory hydraulic canal with two interacting pools. The authors identified model parameters from experimental data by considering pump flow and intermediate gate opening as inputs. They treated the water levels in both pools as outputs. The authors then designed FO controllers and employed them in closed-loop with the identified model. Their findings demonstrate that incorporating FO dynamics into hydraulic canal models improves understanding of complex dynamic behavior. This improvement enables better control system performance.

Sumelka [85] proposed a variable length scale concept within non-local fractional continuum mechanics. The work is motivated by the non-uniform distribution of material characteristic dimensions. The variable length scale approach eliminates the virtual boundary layer observed in constant length scale FO models. The author conducted one-dimensional elasticity analyses with varying length scale distributions, fractional orders, and boundary conditions. The results show that the influence of length scale distribution increases as the fractional order approaches zero. A smooth transition to the classical local solution occurs as the fractional order approaches unity or as the length scale vanishes. The variable length scale concept enables determination of optimal length scale distributions. These distributions act as design parameters encoding microstructural information. This approach is particularly relevant for microstructured and nanostructured materials.

Oprzędkiewicz et al. [86] proposed a FO model to predict the behavior of a thermal mark left by a warm body on cooler ground. The authors employed a scalar fractional DE approximated using CFE. This approach ensures low numerical complexity and accurate estimation. The presented FO approach allows consideration of an initial function. This feature marks a novel contribution in the modeling strategy for thermal traces. Experimental verification of the proposed approach confirmed that the resulting FO model accurately represents the thermal trace behavior on typical surfaces with sufficiently low numerical complexity. This approach enables modeling of the entire temperature field. Their findings suggest that the proposed work could be extended to address measurement uncertainties, such as unknown surface emissivity.

Uncertainty accompanies the measured response from the outset and, through modeling, propagates to the estimated dynamics as well. Sensor non-idealities, bandwidth limits, timing jitters, and simplifying assumptions imprint biases and variability on signals and parameters. In transients these effects evolve in time and propagate through estimators with time-dependent sensitivities [87]. Therefore, the associated measurement uncertainty must be treated as a time-dependent quantity, since the relevant influence quantities vary during both identification and validation. Accordingly, uncertainty shall be evaluated as a function of time, rather than represented by a single static estimate, as recommended in [1, 5]. Consequently, uncertainty components originating in sensors, calibration steps, excitation design, and numerical procedures propagate to the measured data and to the modeled response.

For credible use of experimentally built models, the workflow must include uncertainty-aware data acquisition and calibration, together with explicit dynamic propagation during estimation [1, 2, 5, 88]. In reporting, alongside the model outputs, time-dependent uncertainty should also be presented to ensure transparent interpretation and defensible decisions [89]. Therefore, literature presents methods for time-dependent uncertainty assessment in the modeled dynamics.

2.3.2 Measurement models and dynamic uncertainty

Literature presents several approaches to evaluate and propagate the uncertainty in time-dependent measured quantities.

Measurement models

Dynamic systems are modeled with differential equations linking present and past states through defined parameters. This structure determines the influence of disturbances, drift, and parameter variations on the output response. Several measurement models assume linear transducer characteristics. However, these assumptions hold only within specific ranges of measurement results. These limitations have motivated researchers to investigate this aspect in modeling practical phenomena.

Dienstfrey et al. [90] proposed a convolution model that links a reference input waveform to the response of the measurement system for evaluating dynamic uncertainty. This model shows that finite bandwidth effects significantly distort the measured signal. The study applied regularized deconvolution to recover the input waveform and to quantify uncertainty from waveform distortion, noise, discretization, and regularization bias. The method of uncertainty assessment was implemented using Fourier-based algorithms and regularization techniques in high-speed electrical and optical waveform metrology.

Minkina et al. [91] presented detailed methods for constructing measurement models from the dynamic properties of thermometer sensors. The authors extended these approaches to improve dynamic measurements using neural networks. They introduced analog and digital corrections to enhance the measurement system performance. Moreover, they proposed correction algorithms in both continuous and discrete time domains.

Le Maître et al. [92] presented a generalized Polynomial Chaos scheme based on Wiener-Haar (wavelet) expansions, with stochastic Galerkin formulations for the modal coefficients and compared against Wiener-Legendre spectral expansions [93]. The presented method was applied to propagate uncertainty efficiently in systems whose outputs exhibit steep or discontinuous dependence on random inputs. The approach provided a robust, aliasing-resistant predictions that outperform global polynomial bases in non-smooth regimes.

Ruhm [94] presented terminology that distinguishes properties of signals and systems and clarifies that stability, stationarity, and drift represent separate uncertainty sources. Drift arises from temporal parameter changes and causes systematic deviations in the system response. Stationarity concerns the constancy of statistical characteristics and supports evaluation of random components. These distinctions help identify uncertainty mechanisms in dynamic models with time-dependent inputs or internal variations [94].

Dynamic uncertainty

Eichstädt et al. [95] proposed a software-oriented standardized, GUM-compliant Phython-based software package: `PyDynamic`. The software implements compensation filter design, propagates coefficient and signal uncertainties, and enables efficient Monte-Carlo, and Discrete Fourier Transform (DFT) deconvolution. Therefore, it supports traceable, time-resolved uncertainty statements for transient and high-dimensional measurement results [96]. A continuous frequency-domain bound on the measurand's spectrum to quantify the systematic component is induced by regularization. This bound is combined with variance terms to tune filters and to report total uncertainty for pulse and pulse-train hydrophone data [97]. This method provided reproducible workflows illustrated on shock, hydrophone, and biomedical pressure cases [98]. It reduced user burden and improved reliability of dynamic results.

Sylvain et al. [99] proposed an alternative framework for dynamic uncertainty evaluation in nonlinear, uncertain measuring systems subject to unknown inputs. It constructs an equivalent linear model and augments it with an additive "virtual input." The virtual input aggregates un-modeled dynamics and external disturbances. The framework also introduces measurement models that explicitly account for measurement biases. The methodology is demonstrated by simulation on a triaxial accelerometer for small-force metrology. It compares linear and nonlinear measurement models under passive operation. These studies show practical routes to uncertainty-aware inference in dynamic settings.

Martins et al. [100] presented an uncertainty evaluation for dynamic pavement deflection measurements with a falling-weight deflectometer. They compared the approach with GUM budget against a time-varying, frequency-domain propagation implemented with deconvolution [96] and PyDynamic [95].

Tallawi et al. [16] proposed a practice-oriented framework for DM and a workflow combining compensation filter design with GUM-compliant uncertainty propagation for time-varying signals. The purpose of this study was to align calibration and uncertainty assessment with sensor response time and system dynamics rather than static assumptions. The authors provided clearer terminology and a repeatable method that yields traceable, time-dependent uncertainties suited to industrial dynamic measurements.

Hessling [1] proposed a digital filtering based formulation that converts time-dependent sensitivities into digital filters. The filters are used to compute dynamic measurement uncertainty alongside the estimated measurand. The author extended the GUM-based propagation to transient, non-stationary measurements without resorting to heavy Monte-Carlo simulations [101, 102]. Another study by Hessling et al. [103] presented dynamic simulator utilized to dynamic uncertainty of capacitive voltage dividers. The authors presented a direct mapping methods for synthesis of signal rotation methods for dynamic uncertainty assessment.

The measurement method presented by Minkina [104] determine high steady-state temperatures that exceed a temperature sensor's normal operating range. Using an `IBM PC AT` microcomputer and quadratic mean approximation (least squares regression), the method evaluates partially recorded step-response curves of thermocouples. It was tested theoretically, in a liquid thermostat (linear system), and in industrial furnaces (nonlinear system). Results indicate that the method can extend the measurement range by up to $120\,\%$. with an error of less than $10\,\%$. The approach avoids logarithmic calculations and compensates for irregularities in the temperature response curve. Minkina [105] proposed a low-cost measurement method for molten-steel temperature using reusable thermocouples. The temperature is estimated from the thermocouple's transient step response using nonlinear dynamic models. Several mathematical models are developed in this study to account for temperature-dependent sensor dynamics and radiative heat transfer. Implementation of the proposed model on an `IBM PC-486` achieved approximately $(1–2)\,\%$ measurement accuracy in steel making applications.

Yao et al. [106] proposed dynamic uncertainty assessment based on convolution modeling which supports analysis of the measurement system altering the temporal behavior of a controlled process. This method remains relevant in control design because waveform distortion affects feedback performance and disrupts model-based estimation. Regularized deconvolution provides a stable reconstruction of the true system response. It also enables quantification of uncertainty from noise, discretization, and regularization bias which influence controller accuracy [107]. Studies in control engineering also indicate that controller architectures dynamic stiffness and disturbance rejection. These attributes determine the sensitivity of the closed-loop system to measurement uncertainty [106]. Therefore, a control design approach ensuring the stability and the desired closed-loop performance is crucial. Therefore, the dissertation analyzes the ralated methods out of numerous approaches of control design presented in literature.

2.3.3 Control design approaches

Control design algorithms have historically focused on generating stabilizing feedback laws to ensure robustness, performance, and disturbance rejection across diverse range of applications [108, 109]. The classical frameworks relied on proportional, integral, and derivative actions. These controllers utilized tuning principles based on frequency-domain methods, stability margins, and linear approximations [108, 110]. As systems grew in dynamical complexity, the limitations of single-loop linear controllers became evident. These limitations motivated systematic approaches such as pole placement, loop-shaping, optimal control, and robust control [111, 112]. Across these developments, the central objective stayed unchanged: ensuring that closed-loop systems achieve convergence, maintain robustness, and deliver satisfactory transient response while preserving implementational simplicity.

The IO control, dominated by Proportional Integral Derivative (PID) controllers, remains the standard in industrial automation and process control [113]. It is due to its simplicity, intuitive tuning rules, and compatibility with embedded systems [114–116]. The PID structure is based strictly on IO differentiation and integration. It regulates system errors using present, past, and predicted future information [117]. However, its capability remains limited when handling strong non-linearities, high-order dynamics, or processes with long-memory effects [118]. These limitations motivated the development of non-integer generalizations that naturally capture system properties and enable shaping of dynamical responses [119, 120].

Several studies have addressed the practical design and application of FO controllers based on established theoretical foundations. Frequency-domain design approaches employ fractional TFs and implementable approximations. The Oustaloup recursive filter, provide an effective framework for realizing FO controllers with favorable phase properties [121, 122]. Chen et al. [19] proposed analytical loop-shaping design of FO-PID controllers combined with Bode ideal cutoff filters. The control design method was applied for permanent-magnet synchronous motor speed control. This approach achieved systematic satisfaction of frequency-domain specifications. Moreover, extensive research has investigated direct and indirect auto-tuning methods for FO-PID controllers [123–125]. These methods enable applications across servo drives, industrial processes, robotics, and power systems [126].

Muresan et al. [127] proposed a FO extension of the Ziegler-Nichols autotuning method by shaping the loop frequency response. This approach yields improved tracking performance, reduced overshoot, and enhanced robustness for integrating systems compared with the classical method. Nasiri et al. [128] developed an adaptive FO controller for transmission control protocol and active-queue-management congestion control. This design combines fractional calculus with Lyapunov-based adaptation to achieve robust and fast queue regulation with zero steady-state error under extenternal disturbances. Liu et al. [129] presnted stability-region analysis based design of a robust FO-PID controller for autonomous underwater-vehicle yaw control. The controller designed using this approach demonstrated superior transient response and robustness compared to that with IO-PID control.

Relaño et al. [130] applied a FO-PI controller using an iso-damping design strategy. The controller improved robustness and ensured consistent transient performance under varying payloads compared to classical PI control. Naderipour et al. [131] implemented FO-PID and fuzzy-FO-PID controllers in grid-connected photovoltaic-wind hybrid systems. The controller designed using this method enhanced voltage regulation, reduced total harmonic distortion, and improved grid stability under intermittent conditions.

Oprzędkiewicz et al. [132] presented the implementation of a FO-PID controller to regulate temperature in an isothermal room within a pharmaceutical factory. The authors proposed a controller formula tailored to the TF model of the temperature dynamics. The study investigated stability analysis using the Matignon Theorem. Simulation results demonstrated that the proposed FO-PID controller outperforms the IO-PID controller tuned with the auto-tuning function.

Classical frequency-domain techniques have produced tuning rules for determining the parameters of FO-PID controllers [133–136]. These methods enabled FO controllers to deliver the desired response in systems such as permanent-magnet synchronous motor servo drives [134], robotic manipulators [135], and FO time-delay processes [136].

2.4 Limitations

Modeling physical system dynamics faces challenges due to nonlinear behavior and noisy measurement data. Accurate models require comprehensive understanding of instruments across the entire measurement chain. Applying Linear Time Invariant (LTI) approaches to complex nonlinear systems yields IO models with many poles and zeros [137]. Using LTI models with many parameters increases computational complexity during control design. In contrast, FO operators satisfy Homogeneity and Superposition, which define them as linear operators [38]. Consequently, researchers can apply established LTI control methods to FO control design.

The correctness of analytically developed FO-DIEs depends on the accurate knowledge of the components [138] and memory-like behavior [139]. In contrast, frequency-domain identification depends on input-output data over the entire range for the considered system [82]. As compensation for the lack of accurate knowledge about the system properties, grey-box [140] and black-box [37] identification structures can be applied. When the FO models are developed from the measured data, associated uncertainty propagates into the modeled response. The modeled response depends on the selected FO operators and the applied IO approximation approach. Consequently, the FO operator choice and the approximation method also influence the propagated uncertainty.

Furthermore, the analytical approaches for FO-PI controller design enforce gain and phase constraints on the open-loop frequency response [135, 136]. However, they omit derivative conditions at the gain crossover frequency. This omission can reduce robustness against loop-gain variations in practical systems. Although this limitation has been addressed, the method relies on an optimization procedure that minimizes the integral time absolute error [134]. This mutation-based optimization undermines the main advantages of frequency-domain design, namely its simplicity and straightforward application.

To overcome the stated limitations, this dissertation presents the contributions listed in Section 1.5 of Chapter 1.

Case Studies and Experimental Data

This chapter presents the case studies used to validate the proposed approaches. Three systems are considered: two simulation models in MATLAB/Simulink and one laboratory setup. The first system is a Single-Input Single-Out (SISO) first-order inertia model without delay. The TF of this system is utilized to assess steady-state errors and dynamic inaccuracies from IO approximations. The second system is TRAS which operates as a Multi-Input Multi-Output (MIMO) system. Its nonlinear `Simulink` model is used to evaluate the performance of the FO control design and the influence of IO approximation methods. The third system considered in this study is a nonlinear SISO laboratory flow-rate measurement system. This study configures the flow system via MODBUS, acquires data, and identifies IO and FO models. The same setup verifies uncertainty propagation in the dynamic response of the identified FO model. These three systems, each with distinct configurations, verify the effectiveness of the proposed approaches.

3.1 FO inertia without time delay

This sections explains the representations of FO inertia reported in the literature and presents its model used in dissertation. The description of the FO inertia without delay extends that presented in [13].

3.1.1 FO inertia in practical applications

Several applications in literature have been modeled and presented as FO inertial systems. Common systems represented as the FO inertia are the rotational systems such as Permanent Magnet Synchronous Motor (PMSM) [141], Dual Inertia Servo Inverter (DISI) [142], dynamic behavior of the flexible shaft in motor-generator set [143], etc.

The inertia model for PMSM and DISI applications represents the overall motor and rotating load dynamics. In motor-generator sets with flexible shafts, the model instead represents angular displacement of the shaft. Figure 3.1 shows the block diagram of the experimental motor-generator setup with a flexible shaft [143]. The setup uses two electric motors, M_1 and M_2, connected by a flexible shaft. During operation, one motor acts as a generator, while the other operates as a rotating load. The setup is mounted on a rigid metallic frame.

When one electric motor is operated by applying the input voltage V, the rotational motion produces an angular displacement θ in the flexible shaft causing a rotation of the electric motor on the other end [143]. To capture the viscoelastic properties of the flexible shaft, this dissertation utilizes an FO dynamic model. The model considers the motor

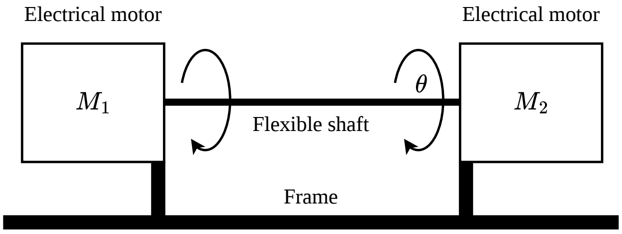

Figure 3.1: Mechanical setup of the fractional order inertia [143].

voltage as the input and the angular displacement as the output of the inertial system.

3.1.2 FO model adopted in this study

A simple and widely used structure for a FO dynamic model without delay is the fractional inertial element [10, 143]:

$$G(s) = \frac{K}{Ts^{\alpha} + 1}, \tag{3.1}$$

where K denotes the system gain, T is a generalized time constant, and α is the order of the FO derivative defining the degree of inertia or diffusion.

Another representation of the FO inertia also exists:

$$G(s) = \frac{K}{(T's)^{\alpha} + 1}, \tag{3.2}$$

where $T = T'^{\alpha}$. In this representation, T' has the unit of second while the unit of T is second only for $\alpha = 1$ [10, 143]. Consequently, mapping Eq. (3.1) to the representation concludes that the unit of T is second for $\alpha = 1$. For the other values of α, the units of T are difficult to interpret physically. An alternative representation given as [79]:

$$G(s) = \frac{K}{(Ts + 1)^{\alpha}}, \tag{3.3}$$

is also available in literature. However, this formulation is not equivalent to Eq. (3.1). This study adopts the model in Eq. (3.1) and discusses the alternative forms only to clarify the interpretation of the generalized time constant T.

For $\alpha = 1$, Eq. (3.1) reduces to the classical first–order model [10]. For $0 < \alpha < 1$, the model yields a fractional response with slower decay and long–memory behavior consistent with viscoelastic or distributed-parameter effects. This type of response is consistent with viscoelastic or distributed media properties.

FO models of this form often achieve improved accuracy compared with IO structures when representing systems that exhibit viscoelasticity or spatially distributed energy storage, such as flexible structures or materials with plastic–viscoelastic characteristics [143]. The parameters of the FO model in Eq. (3.1) are given in Table 3.1.

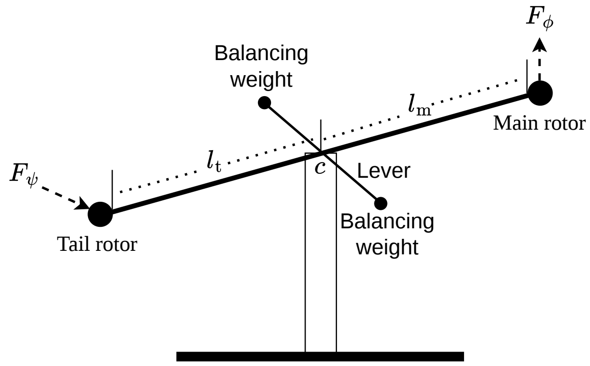

Figure 3.2: Coordinate frame of twin rotor aerodynamic system [147].

3.2 Twin rotor aerodynamic system

This section discusses the nonlinear, linearized and decoupled models of the TRAS. These models extend those presented in the articles [144, 145].

3.2.1 Nonlinear model

The TRAS consists of a rigid beam equipped with two rotors, referred to as the main and tail rotors. Each rotor is operated by a dedicated Direct Current (DC) motor and mounted at opposite ends of the beam [144, 146]. The beam is supported on a central pivot, which enables motion in the vertical and horizontal axes. Counterbalance masses are fixed at the beam extremities to ensure that the pitch angle returns to its equilibrium position in the absence of aerodynamic actuation. The inertial reference frame of the TRAS is illustrated in Figure 3.2.

The mechanical structure constraints the yaw angle ψ and the pitch angle ϕ within the bounds [146, 147]:

$$-180^\circ < \psi < 180^\circ, \qquad -57.3^\circ < \phi < 57.3^\circ.$$

For modeling purposes, a right–handed coordinate system is defined at the center point c. The distances from the pivot to the main and tail rotors are denoted by l_m and l_t, respectively. Moreover, m_m and m_t represent the corresponding counterweights. The variables $m_{c\omega}$ and $l_{c\omega}$ denote the auxiliary masses attached to the lever arms and the associated lever lengths.

Table 3.1: Parameters of the FO inertia without delay [13].

Parameter	Value	Description
K	3	System gain
T	10	Generalized time constant
α	0.5 or 0.8	Degree of inertia of diffusion

These masses act as balancing weights to calibrate the initial positions of the pitch and yaw angles of TRAS. The differential equation representing the mathematical of TRAS is [147]:

$$J_\psi \, \ddot{\psi} = u_\psi + J \, \dot{\psi} \, \dot{\phi} \, \sin(2\phi) - K_\psi \, \psi - C_\psi \, \dot{\psi}, \tag{3.4}$$

$$J_\phi \, \ddot{\phi} = u_\phi - \frac{J \, \dot{\psi}^2}{2} \, \sin(2\phi) - C_\phi \, \dot{\phi} - K_\mathrm{g} \, g, \tag{3.5}$$

where

$$\begin{aligned}
J_\psi &= (m_\mathrm{m} l_\mathrm{m}^2 + m_\mathrm{t} l_\mathrm{t}^2) \cos^2(\phi) + 2 m_{\mathrm{c}\omega} l_{\mathrm{c}\omega} \sin^2(\phi) + J_\mathrm{z}, \\
J_\phi &= m_\mathrm{m} l_\mathrm{m}^2 + m_\mathrm{t} l_\mathrm{t}^2 + 2 m_{\mathrm{c}\omega} l_{\mathrm{c}\omega} + J_\mathrm{x}, \\
J &= m_\mathrm{m} l_\mathrm{m}^2 + m_\mathrm{t} l_\mathrm{t}^2 - 2 m_{\mathrm{c}\omega} l_{\mathrm{c}\omega}, \\
K_\mathrm{g} &= (m_\mathrm{m} l_\mathrm{m} - m_\mathrm{t} l_\mathrm{t}) \cos(\phi) + 2 m_{\mathrm{c}\omega} l_{\mathrm{c}\omega} \sin(\phi).
\end{aligned}$$

The parameters of the TRAS used in this study are given in Table 3.2.

Table 3.2: Parameters of the twin rotor aerodynamic system TRAS [148].

Parameter	Value	Units
l_m	0.202	m
l_t	0.216	m
$l_{\mathrm{c}\omega}$	0.15	m
m_m	0.029	kg
m_t	0.031	kg
$m_{\mathrm{c}\omega}$	0.061	kg
J_x	0.0242	kg m^2
J_z	0.068	kg m^2
g	9.8	m s^{-2}

3.2.2 Linearized model

Jacobian linearization of the nonlinear model in Eqs. (3.4) and (3.5) is performed at the operating points $\phi = \phi_0 = 0°$ and $\psi = \psi_0 = 0°$. Substituting parameter values from Table 3.2 yields the linearized model. The TF of the resulting linearized model is given as:

$$G(s) = \begin{bmatrix} \dfrac{1.246}{s^3 + 0.922 s^2 + 4.97 s + 3.917} & 0 \\ \dfrac{1.481 s + 0.4233}{s^4 + 6.34 s^3 + 7.06 s^2 + 2.09 s} & \dfrac{3.6}{s^3 + 6 s + 5.01 s} \end{bmatrix} \tag{3.6}$$

where $G_{11}(s) = \frac{\phi(s)}{u_\phi(s)}$, $G_{12}(s) = \frac{\phi(s)}{u_\psi(s)}$, $G_{21}(s) = \frac{\psi(s)}{u_\phi(s)}$, and $G_{22}(s) = \frac{\psi(s)}{u_\psi(s)}$. Also, $\phi(s)$ and $\psi(s)$ denote pitch and yaw angles in s-domain while $u_\phi(s)$ and $u_\psi(s)$ denote control inputs to the motors operating main and tail rotors, respectively.

The TF matrix in Eq. (3.6) reveals coupling in the linearized TRAS model. Therefore, pitch and yaw TFs must be decoupled to obtain SISO models for yaw and pitch angles. These SISO models facilitate the design of independent controllers for each mode. The desired decoupled TF matrix is:

$$G_D(s) = \begin{bmatrix} G_p(s) & 0 \\ 0 & G_y(s) \end{bmatrix} \tag{3.7}$$

where $G_p(s)$ and $G_y(s)$ denote the decoupled TFs of pitch and yaw angles of TRAS. The respective TFs are given by

$$G_p(s) = \frac{1.246}{s^3 + 0.922s^2 + 4.97s + 3.917}, \tag{3.8}$$

and

$$G_y(s) = \frac{3.6}{s^3 + 6s + 5.01s}. \tag{3.9}$$

The decoupled TF is obtained as:

$$G_D(s) = D(s)\ G(s), \tag{3.10}$$

where $D(s)$ is a transformation matrix known as the decoupler. The decoupler TF is obtained as:

$$D(s) = G_D(s)\ G(s)^{-1}. \tag{3.11}$$

The decoupler TF to ensure the decoupled TRAS model in Eq. (3.7) is:

$$D(s) = \begin{bmatrix} 1 & d(s) \\ 0 & 1 \end{bmatrix}, \tag{3.12}$$

where

$$d(s) = -\frac{1.189s^7 - 8.567s^6 - 20.54s^5 - 49.29s^4 - 68.88s^3 - 39.41s^2 - 6.667s}{s^7 + 12.34s^6 + 50.11s^5 + 76.21s^4 + 47.91s^3 + 10.47s^2}.$$

3.3 Flow rate measurement system

This section explains the hardware, its configuration with MATLAB, and the data acquisition procedure of the flow rate measurement system. The description and acquisition workflow extend the material presented in the published articles [14, 137]. The fixed-input data acquisition method expands on the approach in [14], while the variable-input acquisition procedure extends the method reported in [137].

3.3.1 Experimental setup

The tests were performed using a water-flowmeter calibration system designed for didactic purpose. The flowmeter includes FT and Flow Indicator (FI). Figure 3.3 presents the experimental setup. The system operates in a closed-loop without external water supply. The main loop contains a Water Pump (P), a storage reservoir T1, a calibrated tank T2, and four flowmeters of different types. The digital flow transmitters include the electromagnetic ENKO MPP02 (FT-E1) with a range up to $60\ \mathrm{m^3/h}$, the turbine NEGELAP NWGY (FT-T1) with a range from $1\ \mathrm{m^3/h}$ to $20\ \mathrm{m^3/h}$, the ultrasonic KHRONE OPTISONIC 3400C (FT-U) with a range up to $18\ \mathrm{m^3/h}$, and the nutating-disk Badger Meter ER-500 (FT-V) with a range up to $38\ \mathrm{m^3/h}$. The pipeline diameter remains constant and equal to $40\ \mathrm{mm}$.

The installation of the flowmeters followed the respective manufacturers' guidelines. The Variable Frequency Drive (VFD) regulates the water flow generated by the pump. After start-up, water always flows from the storage reservoir through the installation and returns to the same reservoir T1. Controlling the pneumatic valve V3 with monostable switch directs water to the calibrated tank T2. During calibration, valve V2 remains open and valve V1 remains closed. Pumping water from T2 back to T1 requires swapping the positions of V1 and V2. The measurements in this dissertation only concern the flow in the closed-loop. Thus, V1 remains closed, V2 remains open, and V3 stays in its default position toward T1. The measurement results are collected for the flow from T1 to T1, excluding both the monostable switch and T2 from the setup.

3.3.2 Configuration with MATLAB

The flow rate of water (expressed in $\mathrm{m^3/h}$) in the pipeline varies with the frequency (expressed in Hz) of the input voltage supplied to the pump. Accordingly, the experimental setup forms a SISO process, with frequency as the input and flow rate as the measured output. The Input-Output Data (IOD) acquisition requires direct configuration of both the VFD and the Turbine Flow Meter (FT-T1) with the personal computer. The study employs MODBUS converters to interface the VFD and FT-T1. Because MODBUS uses a serial communication protocol, and synchronized sampling of input and output is essential, separate MODBUS devices are used for the FT-T1 and VFD. The MATLAB handles device configuration and data acquisition. Figure 3.4 shows the configuration scheme, illustrating MODBUS-based communication for IOD acquisition. The Vortex Flow Meter (FT-V) and FT-T1 generate frequency signals, which are converted into digital data through an integrated frequency-to-data converter. The converted data are transmitted to the computer via MODBUS. The input commands are sent to the VFD over the same protocol, and the VFD supplies the pump with a voltage signal at the specified frequency.

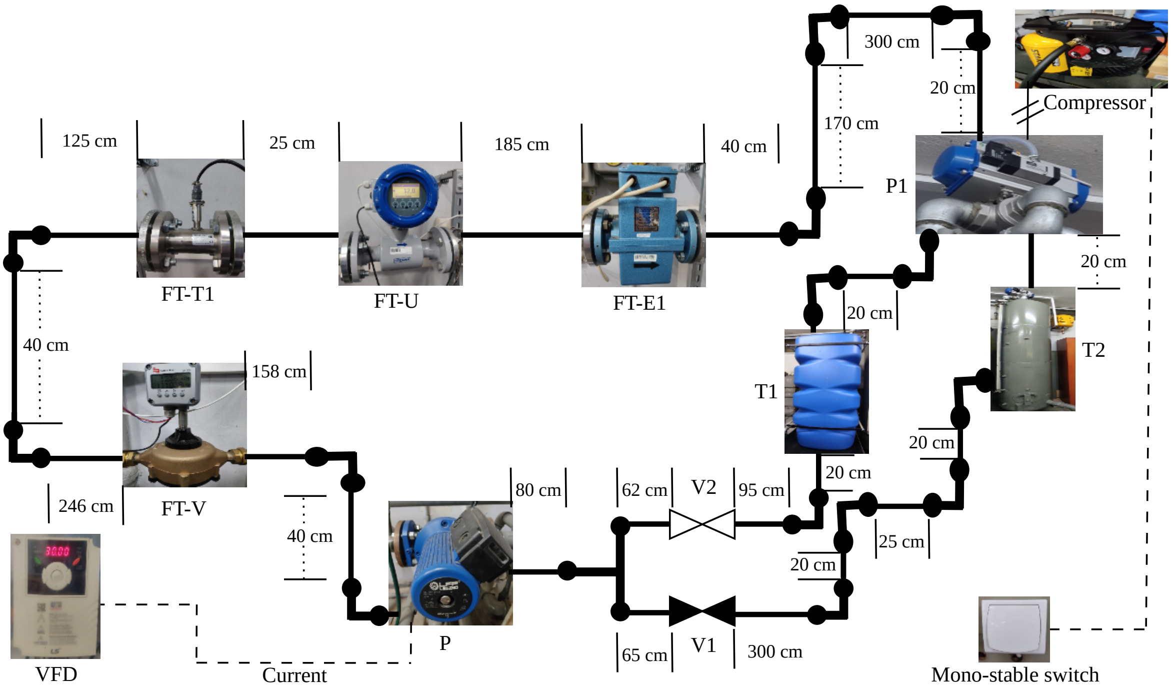

Figure 3.3: Experimental setup in the flow system laboratory (CK-12) at the Department of Measurements and Control Systems. This figure is reproduced from the article [137].

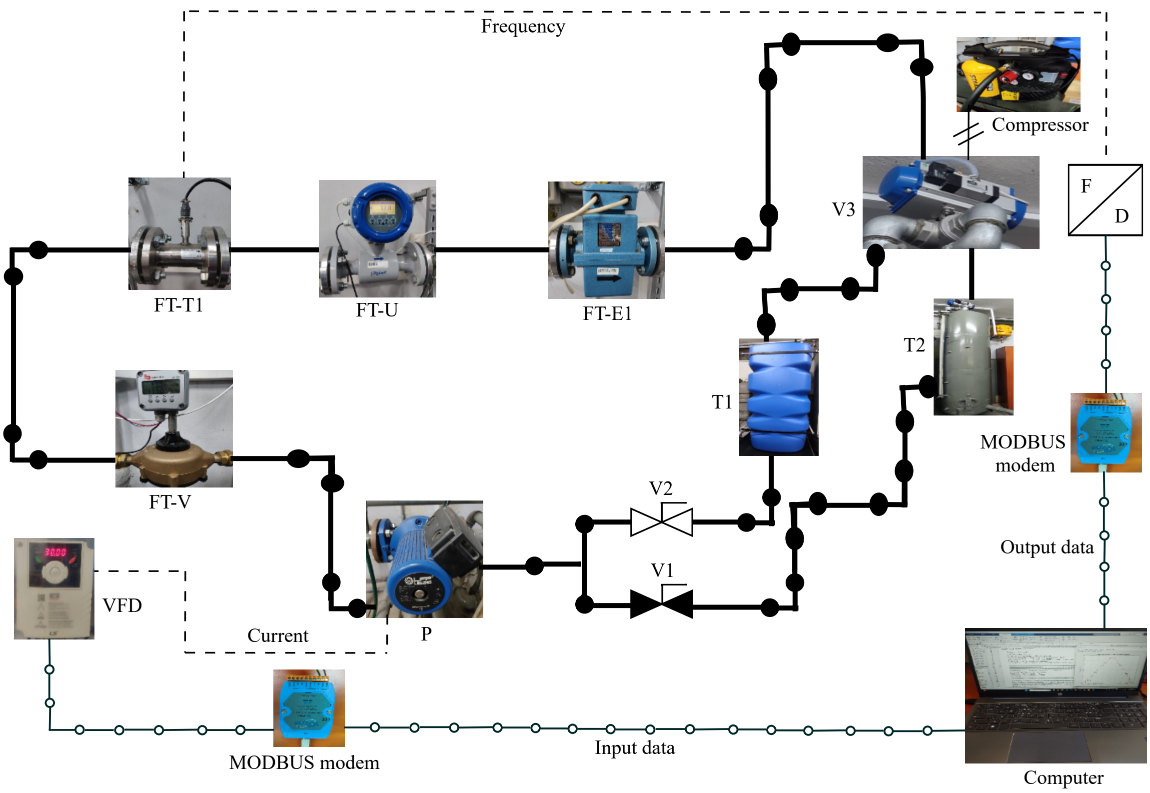

Figure 3.4: Experimental setup – Turbine Flowmeter (FT-T1) and Variable Frequency Converter (VFD) are configured with MATLAB through MODBUS modems. This figure is reproduced from the article [14].

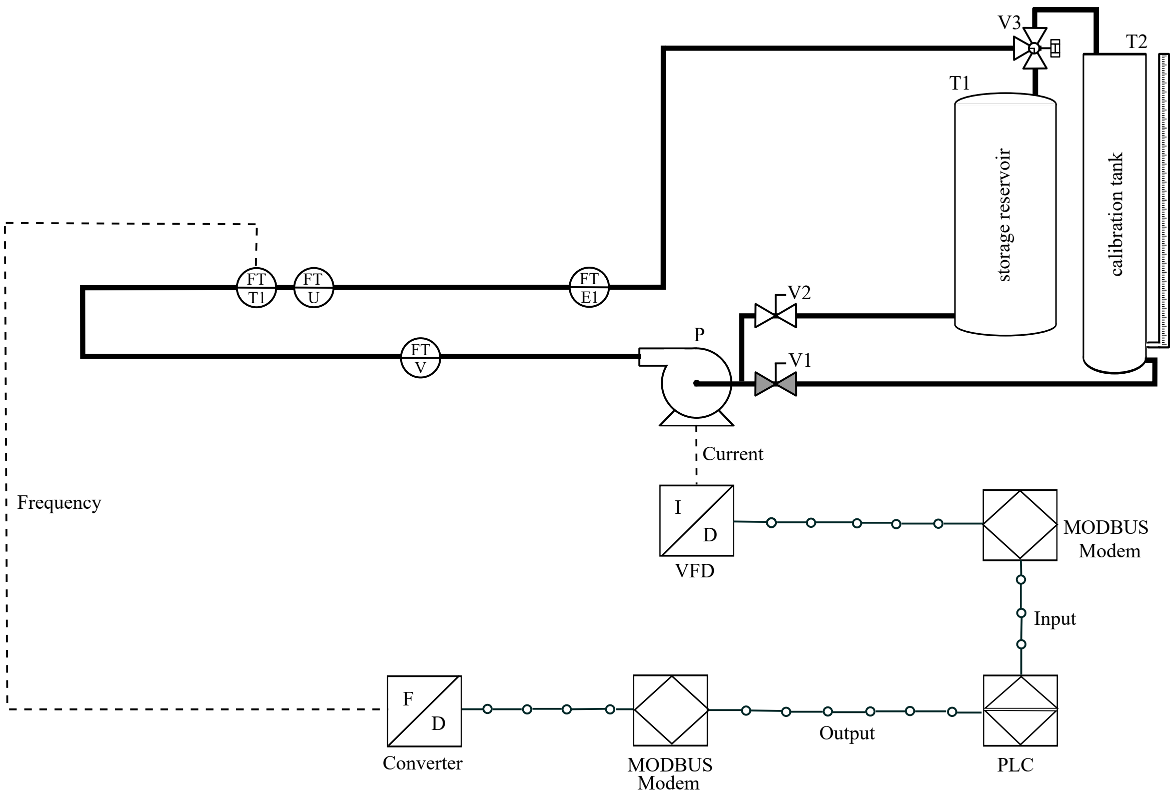

Figure 3.5: Piping and instrumentation diagram of the laboratory flow rate measurement system. This figure is reproduced from the article [14].

Listing 3.1 presents the MATLAB configuration script for the VFD and FT-T1. The Piping and Instrumentation Diagram (P&ID) corresponding to Figure 3.4 is shown in Figure 3.5. A PLC is used because industrial implementations replace the computer in Figure 3.4 with a PLC.

```
% Configuration of VFD
pum_ON_signal = 2;
converter_obj.Timeout = 1;
converter_obj.BaudRate = 9600;
serverId = 1;
converter_obj = modbus('serialrtu', 'COM5');
% Configuration of FT-T1
turbine_flow_meter_obj.Timeout = 1;
turbine_flow_meter_obj.BaudRate = 19200;
serverId = 1;
turbine_flow_meter_obj = modbus('serialrtu', 'COM4');
```

Listing 3.1: MATLAB Code for configuration of VFD and FT-T1

3.3.3 Fixed input data acquisition

Listing 3.2 defines the complete procedure for IOD acquisition. The algorithm first creates independent MODBUS communication objects for the VFD and the FT-T1.

After establishing these communication channels, the algorithm initializes the devices by setting the pump ON-signal, baud rates, timeout intervals, and the required register assignments for reliable data transfer. Once configured, the algorithm writes the desired excitation frequency to the VFD, which adjusts the pump's input to enforce the commanded operation. Data acquisition proceeds in a time-indexed loop. At each sampling instant, the algorithm records the current time and reads the turbine-flowmeter value from the appropriate MODBUS register. These measurements are appended sequentially to form aligned time and flow rate vectors. The loop continues until the desired duration is reached, after which the collected vectors constitute the complete input-output dataset.

```
START

Configure VFD:
    Create 'MODBUS' object for the VFD
    Set pump 'ON-signal' to 2
    Set the VFD object 'Timeout' to 1 second
    Set the VFD object 'BaudRate' to 9600
    Set 'serverId' to 1
    Initialize the VFD using 'serialrtu' on 'COM5'

Configure FT-T1:
    Create 'MODBUS' object for the turbine flow meter
    Set turbine flow meter 'Timeout' to 1 second
    Set turbine flow meter 'BaudRate' to 19200
    Set 'serverId' to 1
    Initialize turbine flow meter using 'serialrtu' on 'COM4'

Send Commands to VFD:
    Write pump 'ON-signal' to register 6 using 'holdingregs'('int16')
    Write input 'frequency' to register 5 using 'holdingregs'('int16')

Loop for Data Acquisition:
    j <- 0
    While t <= t_e:
        j <- j + 1
        Record current time in t(j)
        Read turbine 'flow rate' from register 12 using 'holdingregs'
        Store 'flow rate' in y(j)
    END While

END
```

Listing 3.2: Pseudocode for fixed-input data acquisition of the laboratory flow system.

At each sampling instant, the algorithm records the current time t and the output $y(t)$. The acquisition loop continues until the predefined duration of 30 s is reached. For one study

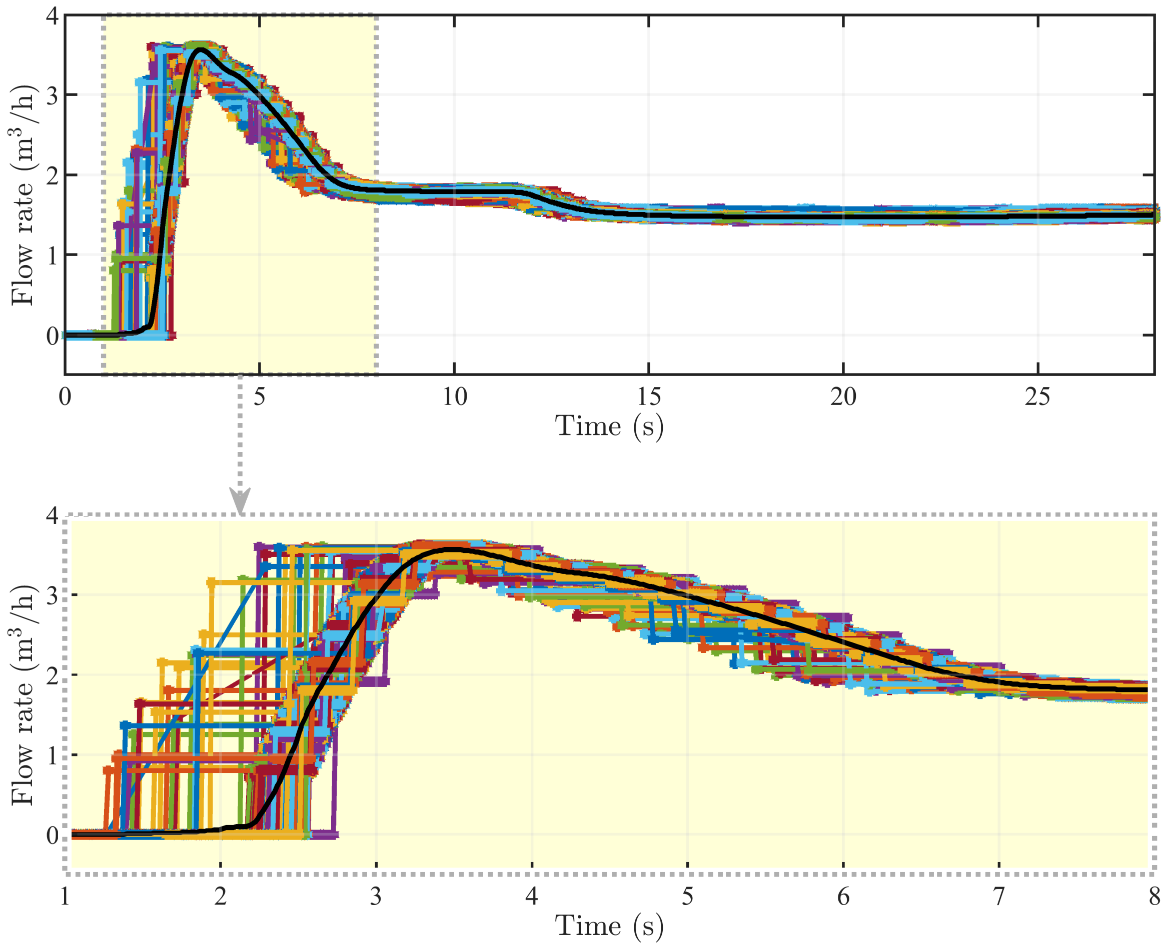

Figure 3.6: Measured flow rates for 1000 measurement passes with input changed from 0 to 20 Hz.

presented in Chapter 6, the input frequency f_{in} was set to 20 Hz, and the corresponding flow rate values were stored. The `for` loop executes 1000 times, and each iteration runs a `while` loop for 30 s to record the output for "one-pass". Measurement results from 1000 passes were collected to capture the variability of the measured data. The resulting flow rates for all passes appear in Figure 3.6.

The figure shows considerable variation among the recorded responses, which indicates pronounced measurement uncertainty. In addition to imperfect calibration of FT-T1, the main contributor to this uncertainty is the non-uniform sampling time, visible in the zoomed view in the lower panel of Figure 3.6. This region corresponds to the section marked in the upper plot and reveals significant scatter during the first 2.20 s. Such dispersion prevents reliable estimation of the transient response and limits the ability of any model to represent the system dynamics. Because the scatter reflects stochastic behavior, resampling the data to a constant sampling interval would introduce artificial dynamics not present in the physical system. After approximately 15 s, the responses show a stable pattern with minimal variation, which is treated as the steady-state region. Mean of the data shown in Figure 3.6 is calculated by re-sampling values of each pass with a sample time ($\bar{T}_{s,m}$) which is the

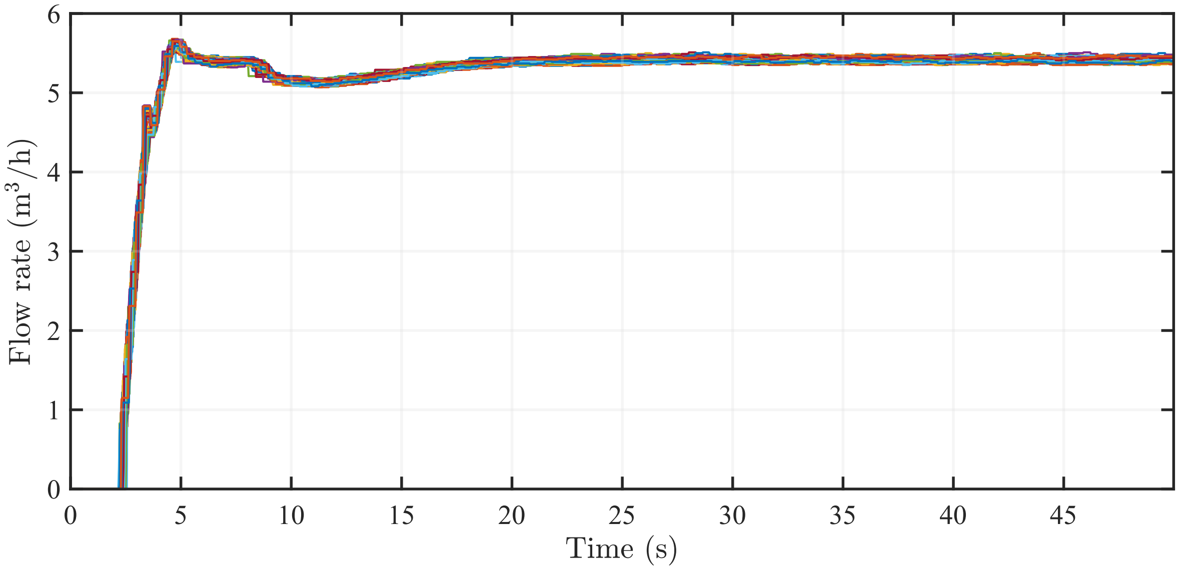

Figure 3.7: Experimental data collected for 200 passes with input changed from 0 to 30 Hz.

average sampling time calculated from all the measurement passes.

Another set of measured data was collected for changing input frequency f_{in} from 0 Hz to 30 Hz. The input signal lasts for 50 s. Furthermore, the system was operated under this scenario 200 times and the corresponding input and output signals were recorded. The output response of the flow system for 200 passes is shown in Figure 3.7. This data is used to develop a FO time-delay model for the flow system. The model supports development of a framework for dynamic uncertainty propagation in the FO model.

3.3.4 Variable input data acquisition

The automated data-acquisition procedure follows the flowchart shown in Figure 3.8. The process begins by initializing all variables listed in Table 3.3. The input frequency steps are given as:

$$f_{\text{in,s}} = [6, 12, 18, 24, 30, 36, 42, 48, 54, 60, 60, 54, 48, 42, 36, 30, 24, 18, 12, 6]. \tag{3.13}$$

Initially, counter is set to $l = 1$, the input frequency-step index to $q = 1$, and the initial excitation frequency to $f_{\text{in}} = 6$ Hz. The experiment executes $N_{\text{p}} = 60$ passes, each containing $Q = 20$ frequency steps. The initial time is $t_{\text{i}} = 0$, while the parameters t_{e} and t_{m} define the step duration and the sampling interval, respectively.

After initialization, the algorithm creates MODBUS communication objects for the VFD and the FT-T1 to ensure reliable communication. Figure 3.8 then directs the sequence of operations. The algorithm first checks whether $l \leq N_{\text{p}}$. If the condition holds, it resets the step index to $q = 1$ and computes the excitation frequency for the current step. For the first half of the sweep ($q \leq Q/2$), the excitation frequency increases as $f_{\text{in}} = q \cdot f_{\text{in}}$. For the second half ($q > Q/2$), the sweep reverses symmetrically, and the frequency becomes

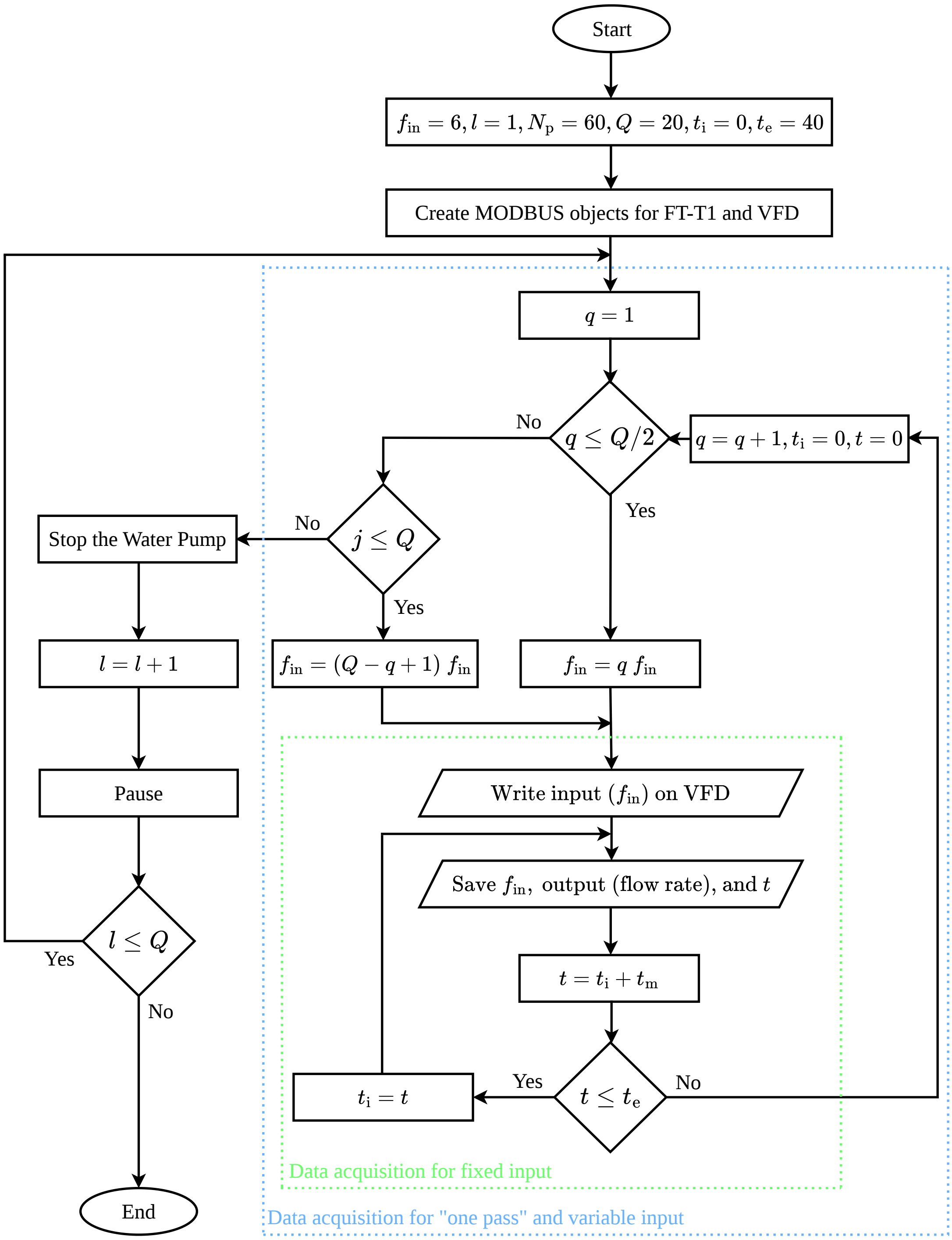

Figure 3.8: Flow chart for variable-input data acquisition of the laboratory flow system shown in Figure 3.4.

$f_{in} = (Q - q + 1) \cdot f_{in}$.

This up-down sweep ensures excitation across the full operating range. The calculated frequency is then written to the VFD, which updates the pump input accordingly. A measurement loop records the turbine-flowmeter output y at intervals of t_m while updating

Table 3.3: Initialization of the variables for data acquisition.

Variable	Value	Description (units)
l	1	Current measurement pass
q	1	Current index of the input frequency steps
f_{in}	6	Input frequency of the voltage operating the water pump (Hz)
N_{p}	60	Total number of passes
Q	20	Total number of frequency steps in one pass
t_{i}	0	Initial time (s)
t_{e}	40	Time duration of one frequency step (s)
t_{m}	–	Time taken to measure the output for one sample (s)

the time variable as $t = t + t_{\mathrm{m}}$. The loop continues until $t \geq t_{\mathrm{e}}$. After each step, the algorithm increments q and repeats the excitation-measurement cycle. When all Q steps are completed, the pass counter is updated to $l = l + 1$, and the next pass begins. The procedure terminates only after all N_{p} passes have been completed. This automated framework, guided by Figure 3.8, ensures reproducible and structured acquisition of IOD suitable for dynamic modelling.

Figure 3.9 presents the measured flow rate obtained during a complete excitation cycle of the flow system. In this cycle, the pump frequency increases stepwise from $6\ \mathrm{Hz}$ to $60\ \mathrm{Hz}$, with a stepwise increment of $6\ \mathrm{Hz}$ and then decreases to $6\ \mathrm{Hz}$, with a stepwise decrement of $6\ \mathrm{Hz}$. The six overlaid curves correspond to six independent measurement passes acquired using the automated IOD acquisition framework described by Figure 3.8. The figure captures key dynamic features of the system, including nonlinear flow behavior, transient responses, and the level of repeatability across passes. The measured data presents a staircase-like progression in the steady-state flow rate, reflecting the discrete changes applied to the pump's drive frequency. For each commanded frequency level, the flow rate moves toward a new operating point.

The figure depicts the regions with pronounced nonlinear and transient behavior especially for low input frequencies. During the initial frequency increments (up to approximately $18\ \mathrm{Hz}$), the measured flow rate exhibits overshoots and irregular transitions in all passes. These distortions align with the transitional flow regime and the reduced accuracy of the turbine flowmeter at low volumetric flow rates; below $1\ \mathrm{m^3/h}$ lies outside its optimal operating range. As a result, the early part of the cycle (first $100\ \mathrm{s}$) shows noticeable variability. Whereas the measurement results stabilize once the flow becomes fully turbulent. At higher frequencies, the flow rate increases almost linearly in time and follows the expected trend for a VFD-controlled pump.

During the decreasing frequency, the settling of the flow occurs more rapidly and without overshoots. This indicates asymmetric dynamics relative to the increasing frequency. The asymmetry reflects the system's inherent hysteresis as the stored momentum in the flow dissipates. The consistency of the repeated passes validates the experimental repeatability

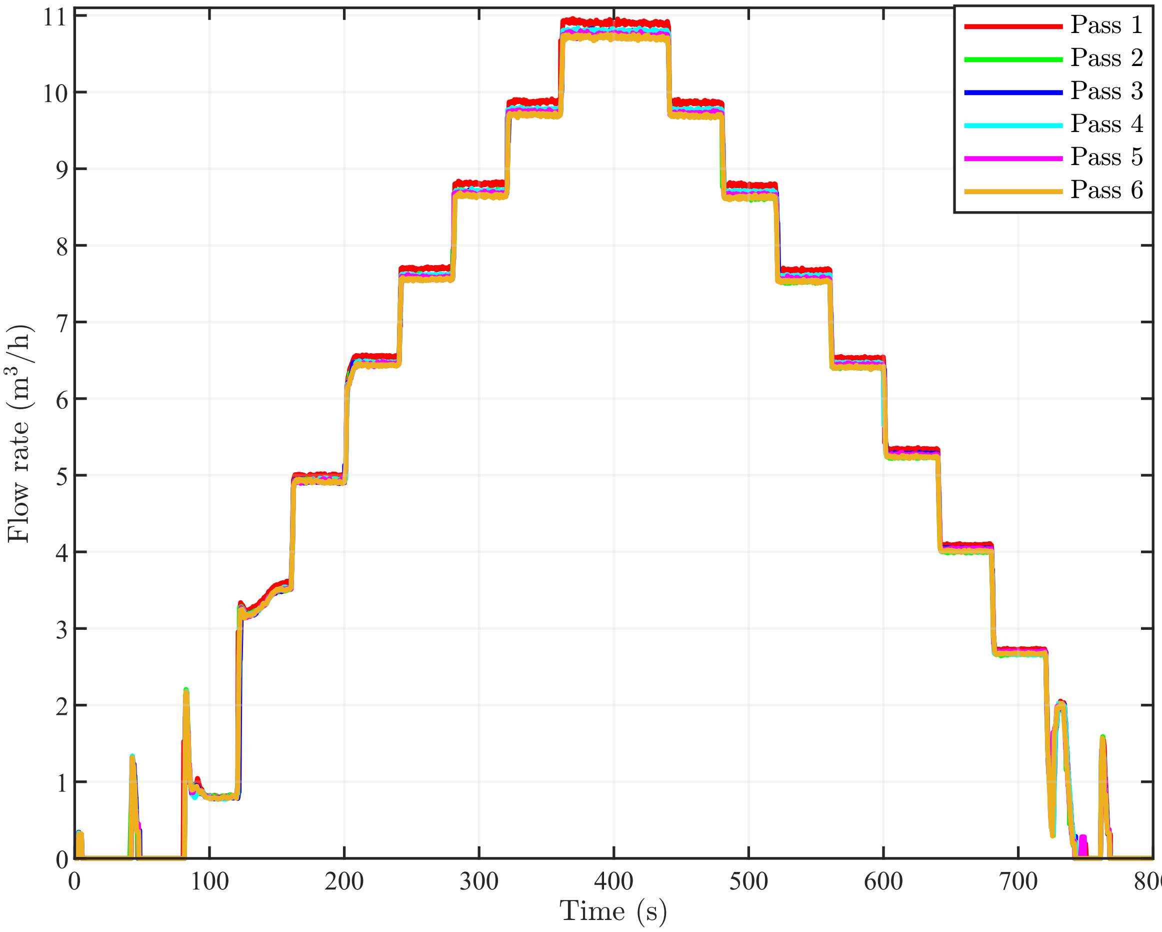

Figure 3.9: Measured flow rates for variable input frequency to operate the water pump for the increase and decrease of the flow.

required for data-driven modelling. Furthermore, the non-linearities observed at low flow conditions highlight the need for an LPV representation capable of capturing behavior across the entire operating range.

The experimental data for variable input (6-passes shown in Figure 3.9) is used for development and experimental validation of a reduced-order LPV model in Chapter 5.

3.4 Software tools and programming languages

This section declares the usage of software tools and programming languages utilized for simulations, numerical computations, hardware configuration, and data acquisition.

3.4.1 Software tools

Numerical computations for IO modeling, FO modeling, and control design were performed in MATLAB® R2024b [149]. The same version of MATLAB was used for configuration and data acquisition of the laboratory flow system. The nonlinear closed-loop structure for TRAS was implemented in Simulink® R2024b [150] to verify the performance of the FO PI and FO-PID controllers.

An online computational tool, State-of-the-Art Solvers for Numerical Optimization (NEOS-server) [151–153], was also used to solve the FO-DIEs as a continuous nonlinear optimization problem. AMPL Integrated Development Environment (IDE) [154] was used to compare the response of FO model obtained through NEOS-server.

3.4.2 Programming languages

The MATLAB programming language was used for hardware configuration, data acquisition, IO model identification, FO model identification, and control design. AMPL was used for FO model identification of the laboratory flow system.

3.5 Chapter summary

The chapter presented the case studies used to verify the proposed approaches in the dissertation. It also described the configuration and data acquisition procedure of the laboratory hardware. The SISO FO model of the inertia without delay is used to analyze the accuracy of the approximation methods. The TRAS model is used to analyze the influence of approximation methods on the performance of the FO-PI and PID controllers in the closed-loop. The same model is also used to propose and validate the tuning rules for FO-PI controllers. The variable input dataset supports the development of the IO-LPV model of the flow rate measurement system, whereas the fixed input dataset is used to construct the FO model. The IOD of the laboratory flow system with fixed input is also used to develop the framework for evaluation of the dynamic uncertainty. The data presented in this chapter is used and referenced in the relevant sections of the subsequent chapters.

CHAPTER 4

Accuracy of Approximation Methods

FO calculus has gained popularity in modeling and control of numerous real-time applications – several studies have been discussed in Chapter 2. However, the struggle to find a real FO element limits the potential in practical realization of such models [155, 156].

Implementing FO-DEs in electronic hardware remains challenging and the physical elements that realize fractional integration or differentiation are scarce [157]. To overcome these limitations, researchers approximate FO-DIEs using IO approximations [158]. Ideally, the approximations should produce a response identical to that of the reference FO models. Therefore, an approximated model exhibiting the same dynamic response as the reference FO model can be considered as "an accurate approximation model". However, these approximations inevitably introduce inaccuracies in the modeled responses. Therefore, this chapter defines accuracy as the extent to which an approximation method reproduces the dynamics of the reference FO model.

This chapter presents an accuracy analysis of IO approximation methods for realizing FO models and controllers. The analysis evaluates approximation accuracy for two systems: FO inertia and TRAS. For FO inertia, the chapter analyzes the accuracy through analytical and numerical calculations. For TRAS, the accuracy analysis is based on numerical calculations. The approximation methods used in this chapter are presented in Chapter 3. Section 3.1 describes the FO inertia model and Section 3.2 describes the TRAS model.

This chapter builds on the findings reported for FO inertia in [13] and for TRAS in [144]. Moreover, the analysis and the findings presented in this chapter cover the successful implementation of **Obj.1** listed in Chapter 1.

4.1 FO inertia without delay

This section presents accuracy analysis of the approximation methods used for analytical and numerical calculations for FO inertia with delay. Symbolic [159], FOMCON [24], and IOFOD [52] toolboxes were used to perform the calculations in MATLAB® R2024b. The mathematical model used in this section is presented in Chapter 3, Section 3.1.

4.1.1 Approximation errors

This section presents six types of errors for the accuracy analysis of the approximated models for FO inertia model. The first one is steady-state error. Three of them are based on the analysis of models in the frequency domain. The last two are used in the analysis of the closed-loop control system when subjected to the unit step input.

Since the steady-state values and magnitudes for fixed frequency are scalar numbers, the suitable measure for evaluating the approximation method is the relative error δy expressed as:

$$\delta y = \frac{y_A - y_o}{y_A} \tag{4.1}$$

where y_A is the actual steady-state value and y_o is the observed value of steady-state using the approximated model.

The relative magnitude error calculated for a specific frequency is [10]:

$$\delta|G| = \frac{|G_A| - |G_r|}{|G_r|} \tag{4.2}$$

where $|G|$ represents magnitude of the Fourier transform $G(j\omega)$. $|G_A|$ and $|G_r|$ denote the magnitudes of the approximated and reference TFs for a specific value of frequency, respectively.

The average magnitude error $\overline{\delta|G|}$ is:

$$\overline{\delta|G|} = \frac{\sum_{i=1}^{N} \delta|G(j\omega_i)|}{N_s}, \tag{4.3}$$

where N_s is the total number of samples in the frequency domain and $\delta|G(j\omega_i)|$ is the magnitude error calculated for a specific frequency.

The phase error $\Delta\varphi$ is [10]:

$$\Delta\varphi = \varphi_A - \varphi_r, \tag{4.4}$$

where φ_A and φ_r are phase angles of the approximated and reference TF for a specific value of frequency. Magnitude and phase are components of the TF (G) in the polar form [10], as:

$$G = \Re(G) + j\Im(G) = |G| \cdot e^{j\varphi}, \tag{4.5}$$

where $\Re(G)$ and $\Im(G)$ are the real and imaginary parts of the TF G, respectively. The frequency response is calculated for $\omega = 2\pi f$. The frequency range is considered as $f \in [0.001, 1]$ Hz.

Step response of the closed-loop system presents output over time when subjected to a unit step as a reference input. Therefore, a time-based error is suitable for comparing the output of the approximated model with the reference input. For FO inertia example, the dissertation selects the commonly used Integral Square Error (ISE) E_{ISE}, which is

$$E_{ISE} = \int_0^{t_k} e(t)^2 dt, \tag{4.6}$$

where t_k is simulation time and e is the difference between the reference and the response y of the approximation method. Other quality measure used in this work is L_1-norm defined as:

$$L_1 = \sum_{k=1}^{N_s} |e_k| \tag{4.7}$$

where $|e_k|$ denotes the absolute value error for k^{th} sample respectively.

4.1.2 Analytical calculations

To analyze the approximation accuracy, the steady-state values obtained using approximation methods are compared with the exact steady-state value calculated from the TF of FO inertia.

Exact steady-state value

From the TF model of the system in Eq. (3.1), the exact steady-state value is:

$$y(\infty) = G(0) = \frac{K}{0^{\alpha}T + 1} = K. \tag{4.8}$$

The system should reach the steady-state equal to the system gain when excited by the unit step.

The steady-state values obtained using approximation methods require replacing the FO element with its approximated model. In this step, the dissertation uses the minimum approximation order (N_F) equal to 0 or 1. Approximation methods beased on OM can generate a zero-order model. Therefore, the minimum order for such models is $N_\mathrm{F} = 0$. In contrast, CFE, MM, CM, and M-SBL yield a minimum first-order model. Consequently, $N_\mathrm{F} = 1$ is used as minimum approximation order for these methods. Moreover, to keep the results comparable, the maximum order for OM based models is set to $N_\mathrm{F} = 4$ and that for CFE, MM, and CM is set to $N_\mathrm{F} = 5$. Furthermore, the lower and upper limits of the frequency for the approximation methods are defined as $\omega_b = 0.001$ rad/s and $\omega_h = 1000$ rad/s, respectively.

Steady-state value with CFE

The CFE in Eq. (2.25) with $N_\mathrm{F} = 1$ provides the approximation:

$$G(s) \approx -\frac{K}{T\left(\frac{\alpha\,(s-1)}{\frac{(\alpha-1)\,(s-1)}{2}-1} - 1\right) - 1}. \tag{4.9}$$

The steady-state value is

$$y(\infty) = -\frac{K}{T\left(\frac{2\,\alpha}{\alpha+1} - 1\right) - 1} \neq K. \tag{4.10}$$

This evidences that the steady-state value of CFE is not the same as in the actual FO model. Furthermore, Eq. (4.10) shows that the first-order CFE depends on α. Only $\alpha = 1$ ensures $y(\infty) = K$. Consequently, the greater value $|1 - \alpha|$ results a larger error in the steady state.

Steady-state value with MM

The MM in Eq. (2.30) for $N_{\mathrm{F}} = 1$ provides the approximation:

$$G(s) \approx \frac{K}{T\left({\omega_b}^{\alpha} - \frac{\omega_b - s}{\frac{\omega_b - \sqrt{\omega_b}\sqrt{\omega_h}}{{\omega_b}^{\alpha} - \left(\sqrt{\omega_b}\sqrt{\omega_h}\right)^{\alpha}} - \frac{\left(s - \sqrt{\omega_b}\sqrt{\omega_h}\right)\left(\frac{\omega_b - \sqrt{\omega_b}\sqrt{\omega_h}}{{\omega_b}^{\alpha} - \left(\sqrt{\omega_b}\sqrt{\omega_h}\right)^{\alpha}} - \frac{\omega_b - \omega_h}{{\omega_b}^{\alpha} - {\omega_h}^{\alpha}}\right)}{\omega_h - \sqrt{\omega_b}\sqrt{\omega_h}}}\right) + 1}. \tag{4.11}$$

The steady-state value becomes

$$y(\infty) = \frac{K}{T\left({\omega_b}^{\alpha} - \frac{\omega_b}{\frac{\omega_b - \sqrt{\omega_b}\sqrt{\omega_h}}{{\omega_b}^{\alpha} - \left(\sqrt{\omega_b}\sqrt{\omega_h}\right)^{\alpha}} + \frac{\sqrt{\omega_b}\sqrt{\omega_h}\left(\frac{\omega_b - \sqrt{\omega_b}\sqrt{\omega_h}}{{\omega_b}^{\alpha} - \left(\sqrt{\omega_b}\sqrt{\omega_h}\right)^{\alpha}} - \frac{\omega_b - \omega_h}{{\omega_b}^{\alpha} - {\omega_h}^{\alpha}}\right)}{\omega_h - \sqrt{\omega_b}\sqrt{\omega_h}}}\right) + 1} \neq k. \tag{4.12}$$

The expression in Eq. (4.12) shows that the steady-state with MM does not only depend on α. It also depends on ω_b and ω_h. Moreover, $\alpha = 1$ in MM results the the steady-state values as $y(\infty) = K$.

Steady-state value with CM

The CM in Eq. (2.33) with $N_{\mathrm{F}} = 1$ for the FO inertia provides the approximation

$$G(s) \approx \frac{K}{\frac{T\,(3\,s+1)}{s+3} + 1}. \tag{4.13}$$

The steady-state value is

$$y(\infty) = \frac{K}{\frac{1}{3}T + 1} \neq K. \tag{4.14}$$

For the first-order CM, the steady-state value has no dependence on the parameters of the approximation method. For the inertia parameters considered in this work (3.1), the steady-state value is 0.692. Therefore, this approximation does not result in $y(\infty) = K$ for $\alpha = 1$.

Steady-state value with OM

The basic OM with $N_{\mathrm{F}} = 0$ provides

$$G(s) \approx \frac{K}{\frac{T\,{\omega_h}^{\alpha}\left(s+\omega_b\left(\frac{\omega_h}{\omega_b}\right)^{\frac{1}{2}-\frac{\alpha}{2}}\right)}{s+\omega_b\left(\frac{\omega_h}{\omega_b}\right)^{\frac{\alpha}{2}+\frac{1}{2}}}+1}. \tag{4.15}$$

The steady-state value is

$$y(\infty) = \frac{K}{T\,{\omega_h}^{\alpha}\left(\frac{\omega_h}{\omega_b}\right)^{-\alpha}+1} \neq K. \tag{4.16}$$

The steady-stated value of basic OM is not equal to that of the FO inertia model. However, the steady-state value obtained through this model Eq. (4.16) is smaller if $|1-\alpha|$ becomes small. Furthermore, $\alpha = 1$ does not result in $y(\infty) = K$.

This work also presents steady-state values for popular Oustaloup variants, namely RO [10] and XO [10].

Steady-state value with RO

The RO with $N_{\mathrm{F}} = 0$ provides

$$G(s) \approx \frac{K}{\frac{T\left(d\,s^2+b\,\omega_h\,s\right)\left(s+\omega_b\left(\frac{\omega_h}{\omega_b}\right)^{\frac{1}{2}-\frac{\alpha}{2}}\right)\left(\frac{d\,\omega_h}{b}\right)^{\alpha}}{\left(s+\omega_b\left(\frac{\omega_h}{\omega_b}\right)^{\frac{\alpha}{2}+\frac{1}{2}}\right)\left(-d\,(\alpha-1)\,s^2+b\,\omega_h\,s+\alpha\,d\right)}+1}. \tag{4.17}$$

The steady-state value is

$$y(\infty) = K. \tag{4.18}$$

The RO is the first OM variant that yields a steady-state value equal to K. This value matches that of the actual FO inertial model. The RO therefore reproduces the steady-state value of the FO inertial for $N_{\mathrm{F}} = 0$ and higher.

Steady-state value with XO

The XO with $N_{\mathrm{F}} = 0$ provides the approximation

$$G(s) \approx \frac{K}{\frac{T\left(s+\left(\frac{d\,\omega_b}{b}\right)^{\alpha}\right)\left(d\,s^2+b\,\omega_h\,s\right)\left(\frac{b\,\omega_h}{d}\right)^{\alpha}}{\left(s+\left(\frac{b\,\omega_h}{d}\right)^{\alpha}\right)\left(-d\,(\alpha-1)\,s^2+b\,\omega_h\,s+\alpha\,d\right)}+1}. \tag{4.19}$$

The steady-state value is

$$y(\infty) = K. \tag{4.20}$$

The XO also results in a steady-state value equal to K regardless the value of N_{F}.

4.1.3 Numerical errors

Table 4.1 and Table 4.2 present the calculated steady-state values and errors for different orders of the approximating models. Table 4.1 contains data for $\alpha = 0.8$ and Table 4.2 for $\alpha = 0.5$. This comparison allows to examine the effect of $|1 - \alpha|$ on the error values. The proposed method considers the two cases based on the model order: with $N_{\mathrm{F}} = 0$ or $N_{\mathrm{F}} = 1$ (when 0^{th} order cannot be obtained) and with $N_{\mathrm{F}} = 5$. This allows to investigate the effect of model order on the steady-state error.

Table 4.1: Approximation errors in steady state calculated for FO inertia with $\alpha = 0.8$.

Approximation method	Order N_{F}	Steady-state value	Error δy (%)
CFE	1	1.420	−53.0
	5	2.650	−12.0
MM	1	2.910	−2.90
	5	2.980	−0.81
CM	1	0.692	−77.0
	5	2.880	−4.00
M-SBL	1	3.050	1.60
	5	2.970	−0.95
OM	0	2.890	−3.80
	5	2.890	−3.80
RO	0	3.000	0.00
	5	3.000	0.00
XO	0	3.000	0.00
	5	3.000	0.00

Table 4.1 shows that the first-order CM has a steady-state value of 0.692 which results in −77 % steady-state error. However, increasing the order to $N_{\mathrm{F}} = 5$ makes a significant improvement and the steady state value is 2.88 which gives an error of −4.0 %. The second model with significant errors is CFE. For the first order, the steady state value is 1.42, which gives an error of −53 %. Increasing the order of the model to five does not provide the same improvement as in the Carlson model. However, the error reduces to −12 %. The Matsuda and M-SBL models give much better results for the first order. The M-SBL model is the only model that produces a steady-state value greater than K for the first order. With these two models, one can see an improvement when the model order is increased. The M-SBL model results in a small steady-state error for the lower order compared to that for the

MM. However, the MM outperforms M-SBL when $N_F = 5$. The basic OM gives a constant steady-state value of 2.89 regardless of the model order. This results in a steady-state error of $-3.8\,\%$. The and XO give the steady-state value equal to K which results in zero error.

Comparing Table 4.2 with Table 4.1, one can see that in most cases the increased difference in $|1 - \alpha|$ results in smaller steady-state values and the greater percentage of error. Increasing the order of the model for CFE in this case does not provide a significant improvement in the steady-state value as is the case for $\alpha = 0.8$. The error for both orders is large ($-77\,\%$ and $48\,\%$). The MM also results in an error of $-23\,\%$ for $\alpha = 0.5$ when $N_F = 1$ and $-14\,\%$ when $N_F = 5$. However, increasing the value of α to 0.8 results in a reduction of error percentage to $-2.9\,\%$ when $N_F = 1$ and $-0.81\,\%$ when $N_F = 5$. Interestingly is that for the CM, there are the same errors in Table 4.1 and Table 4.2. This is because α does not affect the steady-state value. The order N_F has a reverse impact on steady-state error for the M-SBL model when $\alpha = 0.5$. Increasing N_F from 1 to 5 results in an increase in error percentage from $-0.99\,\%$ to $-15\,\%$. In the case of the basic OM, the error is more than 4 times than that of the basic OM when $\alpha = 0.8$ in Table 4.1. It is due to the influence of $|1 - \alpha|$ on the steady-state value. The RO and XO are independent of parameter α and give an exact value equal to K. Therefore, the error for these approximation methods is zero.

Table 4.2: Approximation errors, in steady state calculated for FO inertia with $\alpha = 0.5$.

Approximation method	Order N_F	Steady-state value	Error δy (%)
CFE	1	0.692	−77.0
	5	1.570	−48.0
MM	1	2.300	−23.0
	5	2.590	−14.0
CM	1	0.692	−77.0
	5	2.880	−4.00
M-SBL	1	2.970	−0.99
	5	2.540	−15.0
OM	0	2.280	−24.0
	5	2.280	−24.0
RO	0	3.000	0.00
	5	3.000	0.00
XO	0	3.000	0.00
	5	3.000	0.00

4.1.4 Numerical simulations

This section presents the analysis of the responses with the approximation models. The analysis for FO inertia model is categorizes in two cases:

- unit step responses, and
- Nyquist plots.

Unit step response

This section presents step responses for four distinct configurations. The first configuration considers $\alpha = 0.8$ and the minimum admissible approximation order N_F. The second configuration considers fifth-order approximation methods, excluding the CM. For the CM, selecting $N_F = 5$ yields a TF order 781 causing the parameters to diverge to infinity. Therefore, this study adopts $N_F = 4$ as the maximum admissible order for the CM. The remaining two configurations repeat the previous analyses for $\alpha = 0.5$. To generate the step responses, the approximation methods of FO inertial were applied unity-amplitude input voltages V for 500 s and the corresponding angular displacements θ were recorded.

In contrast to the symbolic steady-state analysis, the reference step response cannot be determined. Therefore, the analysis compares the time responses only with each other. Each figure contains two viewing windows with identical time intervals. The left window shows the overall differences between the responses while the right window displays a magnified view of responses.

Figure 4.1 compares step responses of the FO inertia using different approximation methods. The figure is divided in two panels: Figure 4.1 (a) and the corresponding zoomed version in panel (b). The legend indicates model orders equal to zero or one. The Carlson and CFE approximations produce large steady-state errors. The M-SBL approximation yields the slowest dynamic response. The Xue Oustaloup, Refined Oustaloup, and Matsuda models exhibit similar rise times to achieve the value 2.91. Despite similar rise times, their dynamic behaviors differ. The Matsuda approximation settles at the value 2.91. In contrast, the Refined and Xue Oustaloup models increase linearly toward 3.0. The OM produces a response similar to MM. However, it responds more slowly and exhibits a larger steady-state error.

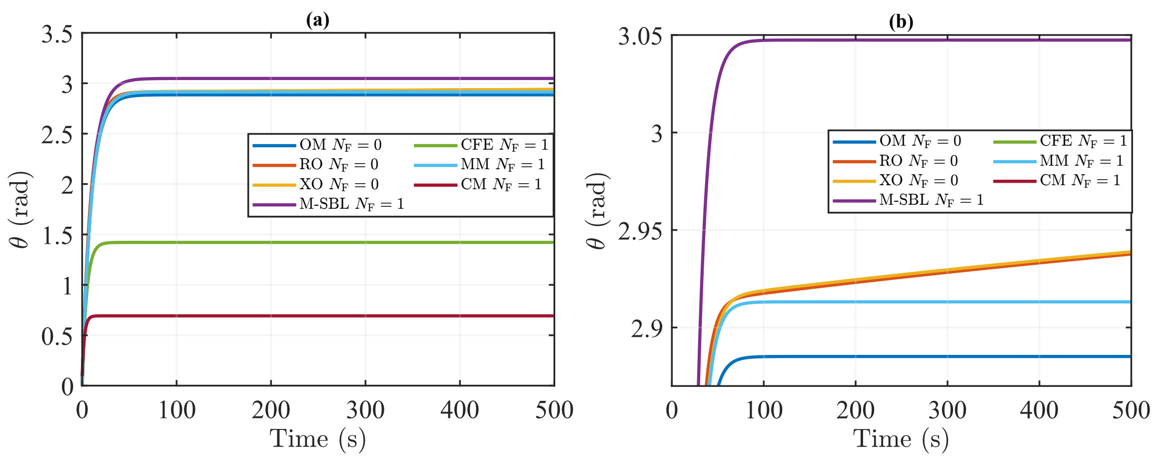

Figure 4.1: Unit step responses of the FO inertia for $\alpha = 0.8$ using different approximation methods for the lowest possible order, i.e., $N_F = 0$ or $N_F = 1$.

Figure 4.2 shows step responses obtained with higher orders of approximation methods. Most models exhibit reduced steady-state errors compared with lower-order cases. Similar to Figure 4.1, Figure 4.2 (b) depicts the zoomed version of the corresponding panel (a). Within the analyzed time interval, the Carlson and CFE models retain relatively larger errors. The CM shows longer rise and settling times than the remaining approximations. This behavior results from the increased order of the corresponding TFs. During the initial transient, the Xue and Refined Oustaloup models respond slightly faster than MM and CM. The analysis emphasizes these models because they yield the smallest steady-state errors. Comparison of Figure 4.1 and Figure 4.2 shows that increasing model order reduces the approximation error. However, this improvement causes approximately a fourfold increase in rise time.

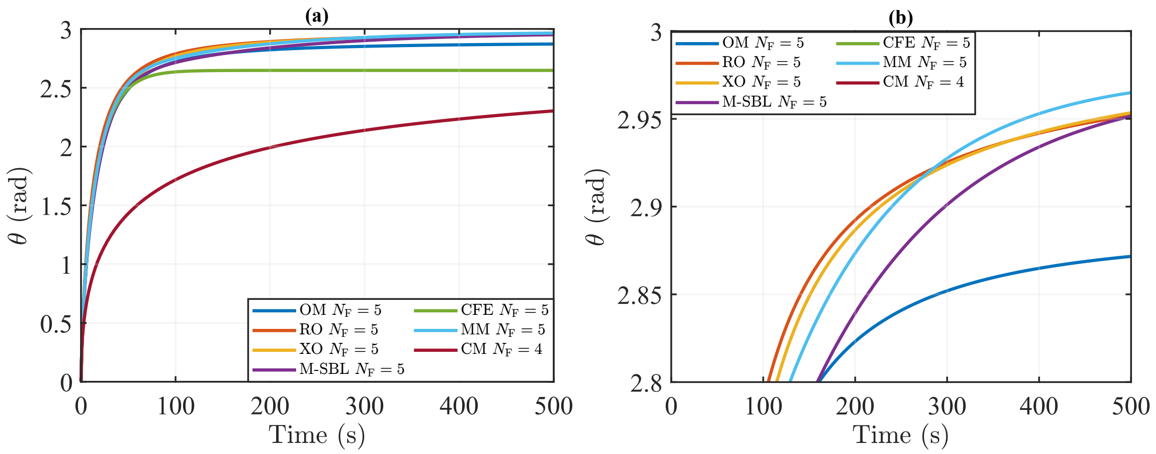

Figure 4.2: Unit step responses of the FO inertia for $\alpha = 0.8$ using different approximation methods for $N_F = 4$ (for CM) and $N_F = 5$ (for the rest).

Figure 4.3 and Figure 4.4 depict the step responses for $\alpha = 0.5$. Figure 4.3 presents two panels: (a) and the corresponding zoomed portion in panel (b). Comparison of Figure 4.1 and Figure 4.3 evidences the presence of larger steady-state errors for value of $\alpha = 0.5$. Within the analyzed time horizon, the M-SBL exhibits the fastest response with the smallest error. The XO and RO models reach actual steady-state, i.e., $K = 3$. However, after $t = 50$ s, their responses increase slowly. For $\alpha = 0.5$, the MM, CFE, and OM models show similar behavior in the step response.

Figure 4.4 presents unit step responses for the approximation methods obtained after increasing N_F to 5 ($N_F = 4$ for CM). Like the preceding figures, Figure 4.4 includes two panels: (a) and the corresponding zoomed region in Figure 4.4 (b). For this order of the FO derivative, the CFE exhibits the largest magnitude of steady-state error. The remaining models present similar dynamic behavior to each other within the considered time horizon. The M-SBL has a slower response when subjected to the unit step input. The RO and XO models fail to reach the steady-state value, i.e., $K = 3$ within the considered time span. This effect results from the delay introduced by higher-order TF structures with these approximations.

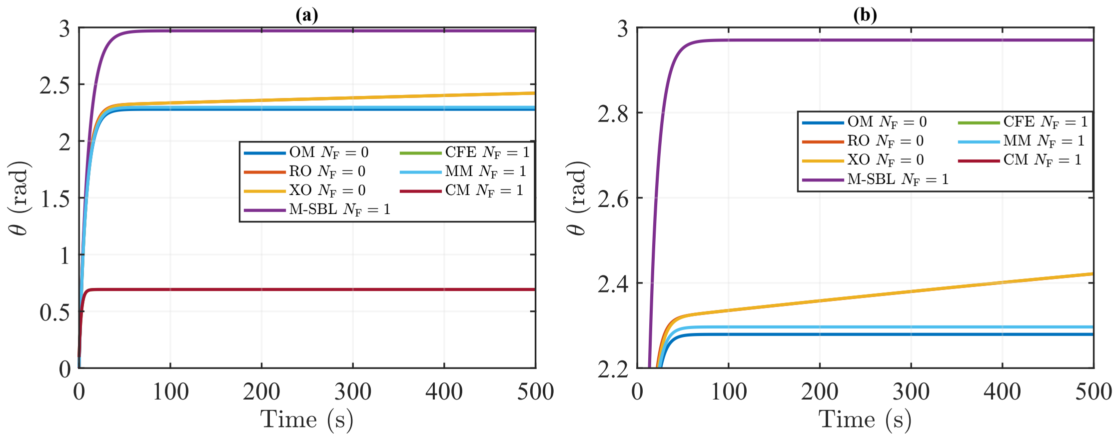

Figure 4.3: Unit step responses of the FO inertia for $\alpha = 0.5$ using different approximation methods for the lowest possible order, i.e., $N_F = 0$ or $N_F = 1$.

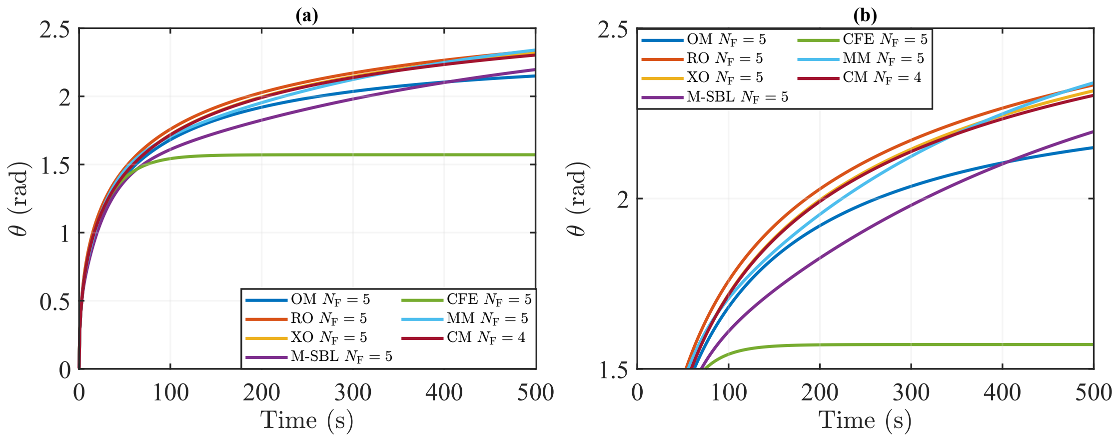

Figure 4.4: Unit step responses of the FO inertia for $\alpha = 0.5$ using different approximation methods for $N_F = 4$ (for CM) and $N_F = 5$ (for the rest).

The CM is relatively complex to implement compared to the other models presented in this chapter. Recursive computation of the terms $H_i(s)$ in Eqs. (2.33)-(2.34) increases the implementation complexity of this method. For the FO inertia, the CM provide an approximated TF model of order N_{TF} equal to 156. Such a high order realization introduces several practical limitations. One of the drawbacks is presence of high-frequency oscillations for different sampling times T_s. Figure 4.5 depicts the step response for sampling times $T_s = 0.1$, $T_s = 0.08$, and $T_s = 0.01$. This figure consists of two panels: (a) and the corresponding zoomed view in panel (b). The step responses shown in the figure are for the approximation order $N_s = 4$. It is evident from the figure that larger values of T_s lead to high magnitude oscillations in the step response. While decreasing the sampling time improves the oscillations, it may cause a significant burden on the computation resources.

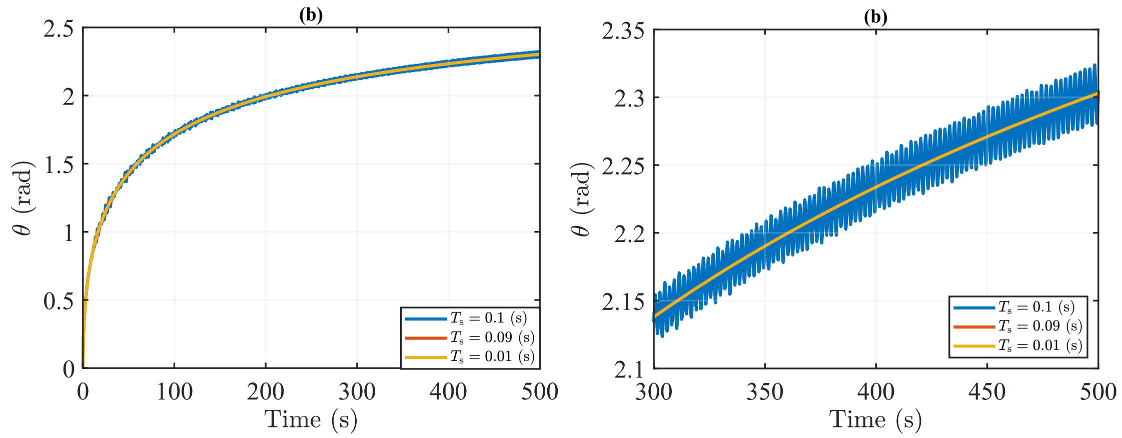

Figure 4.5: Responses of FO inertia for $\alpha = 0.8$ with unit step input calculated for Carlson model with $N_{\mathrm{F}} = 4$ under different sampling times.

Nyquist plot

Unlike the step-response analysis, the Nyquist plot analysis allows direct comparison with the characteristics of the reference FO model. This comparison facilitates the evaluation of magnitude and phase errors across selected values of the frequency. The analysis considers FO systems after substitution $s \to j\omega$. The frequency characteristics are evaluated at sixteen frequency values which are spaced algorithmically. Figure 4.6 shows the Nyquist plots for $\alpha = 0.8$ for different approximation methods. Table 4.3 reports the corresponding magnitude error Eq. (4.2) and phase error Eq. (4.4).

Similarly, Figure 4.7 and Table 4.4 present the frequency characteristics and error values for $\alpha = 0.5$ for the reference FO model and the implemented approximations. Each panel presents the reference characteristic and the response of the approximation method. The models correspond to approximation orders $N_{\mathrm{F}} = 0$ or 1 and $N_{\mathrm{F}} = 4$ or 5, respectively.

Analysis of Figure 4.6 ($\alpha = 0.5$) evidences the poor performance of all approximation methods for lowest possible value of N_{F}. For OM, RO, XO M-SBL, and MM, the magnitudes are overestimated. Consequently, the characteristic points are located outside the reference trajectory. In contrast CFE and Carlson models exhibit the opposite behavior. Their magnitudes remain underestimated resulting the placement of characteristic point inside the reference trajectory. These high frequency-domain errors at low frequencies are produced by high amplitudes of time-domain errors in the approximations for lowest orders of the approximations.

Increasing N_{F} to 4 or 5 improves the results for all approximation methods. For the OM, the trajectory matches well at higher frequencies while small deviations from the reference points are visible at lower frequencies. The RO model for $N_{\mathrm{F}} = 5$ generates points that follow the reference trajectory and exhibit a systematic shift in magnitude. The XO method provides the best performance, with points nearly overlapping the reference.

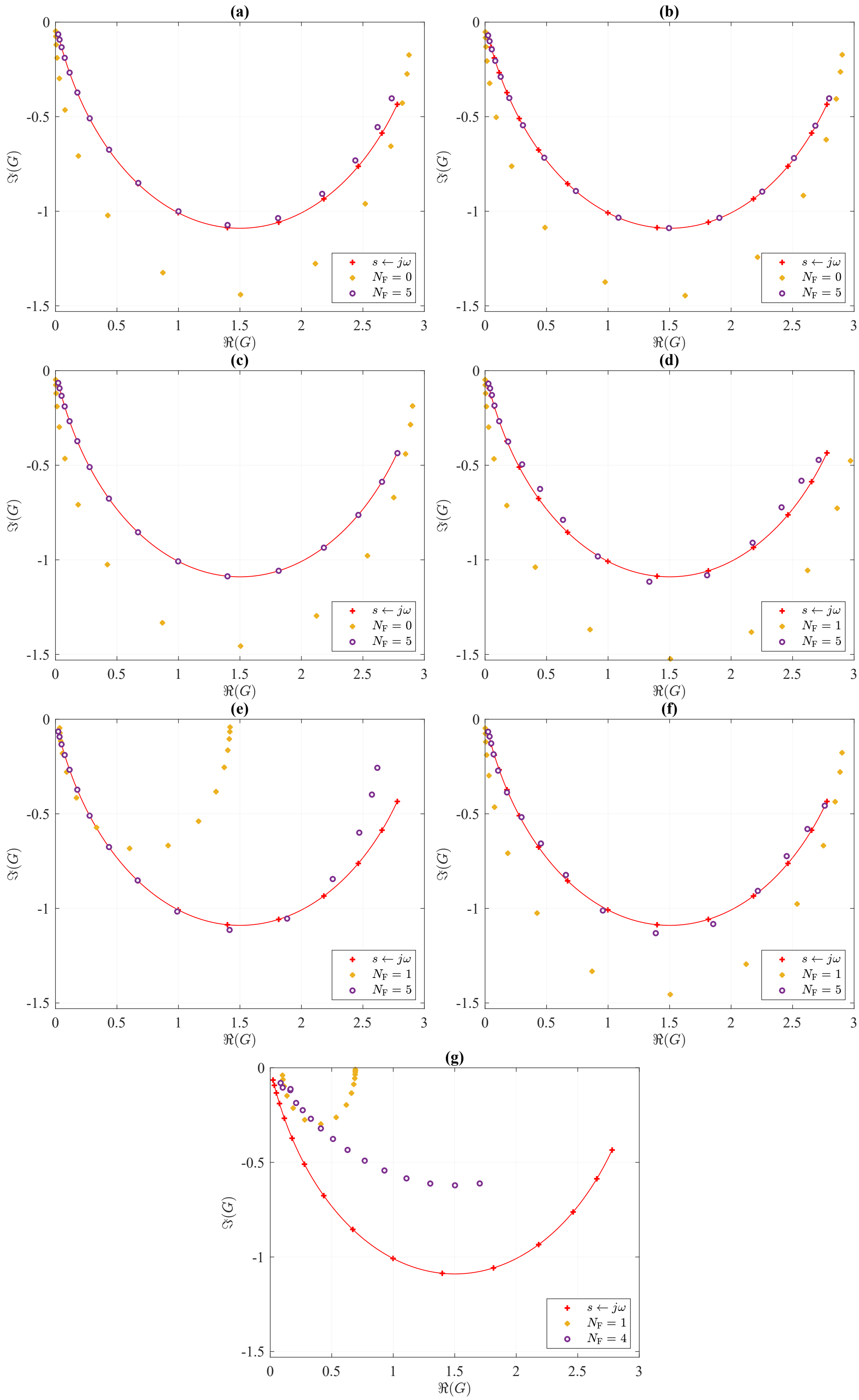

Figure 4.6: Nyquist plots of FO inertia for $\alpha = 0.8$. The approximation methods displayed in different panels are: (**a**) Oustaloup, (**b**) Refined Oustaloup, (**c**) Xue Oustaloup,(**d**) M-SBL,(**e**) CFE,(**f**) Matsuda, and (**g**) Carlson approximation methods.

Table 4.3: Magnitude and phase errors, Eq. (4.2) and Eq. (4.4), of FO approximation methods calculated for FO inertia with $\alpha = 0.8$ and $N_F = 5$ (Carlson model with $N_F = 4$).

Freq. (Hz)	$\delta\lvert G\rvert$ %	$\Delta\varphi$ °	$\delta\lvert G\rvert$ %	$\Delta\varphi$ °	$\delta\lvert G\rvert$ %	$\Delta\varphi$ °	$\delta\lvert G\rvert$ %	$\Delta\varphi$ °
Model	OM		ROM		XOM		M-SBLM	
0.0010	−1.8	0.50	0.45	0.69	0.041	−0.022	−2.2	−0.98
0.0016	−1.5	0.50	0.79	0.94	0.018	−0.017	−3.0	−0.28
0.0025	−1.2	0.51	1.3	1.2	0.034	−0.0057	−2.4	0.52
0.0040	−0.96	0.47	2.1	1.5	0.023	−0.024	−0.69	0.49
0.0063	−0.72	0.45	3.2	1.7	−0.0074	−0.00087	0.16	−0.70
0.010	−0.43	0.38	4.4	1.8	0.042	−0.0067	−1.7	−2.0
0.016	−0.29	0.29	5.6	1.7	−0.020	−0.023	−5.3	−1.7
0.025	−0.15	0.25	6.6	1.4	0.0020	0.019	−6.9	0.63
0.040	−0.044	0.15	7.4	1.1	0.034	−0.022	−4.4	2.8
0.063	−0.081	0.12	7.9	0.86	−0.046	−0.0034	−0.11	2.7
0.10	0.0057	0.11	8.3	0.65	0.032	0.019	1.6	1.0
0.16	−0.0090	0.061	8.4	0.43	0.0058	−0.030	0.022	0.0012
0.25	−0.046	0.11	8.5	0.34	−0.041	0.014	−1.9	0.84
0.40	0.034	0.13	8.7	0.24	0.049	0.0041	−1.1	2.8
0.63	−0.034	0.17	8.7	0.15	−0.023	−0.030	3.2	3.8
1.0	−0.021	0.31	8.7	0.16	−0.019	0.021	7.8	2.5

Freq. (Hz)	$\delta\lvert G\rvert$ %	$\Delta\varphi$ °	$\delta\lvert G\rvert$ %	$\Delta\varphi$ °	$\delta\lvert G\rvert$ %	$\Delta\varphi$ °
Model	CFEM		Matsuda		Carlson	
0.0010	−6.5	3.3	−0.51	−0.51	−36	−11
0.0016	−4.2	3.7	−1.3	−0.025	−40	−10
0.0025	−1.4	3.6	−0.81	0.76	−44	−8.0
0.0040	1.4	2.6	0.92	0.93	−47	−4.6
0.0063	2.7	1.0	2.2	−0.036	−49	−0.079
0.010	1.7	−0.35	1.1	−1.3	−49	5.3
0.016	0.040	−0.48	−1.8	−1.3	−46	11
0.025	−0.31	−0.020	−3.1	0.46	−42	15
0.040	0.023	0.053	−0.63	1.9	−35	19
0.063	0.012	−0.015	2.8	1.2	−27	22
0.10	−0.0052	0.0054	3.2	−0.81	−16	24
0.16	0.00091	−0.0042	0.35	−2.0	−3.6	25
0.25	0.0026	0.0061	−2.8	−1.2	11	26
0.40	−0.0045	−0.017	−3.3	0.82	27	27
0.63	−0.057	0.050	−0.44	2.2	48	27
1.0	0.35	0.059	3.1	1.3	70	27

For the M-SBL, magnitude points approach the reference values more closely than in case of RO method. As a result, the magnitude error is smaller with M-SBL compared to that with RO model. The CFE model achieves a better accuracy at higher values of frequency. Thus, increasing N_{F} extends the frequency range that ensures the acceptable accuracy. The MM exhibits similar frequency behavior to that of M-SBL. A few points deviate from the reference trajectory, while the magnitude error remains smaller than that with RO model. The CM exhibits relatively large magnitude and phase errors across the entire frequency range, indicating poorer performance compared with the other methods.

Figure 4.7 and Table 4.4 present that for $\alpha = 0.5$, the approximation methods with lower values of N_{F} produce larger errors. For small α, the approximation method with $N_{\mathrm{F}} = 0$ and $N_{\mathrm{F}} = 1$, except CFE and CM, deviate significantly from the reference characteristic. Similar to that with $\alpha = 0.8$ (Figure 4.6), increasing the approximation order N_{F} improves the results of approximation methods.

For the OM with $N_{\mathrm{F}} = 5$, a slight increase magnitude error can be observed for low frequencies. The RO method presents the points that are aligned with the reference trajectory with a shift in the magnitude. The M-SBL and Matsuda approximation methods with $N_{\mathrm{F}} = 5$ generate the irregular Nyquist plots depicting oscillations around the reference points. Such oscillation do not appear in these methods for $N_{\mathrm{F}} = 1$ with $\alpha = 0.8$.

For $\alpha = 0.8$, the CFE exhibits poor performance at low frequencies while XO and Carlson models present a superior performance compared to rest of the approximations. The steady-state error analysis concluded the similar analysis to those obtained for $\alpha = 0.5$. Table 4.4 shows that the CM and XO provide the smallest magnitude and phase errors produces small errors independent of α.

Comparison of Table 4.3 and Table 4.4 suggests that the RO with $N_{\mathrm{F}} = 5$ achieves lower phase errors than those with the OM. However, the RO approximation exhibits larger magnitude errors. The CFE generates errors up to $14\,\%$ at low values of the frequency and $0.0086\,\%$ at high frequencies. Further comparison of Table 4.3 and Table 4.4 presents the similar error values for the RO, XO, Matsuda, and M-SBL models over different values of α. The OM and CFE present a comparable behavior at higher frequencies. In contrast, the magnitude and phase errors of the CM are highly sensitive to α.

Table 4.5 lists the mean magnitudes of errors and the order of the corresponding approximated TF N_{TF} for FO inertia with $\alpha = 0.8$. Error evaluation uses approximation methods with N_{F} ranging from the lowest feasible order, i.e., $N_{\mathrm{F}} = 0$ up to $N_{\mathrm{F}} = 5$. The CM is an exception in this scenario as the error evaluation is possible only up to $N_{\mathrm{F}} = 4$. The numerical results evidence that the OM, RO, and CM provide no significant error reduction beyond $N_{\mathrm{F}} = 2$.

Increasing the approximation order N_{F} for the XO, CFE, M-SBL, and MM leads to a significant reduction in the error. The XO approximation exhibits the smallest mean magnitude error, equal to $0.0079\,\%$. This method yields a TF of order $N_{\mathrm{TF}} = 15$ when $N_{\mathrm{F}} = 5$ is selected as an order of approximation.

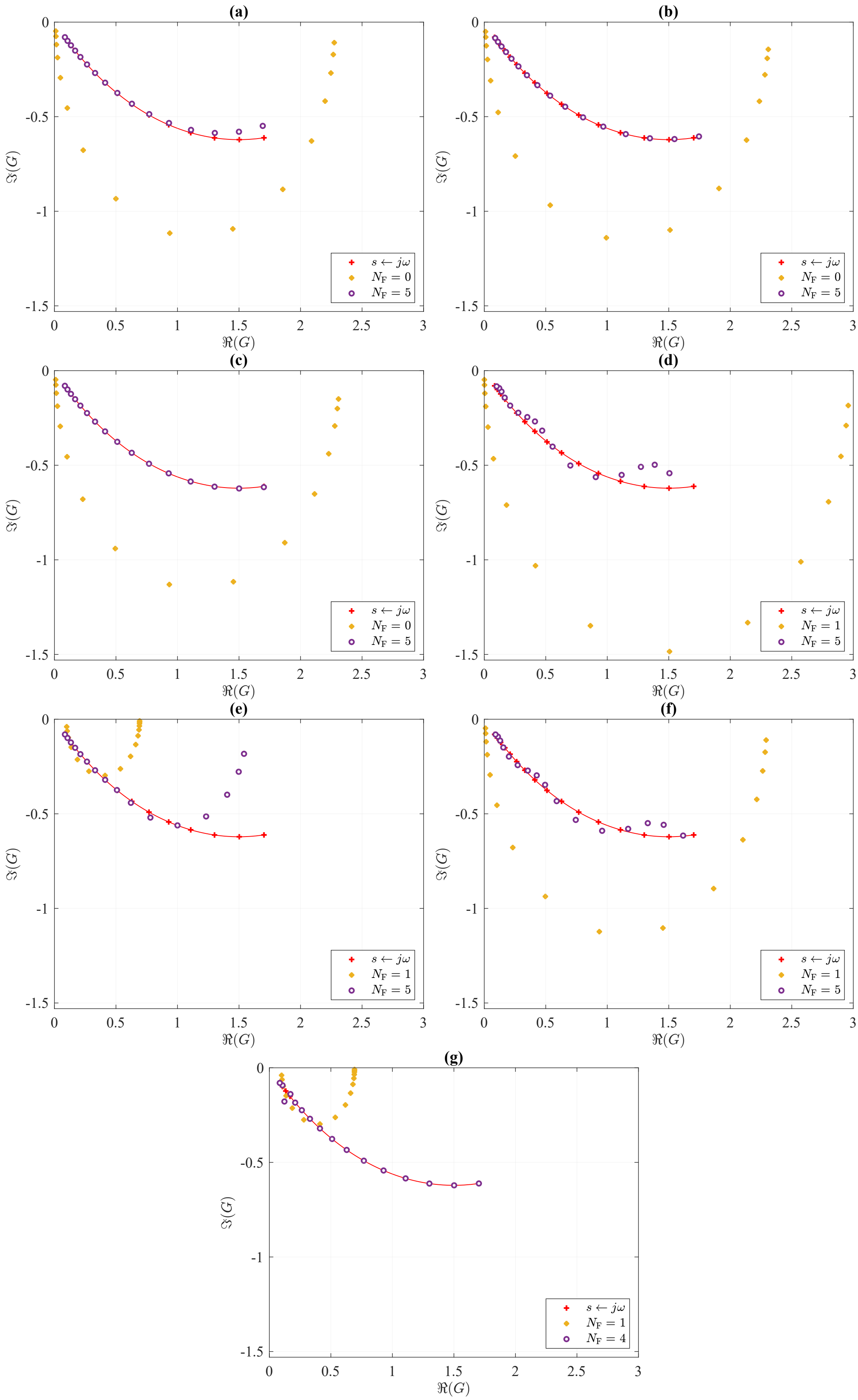

Figure 4.7: Nyquist plots of FO inertia for $\alpha = 0.5$. The approximation methods are same as in Figure 4.6.

Table 4.4: Magnitude and phase errors, Eq. (4.2) and Eq. (4.4), of FO approximation methods calculated for FO inertia with $\alpha = 0.5$ and $N_\mathrm{F} = 5$ (Carlson model with $N_\mathrm{F} = 4$).

Freq. (Hz)	$\delta\lvert G\rvert$ %	$\Delta\varphi$ °	$\delta\lvert G\rvert$ %	$\Delta\varphi$ °	$\delta\lvert G\rvert$ %	$\Delta\varphi$ °	$\delta\lvert G\rvert$ %	$\Delta\varphi$ °
Model	OM		ROM		XOM		M-SBLM	
0.0010	−1.6	1.8	2.1	0.66	0.016	−0.13	−12	−0.041
0.0016	−1.1	1.3	2.5	0.69	−0.029	−0.061	−9.4	2.7
0.0025	−0.61	0.99	3.0	0.68	0.063	−0.038	−4.6	3.4
0.0040	−0.39	0.66	3.3	0.60	−0.011	−0.064	−0.55	1.6
0.0063	−0.26	0.50	3.6	0.60	−0.020	0.0096	−0.81	−1.5
0.010	−0.069	0.32	4.0	0.52	0.068	−0.026	−5.6	−3.0
0.016	−0.12	0.19	4.2	0.43	−0.057	−0.031	−10	−1.2
0.025	−0.037	0.18	4.4	0.43	0.014	0.034	−10	2.5
0.040	0.025	0.072	4.7	0.31	0.048	−0.039	−5.7	4.9
0.063	−0.082	0.070	4.7	0.28	−0.077	−9.2	0.32	4.2
0.10	0.040	0.085	5.0	0.26	0.056	0.030	2.6	1.6
0.16	4.0	0.0096	5.0	0.15	0.0073	−0.049	0.035	0.0014
0.25	−0.063	0.083	5.0	0.18	−0.067	0.025	−3.0	1.4
0.40	0.067	0.083	5.2	0.14	0.081	0.0077	−1.5	4.4
0.63	−0.047	0.075	5.2	0.073	−0.038	−0.048	5.0	5.9
1.0	−0.027	0.21	5.2	0.13	−0.033	0.037	12	4.1

Freq. (Hz)	$\delta\lvert G\rvert$ %	$\Delta\varphi$ °	$\delta\lvert G\rvert$ %	$\Delta\varphi$ °	$\delta\lvert G\rvert$ %	$\Delta\varphi$ °
Model	CFEM		Matsuda		Carlson	
0.0010	−14	13	−4.4	−1.1	0.0080	0.0044
0.0016	−6.3	12	−3.9	1.5	−9.8	-7.0×10^{-4}
0.0025	1.5	9.3	0.055	2.7	−1.2	4.2×10^{-5}
0.0040	6.6	5.2	4.2	1.5	−1.3	-9.2×10^{-7}
0.0063	6.6	1.0	4.6	−1.3	1.6	-1.0×10^{-8}
0.010	2.8	−1.1	0.34	−3.0	1.2	-1.3×10^{-10}
0.016	−0.23	−0.80	−4.3	−1.7	−1.9	3.4×10^{-10}
0.025	−0.49	0.011	−4.7	1.4	−1.4	1.6×10^{-8}
0.040	0.050	0.081	−0.33	3.1	−1.2	4.0×10^{-8}
0.063	0.016	−0.024	4.7	1.8	−4.5	6.2×10^{-6}
0.10	−0.0075	0.0086	5.2	−1.4	9.4	1.6×10^{-4}
0.16	0.0011	−0.0065	0.45	−3.3	0.030	−0.0066
0.25	0.0045	0.0095	−4.7	−1.9	−0.065	0.20
0.40	−0.0082	−0.026	−5.3	1.4	−0.51	−0.29
0.63	−0.083	0.080	−0.66	3.4	−0.74	−0.12
1.0	0.55	0.078	5.1	2.2	−0.012	−0.0042

The analysis also indicates that only the M-SBL, CFE, and MM produce TFs with order N_TF equals the approximation order N_F. For models belonging to the Oustaloup family, each increase in approximation order N_F increase the order of approximated TF

N_F by two. Consequently, the OM starts from order one for $N_F = 0$. The remaining Oustaloup-based models start from order three. The CM exhibits an exponential increase in N_{TF} with increasing N_F. However, this increase does not ensure a decrease in mean magnitude error. For $N_F = 3$ and onwards, the CM always yields the highest order of the approximated TF leading to $N_{TF} = 781$ for $N_F = 5$.

Table 4.5: Average magnitude error Eq. (4.3), and order of the TFs N_{TF} of FO approximation methods calculated for FO inertia with $\alpha = 0.8$ and $0 \le N_F \le 5$.

Order N_F	$\overline{\delta\lvert G\rvert}$ %	N_{TF} –	$\overline{\delta\lvert G\rvert}$ %	N_{TF} –	$\overline{\delta\lvert G\rvert}$ %	N_{TF} –	$\overline{\delta\lvert G\rvert}$ %	N_{TF} –	$\overline{\delta\lvert G\rvert}$ %	N_{TF} –	$\overline{\delta\lvert G\rvert}$ %	N_{TF} –	$\overline{\delta\lvert G\rvert}$ %	N_{TF} –
Model	Ous		Ref		Xue		M-SBL		CFE		Matsuda		Carlson	
0	13	1	19	3	13	3	–	–	–	–	–	–	–	–
1	−1.4	3	4.6	5	−0.99	5	15	1	−16	1	13	1	−30	1
2	−0.43	5	5.7	7	0.017	7	0.91	2	−6	2	3.2	2	−18	6
3	−0.41	7	5.7	9	0.062	9	−7.3	3	−2.3	3	−1.2	3	−17	31
4	−0.45	9	5.7	11	0.011	11	−1.8	4	−0.95	4	0.48	4	−17	156
5	−0.46	11	5.7	13	0.0079	13	−1.1	5	−0.39	5	−0.062	5	–	781

In conclusion, the results indicate that several methods introduce approximation errors. These errors affect steady-state response, transient dynamics, phase characteristics, and stability margins of the approximated model. The RO and XO methods exhibit minimal transient errors and no steady-state error. However, they yield and increased approximation order by two compared to the standard OM. The M-SBL method represents an alternative when considering steady-state error. However, it introduces magnitude and phase errors in the frequency response, which increases with increasing frequency. The CFE method yields the lowest model order but produces the largest steady-state error among the compared methods. Therefore, the method selection requires a trade-off between approximation accuracy and implementation complexity. Based on this trade-off, the chapter selects the standard OM and evaluates its closed-loop performance for TRAS.

4.2 Twin rotor aerodynamic system

Based on the performance analysis and comparative study of approximation methods presented in the previous section, this section selects the Oustaloup approximation. This study sets the approximation order to $N_F = 5$. The lower and upper frequency limits equal $\omega_b = 0.001$ rad s^{-1} and $\omega_h = 1000$ rad s^{-1}, respectively.

The selected approximation evaluates the closed-loop response of the FO-PID controller. The controller is designed using SISO decoupled models of TRAS presented in Chapter 3, Section 3.2.2. The closed-loop response is evaluated by applying the controller to the nonlinear model presented in Section 3.2.1. The analysis and results presented in this section are based on the published article [144].

4.2.1 FO-PID controller

This section applies built-in optimization algorithms from the MATLAB Optimization Toolbox [160] to tune the parameters of the FO-PID controller. These algorithms were selected because they offer simple implementation and low computational burden.

The standard numerical optimization methods were employed to obtain parameter sets that improve closed-loop performance. The functions `fmincon` and `fminunc` solve constrained and unconstrained optimization problems, respectively. The solvers support five algorithms: SQP, Interior Point (IP), Active Set (AS), Sequential Quadratic Programming Legacy (SQPL), and Trust Region Reflective (TRR). This work applies the SQP, IP, AS, and SQPL algorithms. The TRR method requires objective function gradients and was therefore excluded from the analysis in this study [161]. This study demonstrates the the applicability of the tuning approach and performance analysis of OM using the TRAS. The TRAS represents a fast nonlinear dynamical system suitable for evaluating controller performance.

Optimization for parameter tuning

The control design approach uses constrained tracking error for a LTI closed-loop system. The objective minimizes the error between a unit-step reference signal and the closed-loop output. The optimization enforces bounds on percent overshoot, undershoot, and settling time. The resulting optimization problem can be expressed as

$$\begin{aligned} \min_{k_\mathrm{p}, k_\mathrm{i}, k_\mathrm{d}, \lambda, \mu} \quad & \sqrt{\frac{1}{N_\mathrm{s}} \sum_{i=1}^{N_\mathrm{s}} (y_{\mathrm{r},i} - y_{\mathrm{mod},i})^2} \\ \text{subject to} \quad & M_\mathrm{p} \le 0.01 \\ & M_\mathrm{u} \le 0.01 \\ & t_\mathrm{set} \le 1 \end{aligned}, \tag{4.21}$$

where M_p, M_u, and t_set represent the closed-loop percent overshoot, percent undershoot, and settling time (s), respectively. Moreover, y_r, y_mod and N_s denote the reference output, modeled output, and the total number of samples, respectively. The TF of the closed-loop system $G_\mathrm{cl}(s)$ is defined as

$$G_\mathrm{cl}(s) = \frac{G(s)\,C(s)}{1 + G(s)\,C(s)}, \tag{4.22}$$

where $G(s)$ and $C(s)$ are the TFs of the plant and the controller, respectively. The TF $G(s)$ takes the notation $G_p(s)$ for pitch angle Eq. 3.8 and $G_y(s)$ for the yaw angle Eq. 3.9 of the TRAS. The TF of the controller is

$$C(s) = k_\mathrm{p} + k_\mathrm{i}\frac{1}{s^\lambda} + k_\mathrm{d}s^\mu, \tag{4.23}$$

where k_p, k_i, k_d, λ, and μ denote the proportional gain, integral gain, derivative gain, order of the FO integral, and order of the FO derivative of the FO-PID controller.

Controller parameters

Four optimization algorithms, AS, SQP, SQPL, and IP were applied to solve Eq. (4.21) with the initial conditions of the controller parameters as

$$0 \le C_i \le 1, \quad C_i \in \mathbb{R}^{5\times 1}, \tag{4.24}$$

where $C_i = [k_{\mathrm{p}0}\ k_{\mathrm{i}0}\ \lambda_0\ k_{\mathrm{d}0}\ \mu_0]^\mathrm{T}$. Nine random initial conditions were considered with bounds in Eq. (4.24). Each initial condition was evaluated for nine alternative boundary values of k_p, k_i, and k_d. The lower bounds of k_p, k_i, and k_d were set to zero in all cases while the upper bound B_u was selected from

$$B_u \in \{600, 800, 1000, 1200, 1800, 2000, 2400, 3000, 3500\}. \tag{4.25}$$

The selection of different upper bounds for these parameters prevents optimization from converging to boundary solutions.

The bounds of the fractional orders λ and μ remained fixed as

$$0 \le \lambda, \mu \le 1. \tag{4.26}$$

Optimization under this scenario resulted in distinct sets of parameters for FO-PID controllers for pitch and yaw angles. Table 4.6 reports optimized controller parameters and corresponding objective function values for cases that satisfy the optimization constraints in Eq. (4.21).

It can be seen from the table that the RMSE optimization yields comparable values of the objective function. However, each algorithm produces markedly different controller parameters. This variation arises from the non-convex nature of the RMSE criterion [162]. Consequently, distinct parameter sets achieve the same optimal objective value while fulfilling the design constraints in Eq. (4.21). The non-convex objective causes strong sensitivity of the solution to initial conditions and parameter bounds.

4.2.2 Controller performance

The FO integrals and derivatives of the FO-PID controllers were approximated using the Oustaloup approximation method. The controllers were applied in closed loop with the nonlinear TRAS model presented in Section 3.2.1. Figure 2 shows the closed-loop configuration of the TRAS with the FO-PID controllers.

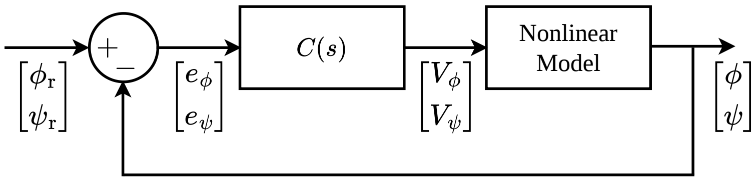

Figure 4.8: Closed-loop block diagram of the FO-PID controllers with nonlinear model of the twin rotor aerodynamic system.

The controller TF, $C(s)$ in Figure 4.8 is

$$C(s) = \begin{bmatrix} C_\phi(s) & 0 \\ 0 & C_\psi(s) \end{bmatrix}, \tag{4.27}$$

where $C_\phi(s)$ and $C_\psi(s)$ denote the TFs of the pitch and yaw controllers. These controllers are generated using Eq. (4.23) with parameters listed in Table 4.6. Moreover, V_ϕ and V_ψ denote voltages applied to the bidirectional DC motors. These motors drive the main and tail rotors of TRAS, respectively.

Refrence trajectories

The reference trajectories of pitch (ϕ_r) and yaw (ψ_r) angles for controller performance evaluation are designed as follows.

- The yaw and pitch angles remain at $0°$ during the initial interval of 6 s.
- Between the time intervals $t = 6$ s and $t = 10$ s, the yaw angle stays at $0°$ and the pitch angle increases linearly. The pitch angle reaches $13.8°$ at $t = 10$ s.

Table 4.6: Optimal parameters for FO-PID controllers for pitch and yaw angles obtained by solving Eq. (4.21).

Algorithm	k_p	k_i	λ	k_d	μ	Objective Value
			Pitch angle			
AS	0.0038	1.5761	0.9086	1.5636	0.9950	1.00×10^{-4}
AS	0.1988	12.3581	0.8334	9.4795	0.9691	1.00×10^{-4}
SQP	0.2770	1.5800	0.9021	2.1465	1.0000	1.00×10^{-4}
SQPL	0.1409	1.9089	0.8844	2.7920	0.8900	1.00×10^{-4}
			Yaw angle			
AS	0.0062	3.2317	0.5312	22.8939	1.0000	0.99×10^{-4}
IP	0.1972	39.8228	0.9250	26.9522	1.0000	0.99×10^{-4}
SQP	0.6314	3.8441	0.1828	7.6087	0.9964	0.99×10^{-4}
SQPL	2.6435	1.5124	0.1612	6.4915	1.0000	0.99×10^{-4}

- For the time interval from $t = 10$ s to $t = 20$ s, the pitch angle remains constant and the yaw angle rises linearly reaching the value $57°$.
- For the next 10 s, the yaw angle remains constant and the pitch angle increases linearly. The pitch angle reaches $31°$ at $t = 30$ s.
- For the following 10 s, the pitch angle remains constant and the yaw angle linearly increases to $86°$. The yaw angle then remains constant until $t = 80$ s.
- At $t = 40$ s, the pitch angle linearly decreases to $19.5°$ at $t = 50$ s and remains at this value until $t = 70$ s. It then decreases linearly to $14°$ at $t = 80$ s.
- After $t = 80$ s, the yaw angle linearly decreases to $57.5°$ at $t = 90$ s. The values pitch and yaw angles then remains constant for the rest of the simulation, i.e., until $t = 100$ s.

Closed-loop response

Figure 4.9 shows the closed-loop pitch angle (ϕ) response of TRAS. The figure presents responses obtained using FO-PID controllers tuned by different algorithms based on the parameters reported in Table 4.6. The results indicate that controllers designed using all algorithms exhibit oscillatory closed-loop behavior. The controller designed using the IP method shows the largest tracking delay relative to that with other algorithms. The figure also shows that the AS-based FO-PID controller generates the largest oscillation magnitudes around $t = 11$ s. Despite these oscillations, the AS-based controller demonstrates good reference tracking compared to other designs.

The oscillatory response is clearly visible in the zoomed lower plot. The oscillations generated by the AS-based FO-PID controller are significantly reduced. In contrast, oscillations persist consistently with the SQP-based FO-PID controller. The IP-based FO-PID controller exhibits almost no oscillations. However, its increased delay makes it unsuitable for feedback control, as TRAS exhibits fast dynamics. The SQPL-based FO-PID has an intermediate performance for pitch angle (ϕ) control compared to other designs.

Figure 4.10 shows the closed-loop yaw angle (ψ) response. Unlike the pitch response in Figure 4.9, the yaw response exhibits almost no oscillations. The figure demonstrates good yaw tracking throughout the simulation duration. Controllers designed using all algorithms exhibit comparable tracking performance. The AS-based FO-PID controller achieves the best tracking while the SQPL-based FO-PID controller exhibits the poorest performance.

Reference tracking becomes clearer in the zoomed lower portion in Figure 4.10. The zoomed view shows that , IP, and SQPL-based FO-PID controllers exhibit minimal oscillations. In contrast, the SQPL-based FO-PID controller exhibits the largest oscillation amplitudes. However, the IP and SQPL-based FO-PID controllers produce larger magnitudes of the tracking error. Therefore, the SQPL-based controller represents a suitable choice for yaw angle (ψ) control. Inspection of controller parameters in Table 4.6 shows $\lambda = 1$ for this case. Hence, this controller does not exhibit FO integral behavior.

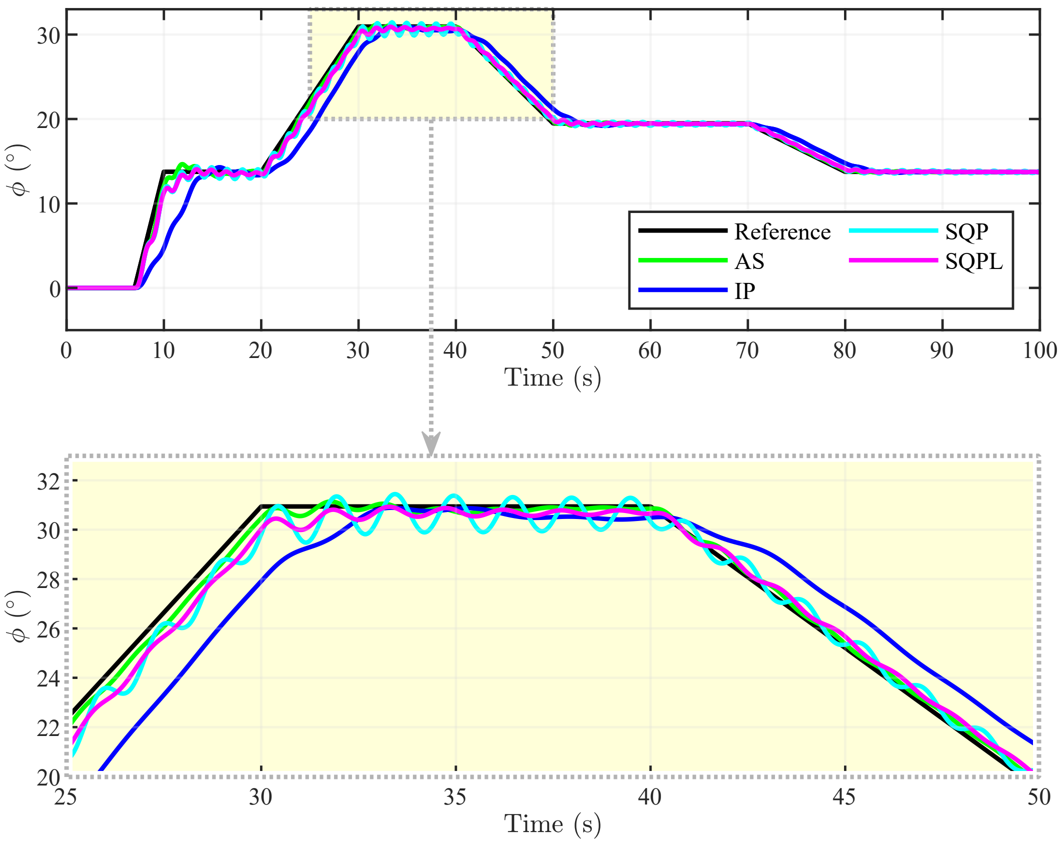

Figure 4.9: Closed-loop response of pitch angle with nonlinear model of TRAS.

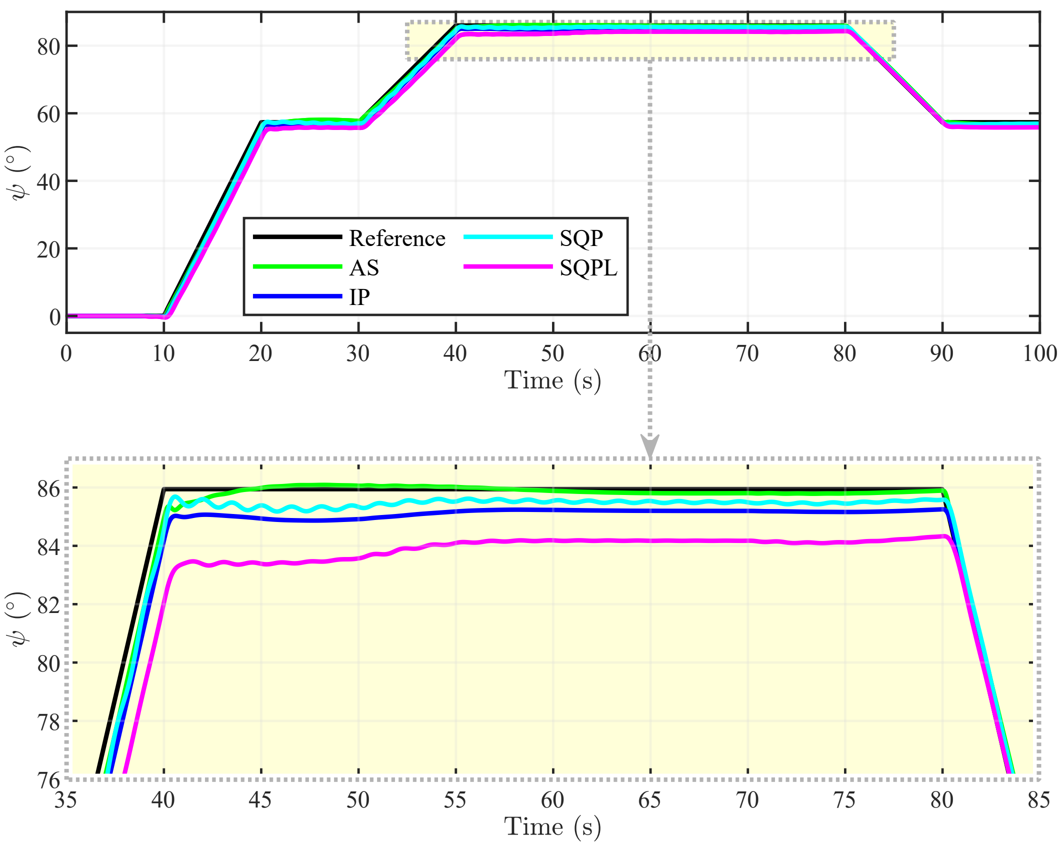

Figure 4.10: Closed-loop response of yaw angle with nonlinear model of TRAS.

The controllers regulate the DC motors using voltage inputs V_ϕ and V_ψ. These inputs drive the pitch and yaw angles, respectively. Fan rotation on the main and tail rotors of the TRAS generates these angular motions. The comparison assesses voltages required to achieve the performances in Figures 4.9 and 4.10. The trajectory was imposed on the closed-loop system using the Adaptive Backstepping Controller (ABSC) [147] and the corresponding control signals were recorded for analysis.

Figure 4.11 compares the control efforts of the FO-PID and the ABSC. The FO controllers generate oscillatory control inputs. However, these oscillations occur at significantly lower frequencies than those produced by the ABSC. This lower frequency directly reduces oscillatory energy in the voltage inputs driving the DC motors. Such limitation of oscillations mitigates wear and mechanical stress in the TRAS actuators.

The figure shows that the SQP-based FO-PID produces the largest control effort magnitudes and introduces pronounced high-frequency oscillations. In contrast, the IP-based FO-PID yields almost oscillation-free control signal for reference tracking. However, this benefit comes at the expense of inferior tracking performance, as shown in Figure 4.9. The AS-based FO-PID is most appropriate for pitch control as it achieves good tracking in Figure 4.9 with minimal oscillations in control effort. The oscillations in V_ϕ are clearly visible in the lower plot of Figure 4.11.

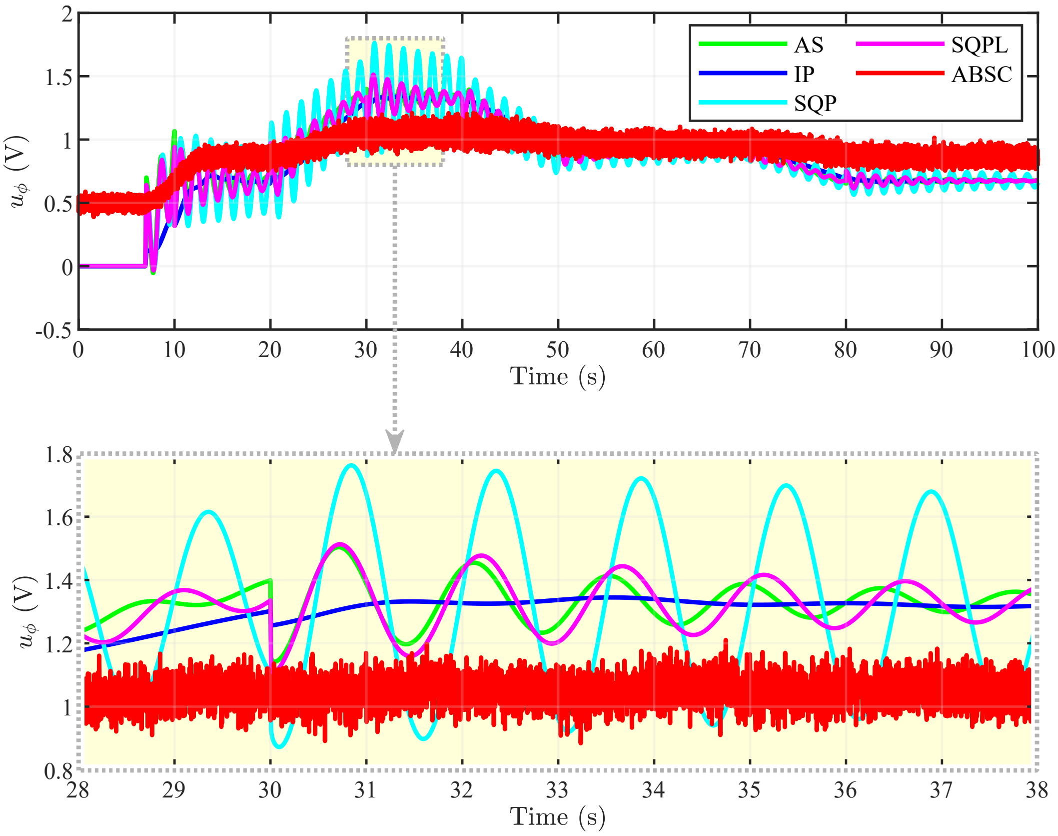

Figure 4.11: Control effort required to ensure the reference tracking of pitch angle shown in Figure 4.9.

Figure 4.12 shows the control effort during yaw-angle reference tracking. The results indicate that the ABSC produces the lowest-magnitude voltage signal V_{ψ}. This signal requires minimal energy from the DC motor driving the tail rotor. However, the voltage signal contains high-frequency oscillations that directly burden the actuating motor. Such oscillations can cause wear and mechanical damage. The IP-based FO-PID controller exhibits almost no oscillations, as shown in the zoomed plot. However, this design method yields poor tracking performance, as shown in Figure 4.10. The AS and SQP-based FO-PID controllers achieve better tracking performance. However, they require higher control effort with pronounced oscillatory behavior. Therefore, controller selection requires a trade-off between tracking accuracy and control effort.

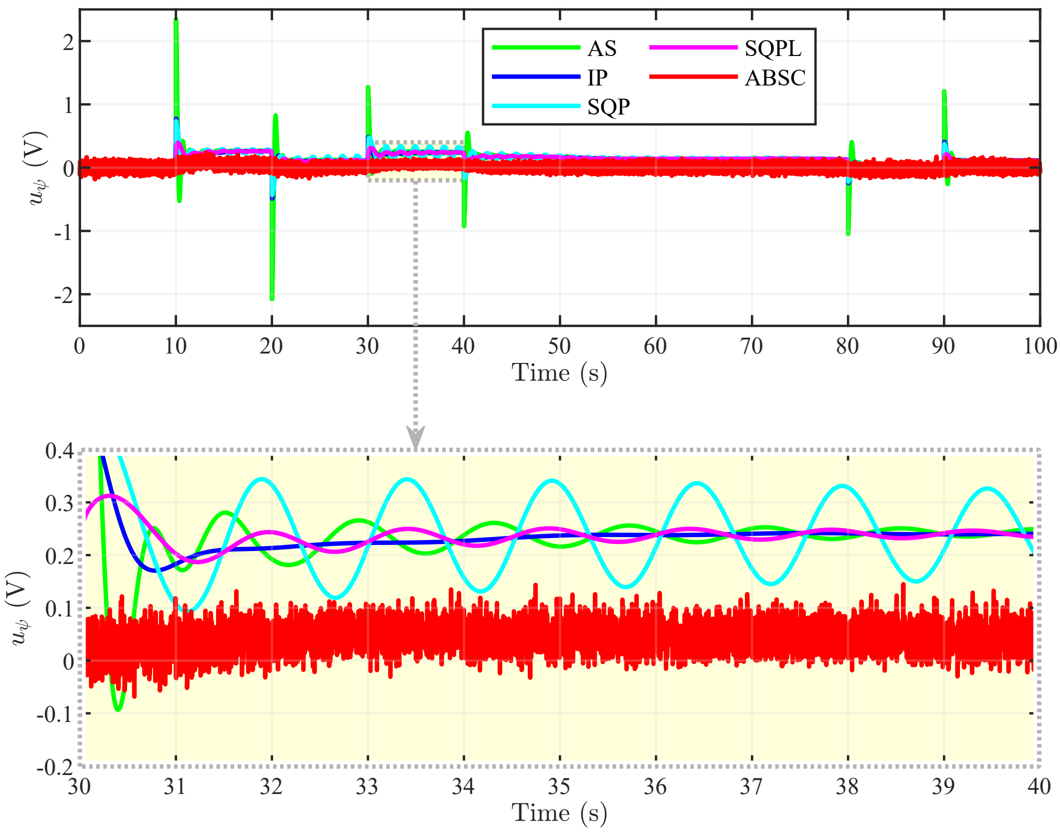

Figure 4.12: Control effort required to ensure the reference tracking of yaw angle shown in Figure 4.10.

4.3 Chapter summary

This chapter examined two core aspects of FO calculus: the fractional-operator approximation and the optimal FO-PID controller design. Practical realization of FO dynamics depends strongly on approximation methods. For this reason, the first part evaluated how approximation choice influences the accuracy of the FO-DIEs. Seven widely used approximation methods were analyzed in steady state, time domain, and frequency domain. The results showed that approximation type, approximation order, and fractional order strongly affect accuracy. Inappropriate selection may cause significant misinterpretation of system dynamics. Several methods introduced steady-state errors linked to model structure and fractional order. Other methods preserved more consistent symbolic behavior across operating conditions. Frequency-domain analysis indicated that higher approximation order generally improves accuracy. However, increased order also raises model complexity and may introduce additional phase delay. These observations confirm the need for careful selection of the approximation method for FO modeling and control.

The second part addressed optimal tuning of FO controllers formulated as a constrained optimization problem. The design incorporated overshoot, undershoot, and settling time as explicit performance constraints. Multiple numerical optimization algorithms were utilized to solve the optimization problem. To reduce sensitivity to initialization and parameter bounds, multiple initial values and boundaries were considered. Finally, building on the conclusion from the first part of the chapter, the Oustaloup approximation method was adopted for realization of the FO-PID controller to analyze the closed-loop performance with a realistic reference trajectory.

In conclusion, the chapter demonstrates the coupled importance of approximation accuracy and controller optimization robustness. The findings confirm that these elements are essential for practical exploitation of FO control systems.

CHAPTER 5

Integer-Order Modeling

This chapter outlines the modeling approach used for the flow system analyzed in this dissertation. Because the system exhibits distinct dynamic behavior at different excitation frequencies, separate third-order transfer functions are identified from experimental IOD. Second-order models are also estimated to provide a basis for comparison. To reduce the complexity of these models, PCA is applied to the identified parameter sets, resulting in simplified transfer functions with one zero and two poles. Finally, the chapter develops a reduced-order LPV model in which the dynamic parameters vary smoothly with the input frequency, enabling a single model to represent the entire operating range. The experimental data used for IO modeling and error analysis are presented in Section 3.3.4.

This chapter extends the findings presented in the published article [137]. Furthermore, the proposed modeling approach and the performance evaluation discussed in this chapter cover the successful implementation of **Obj.2** presented in Chapter 1 Section 1.3.

5.1 Identification of reduced-ordered model

Accurate determination of liquid flow is essential in numerous practical applications. These applications range from domestic installations to large-scale industrial processes [70, 71, 163]. Proper operation of water distribution and treatment systems depends on reliable flow control. The same requirement applies to domestic heating, condensation, and irrigation systems. Liquid pouring and drainage systems also require precise flow regulation.

Several applications demand a prescribed flow rate under steady-state conditions. An intelligent control system enables such regulation. Control design methods rely on accurate mathematical models enabling controller synthesis to ensure the desired system behavior. Therefore, an appropriate dynamic process model constitutes critical information. Such information is fundamental for effective controller design and implementation [112, 164].

The laboratory flow system considered in this chapter exhibits nonlinear varying dynamics (see Figure 3.9). The non-linearities and variations in flow rates across different excitation frequencies make it difficult to derive a single dynamic model valid for the entire input spectrum.

5.1.1 Model identification

The parameters of the dynamic model are obtained by solving the optimization problem based on commonly used Mean Absolute Error (MAE) minimization [13]:

$$\min_{n_1,n_2,n_3,d_1,d_2,d_3} \quad \frac{1}{N}\sum_{i=1}^{N_s} |y_\mathrm{e} - y_\mathrm{m}| \,, \tag{5.1}$$

where n_1, n_2, n_3, d_1, d_2, and d_3 represent the unknown model coefficients, y_m is the measured flow rate, y_e is the estimated response, and N_s is the number of collected samples. In the absence of reference value for the flow rate, Eq. (5.1) treats y_m as a reference signal during optimization.[1]

The optimization minimizes the mean absolute deviation between the estimated model output using Sequential Quadratic Programming (SQP) to identify a third-order model and the experimental data. The TF of the third-order model is given as:

$$G(s) = \frac{n_1 s^2 + n_2 s + n_3}{s^3 + d_1 s^2 + d_2 s + d_3}. \tag{5.2}$$

Additionally, second-order models are also derived as

$$G_{2\mathrm{p}}(s) = \frac{n_a s + n_b}{s^2 + d_a s + d_b}. \tag{5.3}$$

The model $G_{2\mathrm{p}}(s)$ is obtained by solving Eq. (5.1) with $y_\mathrm{e} = y_{\mathrm{e},2\mathrm{p}}$, where $y_{\mathrm{e},2\mathrm{p}}$ denotes the estimated flow rate of the model in Eq. (5.3). Similarly, $y_{\mathrm{e},3p}$ denotes the estimated flow rate obtained with the model in Eq. (5.2). The optimization problem in Eq. (5.1) minimizes MAE between measured and estimated responses without detailed system knowledge. The method represents nonlinear system dynamics using a reduced-order IO model from measured data. Consequently, the identified parameters of both third-order and second-order models lack physical interpretation.

5.1.2 PCA for model order reduction

The PCA determines a pseudo set of inputs that are orthogonal to each other and are linear combinations of the actual inputs. These pseudo set of inputs capture a maximum amount of system dynamics using lesser number of variables [165]. Thus, the idea of PCA is to develop a reduced dimensional pseudo-variable orthogonal input space to facilitate reduced-order modeling. In this chapter, PCA is used to construct the linear combinations of the original parameter set as:

$$\mathbf{P} = \begin{bmatrix} p_1 & p_2 & p_3 & \cdots & p_n \end{bmatrix}^T \quad \in \mathbb{R}^{p_n \times Q}, \tag{5.4}$$

[1] Throughout the dissertation, the residuum is defined as $e = y_\mathrm{e} - y_\mathrm{m}$ i.e., difference between the estimated output and measured value. In this case, the measured value serves as the reference because the reference output is unavailable. This differs from the statistical convention, where residuum $= y_\mathrm{m} - y_\mathrm{e}$. The term *residuum* (symbol e) is used consistently in place of *error* wherever this notation applies. Established compound terms such as *Mean Absolute Error* (MAE) remain unchanged.

where $\mathbf{P}$ contains p_n parameters across Q samples. PCA reduces the dimensionality of this parameter space to n_r by applying the Singular Value Decomposition (SVD)

$$\mathbf{P} = \mathbf{U}\ \mathbf{S}\ \mathbf{V}^T, \tag{5.5}$$

where $\mathbf{S} \in \mathbb{R}^{p_\mathrm{n} \times Q}$ holds the singular values and $\mathbf{U} \in \mathbb{R}^{n_r \times p_n}$ contains the corresponding singular vectors. The matrix of reduced parameters $\hat{\mathbf{P}} \in \mathbb{R}^{n_r \times Q}$ is obtained as:

$$\hat{\mathbf{P}} = \mathbf{U}_{n_\mathrm{r} \times p_\mathrm{n}}\ \mathbf{P}_{n_\mathrm{r} \times Q} \quad \in \mathbb{R}^{n_\mathrm{r} \times Q}. \tag{5.6}$$

The reduced dimension n_r is selected based on the fraction of total variation,

$$v_m = \frac{\sum_{i=1}^{n_\mathrm{r}} s_i}{\sum_{i=1}^{p_\mathrm{n}} s_i}, \tag{5.7}$$

where s_i denotes the i-th singular value of $\mathbf{S}$. The original parameters can be reconstructed from the reduced set using

$$\tilde{\mathbf{P}} = \mathbf{U}^T_{n_\mathrm{r} \times p_\mathrm{n}} \times \hat{\mathbf{P}}, \tag{5.8}$$

where $\tilde{\mathbf{P}}$ is the matrix containing the reconstructed parameters. Using Eq. (5.8), parameters for the third-order model can be regenerated as

$$\tilde{\mathbf{P}} = \begin{bmatrix} \tilde{p}_1 & \tilde{p}_2 & \tilde{p}_3 & \cdots & \tilde{p}_n \end{bmatrix}^T. \tag{5.9}$$

In this study, PCA is employed to reduce the model in Eq. (5.2) to a structure with one zero and two poles. The resulting reduced-order model $\hat{G}(s)$ is expressed as

$$\hat{G}(s) = \frac{\hat{n}_1 s + \hat{n}_2}{s^2 + \hat{d}_1 s + \hat{d}_2}. \tag{5.10}$$

The parameters $\hat{n}_1, \hat{n}_2, \hat{d}_1$, and $\hat{d}_2$ in Eq. (5.10) differ from those in Eq. (5.2) and are obtained through the PCA-based transformation.

5.1.3 Reduced-order LPV model

The reduced-order LPV model is described by

$$G(s,\rho) = \frac{\hat{n}_1(\rho)s + \hat{n}_2(\rho)}{s^2 + \hat{d}_1(\rho)s + \hat{d}_2(\rho)}, \tag{5.11}$$

where ρ denotes the scheduling signal for parameter variation. In this study, the parameter variation depends on the input frequency of the flow system. Parameter values at each sampling instant are computed using linear interpolation [70]:

$$p^i(\rho_h) = \xi_o^i + \sum_{h=1}^{h=Q} \xi_h^i \rho_h^i, \tag{5.12}$$

with $i = 1, \dots, 4$ corresponding to $[\hat{n}_1, \hat{n}_2, \hat{d}_1, \hat{d}_2]$, $Q = 20$ denoting the number of local models – based on the total number of input frequency steps in each pass, and h the current sampling instant. The LPV formulation requires

$$\sum_{h=1}^{h=Q} \xi_h^i = 1. \tag{5.13}$$

Thus, the LPV model at sampling instant h is given by

$$G_h(s, \rho_h) = \frac{p^1(\rho_h)s + p^2(\rho_h)}{s^2 + p^3(\rho_h)s + p^4(\rho_h)}. \tag{5.14}$$

This model captures the dependence of the dynamic parameters on the varying input frequency of the voltage that is used to operate the water pump.

5.2 Analysis of identified and reduced model parameters

A detailed examination of parameter evolution across the operating range is essential to understand the flow response under varying excitation conditions. This examination also helps evaluate the suitability of competing model structures. Repeated identification under identical conditions for different passes produced corresponding parameter sets. The parameters identified for individual passes were then averaged. Their average values are presented in Tables 5.1 and 5.2. To improve readability, the numerical values in the tables have been rounded to two significant digits.

5.2.1 Identified parameters

Table 5.1 presents the averaged dynamic parameters obtained from the third–order and second–order TF models. These parameters were identified across sixty experimental passes for each of the twenty excitation frequencies. The results show a strong dependence on the pump input frequency, which reflects the nonlinear nature of the flow system. At lower frequencies, the parameters exhibit marked irregularities. This behavior agrees with the transitional flow regime observed in the experiments, where the water column accelerates slowly and the flow rates unstable. Sensor accuracy is also reduced during these flow rate. Therefore, this phenomenon generate considerable variability in both numerator and denominator parameters for frequencies between $(6 - -18)$ Hz. As the frequency increases and the system enters the turbulent regime which makes the the parameters change smoothly.

This behavior shows that the system dynamics become progressively linear and predictable at higher flow rates.

Table 5.1 further reveals hysteresis between the increase and decrease of flow rate. Even at the same input frequency, the identified parameter sets differ depending upon whether the input frequency is increasing or decreasing. The directly identified second–order models indicate additional inconsistencies, particularly at low frequencies. This demonstrates that direct order reduction leads to a loss of dynamic estimation and fails to capture the true behavior of the flow system.

5.2.2 Parameters of the PCA-based reduced models

Table 5.2 presents the parameter sets of the PCA–based reduced second-order models. These parameters are obtained by projecting the third-order parameters onto a reduced orthogonal basis while retaining about 92% of the total variance. The resulting parameters indicate a significant coherence compared to those directly identified using the second-order model. In contrast with the directly identified second-order models in Table 5.1, the PCA-reduced parameters vary smoothly with change in the input frequency. They reproduce the expected

Table 5.1: Parameters of the flow system models obtained after solving Eq. (5.1).

	third-order model						second-order model			
f	n_1	n_2	n_3	d_1	d_2	d_3	n_a	n_b	d_a	d_b
				Increase in flow						
6	−0.073	0.16	0.011	0.63	8.2	0.95	−0.043	0.0012	0.39	0.25
12	−0.14	0.15	0.013	1.6	1.5	0.42	0.069	0.0013	0.52	0.22
18	−0.11	0.15	−0.021	1.2	1.8	0.47	0.048	0.022	0.62	0.47
24	0.047	−0.26	0.71	2.3	8.1	6.6	−0.13	0.23	2.4	2.1
30	0.026	−0.11	0.28	3.4	7.2	5.9	−0.043	0.083	1.9	1.8
36	−0.031	−0.038	0.14	1.9	6.2	3.4	−0.071	0.087	3.3	2.1
42	0.027	−0.11	0.27	3.9	10	10	−0.033	0.062	2.1	2.3
48	0.031	−0.11	0.29	3.1	11	13	−0.027	0.059	2.2	2.6
54	0.031	−0.14	0.45	4.0	17	22	−0.032	0.074	2.8	3.7
60	−0.0013	−0.038	0.28	3.9	16	17	−0.036	0.12	4.7	6.9
				Decrease in flow						
6	−0.42	0.68	−0.0012	2.4	2.4	0.70	0.23	0.0012	0.66	0.25
12	−0.10	0.0013	−0.0032	0.32	0.13	0.010	0.011	−0.081	0.58	0.49
18	−0.024	0.28	−1.7	7.3	21	22	0.075	−0.27	3.1	3.6
24	−0.022	0.16	−0.70	4.9	13	14	0.057	−0.16	2.7	3.1
30	−0.051	0.021	−1.3	5.1	22	33	0.044	−0.17	3.0	4.4
36	−0.011	0.095	−0.59	5.3	16	19	0.038	−0.13	3.1	4.2
42	−0.010	0.089	−0.57	5.6	18	22	0.034	−0.12	3.2	4.7
48	0.0071	0.029	−0.69	6.0	24	31	0.11	−0.22	4.6	9.5
54	−0.0082	0.069	−0.48	5.8	19	25	0.026	−0.098	3.4	5.2
60	−0.0013	0.0012	−0.0042	3.3	21	20	0.0013	−0.0014	2.2	6.5

monotonic relationships between the flow rate and dynamic response of the system. This pattern indicates that the PCA is able to successfully isolates the dominant variations in the parameter sets while filtering out noise associated with sensor jitter and pass-to-pass variability.

Furthermore, the PCA-based reduction preserves the inherent asymmetry between the increase and decrease of the flow rates without artificially enforcing symmetry across operating frequencies. The reduced parameters retain the distinct trends associated with each flow condition while offering a substantially cleaner representation of the underlying dynamics. Although the low-frequency regions continue to exhibit the effects of nonlinear behavior, the PCA-based second-order models consistently reproduce both transient and steady-state characteristics. Taken together, Tables 5.1 and 5.2 illustrate the transition from high-order accurate models to low-order models. This enables the construction of an LPV model suitable for real-time control design.

Table 5.2: Parameters of the PCA-based reduced order models obtained by Eq. (5.6).

	Increase in flow				Decrease in flow			
f	$\hat{n}_1$	$\hat{n}_2$	$\hat{d}_1$	$\hat{d}_2$	$\hat{n}_1$	$\hat{n}_2$	$\hat{d}_1$	$\hat{d}_2$
6	0.16	0.063	9.1	0.49	−0.056	0.059	0.14	−0.14
12	0.0012	0.0081	−0.18	0.039	0.0010	−0.0010	0.081	0.043
18	−0.16	0.016	0.45	0.20	−0.42	−0.60	−16	2.5
24	0.48	0.020	−10	−4.0	0.0051	−0.0051	−0.24	−0.075
30	0.014	−0.0052	0.35	−0.035	−0.36	0.70	−15	−26
36	0.072	−0.032	−2.6	−2.9	−0.022	−0.028	1.8	1.1
42	0.027	0.0061	0.34	0.12	0.022	0.025	2.45	−0.59
48	0.036	0.0084	−0.78	0.18	−0.25	0.031	−11	25
54	0.18	0.050	5.0	−24	−0.058	0.020	−6.6	−1.4
60	−0.14	−0.32	−28	4.0	0.0014	0.0012	−22	2.0

As described in Section 5.1.2, PCA enables reconstruction of dynamic parameters through the inverse transformation given in Eq. (5.8). This section provides the identified and reconstructed parameters for selected cases with decreasing flow. The parameters are given in Figures 5.1 to 5.4. These figures use two panels presenting the parameters as follows.

1. Panel (a) depicts the numerator parameters of the models described by Eq. (5.2) and the corresponding regenerated parameters by the inverse transformation in Eq. (5.8). The identified parameters are denoted as: n_1, n_2, and n_3, while the regenerated parameters are denoted by $\tilde{n}_1$, $\tilde{n}_2$, and $\tilde{n}_3$.
2. Panel (b) presents the denominator parameters of the models described by Eq. (5.2) and the corresponding regenerated parameters by the inverse transformation in Eq. (5.8). The identified denominator parameters are denoted by d_1, d_2, and d_3, while the corresponding regenerated parameters are denoted by $\tilde{d}_1$, $\tilde{d}_2$, and $\tilde{d}_3$.

To maintain a clear readability, these figures show the parameters identified and regenerated

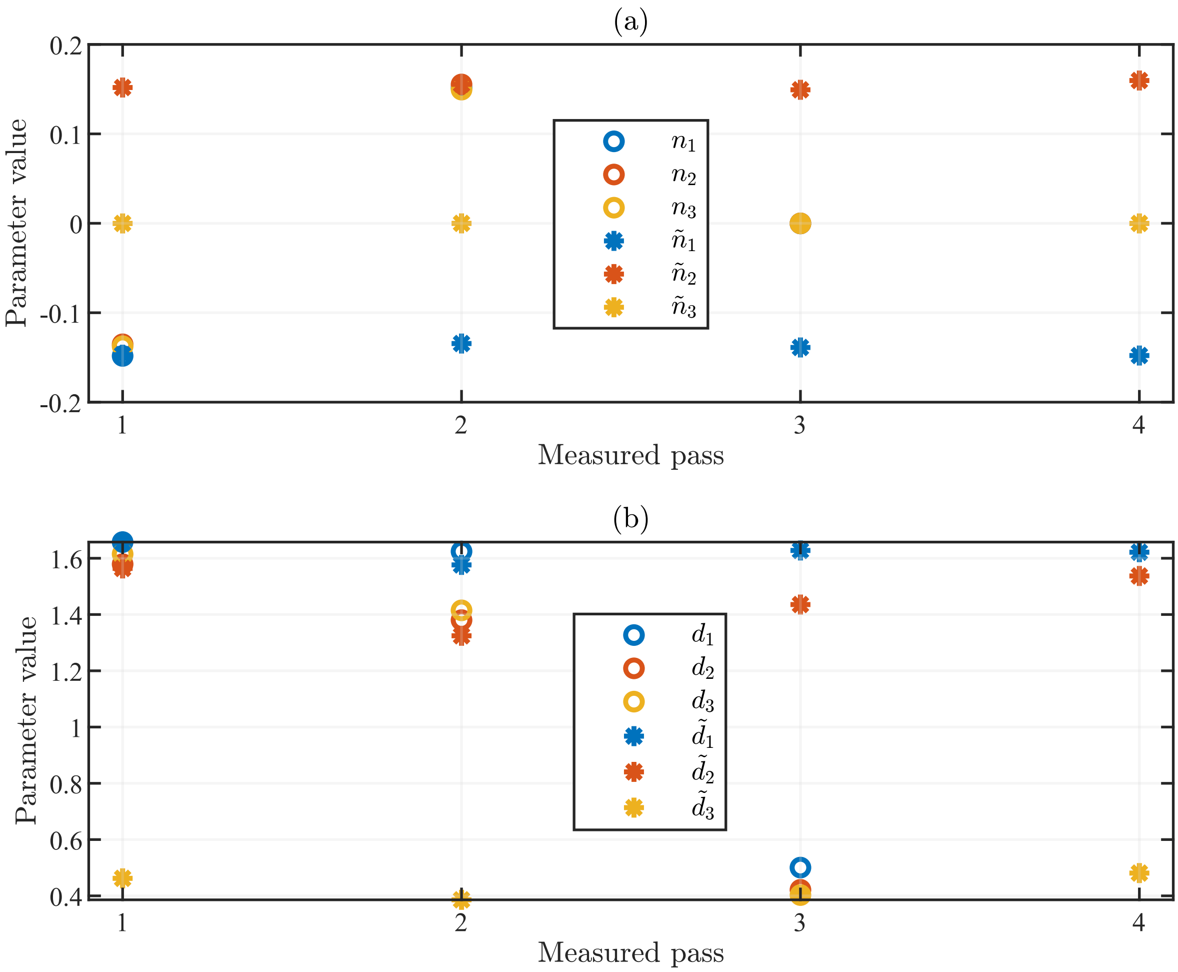

Figure 5.1: Identified and regenerated parameters for change in frequency from 12 to 6 Hz.

using the input-output data from first 4 measurement passes.

Figure 5.1 shows parameters for the case where the input frequency decreases from 12 to 6 s. This case allows evaluation of trends in identified and reconstructed parameters at low input during frequency decay. The figure indicates that numerator parameters in panel (a) attain similar values across the four passes. Almost all parameters are reconstructed, except n_3 for the first two passes. In contrast, denominator parameters in panel (b) show a dispersed behaviour. The inverse transformation based on PCA fails to reconstruct the identified denominator parameters for measurement passes 2 and 3. Measurement pass three exhibits the largest discrepancy between identified and reconstructed parameters when using the inverse transformation matrix.

Figure 5.1 illustrates the dispersion of parameters identified using the IOD when the input frequency decreases from 18 to 12 Hz. Both the numerator parameters in panel (a) and the denominator parameters in panel (b) show increased spread across the measurement passes compared with Figure 5.1. Moreover, the PCA-based reconstruction fails to reproduce the identified values of parameters n_1, n_2, d_1, and d_2 for most measurement passes. In general, the figure does not reveal a consistent trend in parameter reconstruction. Additionally, both

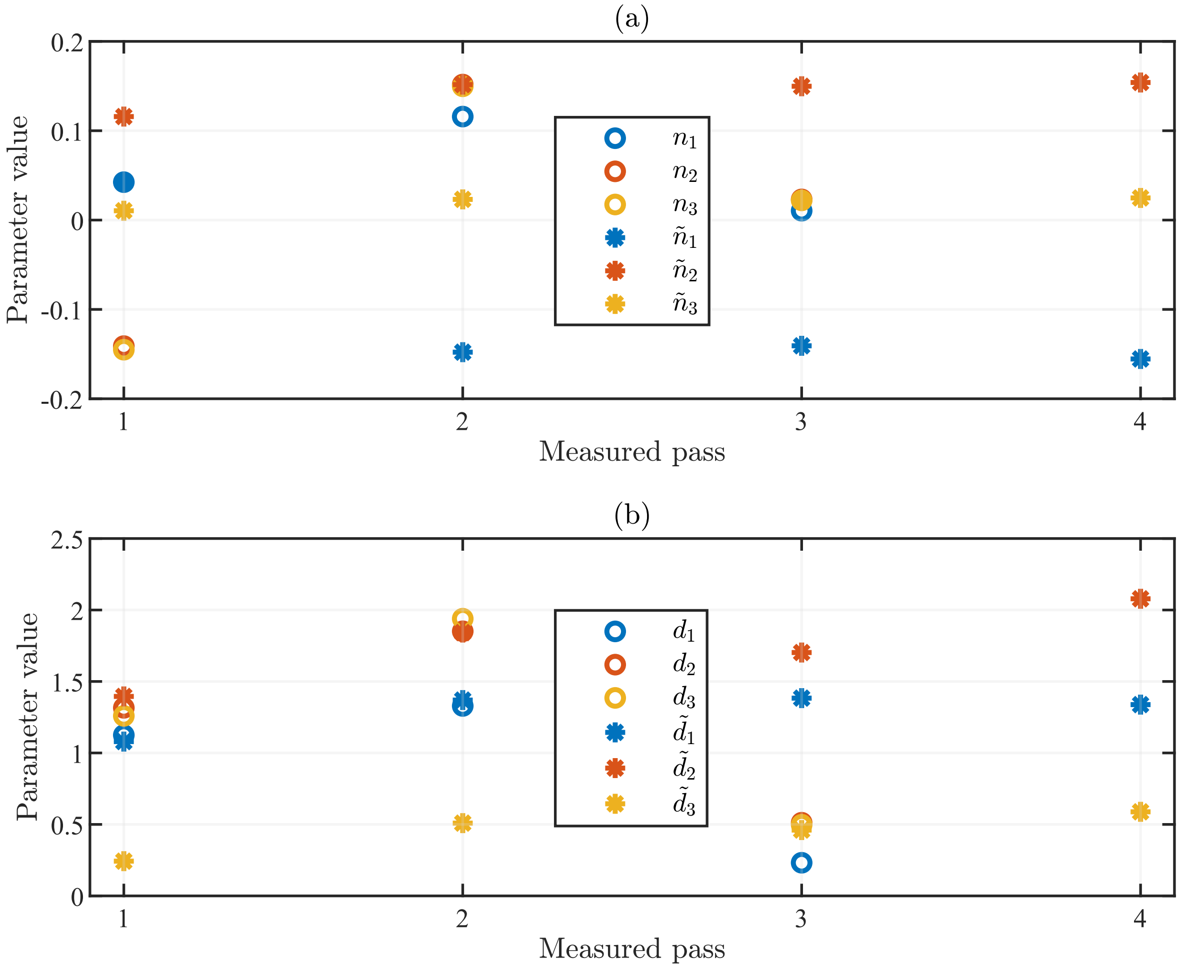

Figure 5.2: Identified and regenerated parameters for change in frequency from 18 to 12 Hz.

the identified and reconstructed denominator parameters attain larger magnitudes than those observed in Figure 5.1. A comparable behavior of the denominator parameters appears in Figures 5.3 and 5.4.

In general, the parameters vary implicitly with changes in the input frequency of the flow system. The PCA-based transformation reduces the number of parameters, as confirmed by its reconstruction capability. The numerator parameters show limited sensitivity to changes in input frequency. In contrast, the denominator parameters exhibit high sensitivity to these variations. This observation is supported by Figures 5.3 and 5.4, where a decrease from higher frequency values produces a nonlinear increase in denominator parameters. The numerator parameters show moderate sensitivity and follow an approximately linear dependence on input frequency. Consequently, these parameters are suitable for reconstruction and for linear interpolation within an LPV modelling framework. The strong sensitivity of the denominator parameters affects their reconstruction accuracy and limits the achievable model fidelity. Denominator parameters determine the pole locations of the system. Therefore, they directly govern the dynamic behavior of the identified model.

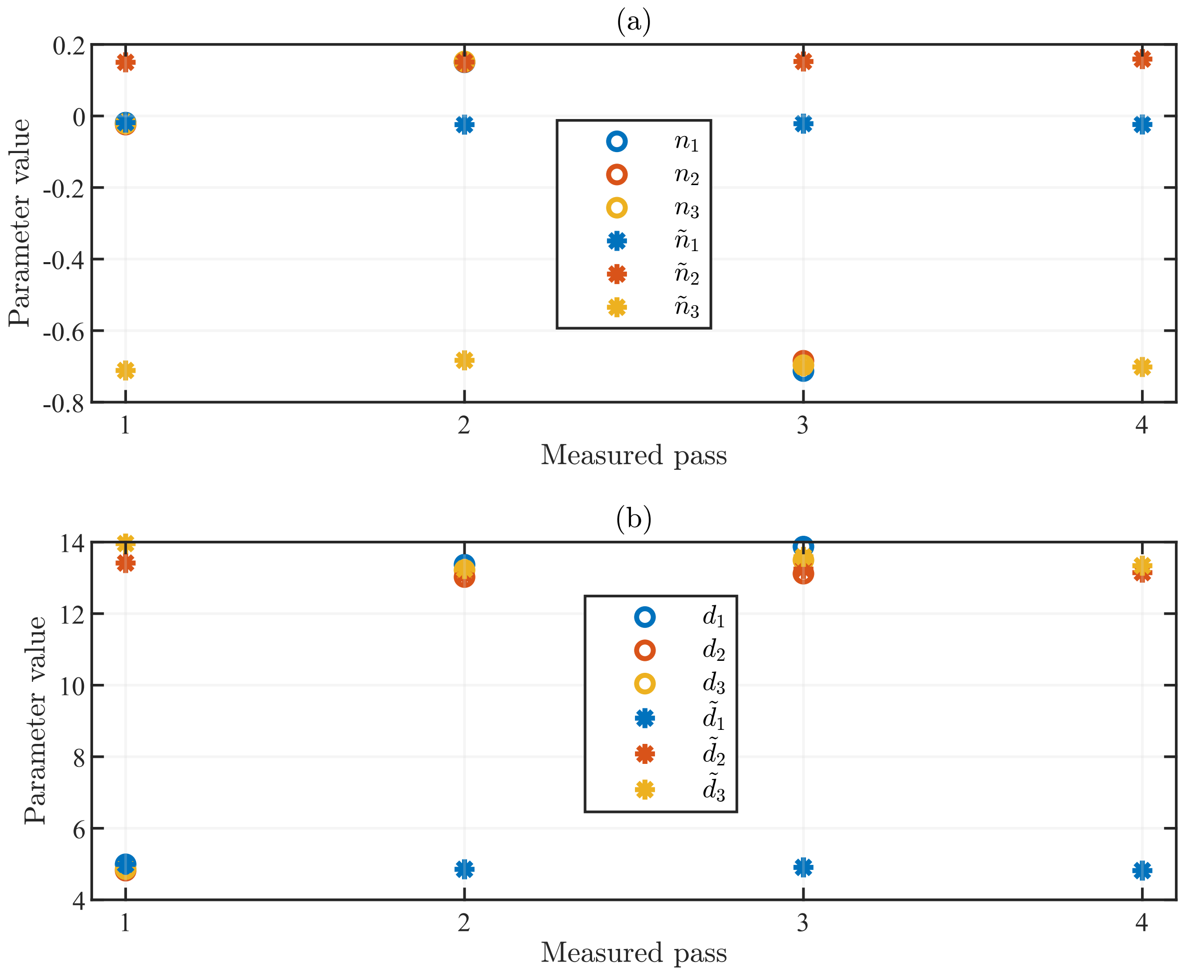

Figure 5.3: Identified and regenerated parameters for change in frequency from 54 to 48 Hz.

5.3 Results and discussion

To evaluate the performance of the proposed modeling approach, this section examines both the time-domain responses and the associated modeling errors. The dynamic responses and the numerical errors are analyzed by a direct comparison between the measured values flow rates. The estimated responses are generated by three models as follows:

1. the third-order identified model,
2. the second-order identified model, and
3. the PCA-based reduced LPV model.

5.3.1 Dynamic response

Figure 5.5 compares the measured flow rate with the outputs of three models: the identified third-order model, the identified second-order model, and the PCA-based reduced-order LPV model. The input consists of stepwise changes in the input, which generate a staircase-like flow rate patterns that increase to the maximum operating range and then decreases symmetrically.

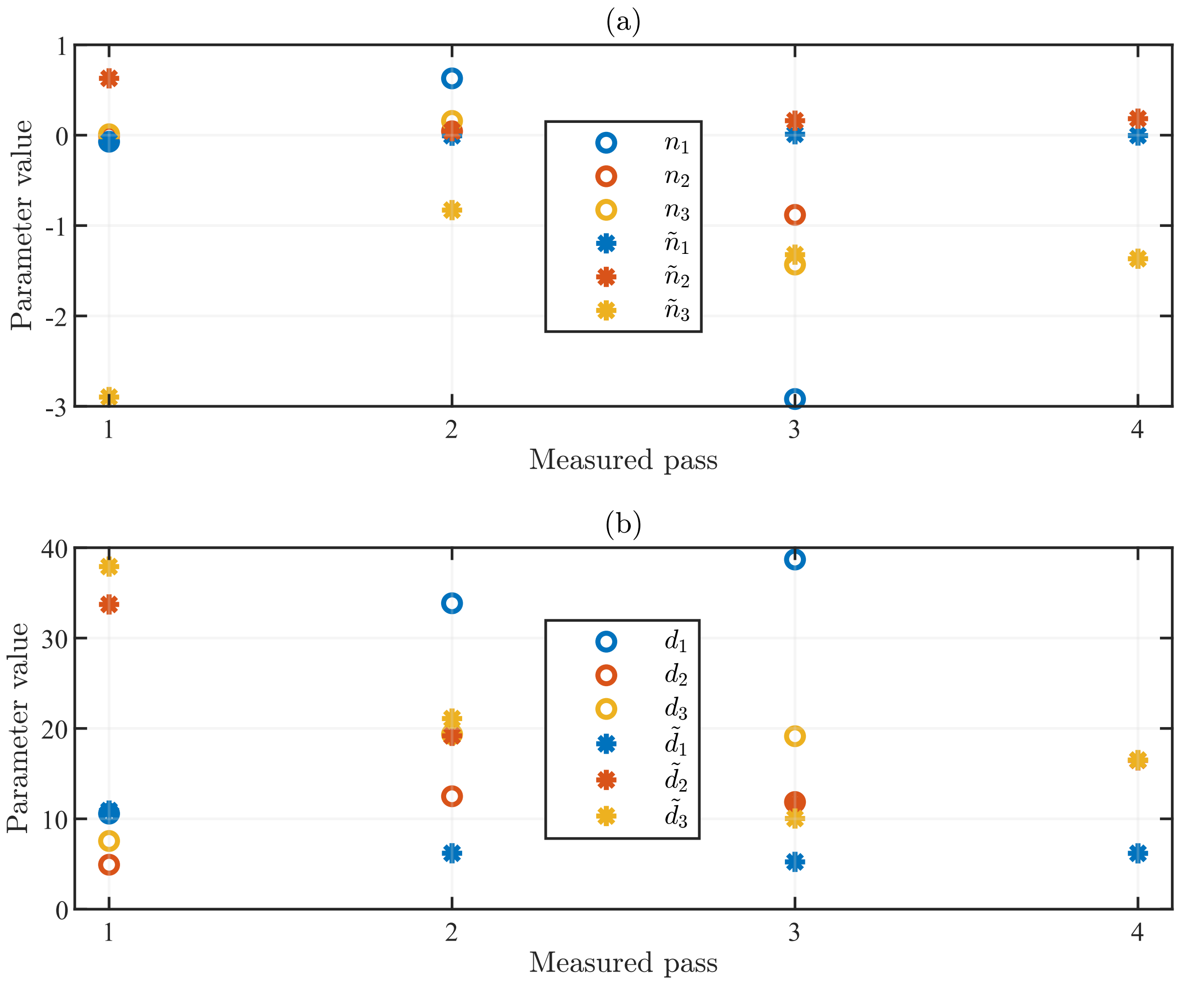

Figure 5.4: Identified and regenerated parameters for change in frequency from 60 to 54 Hz.

This comparison depicts the effectiveness of each model to reproduce both the transient and steady-state dynamic behavior of the laboratory flow system. The third-order identified model presents the closest agreement with the measured data across the entire input range. Its response estimates the measured values with minimal deviation, particularly when the flow rate is high, i.e., for $f_{\text{in}} \geq$ 24 Hz. The model efficiently captures the nonlinear dynamic effects occurring during transitions between frequency levels. This behavior confirms that the third-order model provides sufficient flexibility to represent the distributed and frequency-dependent dynamics of the system. The second-order identified model depicts the clear limitations. Although it approximates the steady-state values for the moderate and high flow rates, it does not reproduce the transient dynamics accurately. Overshoots, undershoots, and delayed responses appear frequently, especially when the flow is decreasing due to decrease in the input f_{in}. These discrepancies indicate that a directly identified second-order model is unable to capture the nonlinearities or the hysteresis arising from the shift between the increase and decrease of the flow rate.

The PCA-based reduced-order model performs substantially outperforms the directly identified second-order model. Its response follows the measured flow rates closely for the in values below 12 Hz. Furthermore, the transient response resembles the third-order model while maintaining a reduced-order for the identified model. The agreement is significantly strong in the central part of the inputs, where the flow lies in the turbulent regime and the measurement quality is high. The small deviations occur at low flow rates due to the sensor limitations and transitional flow effects. However, the PCA-based model captures system dynamics more accurately than the standard second-order model. In conclusion, Figure 5.5 demonstrates that thr PCA-based order reduction preserves the essential dynamic characteristics of the higher-order model. The reduced-order representation achieves both transient and steady-state accuracy across most of the operating range. The figure highlights the main advantage of the proposed method: it produces a compact model that is suitable for real-time LPV control while retaining the fidelity needed to represent a nonlinear process.

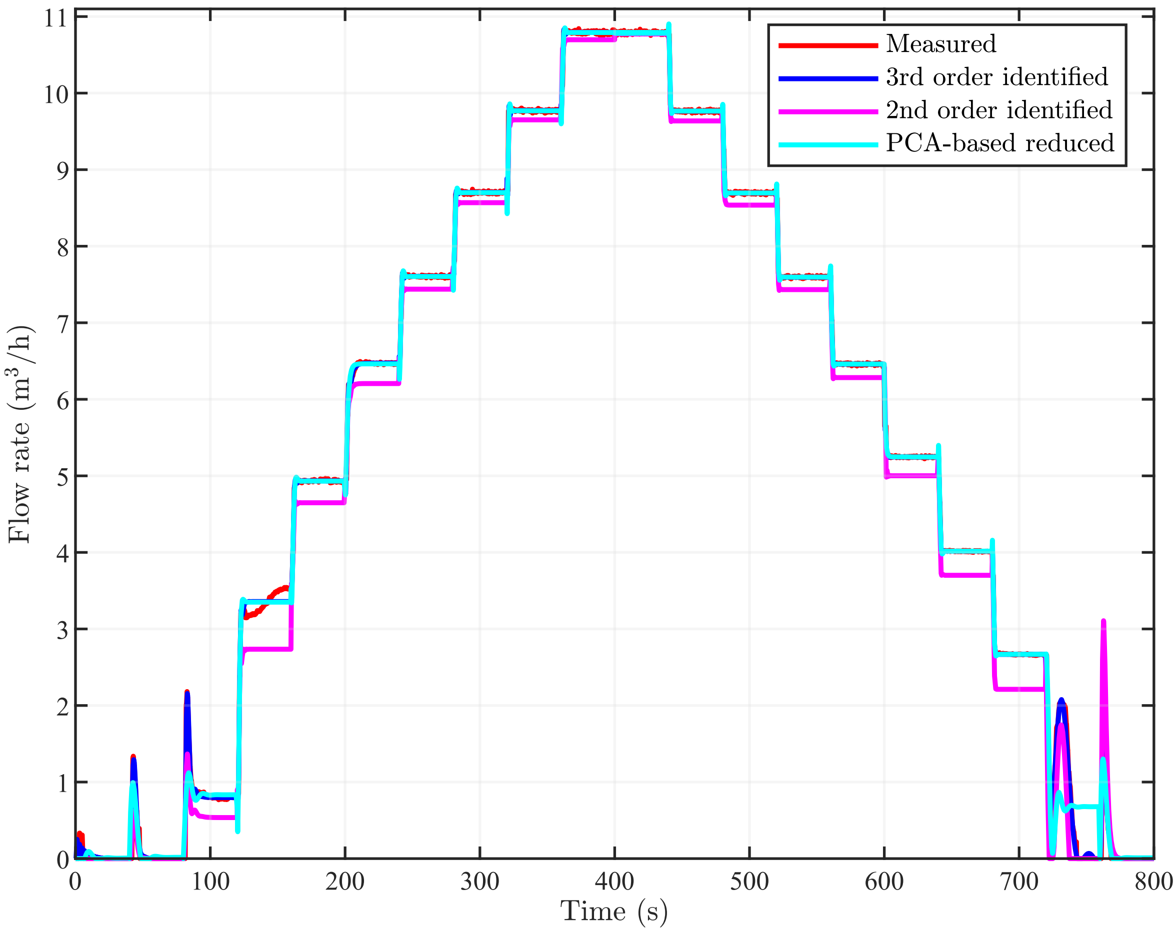

Figure 5.5: Comparison of LPV-based reduced model with measured flow rates, third-order, and second-order reduced models.

Figure 5.6 shows the zoomed portion of Figure 5.5 for the step increase in the input from 54 Hz to 60 Hz in panel (a) and the step decrease from 12 Hz to 6 Hz in panel (b). The figure shows that all models accurately estimate the steady-state flow rates for a frequency change from 54 Hz to 60 Hz, with the exception of the second-order identified model. In the transient region, the PCA-based reduced-order LPV model and the third-order identified model provide improved flow rate estimation, as shown in panel (a). The PCA-based model closely tracks the measured transient response and exhibits a smooth rise with minimal deviation. The third-order model accurately captures the initial overshoot, whereas the second-order model responds slightly faster but shows a significant mismatch in the flow rate estimation.

For the step decrease in the input frequency from 12 Hz to 6 Hz, the third-order identified model accurately estimates the flow rate, as shown in panel (b). The PCA-based reduced-order model exhibits a similar transient response but settles more quickly. In contrast, the second-order model produces a pronounced peak followed by a rapid decay, indicating insufficient damping and a limited ability to capture the nonlinear behavior in this operating region. However, all models eventually converge to the correct steady-state value.

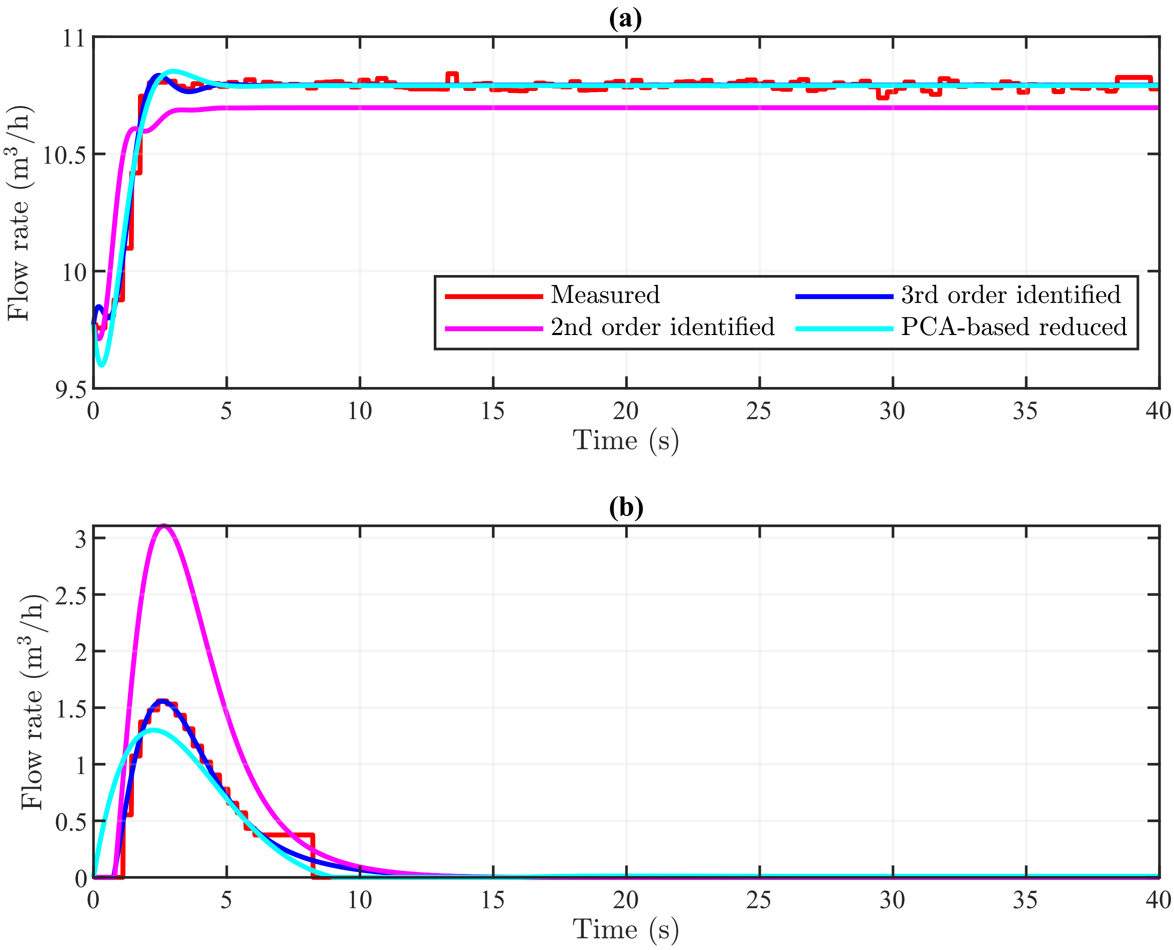

Figure 5.6: Zoomed portion of Figure 5.5: (a) shows the measured and estimated flow rates for change in frequency from 54 Hz to 60 Hz and (b) shows the measured and estimated flow rates for change in frequency from 12 Hz to 6 Hz.

In conclusion, the zoomed results indicate that the PCA-based reduced-order model provides the most favorable balance between transient accuracy and structural simplicity. It tracks the measured flow rates more accurately than the second-order identified model, while maintaining lower complexity than the third-order identified model. Consequently, it represents a suitable candidate for LPV controller synthesis.

Figure 5.7 shows the zoomed portion of Figure 5.5 for the step increase in the input from 48 Hz to 54 Hz in panel (a) and a step decrease from 18 Hz to 12 Hz. panel (a) shows a behavior similar to that presented in Figure 5.6 (a), with the exception that the third-order identified model exhibits a significant overshoot in the transient region. The PCA-based model provides the closest estimation of the flow rate among the considered models. In contrast, the second-order model shows slight deviations in the transient response and a significant error in the steady-state.

For the step decrease in the input from 18 Hz to 12 Hz, the PCA-based model initially follows the overall decay in the flow rate and then settles to a constant value after approximately 15 s, as shown in panel (b). The third-order identified model closely reproduces the measured response. However, the second-order identified model exhibits the poorest performance among all the models.

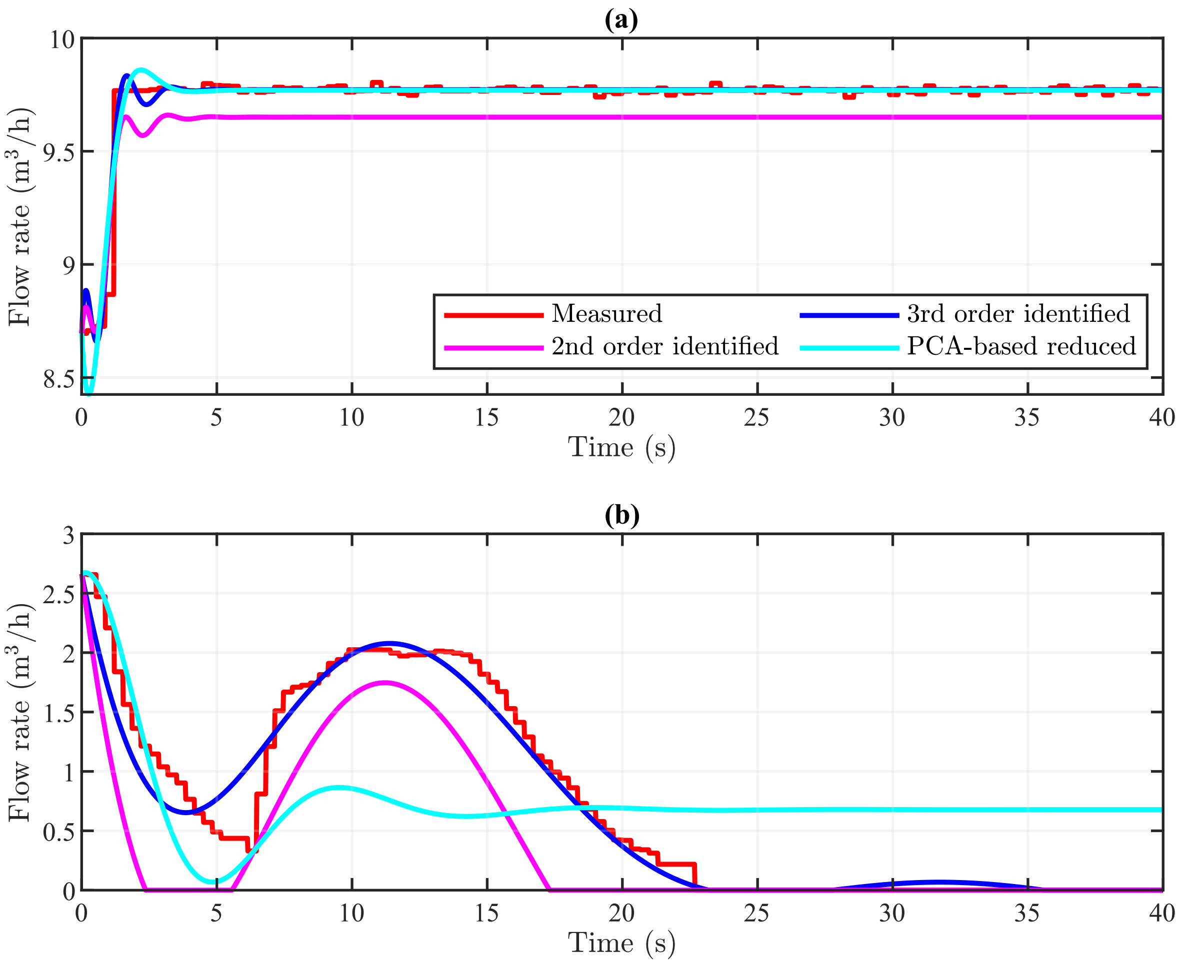

Figure 5.7: Zoomed portion of Figure 5.5: (a) shows the measured and estimated flow rates for change in frequency from 48 Hz to 54 Hz and (b) shows the measured and estimated flow rates for change in frequency from 18 Hz to 12 Hz.

Figure 5.8 presents a zoomed view of Figure 5.5, highlighting the step increase in the input from 12 Hz to 18 Hz shown in panel (a) and a step decrease from 54 Hz to 48 Hz in panel (b). For the step increase in frequency, the third-order identified model estimates the flow rate with high accuracy, closely matching the measured data. In contrast, the second-order identified model exhibits the largest estimation errors in both the transient and steady-state regions. The PCA-based model demonstrates intermediate performance, outperforming the second-order model but remaining less accurate than the third-order model.

The limited ability of the PCA-based reduced model to capture the transient dynamics reduces its accuracy, making it a secondary choice relative to the third-order model. However, its lower model order offers a viable trade-off between model complexity and estimation performance.

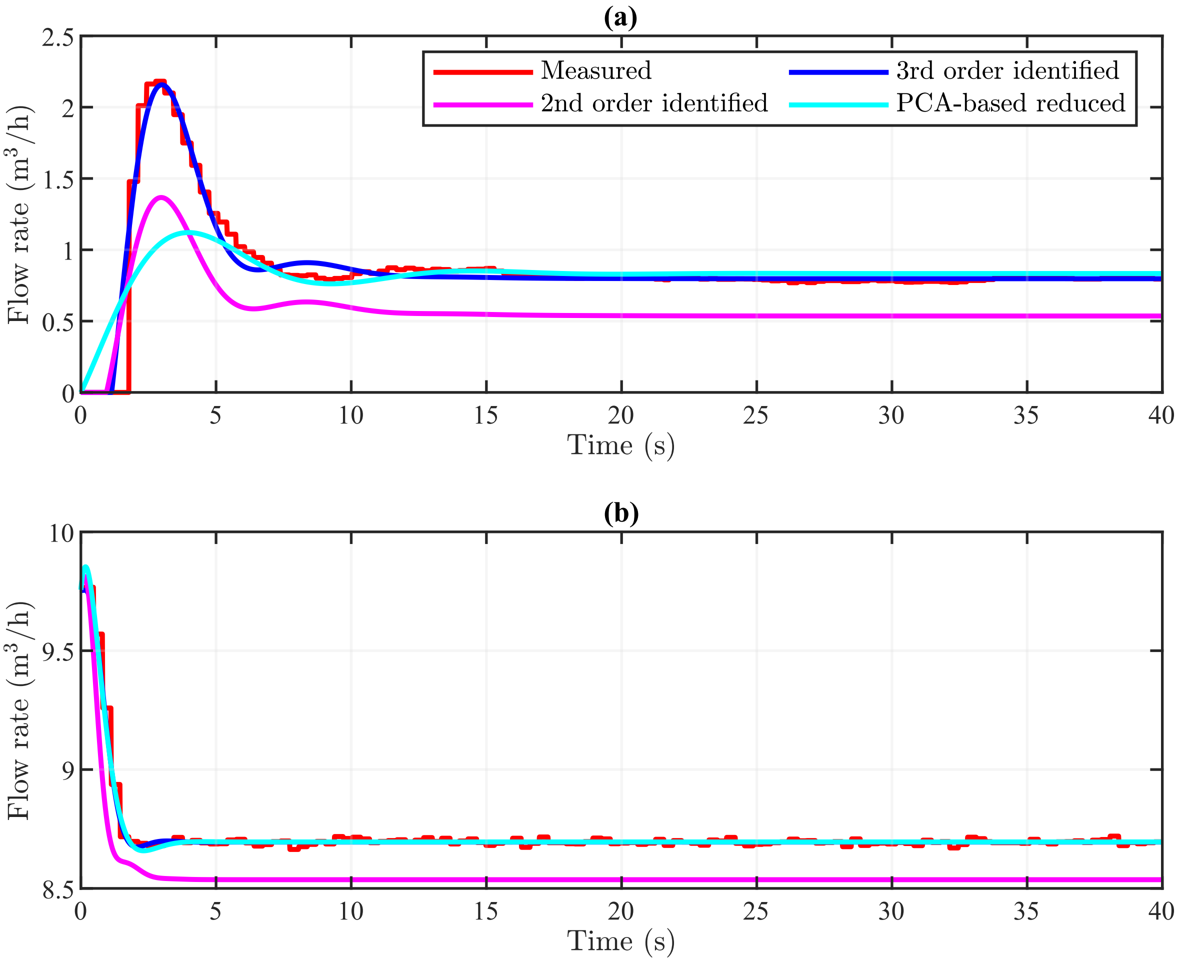

Figure 5.8: Zoomed portion of Figure 5.5: (a) shows the measured and estimated flow rates for change in frequency from 12 Hz to 18 Hz and (b) shows the measured and estimated flow rates for change in frequency from 54 Hz to 48 Hz.

Figure 5.9 shows an estimation pattern of the integer-order models similar to that presented in Figure 5.6. This figure provides a zoomed view of Figure 5.5, highlighting the step increase in the input from 6 Hz to 12 Hz in panel (a) and the step decrease from 60 Hz to 54 Hz in panel (b).

panel (a) indicates that the third-order identified model outperforms the remaining models, whereas the second-order identified model exhibits the poorest estimation accuracy. The PCA-based reduced-order model, which is also of second order, demonstrates intermediate performance. In panel (b), the PCA-based model exhibits estimation performance comparable to that of the third-order model, while the second-order identified model shows significant steady-state estimation error.

Conclusively, the analysis in Figures 5.6 to 5.9 indicates that the second-order identified model lacks accurate estimation of the experimentally collected flow rates. The third-order identified model provides the best estimation performance among the considered models. However, the higher model order requires increased computational resources. The PCA-based reduced-order LPV model exhibits nearly the same accuracy at higher input frequencies. It shows intermediate performance at lower input frequencies. This model has the same order as the second-order identified model. Moreover, parameter variation in the PCA-based LPV model enables a single LPV controller design. This approach ensures the desired closed-loop performance. In contrast, the third-order identified model requires distinct controllers for different input frequencies.

5.3.2 Numerical errors

This section discusses the MAE E_m between the estimated and measured flow rates as[1]

$$E_\mathrm{m} = \frac{1}{N_\mathrm{s}} \sum_{i=1}^{N_\mathrm{s}} |y_\mathrm{e} - y_\mathrm{m}| \tag{5.15}$$

where y_e and E_m denote the estimated flow rate and MAE of the third-order identified model. The second-order identified model has MAE $E_{\mathrm{m,2p}} = E_\mathrm{m}$ when $y_\mathrm{e} = y_{\mathrm{e,2p}}$ – the estimated response of the model with 2 poles. The PCA-based reduced-order LPV model has MAE $E_{\mathrm{m,pca}} = E_\mathrm{m}$ when $y_\mathrm{e} = y_{\mathrm{e,pca}}$ – the estimated flow rate with PCA-based reduced-order model.

Table 5.3 reports MAE computed over a five-second interval. The interval starts at $8\ \mathrm{s}$ and ends at $13\ \mathrm{s}$. This interval emphasizes transient behavior and supports reliable assessment of the proposed method. Notably, the MAE does not follow a monotonic trend with respect to the input. This suggests that the performance of each model is sensitive to the flow conditions rather than presenting the smooth variation in response to the change in the input frequency.

The table show a clear asymmetry in the MAE-based performance evaluation for increase and decrease in the flow rate. This is due to the hysteric and nonlinear behavior of the system. Furthermore, the error values are inconsistent with the system input, i.e., f_in. The error values also indicate that the proposed approach reproduces the experimental response with comparable accuracy. The elevated value of $E_{\mathrm{m,pca}}$ for $f_\mathrm{in} = 12\ \mathrm{Hz}$ results from poor

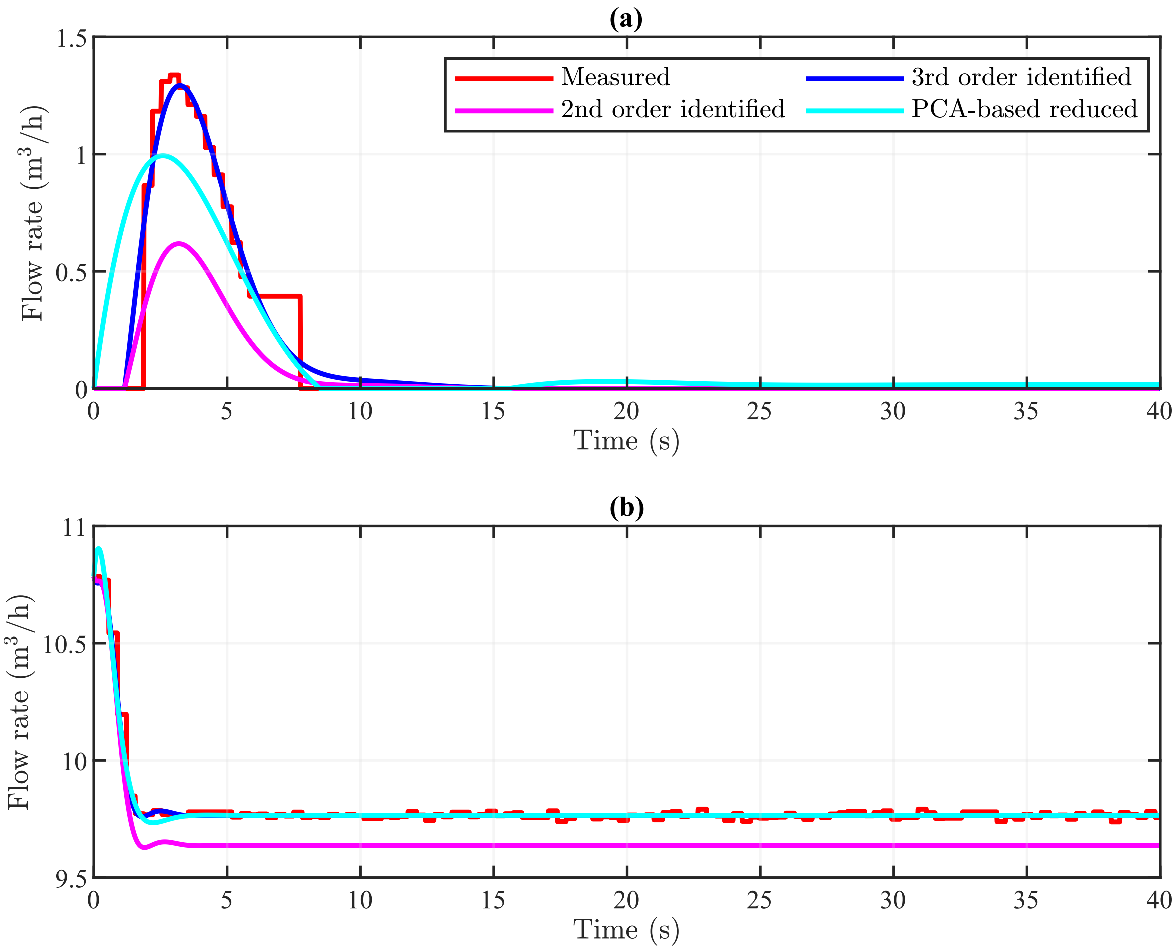

Figure 5.9: Zoomed portion of Figure 5.5: (a) shows the measured and estimated flow rates for change in frequency from 6 Hz to 12 Hz and (b) shows the measured and estimated flow rates for change in frequency from 60 Hz to 54 Hz.

performance during the decrease in flow rate. Overall, the error analysis supports the PCA-based reduced LPV model over the second-order identified model.

Table 5.3: Comparison of numerical errors using different models with PCA-based reduced model. The errors are calculated using Eq. (5.15).

	Increase in flow			Decrease in flow		
f_{in}	E_{m}	$E_{\text{m,2p}}$	$E_{\text{m,pca}}$	E_{m}	$E_{\text{m,2p}}$	$E_{\text{m,pca}}$
6	0.041	0.21	0.080	0.0034	0.038	0.078
12	0.0057	0.029	0.044	0.16	0.56	0.86
18	0.081	0.19	0.036	0.0079	0.46	0.0071
24	0.18	0.44	0.18	0.0044	0.32	0.0033
30	0.0061	0.28	0.0034	0.0018	0.24	0.0032
36	0.0023	0.26	0.0067	0.0081	0.19	0.0071
42	0.0049	0.16	0.0030	0.0010	0.16	0.000 24
48	0.0019	0.13	0.000 24	0.0034	0.16	0.0028
54	0.000 91	0.12	0.0032	0.0043	0.12	0.0053
60	0.011	0.11	0.013	0.0048	0.021	0.0061

5.4 Chapter summary

This chapter investigated model identification and reduction for a flow system exhibiting nonlinear behavior. The analysis showed pronounced nonlinear response characteristics at low excitation frequencies. Independent identification produced different parameter sets for different input conditions. The primary contribution is a structured identification and reduction framework. The method first identified third-order TF from the data collected under different input conditions. It then applied a PCA-based transformation to obtain the reduce-order models. This step resulted in second-order representations while preserving dominant dynamic characteristics of the experimental setup.

The reduced-order models were then used to develop the LPV model. The resulting model is a universal second-order TF with varying parameters. Parameter variations depend on the measured flow rates and changes in the input frequency. The chapter validated the model developed through proposed approach by evaluating the mean absolute errors. Comparisons between the PCA-based LPV model and experimental data demonstrated improved accuracy compared to the second-order identified model.

Chapter 6

Fractional-Order Modeling

The chapter develops a FO modeling framework for the laboratory flow rate measurement system in Figure 3.4 under a fixed input. The proposed algorithm accounts for nonlinear system behavior and associated uncertainty component by constructing a nominal-FO model. The physical system does not intrinsically exhibit FO dynamics, such as memory or hereditary effects. The aim is instead to examine whether a FO modeling framework can effectively represent the complex nonlinear behavior of the system.

A black-box optimization scheme based on the Grünwald-Letnikov definition of FO derivative and integral is used for model identification. A compact FO representation with five adjustable parameters is then identified through numerical optimization with NEOS-server and results are compared with AMPL-IDE and MATLAB-based optimization. The IOD from repeated experimental passes in Figure 3.6 supports model construction and validation. Furthermore, the FO representation is compared with classical IO models of different orders. Sensitivity analysis of the parameters of the FO model under limited perturbations is also presented to investigate the influence of parameters on the model output.

This chapter discusses the findings presented in the published article [14]. Moreover, it covers the successful implementation of the objectives **Obj.3** and **Obj.4** listed in Section 1.3.

6.1 Proposed framework for fractional-order modeling

This section presents the proposed FO modeling structure and the Grünwald-Letnikov based optimization framework. It also introduces IO models for comparison purposes. Furthermore, it provides AMPL-based pseudocode to solve the proposed optimization problem using NEOS-server.

Existing literature presents limited use of FO modeling for flow rate measurement systems, although fluid-flow systems have been studied extensively. Reported approaches include constitutive formulations based on FO-DIEs [7, 166] and data-driven identification methods [6, 37].

Analytical approaches typically begin with IO flow dynamics and extend them by assigning non-integer derivative orders [167], based on assumed physical properties. This extension often represents memory-type effects in system dynamics [168, 169] or approximates the frequency-domain behavior [170]. The validity of such formulations depends on accurate knowledge of system components [138] and the presence of memory-like characteristics [139].

Grey-box methods require prior knowledge of the system structure and use optimization techniques to estimate unknown parameters [140]. In contrast, black-box modeling does not require a predefined structure and relies solely on IOD [37]. In this study, the system structure and model order are unknown. Therefore, the FO model is identified directly from the measured data.

6.1.1 FO modeling structure

A single fractional derivative combined with a fractional integral provides a compact yet expressive structure to represent the dynamics of complex nonlinear systems using a reduced set of parameters [171]. Following the concept of one fractional pole and one fractional zero, the proposed formulation adopts a FO model with five tunable parameters. This configuration provides five Degree of Freedom (DOF) during the optimization process. The equivalent representation of the proposed model in the Laplace domain can be given as follows:

$$G(s) = \frac{Y_e(s)}{U(s)} = K \cdot \frac{s^{\alpha} + a}{s^{\beta} + b}, \tag{6.1}$$

where α, $\beta \in \mathbb{R}$ denote the orders of the fractional derivative and fractional integral, respectively. The parameters a and b define the model parameters, while K represents the gain of the TF model. Equation (6.1) indicates that the FO model contains one pole and one zero. The locations of the pole and zero in the complex plane can be determined by:

$$s = (-a)^{\frac{1}{\alpha}} \tag{6.2}$$

and

$$s = (-b)^{\frac{1}{\beta}}, \tag{6.3}$$

respectively. Since α and β take non-integer values, the corresponding roots are multivalued and generally complex. Their locations in the complex plane can be expressed in polar form as:

$$s_k = |a|^{\frac{1}{\alpha}} e^{j\frac{(2k+1)\pi}{\alpha}} \quad k = 0, 1, 2, \ldots \tag{6.4}$$

and

$$s_k = |b|^{\frac{1}{\beta}} e^{j\frac{(2k+1)\pi}{\beta}} \quad k = 0, 1, 2, \ldots, \tag{6.5}$$

respectively. In contrast to IO systems, where stability is restricted to the left half of the complex plane, FO systems exhibit an extended stability region that includes a portion of the right half plane [172]. This attribute allows FO models to represent stable system dynamics more accurately with a reduced number of parameters compared to IO formulations.

6.1.2 Grünwald-Letnikov based FO model for the flow system

The considered flow system exhibits complex nonlinear behavior, with dynamics that vary under different excitation conditions [137]. The physical system does not inherently display FO characteristics, such as memory effects or long-range dependence on input signals. The objective is therefore to construct a FO model that accurately represents the observed dynamic response. Consequently, the parameters α, β, a, b, and K have no physical interpretations.

The inverse Laplace transform of Eq. (6.1) yields the corresponding time-domain representation in the form of a FO-DE:

$$\mathscr{D}^{\beta} y_e(t) + b \cdot y_e(t) = K \cdot \mathscr{D}^{\alpha} u(t) + K \cdot a \cdot u(t), \tag{6.6}$$

where y_e and u denote the estimated output and the input, respectively. Based on the fundamental properties of FO differentiation operators [38]:

$$\mathscr{D}^{-\beta}\Big(\mathscr{D}^{\beta} y_e(t)\Big) = \mathscr{D}^{-\beta}\Big(K \cdot \mathscr{D}^{\alpha} u(t) + K \cdot a \cdot u(t) - b \cdot y_e(t)\Big), \tag{6.7}$$

$$y_e(t) = \mathscr{I}^{\beta}\Big(K \cdot \mathscr{D}^{\alpha} u(t) + K \cdot a \cdot u(t) - b \cdot y_e(t)\Big). \tag{6.8}$$

The imperfect identification of parameters describing models of the measuring transducer, together with non-uniform sampling intervals, introduces errors into the measured data. The measurement errors are assumed to follow a normal distribution for the purpose of system representation. Under this assumption, the RMSE becomes an appropriate cost function for optimization, as it reflects the variance of the estimation error [173].

The optimization minimizes the RMSE between the measured and estimated outputs. The error is evaluated separately for the transient and steady-state regions. The transient interval is identified automatically during the optimization. The transient interval is defined as the time horizon over which the measured output exceeds $5\,\%$ of the steady-state value.

In addition, the difference between the rates of change of the estimated and measured responses is included to enforce smoothness of the estimated output. The resulting constrained cost function is given as follows:

$$\begin{aligned}
\min_{K,\alpha,\beta,a,b} \quad & \frac{1}{\sqrt{N_{\mathrm{s}}}}\sqrt{\int_{t_0}^{t_{\mathrm{T}}} e(t)^2 dt + \int_{t_T}^{t_{\mathrm{N_s}}} e(t)^2 dt + \int_{t_1}^{t_{\mathrm{N_s}}} \Delta e(t)^2 dt} \\
\text{s.t.} \quad & \max_{t \in [t_0, t_{\mathrm{T}}]} |e(t)| \le e_{\mathrm{m}} \\
& \max_{t \in [t_{\mathrm{T}}, t_{\mathrm{N_s}}]} |e(t)| \le e_{\mathrm{m}} \\
& a \le b - \epsilon \\
& \alpha \ge \beta + \epsilon
\end{aligned}, \tag{6.9}$$

where ϵ denotes a small positive constant introduced to ensure that the optimization yields a well-posed FO integro-differential model with a proper TF in the Laplace domain, as defined in Eq. (6.1). In this study, ϵ is set to 1×10^{-12}.

Furthermore, $e(t)$ represents the difference between the estimated and measured responses. The symbol $\Delta e(t)$ denotes the difference between the rates of change of the estimated and measured responses.[1] These differences are calculated as:

$$e(t) = y_{\mathrm{e}}(t) - y_{\mathrm{m}}(t) \tag{6.10}$$

and

$$\Delta e(t) = \frac{y_{\mathrm{e}}(t) - y_{\mathrm{e}}(t - i \cdot \Delta t)}{\Delta t} - \frac{y_{\mathrm{m}}(t) - y_{\mathrm{m}}(t - i \cdot \Delta t)}{\Delta t}, \tag{6.11}$$

where $y_e(t)$ and $y_{\mathrm{m}}(t)$ denote the estimated and measured flow rates, respectively, and i represents the discrete sampling index.

The parameters α, β, a, b, and K in Eq. (6.9) are constrained within the predefined lower and upper bounds. The optimization models a physical system. Therefore, the corresponding TF is constrained to be proper in order to preserve the causality [174]. The time intervals $[t_0\ t_{\mathrm{T}}]$ and $[t_{\mathrm{T}}\ t_{\mathrm{N_s}}]$ represent the transient and steady-state regions, respectively. The maximum permissible percentage error e_{m}, is imposed as a constraint on the RMSE and is set to 2% of the steady-state value.

Since the parameters α, β, a, b, and K have no physical interpretation, their bounds cannot be defined a priori. The initial bounds of these parameters were selected as $0 \leq \alpha, \beta \leq 1$, $0 \leq K \leq 10$, $0 \leq a \leq 10$, and $\epsilon \leq b \leq 10$. During optimization, these bounds were progressively expanded whenever the optimal solution approached the imposed limits and the resulting model accuracy remained unsatisfactory. Through successive refinement, the parameter bounds were adjusted to:

$$\begin{aligned} 0.1 \leq \alpha\beta \leq 5 \\ 0.001 \leq K \leq 100 \\ 0.001 \leq a \leq 100 \\ \epsilon \leq b \leq 100 \end{aligned} .$$

These final bounds enabled stable optimization without convergence to the boundary values.

The estimated flow rate $y_e(t)$ is obtained by solving Eq. (6.8) using GL implementations of FO derivative Eq. (2.12) and FO integral Eq. (2.13).

6.1.3 IO models for comparison

To enable a direct comparison between the proposed approach and classical IO methods, second-order and third-order models are considered. The third-order IO model contains three poles and two zeros, resulting in six parameters to be optimized. This configuration provides 6-DOF during the optimization process. A third-order model identified by minimizing the MAE has been reported in [137]. However, in this chapter, the RMSE is used as the optimization criterion for both IO and FO models to ensure consistency in performance evaluation. The third-order IO model is given by [137]:

$$G_I(s) = \frac{n_2 s^2 + n_1 s + n_0}{s^3 + d_2 s^2 + d_1 s + d_0}. \tag{6.12}$$

After completing the optimization over 79 passes to obtain the third-order model, the average value of d_1 was observed to be 0.998. Since this value is close to unity, this parameter was fixed at value $d_1 = 1$ to evaluate its effect on the resulting response. Fixing $d_1 = 1$ while tuning the remaining parameters preserves the same number of DOF during optimization. The third-order 5-DOF model and the second-order time-delay model considered for comparison are given as:

$$G_I(s) = \frac{n_2 s^2 + n_1 s + n_0}{s^3 + d_2 s^2 + 1 \cdot s + d_0}, \tag{6.13}$$

and

$$G_D(s) = \frac{n_b s + n_a}{s^2 + d_b s + d_a} \cdot e^{-\tau s}, \tag{6.14}$$

where τ represents the time delay with units in seconds.

6.1.4 NEOS-server for optimization

The NEOS-server provides a free online platform offering a wide range of optimization algorithms implemented in multiple programming languages for diverse classes of optimization problems [151–153]. The server supports the concurrent execution of multiple optimization jobs and delivers efficient computational performance.

Since the problem defined in Eq. (6.9) belongs to constrained nonlinear optimization class, the AMPL modeling environment was selected for its straightforward formulation capabilities. The Interior Point Optimizer (IPOPT) was chosen as the numerical solver due to its effectiveness in handling large-scale nonlinear problems and its ability to address both convex and non-convex formulations [175]. The pseudocode describing the formulation of the optimization problem in AMPL and its solution using the NEOS-server is presented in Listing 6.1.

The optimization procedure executed on the NEOS-server consists of two main steps: preparation of the AMPL files and their submission to the online platform. The optimization requires three different types of files. The `MOD` file defines the decision variables and their associated bounds, implements the detection and separation of the transient and the steady-state regions, and formulates the optimization problem given in Eq. (6.9). It also includes the GL fractional derivative in Eq. (2.12), the corresponding fractional integral in Eq. (2.13), and the error definitions in Eqs. (6.10) and (6.11).

```
START

Create AMPL Model File:
    Define index sets for time samples
    Define parameters for experimental data t, y_m(t), and f_in(t)
    Define decision variables K, α, β, a, and b
    Define lower and upper bounds for the decision variables

Detect Transient Region:
    Compute the index corresponding to the last time sample t_T
    Evaluate |y_m(t_T) − y_m(t_{N_s})| ≥ 5%

Define Estimated Model Dynamics:
    Define recursive coefficients
    Define Grünwald-Letnikov derivative
    Define Grünwald-Letnikov integral
    Define expressions for estimated response y_e(t)
    Define the difference between the measured and the estimated
           responses e(t)
    Define the difference in the rate of change between the measured
           and the estimated responses Δ e(t)

Formulate Optimization Problem:
    Define the cost function
    Define subject-to constraints

Create AMPL Data File:
    Store measured data t, y_m(t), and f_in(t)

Create AMPL Run File:
    Specify the optimization solver
    Load 'MOD' and 'DAT' files
    Execute the 'solve' command
    Display optimized decision variables

Submit Optimization Job:
    Upload 'MOD', 'DAT', and 'RUN' files to the AMPL server
    Run the optimization process
    Collect optimized parameter values and results

END
```

Listing 6.1: Pseudocode to formulate the optimization problem in AMPL and solve it using the NEOS server.

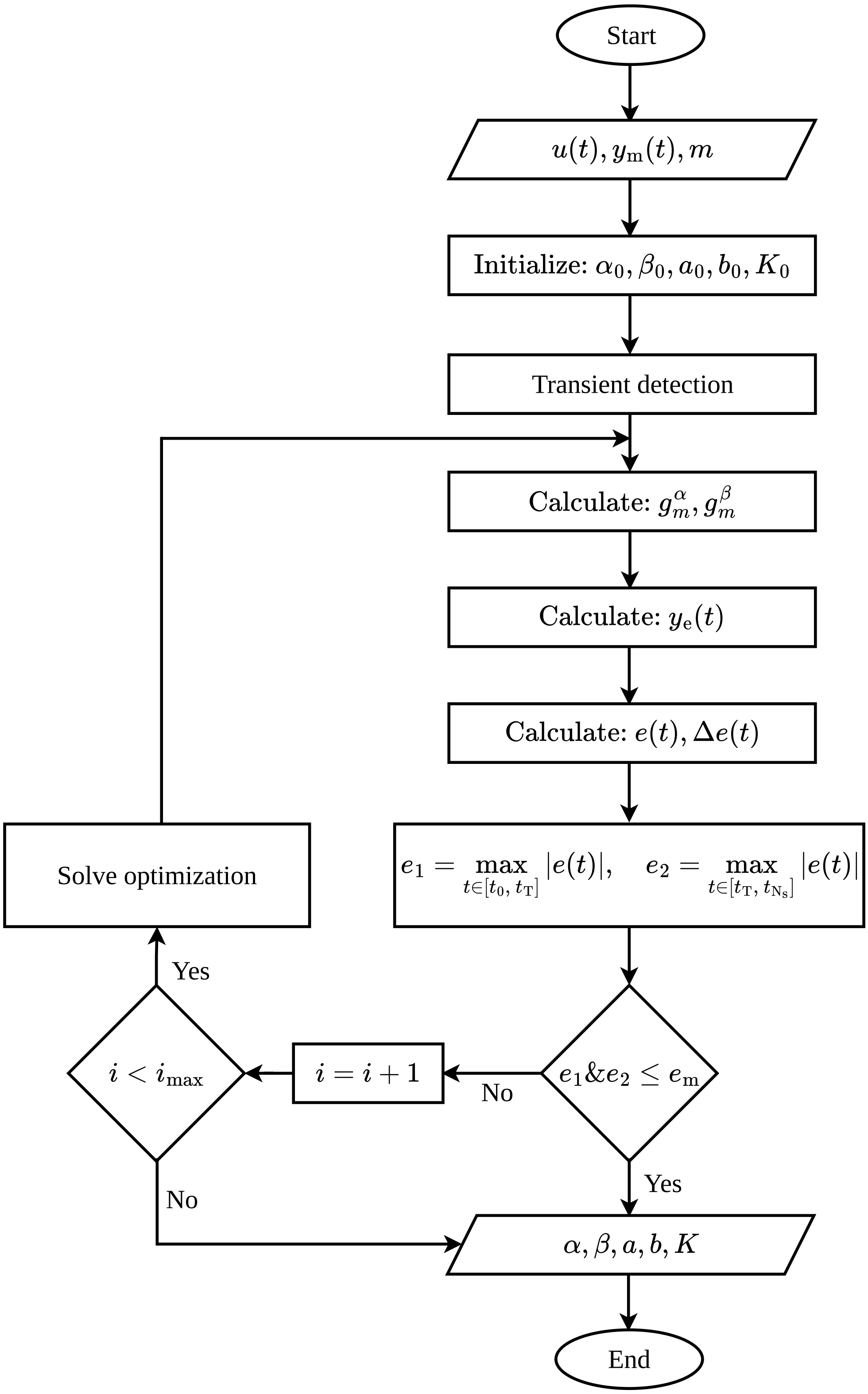

Figure 6.1: Flow chart of the proposed optimization scheme. The symbols i and $i_{\max}$ denote the current iteration of number and the maximum number iterations, respectively.

The DAT file stores the IOD, namely $y_m(t)$ and $u(t)$, together with the corresponding time vector t. The RUN file specifies the execution procedure, including solver invocation, output display, and storage of results in a CSV file. After completing the optimization process, the procedure computes the optimal values of α, β, a, b, and K. Users can obtain these values by downloading the result files from NEOS-server.

The iterative procedure for optimizing the parameters of the FO model is illustrated by the flowchart in Figure 6.1. The process begins with the input data to the algorithm, namely the system input $u(t)$, the measured flow rate y_m, and the truncation order m. An initial parameter set $\{\alpha_0,\ \beta_0,\ a_0,\ b_0,\ K_0\}$ is then defined.

The transient region is identified according to the procedure described in Listing 6.1. Subsequently, the GL coefficients for the fractional derivative g_m^α Eq. (2.17) and the fractional integral g_m^β in Eq. (2.18) are computed. These coefficients are used to produce the estimated response y_e from Eq. (6.8).

The errors $e(t)$ and $\Delta e(t)$ are then evaluated using Eqs. (6.10) and (6.11), respectively. Two performance measures are evaluated: the maximum absolute error in the transient region

$$e_1 = \max_{t\in[t_0,\ t_T]} |e(t)|,$$

and the maximum absolute error in the steady-state region

$$e_2 = \max_{t\in[t_T,\ t_N]} |e(t)|.$$

If both errors satisfy the prescribed tolerance e_m, the corresponding parameter set $\{\alpha,\ \beta,\ a,\ b,\ K\}$ is accepted. Otherwise, the optimization defined in Eq. (6.9) updates the parameters, and the procedure iterates. The iterations continue until either the convergence is achieved or the maximum number of iterations i_{max} is reached. This approach promotes optimal parameter estimation while maintaining the error within predefined bounds.

6.2 Experimental data for modeling

The chapter considers a test case corresponding to an input frequency $f_{in} = 20$ Hz – the corresponding measured output y_e is presented in Figure 3.6. Variations in the input f_{in} produce distinct dynamic responses, which in turn require re-optimization of model parameters for the corresponding experimental data [137].

6.2.1 Preprocessing the measured data

This section describes the preprocessing of the measured data and the data segmentation for constructing and testing the proposed FO model.

The measured data exhibits variations in the output across multiple passes. These variations indicate the presence of measurement uncertainty. In addition to imperfect calibration of the measurement transducer (FT-T1), the dominant contribution to the uncertainty results from non-uniform sampling intervals. Resampling the measured data to enforce a constant sampling interval introduces artificial dynamic effects which can lead to model distortion. This limitation arises because the exact flow rate values at each sampling instant are not known. To address this issue, a preprocessing stage is introduced in which experimental passes with large sampling intervals T_s are discarded. The preprocessing of the measured data was completed in two steps:

1. a common time interval representing the transient response is selected for all measurement passes defined as $t \leq 15$ s,
2. the measured passes satisfying the criterion $T_s \geq \bar{T}_{s,m}$ were discarded,

where T_s and $\bar{T}_{s,m}$ denote the sampling time of an individual pass and the average sampling time of all pass, respectively. This eliminates 842 passes, leaving 158 valid passes, which are shown in Figure 6.2. The figure shows that the retained passes exhibit consistent variation in the measured flow rates. The average value computed at each time instant across the accepted passes is represented by the black line, which is more clearly visible in the zoomed plot in the lower panel. Since the average of repeated measurements provides the best available estimate of the true value [4], this averaged signal is used as the reference for evaluating discrepancies between measured and modeled responses.

6.2.2 Data segmentation

The accepted dataset is divided into two equal subsets, each consisting of 79 passes. The first subset is referred to as the training data and is used to optimize the parameters of the FO models. The second subset is referred to as the testing data and is employed to validate the identified models against independent measurements.

6.3 Identified parameters

This section presents the identified parameters of the FO model Eq. (6.8) obtained by solving the GL-based optimization problem in Eq. (6.9). It also reports the identified parameters of the IO models presented in Eqs. (6.12) to (6.14).

6.3.1 Parameters of the FO model during optimization

Solving the optimization as shown in the pseudocode in Listing 6.1 for the training dataset provides the dynamic parameters α, β, a, b, and K of the FO model defined in Eq. (6.6). The numerical solution of the corresponding FO-DIE is obtained using the GL coefficient with truncation order of $m = 3$.

The optimization performed for each pass in the training set produces distinct parameter

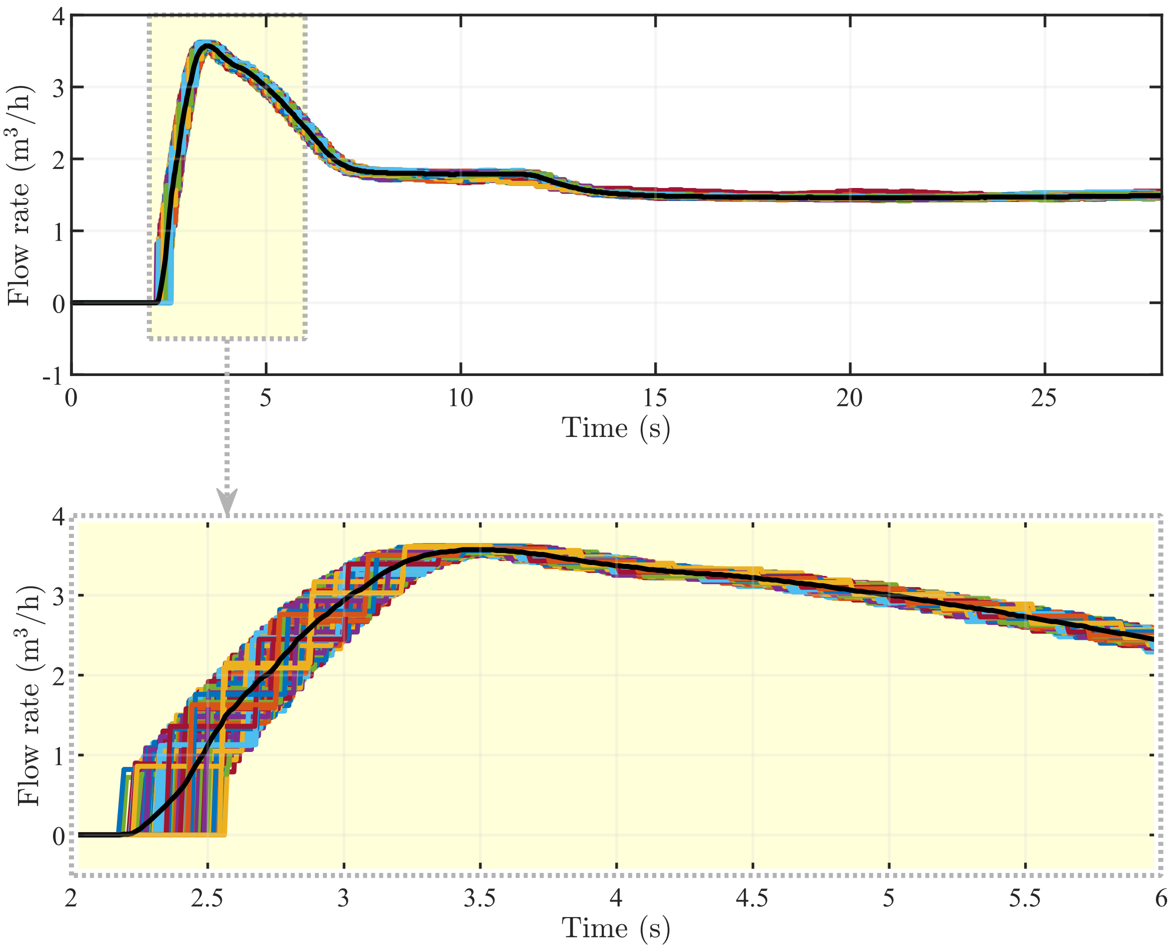

Figure 6.2: The preprocessed data to support development and validation of the FO model. The black line represents the average flow rates computed from the preprocessed data.

values. To illustrate the convergence behavior and parameter variability, the evolution of the parameters over 100 iterations of the optimization is presented in Figure 6.3 for a representative pass selected from the training dataset. The figure shows rapid variations in the parameters during the initial 20 iterations, while the value of the cost function (e_r) decreases slowly. As the optimization progresses, the parameters begin to stabilize, whereas the e_r decreases more rapidly. During the initial stage, up to approximately 20 iterations, the value of the cost function remains nearly constant, indicating slow convergence of the optimization algorithm. In this region, the parameters undergo significant variations. These variations may indicate that the algorithm explores a flat region of the solution space or remains close to a local minimum. As the iterations progress, the optimization exhibits improved convergence behavior. The value of the cost function decreases with a steeper trend, and the parameters approach stable values. In particular, the fractional orders α and β exhibit more pronounced changes before settling. The average values and standard deviations of the parameters provide quantitative measures of these variations. These statistics are reported in Table 6.1, where the values are rounded to two significant digits for clarity.

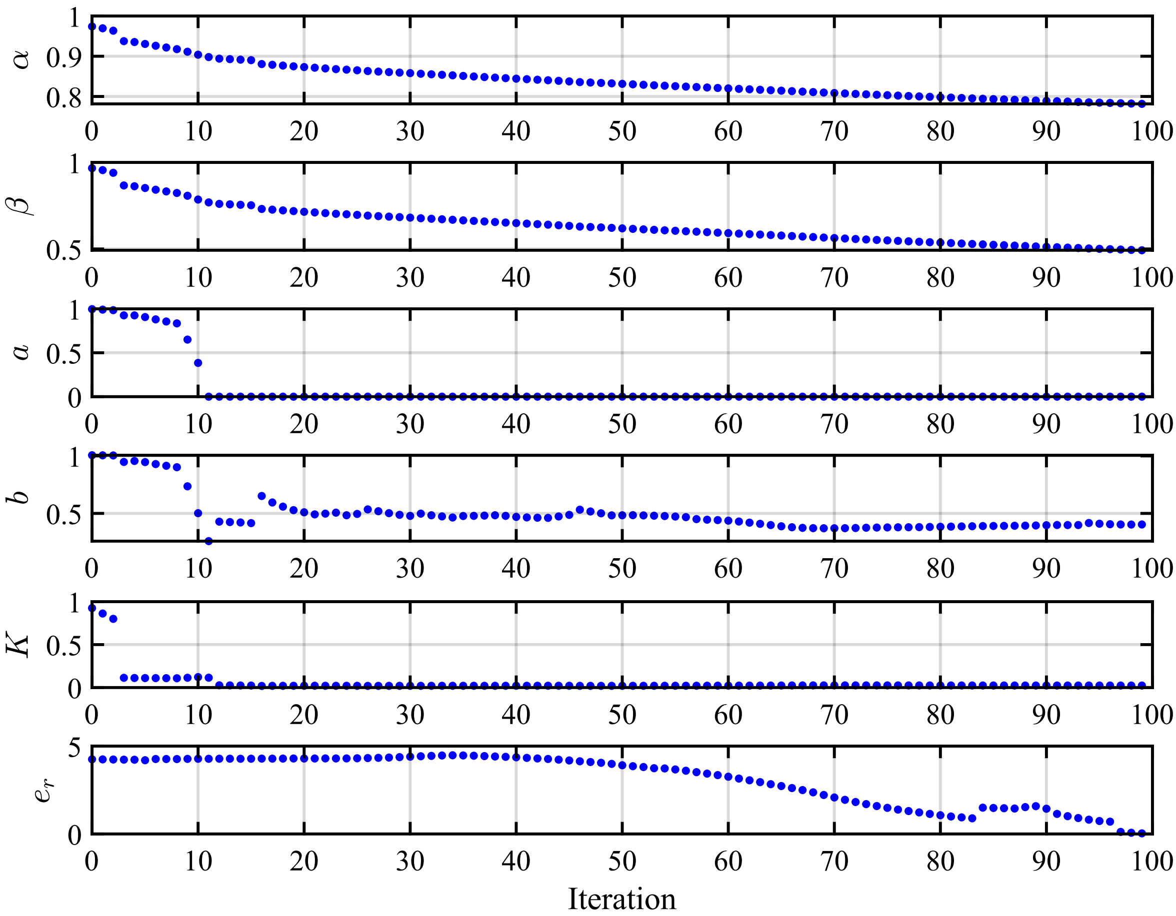

Figure 6.3: Variations of model parameters and objective value during the optimization process for 100 iterations with a randomly selected pass optimized using AMPL-IDE.

The large values of the standard deviation in Table 6.1 indicate a broad dispersion of the optimized parameters. This trend suggests that additional iterations should be allowed to achieve satisfactory convergence of the model response. Despite this variability, an identifiable trend in the tuning of the parameters can be observed throughout the optimization process. In this study, 1000 iterations are used for each pass in the training dataset to ensure stable parameter estimation.

6.3.2 Optimal parameters of the FO models

The training set contains 79 preprocessed passes. For each pass, the optimization procedure presented in Listing 6.1 was applied separately. The optimization was executed on NEOS-

Table 6.1: Coefficients of parameter variations during the optimization process for the scenario presented in Figure 6.3.

Quantifier	α	β	a	b	K	e_r
Mean value	0.84	0.64	0.093	0.49	0.055	3.1
Standard deviation	0.46	0.11	0.27	0.16	0.14	1.4

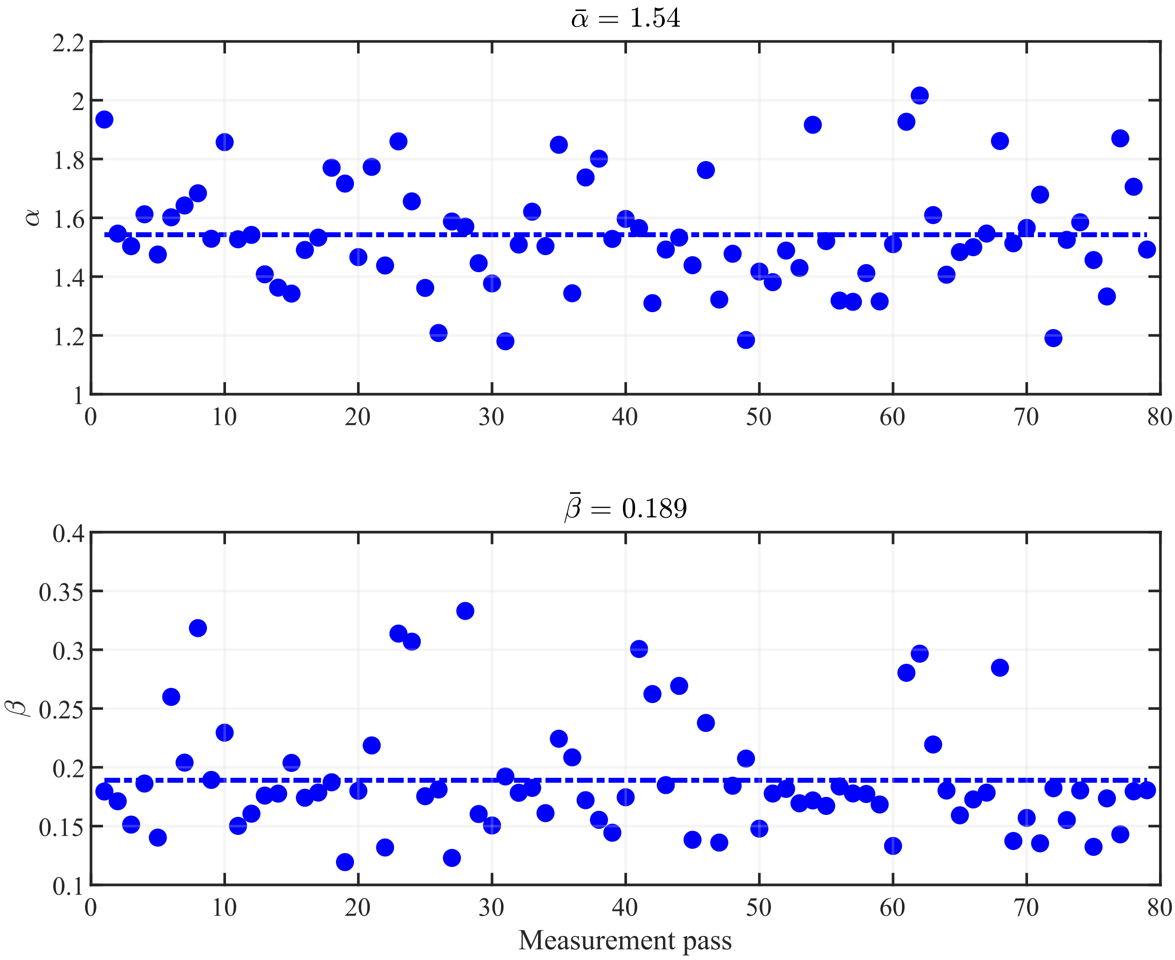

Figure 6.4: The optimal orders of FO derivative (α) and integral (β) of the FO model.

server using the AMPL environment. Each optimization run used 1000 as the maximum number of iterations. At the end of the optimization in each pass, the optimal values of the parameters α, β, a, b, and K were collected.

The variability observed in the preprocessed data in Figure 6.2 propagates to the parameters of the identified models. Consequently, Figures 6.4 and 6.5 depict the dispersion of the FO model parameters. The average values of the respective parameters are denoted by $\bar{\alpha}$, $\bar{\beta}$, $\bar{a}$, $\bar{b}$, and $\bar{K}$.

The figures show that the order of the FO derivative α exhibits the largest spread. The remaining parameters have values closer to their respective averages in each pass. This observation indicates that data variability affects α most strongly. Furthermore, the order of the FO integral β shows considerable variability. The variability of β remains smaller than that of α. However, it exhibits stronger variations than the parameters a, b, and K in Figure 6.5. Therefore, the results indicate that the parameters a, b, and K are only slightly influenced by variations in the preprocessed data in Figure 6.2.

A model constructed using the average values of the parameters can reproduce the variation in the measured output of the system with a small residual. In this chapter the model is constructed using the average values of the optimal parameters across all passes

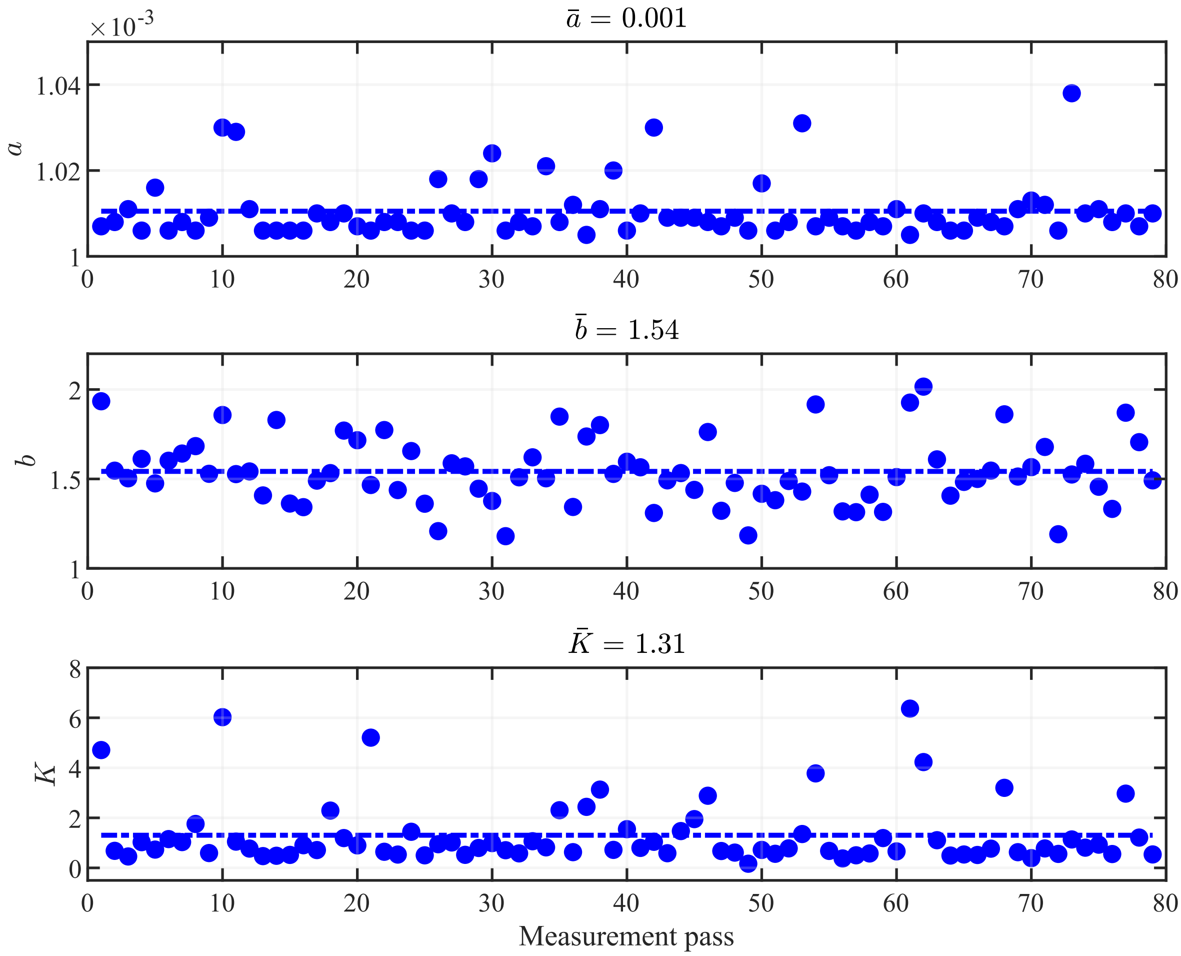

Figure 6.5: The optimal values of the FO parameters a, b, and K of the FO model.

and defines it as the nominal-FO model. The nominal-FO model also supports analysis of variations in the estimated response y_e. This analysis introduces perturbations in the parameter values and analyzes the corresponding changes in y_e.

6.3.3 Optimal parameters of the IO models

Figures 6.6 and 6.7 present the parameters of the third-order IO models. The figures show the dispersion of the parameters obtained from 79 training passes. The third-order models are categorized into two structures: a 6-DOF model, where all parameters are optimized and a 5-DOF model, in which $d_1 = 1$. The blue markers show the parameter spread for the 6-DOF formulation and the black markers represent the corresponding spread for the 5-DOF formulation. The dashed lines indicate the average values of the parameters. The numerical values of these averages are reported above the corresponding subfigures.

The visual analysis of the parameters indicates that the spread of the 6-DOF-IO model remains close to the average values of n_2, n_0, d_2, and d_0. The parameters n_1 and d_1 exhibit a wider dispersion. However, their deviation from the average value is very small, approximately $1\,\%$.

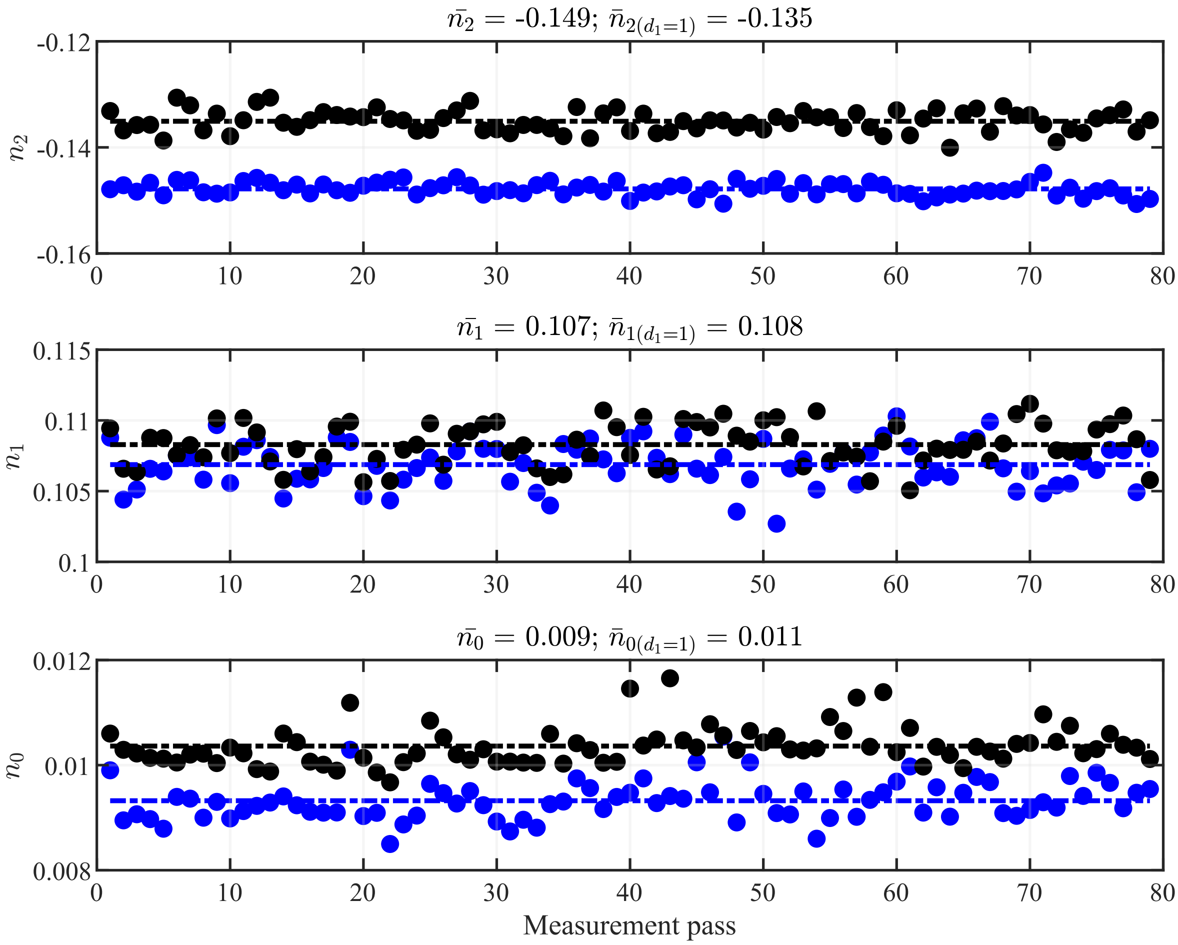

Figure 6.6: Numerator parameters of the third-order IO models. The blue markers indicate the values of parameters of the model in Eq. (6.12) while the black ones represent parameters corresponding to the parameters in Eq. (6.13).

This variability can represent the measurement uncertainty present in the training data, as shown in Figure 6.2. The average value of d_1 is very close to 1, which justifies the assumption $d_1 = 1$. Fixing d_1 and optimizing the remaining parameters results in a parameter spread where dispersion remains preserved. However, the average values of the parameters shift to new levels. This shift is illustrated by the black markers in the panels of Figures 6.6 and 6.7. Therefore, the third-order IO model with 5-DOF can also represent the dynamic behavior of the flow rate measurement system.

Figures 6.8 and 6.9 show the variation of parameters of the second-order IO model with time delay defined in Eq. (6.14). For most training passes, the parameter values cluster around their average values.

The variation of the delay parameter τ is consistent with the preprocessed data in Figure 6.2. After the input is applied, the flow rate measured by FT-T1 remains at $0.00\ \mathrm{m^3/h}$ for approximately $2.10\ \mathrm{s}$. The average value $\tau = 2.08\ \mathrm{s}$ supports the use of a time-delay component to represent the system dynamics.

Some passes provide parameter values that deviate strongly from the average values.

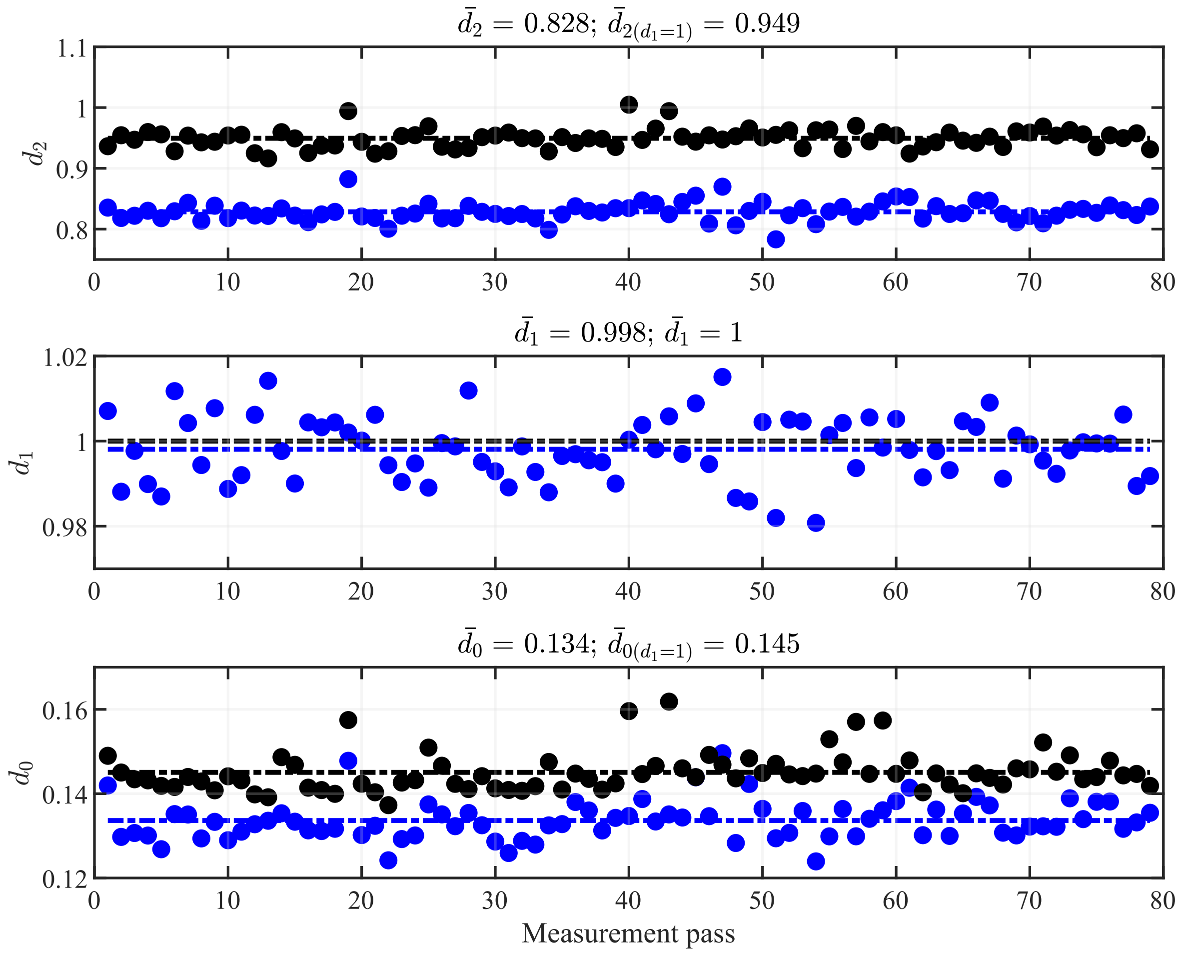

Figure 6.7: Denominator parameters of the third-order IO models. The notation of colors is same as described in Figure 6.6.

This effect can result from parameter interdependence during the optimization process. However, these deviations have small magnitudes. Therefore, they have a negligible influence on the average values, which are indicated by dashed lines in the figures.

6.4 Dynamic response

This section examines the dynamic responses of the models for two cases. In the first case, the FO and IO models are constructed using the parameters obtained from optimization based on the first training pass. The results for this case are referred to as "one-pass". In the second case, the average values of the optimized parameters are used to define the nominal-FO and IO models according to Eqs. (6.6) and (6.12) to (6.14). Figure 6.10 presents a comparison of the models obtained from the first training pass with the corresponding first pass of the preprocessed testing data.

The comparison of dynamic responses for one-pass indicates that the FO model estimates the flow rate more accurately than the IO models for the first testing pass. The variability of the testing data is denoted as Preprocessed Data Variation (PDV) and is represented by

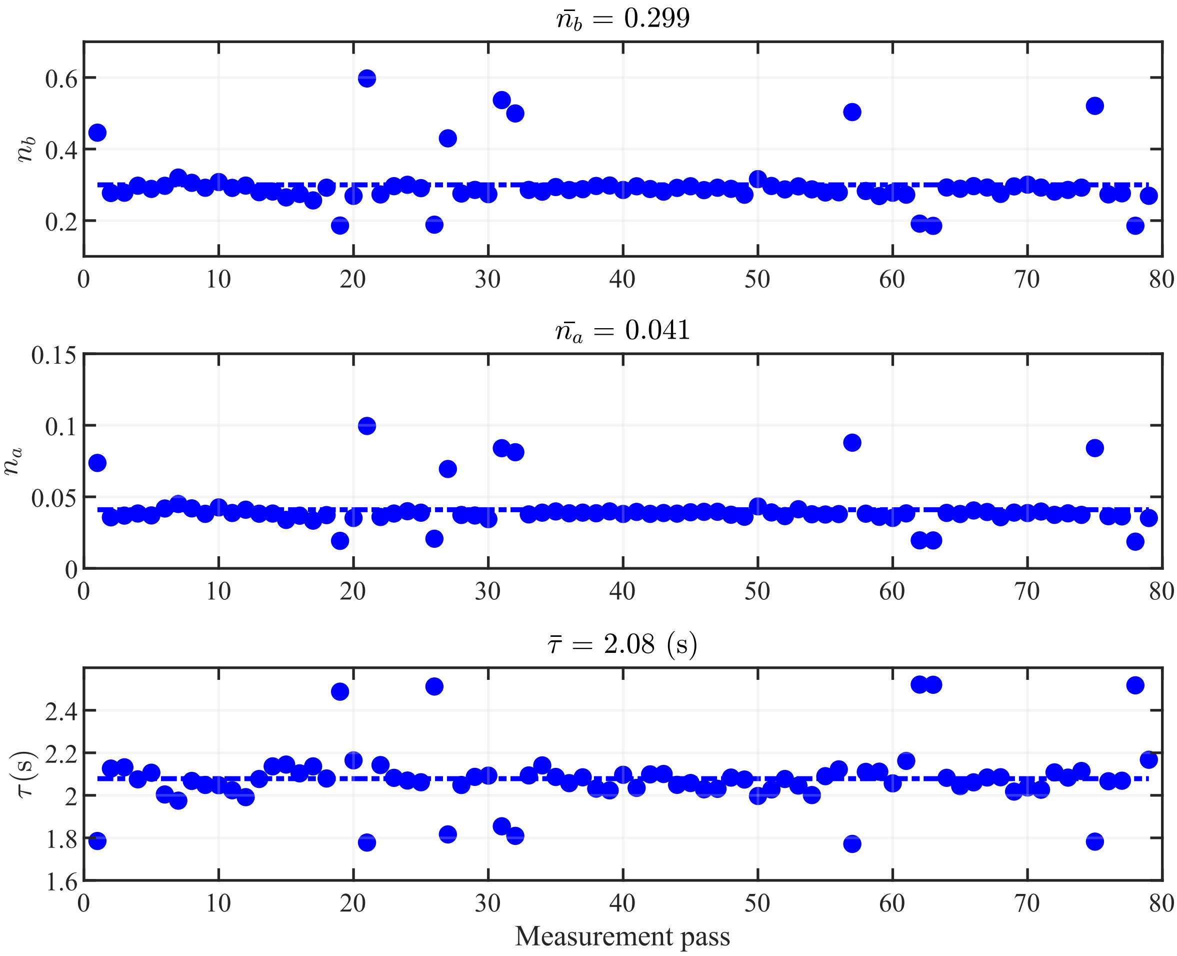

Figure 6.8: Numerator parameters and time delay (τ) of the second-order IO model with time delay presented in Eq. (6.14).

the semi-transparent region in Figure 6.10. The response of the FO model remains within this region for all times greater than 2.10 s. In contrast, the responses obtained from the IO models lie outside this region during a significant part of the transient phase. This deviation is more pronounced in the zoomed view shown in the lower panel of Figure 6.10.

These results indicate that the FO model, identified using a single training pass, provides the closest agreement with the testing data. The third-order IO models with five and six DOF produce similar responses to each other. The second-order IO model with time delay exhibits the largest discrepancy during the transient response. However, all the models provide comparable responses in the steady-state region.

6.4.1 Robustness of the nominal-FO model

To assess the robustness of the nominal-FO model, this section analyzes its response using unprocessed data from the testing set. The estimated dynamic response obtained using the nominal-FO model is compared with that of the nominal IO models. The comparison is shown in Figure 6.11. The semi-transparent background in the figure shows the Unprocessed Data Variation (UDV). Furthermore, MOM denotes the mean values of measured data from

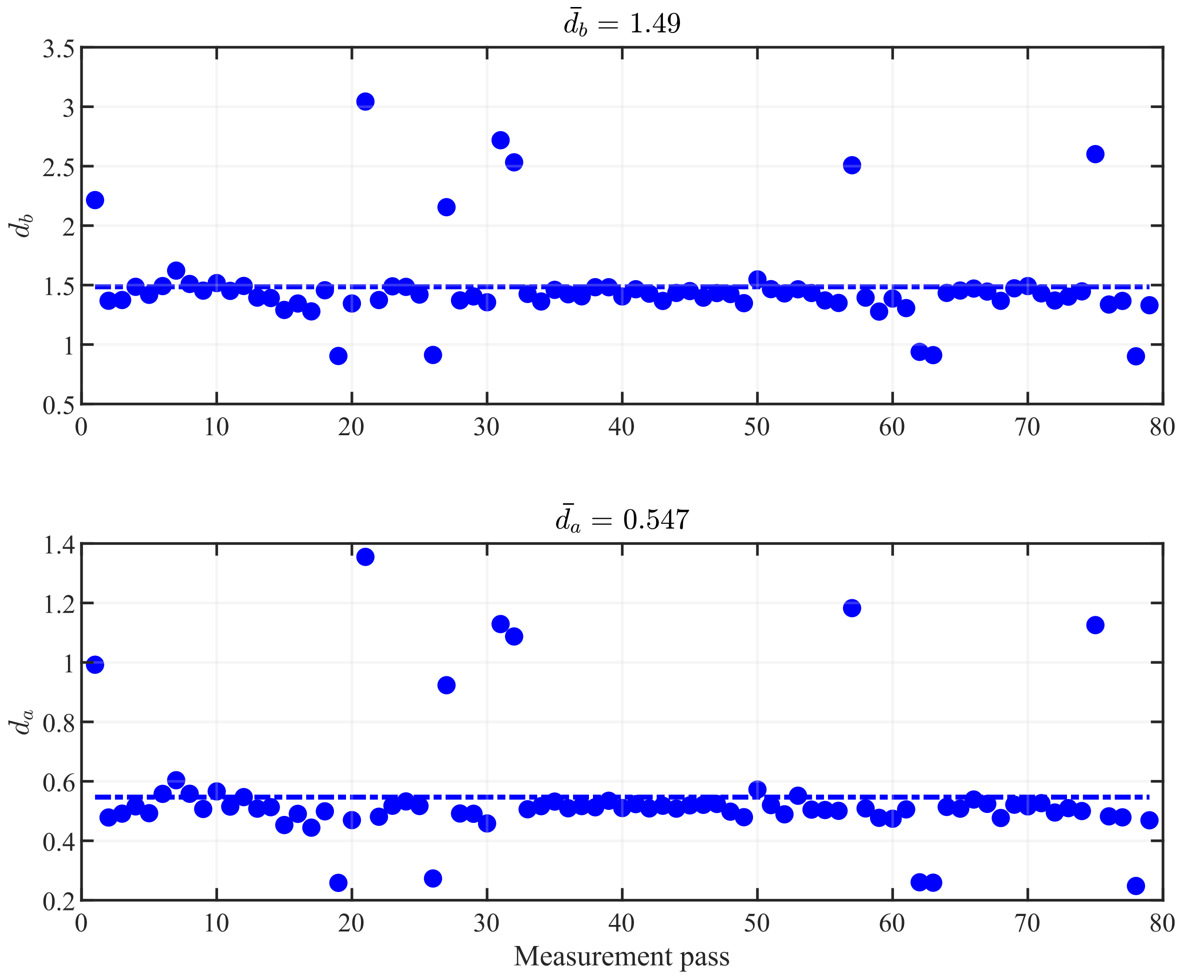

Figure 6.9: Denominator parameters of the second-order IO model with time delay presented in Eq. (6.14).

the unprocessed testing set. Moreover, MOP represents the mean values of preprocessed data from the respective testing set. The Nominal Fractional-Order (NFO) model provides the most accurate estimation of the measured values and exhibits a response consistent with that observed in Figure 6.10. The slight non-smooth behavior around 2.25 s arises from the numerical implementation of the GL approximation.

The figure shows that the predicted dynamic response of the NFO model remains within the range of UDV. In addition, the estimated response closely coincides with the average values obtained from both the unprocessed and preprocessed data. The nominal-IO models exhibit dynamic responses that slightly differ from the corresponding one-pass responses. The nominal second-order time-delay model improves the estimated response and better matches the average measured data. However, the nominal third-order 5-DOF and 6-DOF IO models produce poorer estimates. These estimations are inferior to those obtained from the respective one-pass responses presented in Figure 6.11. This analysis confirms the accuracy and reliability of the proposed modeling approach compared with the IO models.

The third-order 6-DOF nominal IO model exhibits the lowest performance among the

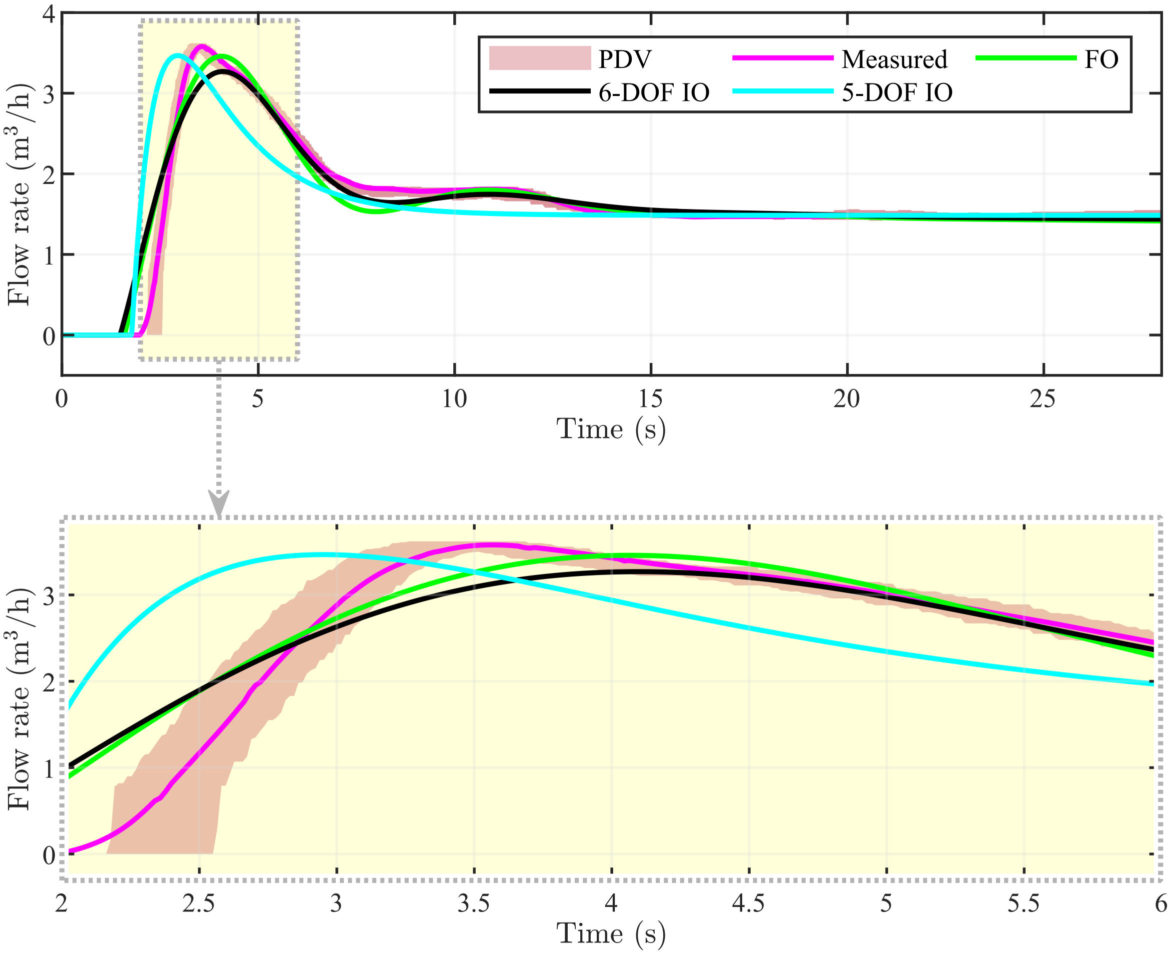

Figure 6.10: One-pass comparison of FO and IO models with experimental measurements. Semi-transparent orange background depicts the variations of the preprocessed data.

considered models. The largest contribution to the discrepancies in the dynamic response occurs during the transient phase. The response estimated by this model deviates beyond the range of variation observed in the UDV. This behavior indicates that the average values of the parameters of this model are not sufficient to capture the underlying system dynamics.

Fixing d_1 to 1 and optimizing the remaining parameters improves the estimation of the dynamic response of the system. This indicates that the shifted average values of the parameters, observed in Figures 6.6 and 6.7, provide a more suitable representation of the system dynamics than the 6-DOF nominal IO model. The nominal time-delay model achieves better performance than the third-order nominal models. The differences in model performance are clearly visible in the zoomed section of Figure 6.11 in the lower panel.

To further assess the accuracy and robustness of the proposed approach, the next section analyzes the parametric sensitivity of the nominal-FO model.

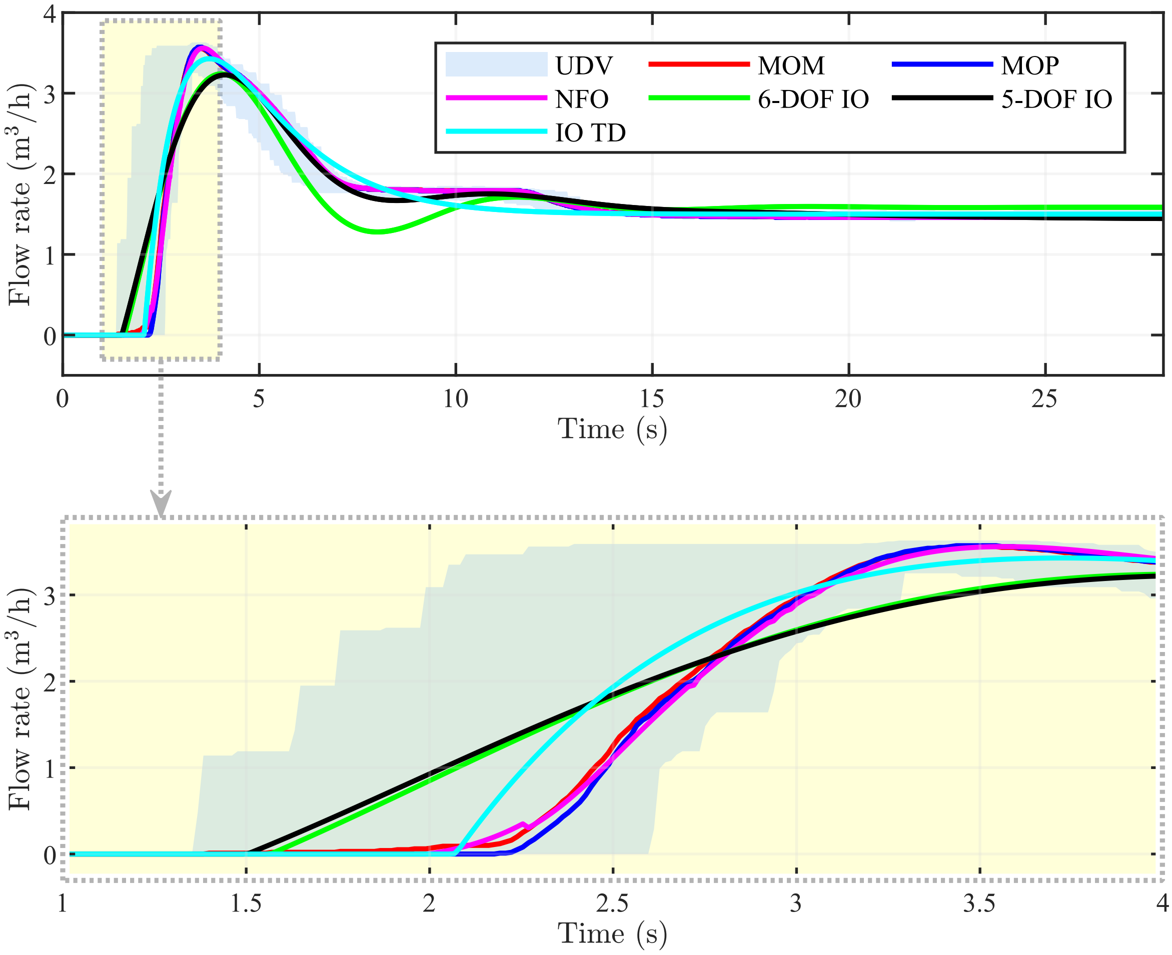

Figure 6.11: Robustness analysis of the proposed nominal-FO model in the presence of the noisy data. The sky blue semi-transparent background represent the variation of unprocessed 500 passes from the testing data set.

6.4.2 Sensitivity analysis of the nominal-FO model

This section introduces two levels of parameter perturbations for the sensitivity analysis. Specifically, the average value of each parameter of the nominal-FO model is increased by 10% and 20%. This procedure facilitates the assessment of the influence of parameter variations on the estimated dynamic response of the nominal-FO model. The sensitivity analysis for the 10% perturbation case is presented in Figure 6.12.

The figure shows that the nominal-FO model is sensitive to the orders of the fractional derivative α and the fractional integral β. An increase of in these parameters by 10% introduces a noticeable deviation in the estimation during the transient phase, while the steady-state response remains unchanged. In contrast, perturbations applied to a, b, and K produce responses that nearly coincide with that of the nominal-FO model. Their effect is limited to small changes in amplitude, with negligible influence on the rise time or damping characteristics. The zoomed view in the lower panel of Figure 6.12 depicts these differences more clearly. It can be concluded that the model demonstrates sufficiently high robustness to 10% variations in a, b, and K. However, it shows moderate sensitivity to α and β, primarily affecting the transient behavior.

The jitter observed in the response under perturbations of α and β results from the numerical approximation used to solve the GL-based DIE in Eq. (6.8). This effect arises from discretization and approximation errors inherent to the method. This effect can be reduced by selecting a sufficiently small sampling time. In some cases, changing the numerical solver can also improve the smoothness of the response. This property of the proposed model supports the development of accurate representations of the system dynamics, which in turn enables the design of robust controllers suitable for real-time implementation.

The large residuals observed in the transient region in Figure 6.12 arise from the sensitivity of the system dynamics to the orders of the FO derivative and integral, as well as from variability in the unprocessed data. Variations in α and β during optimization influence the transient characteristics of the dynamic response. Measurement noise and nonlinear effects at the beginning of the response further increase these discrepancies. Moreover, the numerical implementation of the GL operator introduces additional errors during periods of rapid signal variation. These limitations can be mitigated by applying transient-weighted optimization and refining the sampling strategy.

The effect of 20% perturbations in the parameters of the nominal-FO model, shown in Figure 6.13, supports the previous observations. Larger variations in α and β increase oscillations and overshoot. This effect confirms their dominant influence on the transient dynamics. In contrast to the 10% perturbation shown in Figure 6.12, the deviations with 20% perturbations in all parameters are more pronounced, yet they remain bounded.

This sensitivity to parameter variations can be improved for moderate variations, such as a 20% increase in individual parameters, by applying regularization techniques, for example L_2 regularization. These methods limit excessive parameter growth and reduce the risk of overfitting. Alternatively, Bayesian optimization can provide a systematic framework by incorporating prior distributions and uncertainty quantification. This approach can enable more reliable parameter estimation under noisy measurement conditions [176, 177].

The observed robustness can be attributed to the method of construction of the nominal-FO model. The model was trained using the IO data from 79 passes. For each pass, the optimization algorithm was run for 1000 iterations and the optimal set of parameters α, β, a, b, and K was obtained. The average values of these parameters were then used to define the nominal model. As a result, moderate variations in individual parameters tend to preserve the overall response captured during training.

6.5 Accuracy of the models

The true value of the flow rate at any given time remains unknown due to measurement uncertainty. The best estimate of this quantity can be given by the experimental mean of

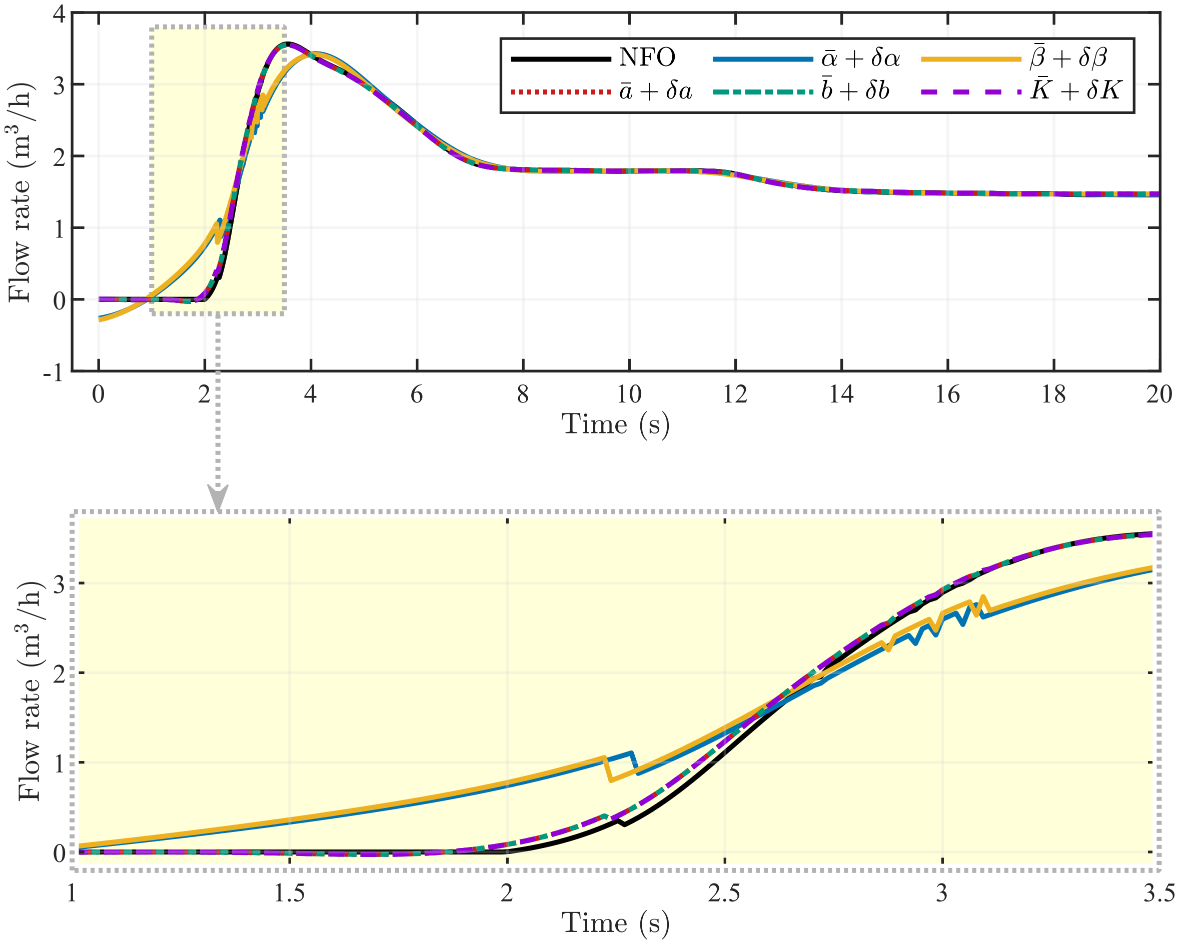

Figure 6.12: Sensitivity analysis of the nominal-FO model over a change in individual parameters by +10% of the respective mean value. The lines representing response with perturbations in $\bar{a}, \bar{b}$, and $\bar{K}$ nearly overlap. This behavior demonstrates a strong robustness of the model to these parameters.

the measured values [4].

Therefore, the mean values of the measured outputs are calculated at each time instant using the unprocessed testing data. These values serve as reference values for evaluating the residuals and numerical errors of the dynamic models.

6.5.1 Residual analysis

This section presents residuals of the model responses for two cases: the models constructed from the IOD of the first pass and the nominal models. For the "one-pass" analysis, this sections defines the residual as the difference between the measured output from the first pass of the testing data and the responses of the models identified using the first pass of the training data. For the nominal models, the residual is computed as the difference between the mean of the unprocessed testing data and the responses of the nominal models. The same dataset is used to evaluate the numerical errors.

For the "one-pass" analysis, the residual variation is expressed with respect to the

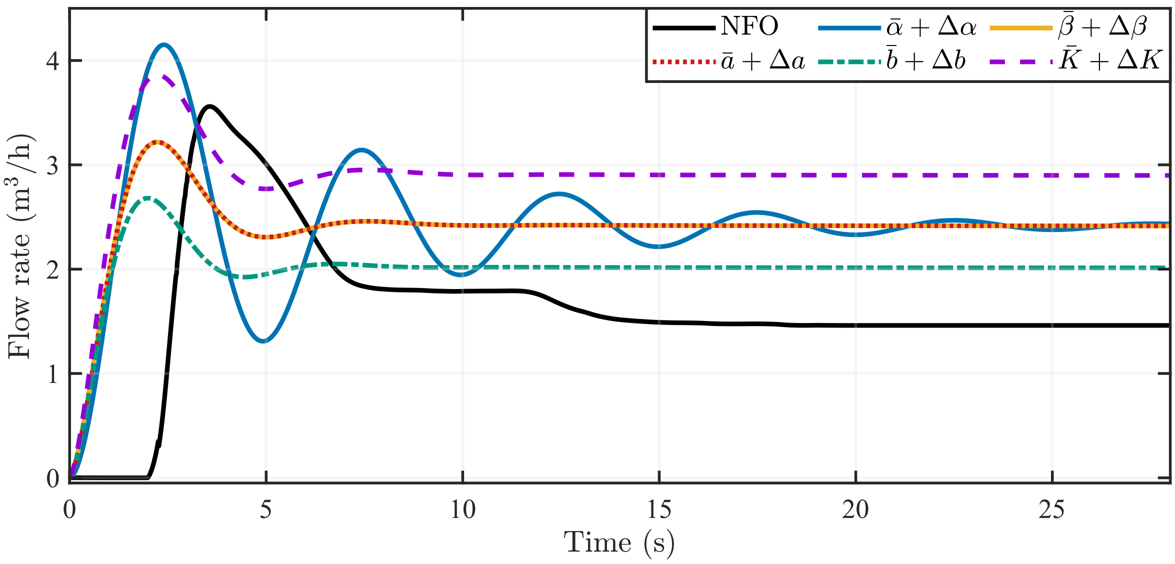

Figure 6.13: Sensitivity analysis of the nominal-FO model for the perturbations introduced in the individual parameters by $+20\,\%$ of the respective mean values.

mean values of the preprocessed measured data. In contrast, for the nominal models, the residual variation is determined using the mean values derived from the unprocessed testing data. Since all measurement passes contribute to the computation of these mean values, the method provides improved insight into model robustness under noisy measurement conditions.

Figures 6.14 and 6.15 show that the residuals attain large magnitudes during the transient phase, i.e., for $t \leq 15$ s. However, the residuals have reduced magnitudes in the steady-state region. Figure 6.14 shows the "one-pass" comparison of the residuals for different models while Figure 6.15 presents the corresponding results for the nominal models. In both figures, the lower panels provide a zoomed view of the steady-state region.

The one-pass comparison shows that the time-delay model yields the largest residuals in the transient region, whereas the FO model produces the smallest residuals. The third-order IO models with five and six DOF provide comparable residual magnitudes. Both IO models have better performance than the time-delay model. However, the inability to accurately approximate the true flow rate from a single pass limits the conclusiveness of these results. The analysis is presented with respect to a semi-transparent background defined as the Preprocessed Residual Variation (PRV). Therefore, this section also analyzes the residuals using the mean values obtained from the unprocessed testing data.

The residual analysis of the nominal models is shown in Figure 6.15. The figure shows that the nominal-FO model achieves the lowest residual magnitudes over the entire time response. The sky-blue semi-transparent background depicts the Unprocessed Residual Variation (URV).

The third-order 5-DOF IO model exhibits the highest residual magnitudes during the first 5 s. However, its performance improves after 5 s and achieves better performance than

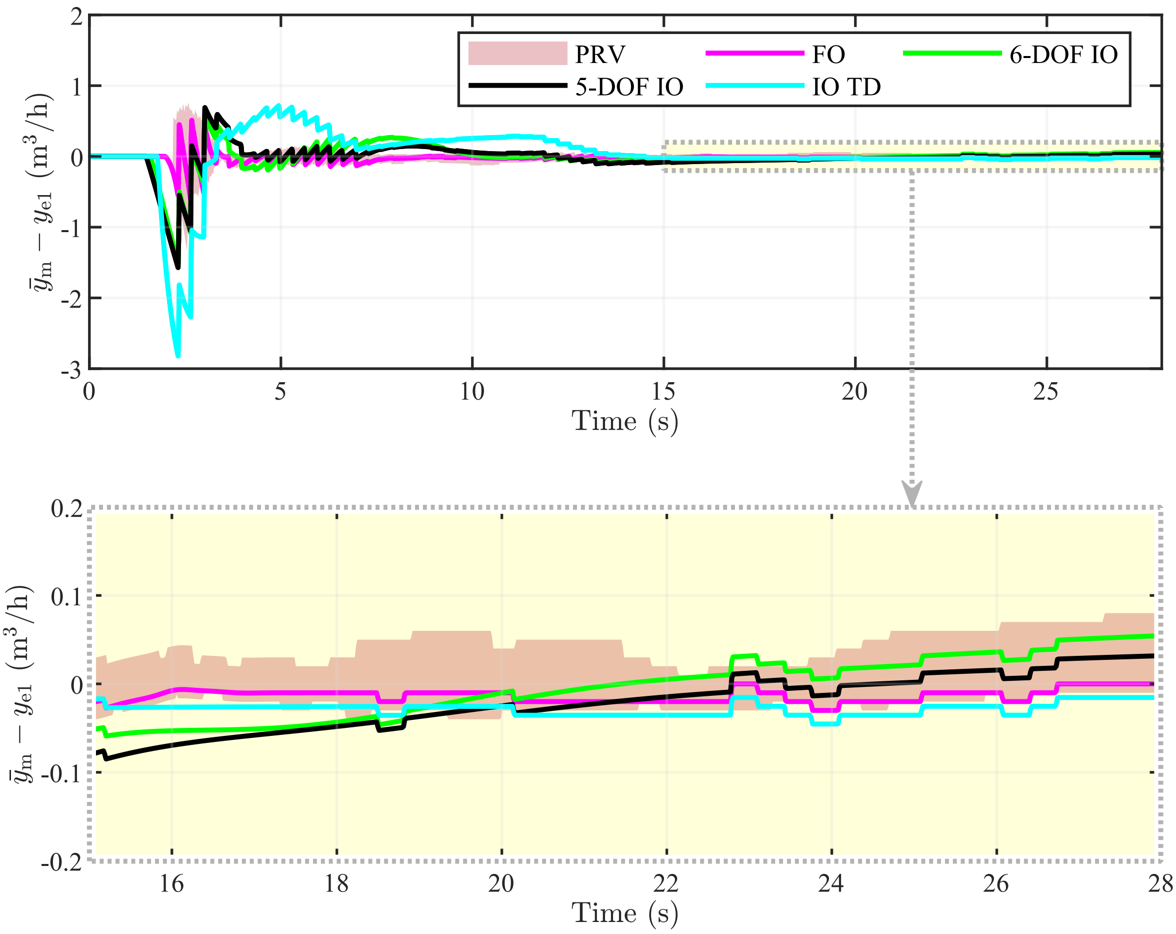

Figure 6.14: Residual comparison of the FO model constructed from the first set of the identified parameters. The mean values of preprocessed 79 passes from the testing data set are considered as reference values to enable this comparison.

the 6-DOF IO model. The second-order IO model with time delay shows relatively smaller residual magnitudes in both the transient and steady-state regions. Its performance exceeds that of the third-order IO models. Moreover, the third-order 6-DOF IO model produces the largest residual magnitudes, especially in steady-state region. This result makes it the least suitable choice for modeling the flow system under the considered conditions. Based on this analysis, the second-order time-delay model can serve as the second most suitable representation of the flow rate measurement system for the considered scenario.

6.5.2 Numerical error analysis

This section analyzes numerical errors to evaluate the accuracy of the models presented in this chapter. In the absence of true values of flow rate, the evaluation method uses the average values of flow rate from the unprocessed data as reference values.

Several norms, including L_1, L_2, and L_∞, are commonly used to quantify the quality of estimated models [13, 173, 178]. The L_1 norm has low sensitivity to measurement errors and other gross disturbances [173]. In contrast, the L_∞ norm is highly sensitive to estimation

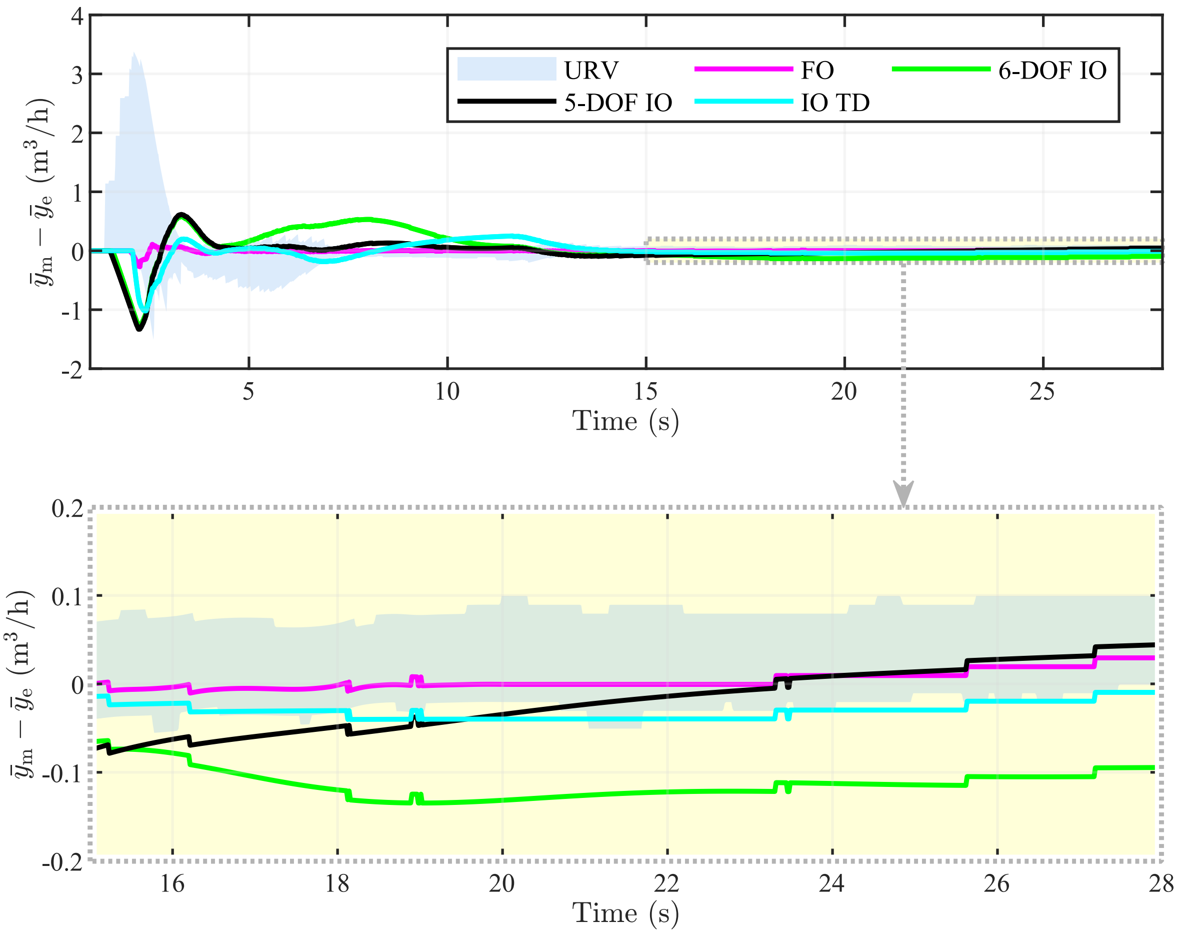

Figure 6.15: Residual comparison of the nominal-FO model. The mean values of unprocessed 500 passes from the testing data set are considered as the reference values for this comparison.

errors [178]. Therefore, it is not suitable as a general quality metric for the accuracy analysis of the models. Its applicability is limited to cases where the error distribution is known.

The L_2 norm is commonly used in measurement systems and model identification through optimization. This approach typically assumes a normal distribution of the measurement data. Considering this assumption, and the limited sensitivity of the L_1 norm to large errors, this section uses RMSE and MAE as numerical indicators of the model quality. The MAE E_{m} is given by Eq. (5.15) in Section 5.3.2 while the RMSE e_{r} is defined as:

$$e_{\mathrm{r}} = \sqrt{\frac{1}{N_{\mathrm{s}}} \sum_{i=1}^{N_{\mathrm{s}}} e_i^2}, \tag{6.15}$$

where $e_i = y_{\mathrm{e},i} - y_{\mathrm{m},i}$.[1] The variables $y_{\mathrm{e},i}$ and $y_{\mathrm{m},i}$ denote the estimated and measured outputs of the system at i-th sample interval, respectively. The parameter N_{s} represents the total number of samples in the output data. The Mean Absolute Percentage Error (MAPE) E_{MAPE} is:

$$E_{\mathrm{MAPE}} = \frac{1}{N_{\mathrm{s}}} \sum_{i=1}^{N_{\mathrm{s}}} \left| \frac{e_i}{y_{\mathrm{m},i}} \right| \cdot 100\,\%. \tag{6.16}$$

Numerical errors for one-pass

The error analysis for the one-pass comparison between measured and estimated data is presented in Table 6.2. The table shows that the proposed FO model achieves the highest accuracy. In contrast, the IO time-delay model exhibits the highest errors and thus, the lowest performance.

Using the third-order IO models reduces the error by more than $50\,\%$ compared with the time-delay model. The 5-DOF and 6-DOF third-order models yield comparable results to each other. However, the six-parameter optimization imposes a higher computational cost than the five-parameter case. Therefore, a fair comparison should consider models with the same DOF during optimization.

This analysis indicates that the third-order IO model provides a more efficient representation than the IO time-delay model. Nevertheless, the FO model achieves significantly higher accuracy. It reduces the error by approximately a factor of six compared with the IO time-delay model and by a factor of three compared with the third-order 5-DOF IO model. A more reliable comparison can be obtained by using the mean of the measured data as a reference, as it approximates the reference value of the flow rate.

Numerical errors with respect to average of the measured value

Table 6.3 presents the corresponding comparison of errors for the nominal models. The table presents the numerical errors between the mean of the unprocessed measured data from the testing passes and the responses estimated by different models. The analysis shows that the time-delay model yields smaller errors than the third-order IO models. The RMSE and MAE are smaller by approximately a factor of three for the time-delay model when compared with the third-order model with the same number of DOF, i.e., 5-DOF, under identical conditions. The FO model achieves the highest accuracy. Using this model reduces the RMSE and MAE by about $23\,\%$ and $24\,\%$, respectively, and the MAPE by $7.3\,\%$ relative

Table 6.2: Numerical errors between the measured and modeled responses. The errors correspond to one-pass comparison.

Model type	e_{r} ($\mathrm{m^3/h}$)	E_{m} ($\mathrm{m^3/h}$)	E_{MAPE} (%)
nominal-FO model	0.027	0.064	1.5
3^{rd}-order 6-DOF IO model	0.19	0.091	4.6
3^{rd}-order 5-DOF IO model	0.20	0.086	4.1
IO time-delay model	0.41	0.18	8.8

to the time-delay model.

In contrast, the 6-DOF IO model exhibits inferior error characteristics compared with the remaining models. This behavior may result from parameter interdependence during the optimization process. For the same number of iterations as used for the 5-DOF model, the six-parameter formulation may not reach convergence. Increasing the number of iterations could improve the performance of the 6-DOF IO model. However, the current study does not investigate this aspect of the modeling.

Numerical errors of the nominal-FO with perturbed parameters

To assess the robustness of the nominal-FO model, this section evaluates the effect of moderate perturbations of individual parameters on numerical error metrics. The corresponding errors are presented in Table 6.4.

Each parameter was individually increased by $10\,\%$ relative to its mean value, and the resulting errors were evaluated. The parameters of the FO model after a $10\,\%$ increase in those of the nominal-FO model are denoted as: $\alpha^* = \bar{\alpha} + \bar{\alpha} \cdot 10\,\%$, $\beta^* = \bar{\beta} + \bar{\beta} \cdot 10\,\%$, $a^* = \bar{a} + \bar{a} \cdot 10\,\%$, $b^* = \bar{b} + \bar{b} \cdot 10\,\%$, and $K^* = \bar{K} + \bar{K} \cdot 10\,\%$. This method enables the evaluation of the effect of a $+10\,\%$ perturbation in each parameter on the statistical error measures. By introducing the perturbation in a single parameter at a time while keeping the remaining parameters unchanged, five distinct models are obtained – as listed in Table 6.4. This analysis quantifies the influence of individual parameters and provides a measure of the model sensitivity to the parameters. Table 6.4 reports the sensitivity of each parameter in terms of numerical errors. These errors were computed with respect to the mean of the unprocessed measured data obtained from 500 passes of the testing set.

The analysis shows that the RMSE (e_{r}) of the FO model is strongly affected by perturbations in α, β, and K. The MAE exhibits moderate sensitivity to parameter variations, except for α. A perturbation in α produces a more pronounced effect. For perturbed values of α, the MAE increases by approximately a factor of 2.4 compared with the value obtained using the average α (see Table 6.3). Perturbations in β lead to an increase in E_{m} of approximately $85\,\%$. A $10\,\%$ increase in the average value of b results in a $43\,\%$ rise in E_{m}. A similar increase in K produces an increase of $31\,\%$ relative to the

Table 6.3: Comparison of the error analysis of the nominal-FO model to verify the robustness. These calculations assume the mean values of the unprocessed 500 passes from the testing data set as the reference data.

Model type	e_{r} ($\mathrm{m^3/h}$)	E_{m} ($\mathrm{m^3/h}$)	E_{MAPE} (%)
nominal-FO model	0.027	0.016	3.5
3^{rd}-order 6-DOF IO model	0.24	0.17	37
3^{rd}-order 5-DOF IO model	0.18	0.083	35
IO time-delay model	0.12	0.067	8.8

nominal model in Table 6.3.

The MAPE (E_{MAPE}) is significantly influenced by perturbations in α and β. However, it remains nearly the same when a, b, and K are perturbed. Although the proposed model preserves the overall dynamic behavior, as shown in Figure 6.12, it exhibits high sensitivity to the orders of the fractional derivative (α) and integral (β). This sensitivity may arise from several factors associated with the numerical implementation of the FO-DIE. These factors include the choice of solver, the selected sampling time, and the TO m of the binomial coefficients in GL implementations given in Eqs. (2.17) and (2.18).

6.5.3 Distribution of residuals

An alternative approach to evaluate the accuracy of the nominal-FO model is to analyze the distribution of residuals in the modeled response. Direct evaluation with respect to the flow rate is not possible, as the true values of the flow remain unknown. To overcome this limitation, this section analyzes the distributions of the residuals obtained from the FO model. This section assesses these distributions using the Root Mean Square (RMS), Mean Absolute (MA), and Mean Absolute Percentage (MAP) measures of the residuals. The residual analysis is based on two cases: the first case considers the FO model constructed from the first set of identified parameters, while the second case uses the nominal-FO model.

The RMS, MA, and MAP measures of residuals are calculated in the same manner as defined in Eqs. (5.15), (6.15) and (6.16) except that the error term e_i replaced by the residual r_i. The residual is defined as the difference between the measured output of a given pass and the corresponding model response, i.e., $r_i = y_{\mathrm{m},p}(t) - y_{e1}(t_i)$, where $p \in \{1, 2, \ldots, 500\}$ denotes the index of the measured pass.

Figure 6.16 shows the probability densities of the residuals for the FO model constructed from the parameter set obtained from the optimization run using the first pass of the measured data and implemented in AMPL-IDE with the IPOPT solver. These distributions correspond to 500 passes of the unprocessed testing data.

The figure shows that the RMS density (R_r) concentrates at low values, approximately in the range (0.02–0.06) $\mathrm{m^3/h}$, and exhibits a rapidly decreasing tail. This indicates that large deviations occur with low probability. The MAE density (R_m) has its maximum near

Table 6.4: Sensitivity analysis of model parameters to the estimated response by increasing the individual parameters by 10 % of the respective mean values. This comparison considers the mean of unprocessed data in the testing set, as in Figure 6.12.

Error	Nominal	α^*	β^*	a^*	b^*	K^*
e_{r} ($\mathrm{m^3/h}$)	0.027	0.096	0.073	0.056	0.061	0.093
E_{m} ($\mathrm{m^3/h}$)	0.016	0.037	0.029	0.029	0.023	0.021
E_{MAPE} (%)	3.5	12	10	4.0	3.8	3.8

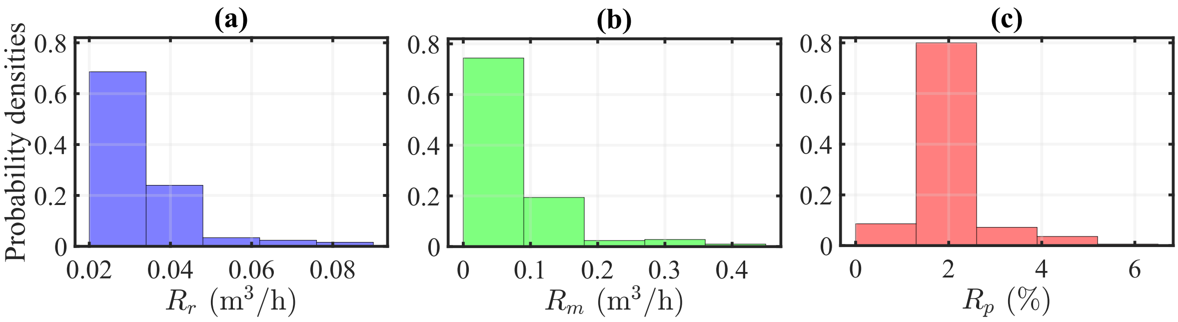

Figure 6.16: Distributions of residual metrics for the FO model constructed from the first set of the identified parameters. The remainders are calculated as the difference between the reference values, as in Figure 6.12 and the response of the FO model constructed from the first set of the identified parameters.

the lower range, approximately $(0.05–0.15)$ m^3/h, and then shows a narrow spread. This pattern reflects consistent absolute residuals across the all passes in the testing set. The MAP density (R_p) has the highest probability below $(2–3)\,\%$ with very low probabilities beyond $(4–6)\,\%$. This result indicates a small relative deviation of the estimated response using the FO model. All three distributions are right-skewed, with the highest probability concentrated at small values of residuals. This distribution pattern confirms the accuracy and consistency of the FO model under nominal operating conditions.

Figure 6.17 presents the probability densities R_r, R_m, and R_p for the nominal-FO model. These distributions were evaluated using 500 passes of the testing data.

The figure shows that the RMS residual R_r is concentrated within a narrow range, approximately $(0.02–0.06)$ m^3/h, and then decreases rapidly beyond 0.98 m^3/h. This indicates that the large quadratic residuals occur with low probability. The MA residual R_m shows an even tighter concentration near the smallest values, which reflects consistent absolute residuals across repeated evaluations. The MAP residual R_p has the highest probability below $2\,\%$, with very low probability above $4\,\%$. This observation indicates strong proportional agreement between the response of the nominal-FO model and the measured data. Therefore, it can be concluded that the nominal-FO model maintains small residual bounds and demonstrates stable performance across multiple realizations of the testing data.

The analysis of residual distributions for both cases of the FO models shows right-skewed distributions concentrated at low values, which confirms high accuracy. The nominal-FO model exhibits slightly tighter clustering for R_m and R_p, which indicates more consistent absolute and relative performance. These results demonstrate that the considered configurations of the FO model yield small residuals and maintain strong proportional accuracy. This outcome evidences the robustness of the FO modeling approach for flow rate estimation.

This section covers the successful implementation of the objectives **Obj.3** and **Obj.4** listed in Section 1.3. Moreover, it validates hypothesis **H.1** of the dissertation listed in

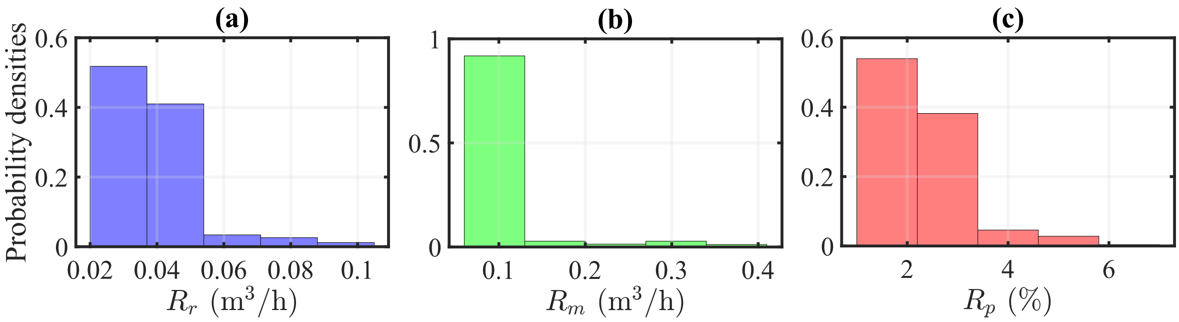

Figure 6.17: Distributions of residual metrics for the nominal-FO model. The remainders are calculated as the difference between the reference, as in Figure 6.12 and the response of the nominal-FO model.

Section 1.4. Finally, it also presents contribution **C.1** listed in Section 1.5.

6.6 Influence of the coefficient truncation order and solver selection

Although the results in the previous sections use the truncation order m with $m = 3$ for calculating the GL coefficients given in Eqs. (2.17) and (2.18) and use the IPOPT solver, the analysis requires further investigation. This section investigates the influence of the truncation order m on the accuracy of the nominal-FO model. Furthermore, it analyzes the effect of multiple solvers used to optimize the parameters of the FO model on the estimated response.

6.6.1 Influence of the truncation order

The selection of the truncation order m for the coefficients in the GL-DIE, as given in Eqs. (2.17) and (2.18), directly affects the computational effort. This section presents a comparison between different truncation orders and the resulting numerical errors. To quantify the influence of m m on both accuracy and Computation Time (CT), a randomly selected measurement pass was analyzed, and the corresponding results are reported in Table 6.5.

The errors are computed with respect to the mean values of the unprocessed testing data. The table shows that increasing the truncation order, while keeping the number of iterations fixed, generally reduces the approximation error in the FO model (6.8). However, choosing a higher value of m also increases the computational burden. The CT rises up to $m = 3$, which indicates slower convergence of the optimization algorithm. In this case, the algorithm requires additional time to complete the same number of iterations. For lower values of m, such as $m = 2$ and $m = 3$, convergence is faster. However, the approximation error remains relatively large. When the value of $m = 3$, the computation time decreases, which indicates an improved convergence behavior. In particular, the case $m = 5$ results in the lowest RMSE, as reported in Table 6.5.

These observations indicate that m introduces a trade-off between numerical accuracy and computational cost. Since Table 6.5 is based on a limited number of iterations, it cannot provide conclusive evidence that increasing m always leads to a lower objective value. To further analyze the influence of m on the estimated response, the FO model is evaluated for $m \in 1, 2, 3, 4, 5$. The results are reported in Tables 6.6 and 6.7. The maximum number of iterations for this analysis were set to 1000 for all cases. The comparison of the estimated responses and the respective residuals is also presented in Figures 6.18 and 6.19. To ensure clarity and avoid overlap of multiple curves, Figures 6.18 and 6.19 presents representative results for the selected cases $m = 1$, $m = 3$, and $m = 5$.

For $m = 1$, the estimated response exhibits a noticeable offset and a slower decay leading to poor estimation in both transient and steady-state regions. For $m = 3$ and $m = 5$, the differences between the estimated responses are small. However, the magnified view in the lower plot of Figure 6.18 shows oscillations in the steady state for $m = 5$. This behavior occurs because the optimization terminates after reaching the maximum number of iterations rather than satisfying the imposed constraints as mentioned in Table 6.6.

Table 6.7 shows the improvement in accuracy with increasing truncation order. For $m = 1$ and $m = 2$, the errors remain high, with $e_{\mathrm{r}} \approx 1.0\ \mathrm{m^3/h}$, $E_{\mathrm{m}} \approx 0.9\ \mathrm{m^3/h}$, and $E_{\mathrm{MAPE}} \approx 400\,\%$. This shows that the errors decrease significantly as m increases. The results in Table 6.7 present minimum values of $e_{\mathrm{r}} = 0.027\ \mathrm{m^3/h}$ for $m = 3$ and $m = 4$, the smallest $E_{\mathrm{m}} = 0.016\ \mathrm{m^3/h}$ at $m = 3$, and the lowest $E_{\mathrm{MAPE}} = 3.64\,\%$ at $m = 5$.

It is worth mentioning that the optimization procedure terminates prematurely for all cases except $m = 3$. Allowing additional iterations for higher values of m may improve the accuracy of the FO model parameters. However, increasing the number of iterations also adds to the computational cost.

These observations evidence a trade-off between numerical accuracy and computational cost. In this study, the choice $m = 3$ provides a suitable balance between these factors. For applications that require higher accuracy, adaptive tuning of the m during optimization may improve the estimation of dynamic response of the FO model in both transient and

Table 6.5: Influence of coefficient truncation order m on truncation errors and computation time analyzed for 100 iterations with a randomly selected pass optimized using AMPL-IDE on an `Intel(R) Core(TM) i7-1260P` CPU with 32 GB RAM.

m	e_{r} ($\mathrm{m^3/h}$)	E_{m} ($\mathrm{m^3/h}$)	E_{MAPE} (%)	CT (s)
2	3.2	1.9	21	676
3	3.1	1.7	17	1005
4	3.0	1.6	14	1685
5	1.8	0.47	7.5	1194
6	2.4	0.39	6.0	718

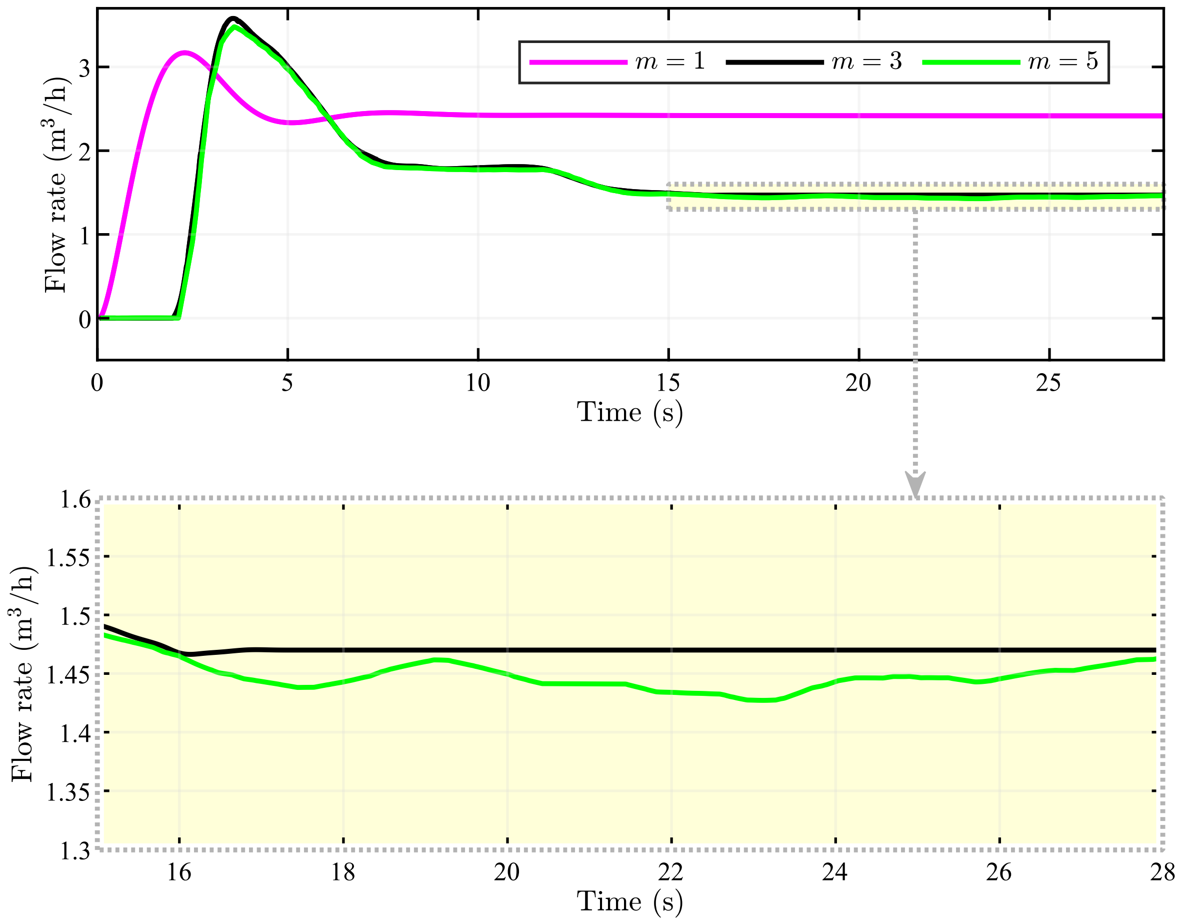

Figure 6.18: Comparison of estimated responses with different truncation orders (m) of the Grünwald-Letnikov derivative and integral on the optimization results.

steady-state regions.

6.6.2 Influence of optimization solvers in NEOS-server

The AMPL-IDE provides only one freely available solver, namely IPOPT. The NEOS-server offers a wider selection of AMPL-compatible solvers. From the eight solvers listed under nonlinear constrained optimization [151–153], this section selects `Knitro` and `filter` for benchmarking against the preselected `IPOPT`. These solvers were selected based on their

Table 6.6: Optimal parameters and solver error metrix with AMPL-based IPOPT solver in NEOS-server.

m	α	β	a	b	K	Status
1	1.04	1.01	0.001	0.002	0.001	maximum iterations reached
2	1.0	0.28	0.001	1.72	1.20	maximum iterations reached
3	1.83	0.28	0.001	1.49	1.50	constraints satisfied
4	1.20	0.31	0.001	1.18	4.11	maximum iterations reached
5	1.78	0.29	0.001	1.46	1.49	maximum iterations reached

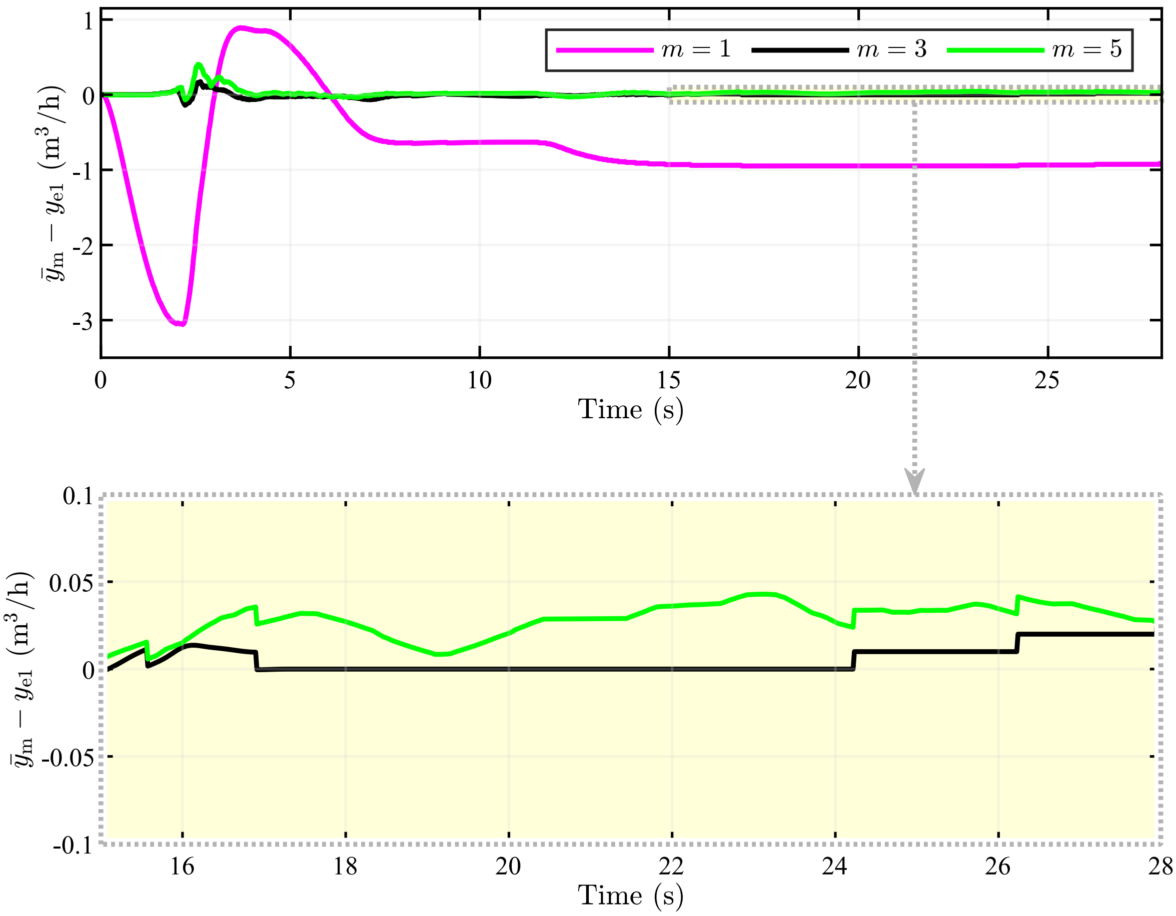

Figure 6.19: Residual comparison with different values of m.

reported computational efficiency and their established use in constrained optimization problems [14]. The corresponding estimated responses are shown in Figure 6.20.

Figure 6.20 compares the estimated responses obtained from FO models identified using IPOPT, `Knitro`, and `filter`. The model based on IPOPT accurately estimates the measured flow rate and yields small residuals that decay rapidly. The model obtained using `Knitro` achieves nearly zero residuals in the steady state. However, it exhibits moderate deviations during the transient region. In contrast, the model identified using `filter` underfits both the transient and steady-state responses and produces a persistent offset in

Table 6.7: Influence of coefficient Truncation Order (m) on truncation errors and Computation Time (CT) analyzed for full optimization (1000 iterations) with a randomly selected pass optimized using AMPL-based IPOPT solver in NEOS-server.

m	e_r (m^3/h)	e_m (m^3/h)	e_p (%)	CT (s)	Iterations
1	1.03	0.91	439	726	1000
2	1.0	0.88	414	887	1000
3	0.027	0.016	4.48	1497	957
4	0.027	0.027	4.26	1238	1000
5	0.049	0.031	3.64	1053	1000

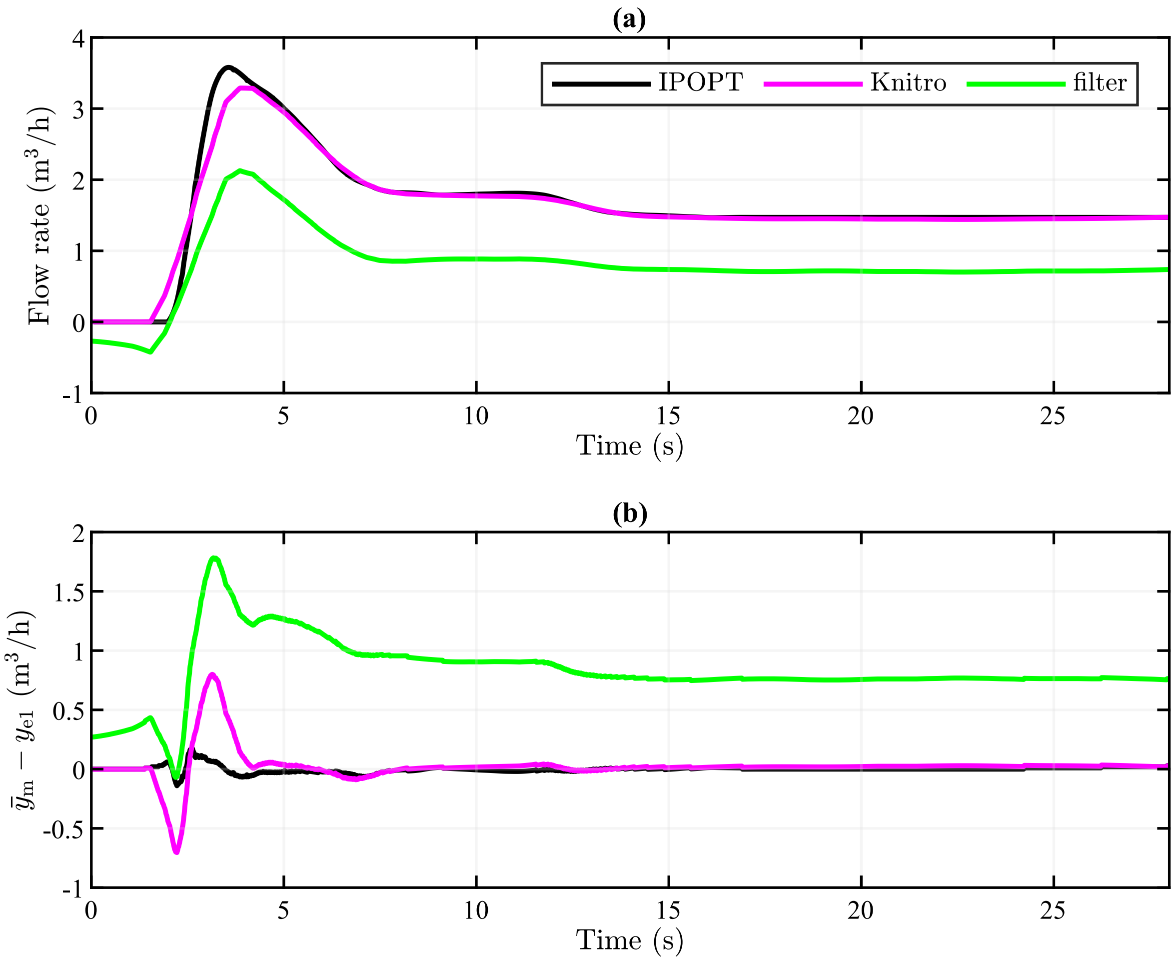

Figure 6.20: Comparison of the FO models constructed by optimizing with different AMPLE-based solvers available in NEOS-server: (a) shows the estimated response and (b) shows the corresponding residual.

the residuals. The optimization results and solver termination statuses reported in Table 6.8 explain these differences. The IPOPT terminates the optimization with the constraints satisfied. In contrast, `Knitro` reaches the maximum number of iterations. The `filter` solver exits with an unexpected failure status.

The error analysis presented in Table 6.9 provides further insight into the optimization results acquired with the selected solvers. The IPOPT solver achieves the lowest errors, with values $e_{\mathrm{r}} = 0.027$ m^3/h, $E_{\mathrm{m}} = 0.016$ m^3/h, and $E_{\mathrm{MAPE}} = 4.48\,\%$, and converges after 957 iterations. In contrast, the FO models identified using `Knitro` and `filter` exhibit significantly higher values of errors. The comparison of estimated responses, residual behavior, and numerical errors indicates that IPOPT offers the the most reliable performance for the considered problem. Despite the shorter CTs with `Knitro` and `filter`, the overall results support the selection of IPOPT as a suitable solver for this class of nonlinear constrained optimization problems. This section validates hypothesis **H.2** of the dissertation listed in Section 1.4.

Table 6.8: Performance comparison of AMPL-based solvers available with NEOS-server to solve the constrained nonlinear optimization problems. The optimized parameters, and the exit status of the optimization are analyzed for each solver. The maximum number of iterations were set to 1000.

Solver	α	β	a	b	K	Status
IPOPT	1.83	0.28	0.001	1.49	1.50	constraints satisfied
Knitro	1.3	0.17	0.001	1.48	0.14	maximum iterations reached
filter	1.5	0.19	0.001	1.54	0.14	unexpected ifail

Table 6.9: Numerical and computational efficiency of different solvers. The analysis was done with 1000 as maximum number of iterations for a randomly selected pass optimized using different AMPL-based solvers in NEOS-server.

Solver	e_r (m^3/h)	e_m (m^3/h)	e_p (%)	CT (s)	Iterations
IPOPT	0.027	0.016	4.48	1497	957
Knitro	0.51	0.68	292	64	1000
filter	0.48	0.68	309	12	1

6.7 Computational time for the optimization and solution

This section compares the computational time obtained using the two computational resources employed to identify the FO model. The analysis uses $m = 3$ and the IPOPT solver, with the maximum number of iterations set to 1000.

Two types of computational analysis was performed to compare the proposed FO model with the IO models. The first analysis evaluates the computational time required for to optimize the model parameters. The second analysis determines the time required to solve the FO-DIE in (6.8) to obtain the estimated response with the FO model. The optimization time is calculated using the training data and the average time for 79 passes is reported in Table 6.10. This section also evaluates the average computational time required to solve Eqs. (6.8) and (6.12) to (6.14) for comparison with the testing data. These results are reported in Table 6.11.

The optimization problem in Eq. (6.9) was solved using two computational environments: the offline AMPL-IDE and the online NEOS-server. The AMPL-IDE-based execution was implemented on a personal computer equipped with an `Intel(R) Core(TM) i7-1260P` processor and 32 GB of RAM. Table 6.10 presents the optimization times required for different model structures obtained with these tools.

The table shows that the optimization required for the FO model is approximately 4.8 times longer in the AMPL-IDE than on the NEOS-server. This difference is less pronounced for the IO models. The increased computational cost for the FO model arises from the recursive evaluation of the GL coefficients defined in Eqs. (2.17) and (2.18) during the numerical solution. Recursive computation of these coefficients at each iteration further increases the overall optimization time. This iteration-based recursive computation of the GL coefficients during the optimization procedure is clearly visible the flow chart presented in Figure 6.1. Compared with the third-order IO model with the same DOF, the time-delay model requires approximately three times less CT. To further investigate the computational cost, Table 6.11 reports the average time required to solve the dynamic models.

Table 6.10: Average computational time required to solve the optimization problem in Eq. (6.9) for for obtaining the optimal parameters of the dynamic models.

Model type	AMPL-IDE	NEOS-server
nominal-FO model	5160 s	1080 s
3^{rd}-order 6-DOF IO model	2.8 s	2.1 s
3^{rd}-order 5-DOF IO model	1.5 s	1.2 s
IO time-delay model	0.32 s	0.25 s

The FO and IO models were applied a 20 Hz input signal defined in Eqs. (6.6) and (6.12) to (6.14) using the optimized parameters shown in Figures 6.4 to 6.9. The simulations for this case were performed in `MATLAB R2024b` on a system equipped with an `Intel(R) Core(TM) i7-1260P` processor and 32 GB of RAM and the corresponding computational time was recorded. Table 6.11 reports the average values of these computational times.

The results show that the FO model requires the longest time to compute the estimated response, whereas the IO models require significantly less time. This increased the computational cost for the FO model arises from the recursive computation of the GL coefficients. Among the IO models, the 6-DOF model exhibits the highest computational cost. This behavior results from the presence of an additional integrator compared with the 5-DOF third-order model and the time-delay model. It is important to note that, despite a higher computational cost in simulation, solving the FO-DIE for the estimated response is substantially faster than the corresponding parameter optimization.

Although the optimization of the FO model requires substantially large computational effort, it provides a more accurate approximation of the system dynamics. The residual and error analyses presented in Figure 6.15 and Table 6.3 demonstrate the superior performance of the proposed FO model. Therefore, implementation of FO models involves a trade-off between computational cost and modeling accuracy. Since this study prioritizes accurate estimation of the dynamic response, use of the FO model is justified by its superior estimation performance.

Table 6.11: Average computational time required to solve the FO-DIE Eq. (6.8) in MATLAB for performance comparison of nominal-FO model with the experimental data.

Model type	Computation time (s)
nominal-FO model	0.18
3^{rd}-order 6-DOF IO model	0.094
3^{rd}-order 5-DOF IO model	0.088
IO time-delay model	0.065

In engineering practice, systems that exhibit memory effects or whose dynamics originate from spatially distributed components often display FO behavior. In contrast, FO modeling is generally inappropriate for systems with well-defined dynamics that can be accurately estimated using IO-DIEs. Moreover, the applicability of the proposed FO model is limited in real-time applications with strict computational constraints. In such cases, the numerical complexity associated with FO operators can introduce practical implementation challenges.

6.8 Chapter summary

This chapter presented a FO modeling approach for a laboratory flow rate measurement system exhibiting nonlinear dynamics, measurement uncertainty, and variable sampling intervals. The chapter developed a black-box identification framework based on the Grünwald-Letnikov formulation of FO-DIE to obtain a compact dynamic model that accurately represents the system behavior. The model identification task was formulated as an optimization problem, and the model parameters were estimated directly from experimental data. The presented approach accounts for measurement uncertainty while preserving the dynamic characteristics of the system.

To improve computational efficiency, the optimization problem was implemented in AMPL and solved using NEOS-server, an online optimization platform. The procedure first preprocesses experimental data from repeated measurements to reduce measurement noise and variability. It then divides the preprocessed data into training and testing datasets. The training dataset comprises preprocessed data from 79 passes. The study uses this dataset to identify the optimal parameters of the FO model. The procedure executes the optimization over 79 passes and averages the resulting optimal parameters. It then constructs the nominal-FO model using these averaged parameters. The FO model constructed using this approach is validated using unseen raw measurement data. Its robustness is further assessed through parametric sensitivity analysis under controlled perturbations. The results demonstrate stable and reliable performance despite moderate variations in the parameters of the nominal-FO model.

A comparative analysis with classical IO models evidences that the proposed FO model provides superior estimation of the dynamic response. This improvement is particularly evident during the transient region of operation. The model achieves significant reductions in root mean square error, mean absolute error, and mean absolute percentage error, which confirms its improved accuracy. The residual analysis further indicates reduced error distributions and enhanced robustness. These results demonstrate the effectiveness of FO modeling as a reliable and accurate framework for the identification of flow systems.

This chapter validates the hypotheses **H.1** and **H.2** listed in Section 1.4. Furthermore, it presents the contribution **C.1** listed in Section 1.5.

Chapter 7

FO controller design

This chapter proposes simple tuning rules for FO-PI controller parameters based on frequency-domain methods. The approach avoids excessive complexity while maintaining the benefits of fractional dynamics. Furthermore, it compares three approximation methods to enable practical realization of the controller. The FO-PI controller is then applied to the nonlinear MIMO TRAS to analyze the effectiveness of the proposed approach. Finally, it compares the controller design obtained through the proposed approach with a FO-PID controller to demonstrate the improved smoothness of tracking and more favorable behavior for long-term hardware operation.

The contents of this chapter are based on the published article [145]. Moreover, the findings presented in this chapter demonstrate the successful implementation of **Obj.5** listed in Section 1.3.

7.1 Control design approach

Classical frequency-domain methods have enabled the development of tuning rules for FO-PID [133–136]. These methods support the design of FO controllers that achieve the desired dynamic responses in several applications. These approaches impose gain and phase constraints on the open-loop frequency response [135, 136]. However, they do not include a condition on the derivative at the gain crossover frequency. This omission reduces robustness to loop-gain variations in numerous practical systems.

Zheng et al. [134] addressed this limitation by introducing an additional condition to improve robustness. However, it requires an optimization procedure that minimizes the closed-loop error. This requirement increases computational complexity and complicates the design process. This mutation diminishes the main advantages of frequency-domain methods by limiting their simplicity and direct applicability in engineering practice.

To address the said limitation, this section presents simple tuning rules for the FO-PI controller using classical frequency-domain methods. The proposed approach derives results for a linear SISO TF with three poles and no zeros. However, its applicability and performance are verified on a nonlinear MIMO TRAS.

7.1.1 Tuning rules for fractional-order PI controllers

Consider $G(s)$ and $C(s)$ denote the TFs of the plant and the controller, respectively. The feedback control system is constructed such that it provides a closed-loop $G_{\text{cl}}(s)$ as

$$G_{\text{cl}}(s) = \frac{G(s)C(s)}{1 + G(s)C(s)}. \tag{7.1}$$

The open-loop TF of the same control system, denoted by $L(s)$, is

$$L(s) = G(s)C(s), \tag{7.2}$$

where the TF of the FO-PI controller can be defined by $C(s)$ as

$$C(s) = k_{\mathrm{p}} + k_{\mathrm{i}} \cdot \frac{1}{s^{\lambda}}. \tag{7.3}$$

The parameters of the controller k_{p}, k_{i}, and λ denote the proportional and integral gains, and the order of the FO integral, respectively.

The specified time-domain requirements, namely peak overshoot, settling time, and steady-state error, can be translated into the corresponding frequency-domain characteristics. This transformation simplifies subsequent controller design. The controller parameters can then be determined by enforcing magnitude and phase conditions by following the Bode representation of Eq. (7.2) as [136]:

$$|C(j\omega_{\mathrm{gc}}) \cdot G(j\omega_{\mathrm{gc}})| = 1, \tag{7.4}$$

and

$$\varphi = \angle\big(C(j\omega_{\mathrm{gc}})\, G(j\omega_{\mathrm{gc}})\big) = -\pi + \varphi_{\mathrm{m}}, \tag{7.5}$$

where ω_{gc} represents the gain crossover frequency and φ_{m} denotes the desired phase margin.

This section structures the problem to find three parameters of a FO-PI controller, i.e., k_{p}, k_{i}, and λ, using Eqs. (7.4) and (7.5) by imposing an additional constraint for the desired phase margin φ_{m} at the gain crossover frequency ω_{gc}. The introduced constraint is

$$\frac{d\varphi(\omega_{\mathrm{gc}})}{d\omega_{\mathrm{gc}}} = 0. \tag{7.6}$$

This addition ensures phase flatness around the gain crossover frequency ω_{gc}, which enhances controller robustness to limited variations in the open-loop parameters. Furthermore, it also provides the possibility of solving three equations, Eqs. (7.4) to (7.6), for three unknowns (k_{p}, k_{i}, and λ). This formulation increases the likelihood of a unique solution within the search space.

7.1.2 Calculating parameters of the controller

Consider a TF with three poles and no zeros as

$$G(s) = \frac{a}{s^3 + b_1 s^2 + b_2 s + b_3}. \tag{7.7}$$

The design approach uses the specified closed-loop time-domain performance indices defined by the settling time t_{set} and the percent peak overshoot P_{o} The objective is to determine the parameters of the FO-PI controller in Eq. (7.3) to satisfy the closed-loop performance criteria.

The phase margin and the natural frequency of the system can be determined from t_{set} and P_{o} using standard second-order system relationships as [164]

$$\begin{aligned} P_{\text{o}} &= e^{-\pi\zeta/\sqrt{1-\zeta^2}}, \\ t_{\text{set}} &\approx \frac{4}{\zeta \cdot \omega_n}, \\ \varphi &= \tan^{-1}\left(\frac{2\zeta\sqrt{(4-\zeta^2)}}{1-4\zeta^2}\right), \end{aligned} \tag{7.8}$$

where ω_{n} and ζ denote the natural frequency and damping ratio of the system described by $G(s)$, respectively. In a later step, $s = j\omega_{\text{gc}}$ is substituted into Eqs. (7.3) and (7.7), and the resulting expressions are inserted into Eq. (7.4), which yields the following simplified form:

$$\left(k_{\text{p}} + k_{\text{i}} \cdot \omega_{\text{gc}}^{-\lambda} \cdot \cos(\lambda\pi/2)\right)^2 + \left(k_{\text{i}} \cdot \omega_{\text{gc}}^{-\lambda} \cdot \sin(\lambda\pi/2)\right)^2 = M_{v1}, \tag{7.9}$$

where

$$M_{v1} = \frac{(-b_1 \cdot \omega_{\text{gc}}^2 + b_3)^2 + (-\omega_{\text{gc}}^3 + b_2 \cdot \omega_{\text{gc}})^2}{a^2}.$$

The Euler's identity

$$\frac{1}{(j\omega)^\alpha} = \omega^{-\alpha} \cdot e^{-j\frac{\pi}{2}\alpha}$$

plays a crucial role in deriving Eq. (7.9).

Similarly, the following relation can be derived from the phase condition presented in Eq. (7.5)

$$\left(\frac{-k_{\text{i}} \cdot \omega_{\text{gc}}^{-\lambda} \cdot \sin(\lambda\pi/2)}{k_{\text{p}} + k_{\text{i}} \cdot \omega_{\text{gc}}^{-\lambda} \cdot \cos(\lambda\pi/2)}\right) - P_{v_1} = -\tan(\pi) + \tan(\varphi_{\text{m}}), \tag{7.10}$$

where

$$P_{v1} = \frac{-\omega_{\text{gc}}^3 + b_2 \cdot \omega_{\text{gc}}}{-b_1 \cdot \omega_{\text{gc}}^2 + b_3}.$$

From Eq. (7.10), the phase angle of the open-loop system can be obtained as

$$\varphi(\omega_{\text{gc}}) = \tan^{-1}\left(\frac{-k_{\text{i}} \cdot \omega_{\text{gc}}^{-\lambda} \cdot \sin(\lambda\pi/2)}{k_{\text{p}} + k_{\text{i}} \cdot \omega_{\text{gc}}^{-\lambda} \cdot \cos(\lambda\pi/2)}\right) - \tan^{-1}(P_{v1}). \tag{7.11}$$

Substituting Eq. (7.11) into Eq. (7.6) and simplifying the calculations results in the following expression:

$$\frac{\lambda \cdot k_{\mathrm{i}} \cdot k_{\mathrm{p}} \cdot \omega_{\mathrm{gc}}^{-\lambda-1} \cdot \sin(\lambda\pi/2)}{[k_{\mathrm{p}} + k_{\mathrm{i}} \cdot \omega_{\mathrm{gc}}^{-\lambda} \cdot \cos(\lambda\pi/2)]^2 + [k_{\mathrm{i}} \cdot \omega_{\mathrm{gc}}^{-\lambda} \cdot \sin(\lambda\pi/2)]^2} = D_{v1}, \tag{7.12}$$

where

$$D_{v1} = \frac{b_1 \cdot \omega_{\mathrm{gc}}^4 - 3b_3 \cdot \omega_{\mathrm{gc}}^2 + b_1 b_2 \cdot \omega_{\mathrm{gc}}^2 + b_2 b_3}{(-b_1 \cdot \omega_{\mathrm{gc}}^2 + b_3)^2 + (-\omega_{\mathrm{gc}}^3 + b_2 \cdot \omega_{\mathrm{gc}})^2}.$$

For a system with a known TF, the parameter values and the corner frequency remain specified. Therefore, three simultaneous equations Eqs. (7.9), (7.10) and (7.12) can be solved to determine the three unknown parameters k_{p}, k_{i}, and λ of the FO-PI controller in Eq. (7.3).

7.1.3 Pitch and yaw control of TRAS

To demonstrate the simplicity and effectiveness of the proposed method, the approach is applied to the nonlinear model of the TRAS in Eqs. (3.4) and (3.5) presented in Chapter 3, Section 3.2.1. Two FO-PI controllers are designed independently using the decoupled TFs $G_p(s)$ Eq. (3.8) and $G_y(s)$ Eq. (3.9), associated with pitch and yaw angles, respectively.

By specifying the time-domain performance indices as $t_{\mathrm{set}} = 15$ s and $P_{\mathrm{o}} = 2\,\%$, the corresponding frequency-domain characteristics are computed using Eq. (7.8). Subsequently, Eqs. (7.9), (7.10) and (7.12) are solved simultaneously to calculate the controller parameters k_{p}, k_{i}, and λ.

7.2 Solution of simultaneous equations and controller parameters

This section presents a procedure to solve the simultaneous equations, Eqs. (7.9), (7.10) and (7.12), and lists the parameters of FO-PI controllers for TRAS. Furthermore, it presents the controller parameters used for performance comparison of the proposed approach.

The system of equations, Eqs. (7.9), (7.10) and (7.12), is coupled, and its dependence on the parameters k_p, k_i, and λ exhibits strong nonlinearity. Therefore, these equations are solved numerically using the `Optimization Toolbox` in `MATLAB R2024b` with the `lsqnonlin` routine. The solution of equations for the pitch angle controller $C_\phi(s)$ required 1.58 s on an `Intel(R) Core(TM) i7-1260P` processor. The parameters of the yaw angle controller $C_\psi(s)$ were computed in 1.12 s using the same hardware. In both cases, the solver converged in iterations fewer than 30, and the residuals of all equations remained below 10^{-10}. The parameters for the pitch and yaw controllers obtained following this procedure are listed in Table 7.1.

The table shows that the order of the FO integral for the pitch angle controller is close to 1. However, the corresponding value for the yaw controller deviates significantly from 1. The tuning rules adopt an analytical approach; therefore, these parameters vary with different desired time-domain characteristics. Nonetheless, both FO controllers operate in closed loop with the plant to assess the performance of the proposed tuning method.

To validate the performance of the controllers designed using the proposed tuning rules, this chapter compares the closed-loop response of the FO-PI controller with two other controllers. The controllers used for comparison are:

1. The IO-PID controller with parameters tuned using the `pidtune` function available in the Control System Toolbox in `MATLAB` [179], and
2. The FO-PID controllers designed for pitch and yaw control of the TRAS presented in [144].

The parameters of these controllers are listed in Table 7.2.

7.3 Results and discussion

This section presents the Bode diagrams of the open-loop TF Eq. (7.2), the closed-loop step responses, and the closed-loop performance comparison of the FO-PI controller with the IO-PID and FO-PID controllers under realistic reference signals. Furthermore, it presents the analysis of control efforts to ensure the desired performance of each controller.

The controller TFs are realized using three different approximation methods, namely OM in Eq. (2.45), MM in Eq. (2.30), and CA in Eq. (2.48). The approximation order is set to $N_{\mathrm{F}} = 5$, and the realizations are performed for the frequency range $[\omega_b,\ \omega_h] = [0.01,\ 1000]$ for all methods. The resulting approximated controller TFs of $C_\phi(s)$ and $C_\psi(s)$ are then utilized with pitch and yaw TFs denoted by $G_p(s)$ Eq. (3.8) and $G_y(s)$ Eq. (3.9), respectively, for Bode diagram analysis of the open-loop TF Eq. (7.2). Furthermore, the step responses for the yaw and pitch angles in the closed loop using the same TFs is evaluated over a time duration of 100 s.

7.3.1 Analysis of Bode plots

This section analyzes the Bode plots of the open-loop TFs for the pitch and yaw angles using the respective controller TFs approximated with OM, MM, and CA. The Bode diagram for compensated pitch angle, i.e., $C_\phi(s)G_p(s)$, is presented in Figure 7.1. It illustrates that all approximations exhibit different magnitudes and phases at low frequencies. The magnitude and phase responses above 10^{-2} rad/s become similar for OM and MM. However,

Table 7.1: Parameters of the FO-PI controllers designed with the proposed approach.

Controller	k_{p}	k_{i}	λ
$C_\phi(s)$	1.0972	0.2948	0.9978
$C_\psi(s)$	0.3580	0.0100	0.9220

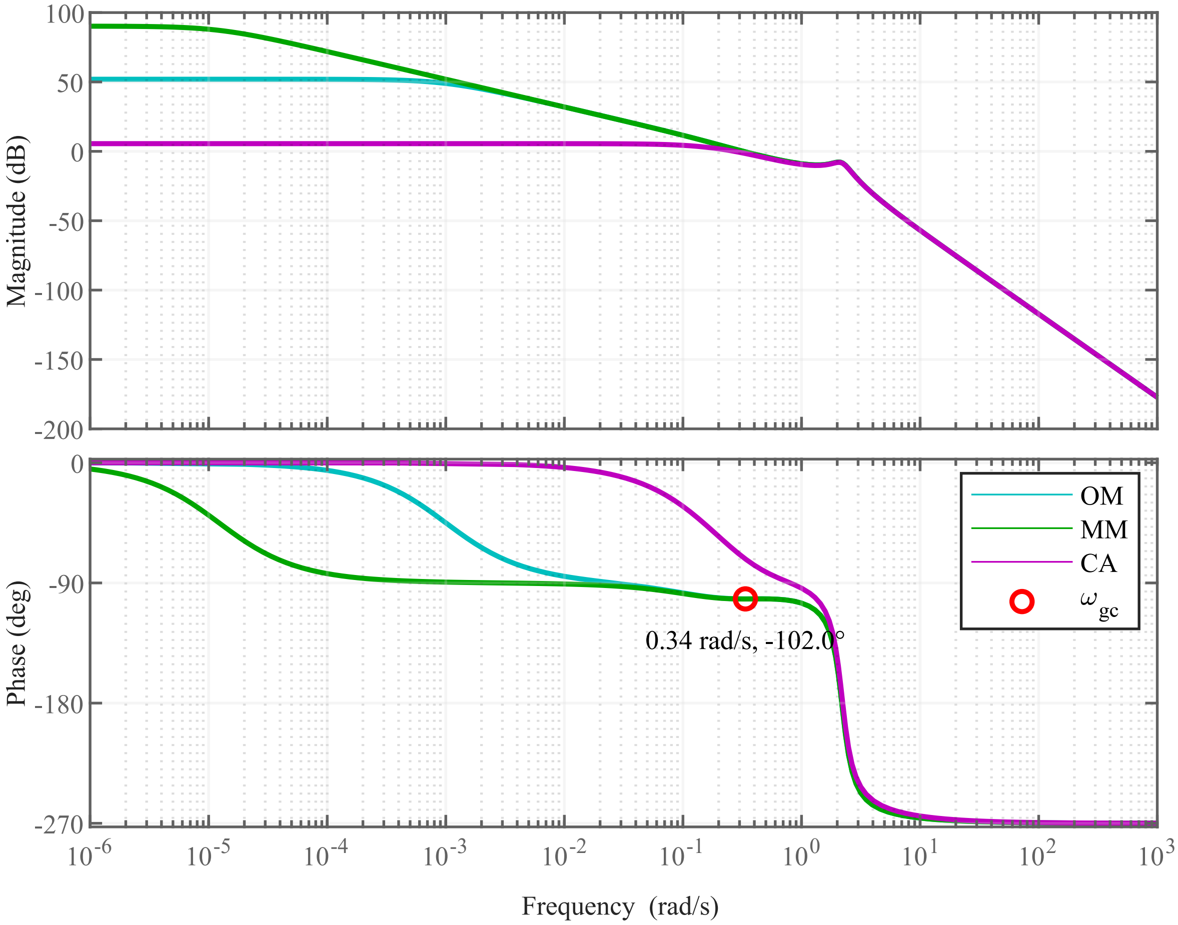

Figure 7.1: Bode plot of the open-loop transfer function of pitch angle with the corresponding FO-PI controller.

the magnitude and phase responses for CA become similar to OM and MM only well beyond the gain crossover angular frequency ω_{gc}.

Furthermore, a nearly constant phase in the vicinity of the gain crossover frequency can be observed in Figure 7.1. The phase remains approximately flat at $-102°$ around 0.34 rad/s, which indicates robust behavior of the pitch controller implemented using the Oustaloup

Table 7.2: Parameters of IO and FO-PID controllers used for comparison.

Controller	k_p	k_i	λ	k_d	μ
PID controllers designed using `pidtune.m`					
$C_\phi(s)$	1.5761	0.7155	–	0.4900	–
$C_\psi(s)$	0.7282	0.0607	–	0.8101	–
FO-PID controllers [144]					
$C_\phi(s)$	2.2709	7.2444	0.7744	8.1717	0.9380
$C_\psi(s)$	2.6101	0.6675	0.2190	4.8659	0.9488

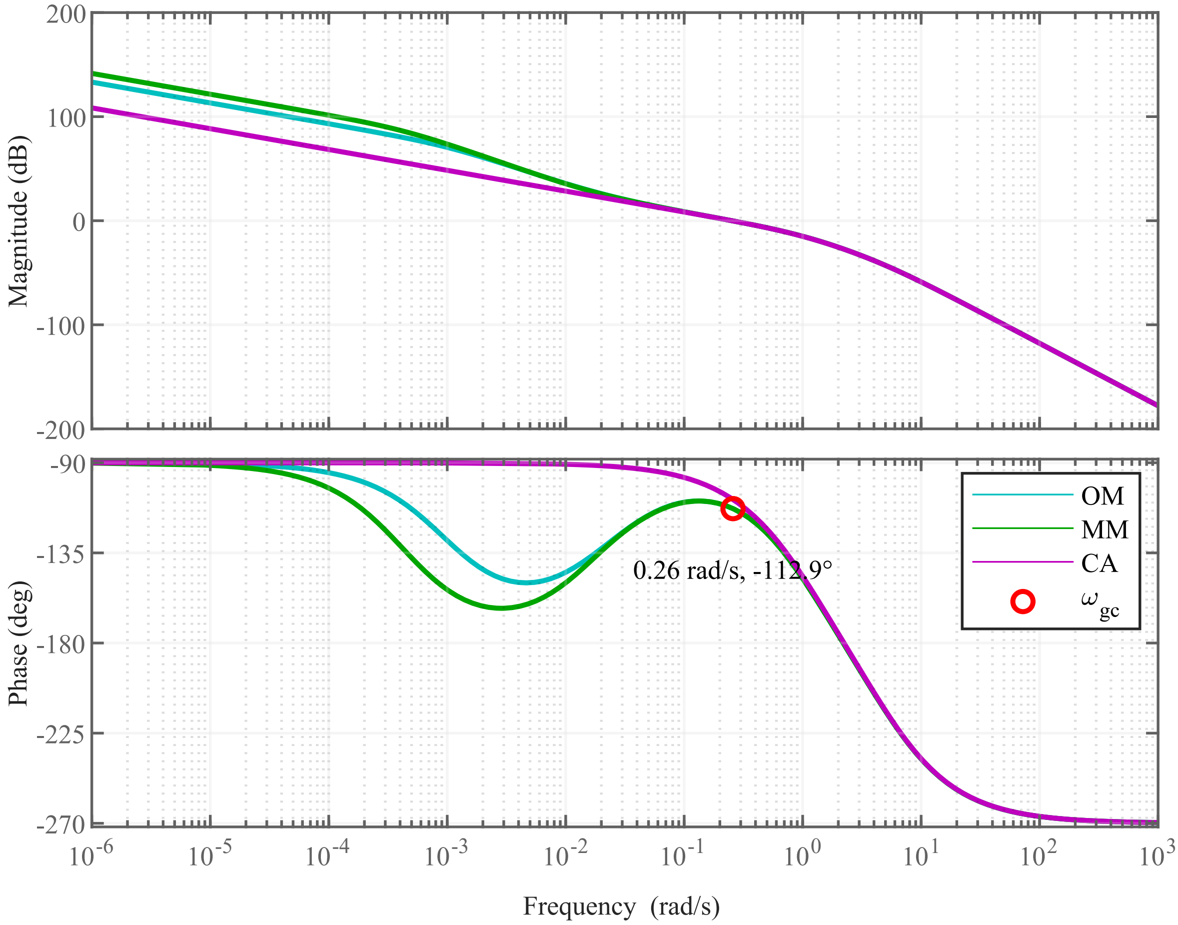

Figure 7.2: Bode plot of the open-loop transfer function of yaw angle with the corresponding FO-PI controller.

and Matsuda approximation methods. In an ideal case, the phase should remain constant at $-90^\circ \times 0.9978 = -89.2^\circ$. However, the approximation methods used to realize the controller TF lead to a deviation, resulting in a phase value of -102°. This phase flatness improves disturbance rejection capability, increases robustness to parameter variations, and ensures smoother control action. Smooth control signals reduce mechanical stress on actuators, whereas oscillatory behavior may cause wear and degradation in practical systems.

The Bode diagram of the open-loop TF for the yaw angle is presented in Figure 7.2. A pattern similar to Figure 7.1 is observed at low frequencies for different approximations. All the approximations exhibit different magnitudes and phases in this frequency range.

In contrast to the pitch angle case, phase flatness around the gain crossover frequency is not clearly evident. This behavior may result from strict time-domain design specifications, namely $2\,\%$ peak overshoot and 15 s settling time t_{set}. Since the yaw response of the TRAS is slower than the pitch response [146], relaxing these design specifications can produce a constant phase over a wider frequency range. However, even with the current design requirements, the phase variation on the left side of the gain crossover frequency remains very small for OM and MM.

7.3.2 Closed-loop step response

The closed-loop TF defined in Eq. (7.1) is constructed for the pitch and yaw angles using the respective TFs with controller realizations based on OM, MM, and CA. The individual closed-loop TFs for the pitch and yaw angles were excited with unit step inputs. The outputs were observed over 100 s, and the corresponding results for different approximation methods are presented in Figure 7.3. panel (a) depicts the unit step response of the closed-loop system for the pitch angle. panel (b) shows the corresponding response for the yaw angle.

The figure illustrates that the Oustaloup and Matsuda approximations exhibit nearly identical behavior, as indicated by their overlapping responses. In contrast, the Charef approximation introduces a steady-state error of approximately 40%. The settling time remains within 15 s for all the approximations, and each method produces the response with decaying oscillations. However, the step response of yaw angle with the CA appears more favorable compared with OM and MM. This improvement is not a result of accurate realization with CA. Rather, the closed-loop characteristics of the yaw controller are more effectively captured by OM and MM. This observation is supported by their closely overlapping responses both in pitch and yaw angles.

The degraded performance of CA for the pitch angle arises from the value of λ being very close to unity (Table 7.1), which corresponds to a pure integrator. The Charef approximation distributes pole-zero pairs logarithmically, as given in Eq. (2.49). Under this placement, the operator $1/s^{0.9978}$ closely approximates an ideal integrator. With a lower approximation order, this representation produces a steeper phase slope, as observed in Figure 7.1. To achieve an improved response in such cases, CA requires a significantly higher value of the approximation order N_{F} than 5.

7.3.3 Performance analysis of the proposed approach

This section presents a comparison of the FO-PI controller with the IO and FO PID controllers.

The FO-PI controllers were realized using three approximation methods, namely OM, MM, and CA. In contrast, the FO-PID controller was realized only using OM. The parameters of the FO-PI controllers are presented in Table 7.1. The parameters of the controllers used for comparison are listed in Table 7.2. The performance comparison of the controllers was analyzed by applying them in closed loop with the nonlinear model of TRAS Eqs. (3.4) and (3.5), as shown in Figure 4.8.

Reference trajectory

The reference trajectory used to compare the closed-loop performance is generated as follows.

- Initially, the reference values of pitch ϕ_{r} and yaw ψ_{r} are zero for 5 s.

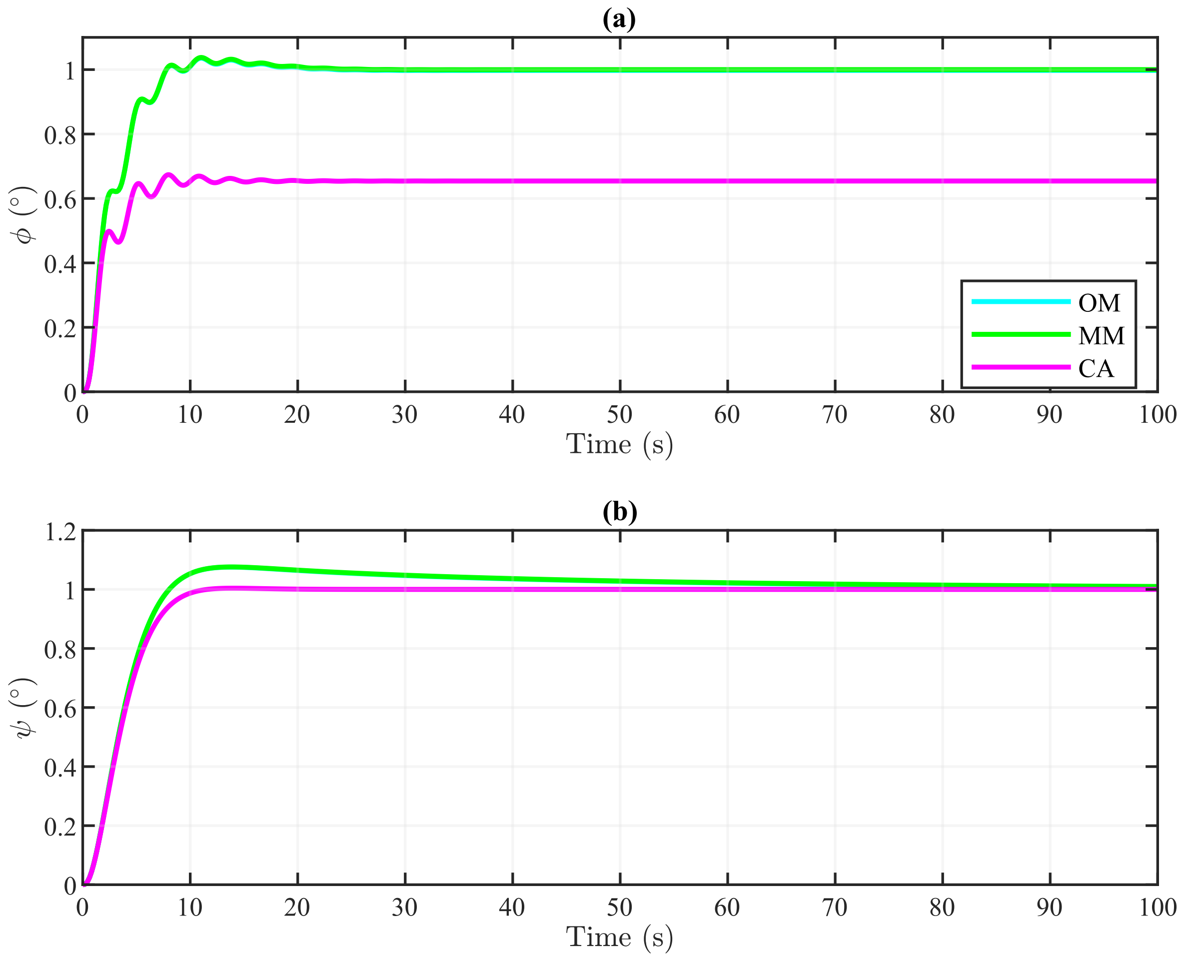

Figure 7.3: Step response of the closed-loop system: (a) shows the pitch angle response and (b) shows the yaw angle response.

- The reference value of pitch angle changes from $0°$ to $15°$ at $t = 5$ s and remains at this angle for the next 55 s.
- At $t = 20$ s, when $\phi_r = 15°$, the reference value of yaw angle ψ_r changes from $0°$ to $30°$ and remains constant for the next 60 s.
- At $t = 60$ s, when $\phi_r = 30°$, ϕ_r increases from $15°$ to $31°$ and remains constant for the next 60 s.
- At $t = 80$ s, when $\phi_r = 31°$, ψ_r increases from $30°$ to $57°$ and remains constant for the next 60 s.
- At $t = 120$ s, when $\psi_r = 57°$, ϕ_r decreases from $31°$ to $21°$ and remains constant for the next 60 s.
- At $t = 140$ s, when $\phi_r = 21°$, ψ_r decreases from $57°$ to $17°$ and remains constant for the next 60 s.
- At $t = 180$ s, when $\psi_r = 17°$, ϕ_r decreases from $21°$ to $5°$ and remains constant at this value.
- At $t = 200$ s, when $\phi_r = 5°$, ψ_r increases from $17°$ to $32°$ and remains constant at this value for the remaining time.

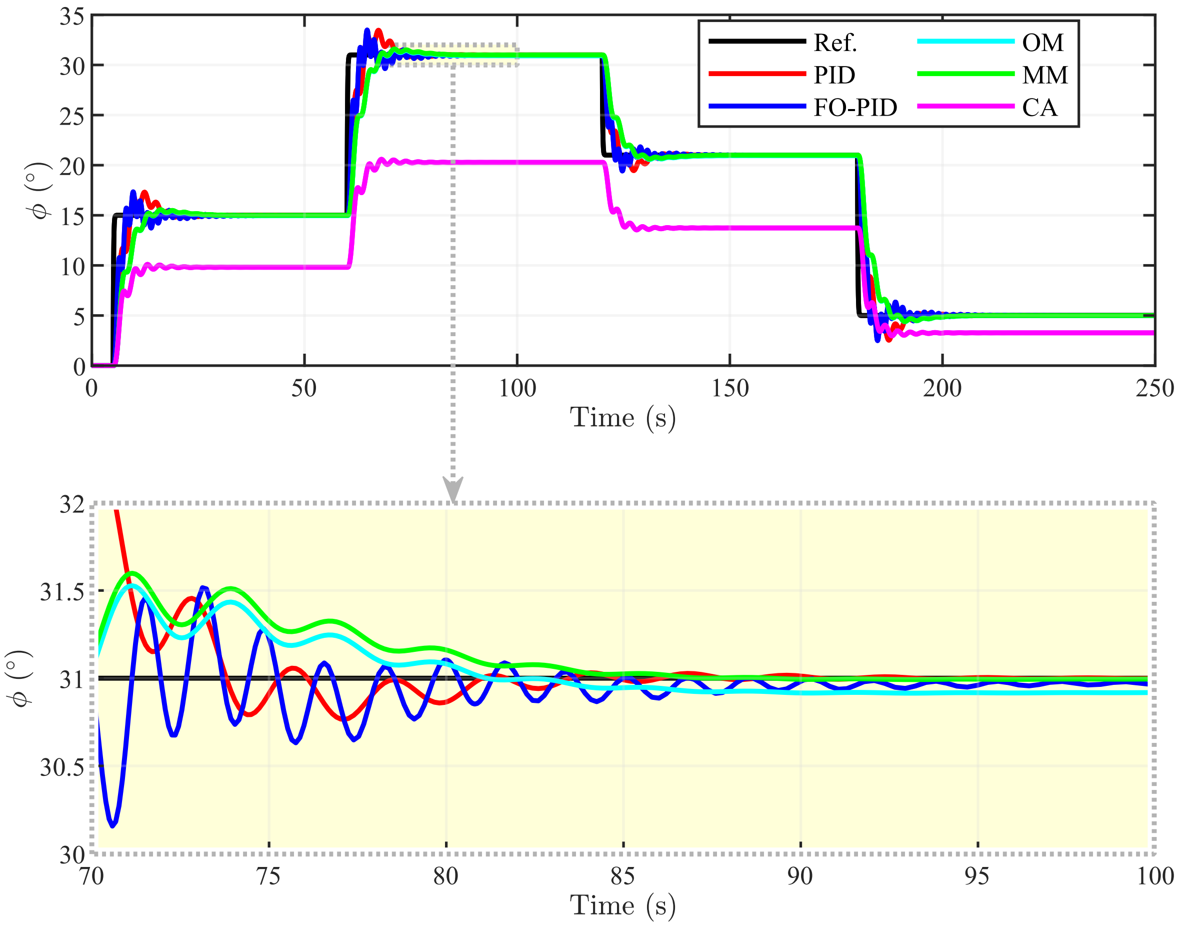

Figure 7.4: Reference tracking comparison for pitch angle using the proposed controllers realized through different approximations with the FO-PID controller presented in [144].

This step-based alternating reference trajectory of pitch and yaw angles allows a systematic evaluation of the robustness of the proposed approach.

Reference tracking

Figure 7.4 shows the reference tracking comparison of the controller designed using the proposed tuning rules with the IO and FO PID controllers for the pitch angle. The figure shows that the IO and FO PID controllers achieve better reference tracking than the FO-PI controllers approximated using OM, MM, and CA. The FO-PI controller approximated using CA exhibits the largest tracking error throughout the simulation and thus provides the lowest tracking accuracy. The FO-PI controllers realized using OM and MM improve tracking compared to CA but exhibit a longer delay in reaching the reference value at each step.

Although the IO and FO PID controllers ensure fast tracking, this response introduces high-frequency oscillations in the closed-loop response. Furthermore, these controllers exhibit larger overshoot magnitudes than the FO-PI controllers realized using OM and MM. These high-frequency oscillations are clearly visible in the zoomed section of the lower panel in Figure 7.4.

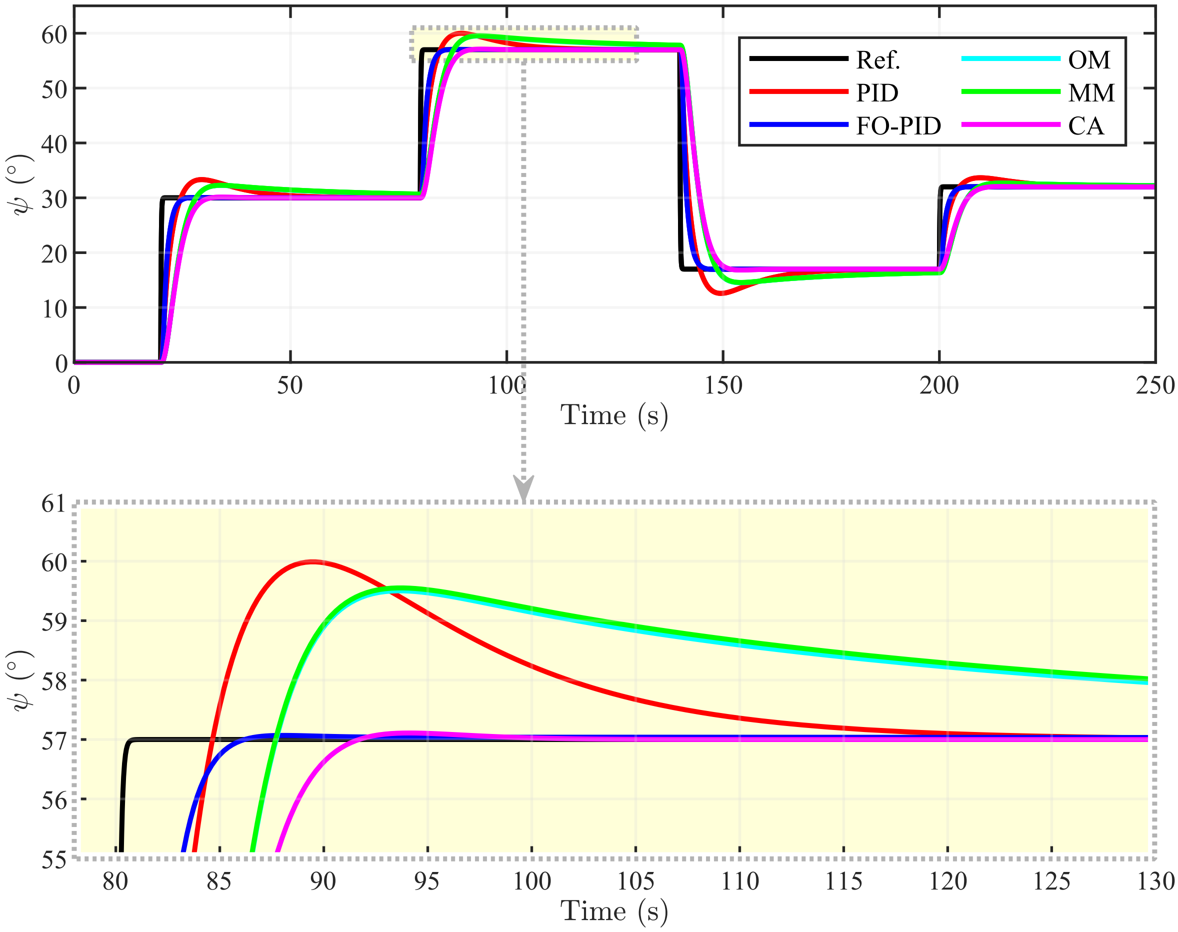

Figure 7.5: Reference tracking comparison for yaw angle using the proposed controllers realized through different approximations with the FO-PID controller presented in [144].

Figure 7.5 presents the reference tracking comparison for the yaw angle ψ. The figure shows that the FO-PID controller outperforms the IO-PID and FO-PI controllers realized with all three approximation methods. The FO-PI controller realized using CA provides the second-best reference tracking performance. The FO-PI controllers realized using OM and MM exhibit overshoot in the closed-loop response. Although the overshoot magnitude is lower than that of the IO-PID controller, it persists for a longer duration than in the IO-PID case. This comparison appears more clearly in the zoomed view in the lower panel of Figure 7.5.

Furthermore, in contrast to the pitch angle response in Figure 7.5, no high-frequency oscillations appear in the yaw angle reference tracking. This behavior results from slower yaw dynamics compared to the pitch response. Therefore, the controllers are able to track the yaw reference trajectory smoothly.

Control efforts

The control signals driving the actuators (DC motors) directly influence the durability of the hardware setup. Therefore, a complete control system analysis requires the assessment of the

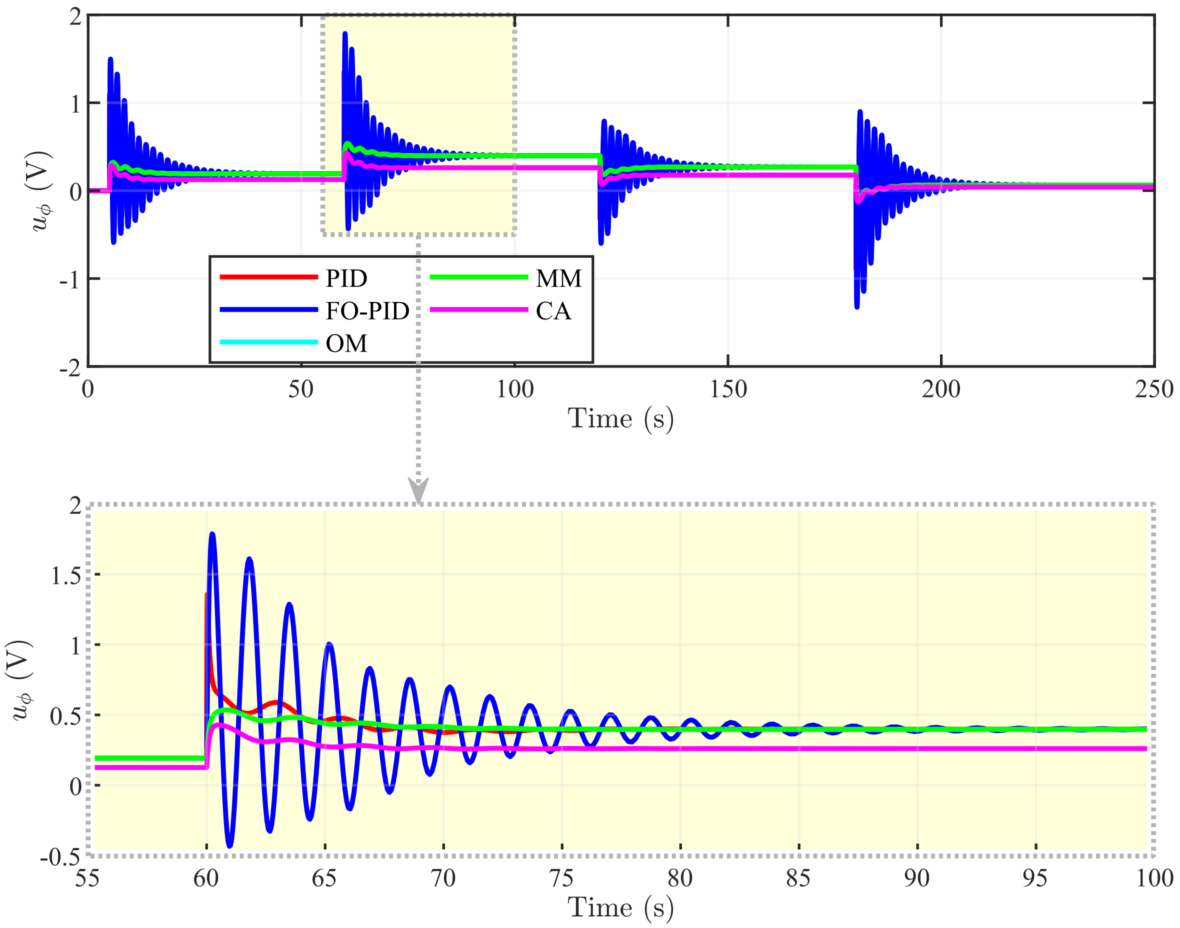

Figure 7.6: Comparison of the control efforts corresponding to the reference tracking of pitch angle shown in Figure 7.4.

control efforts generated by the controllers that ensure the desired closed-loop performance. Figure 7.6 shows the control efforts of all controllers corresponding to the closed-loop performance presented in Figure 7.4.

Figure 7.6 shows that the control effort required for reference tracking of the pitch angle ϕ is lowest for the FO-PI controller realized using CA. This result makes it favorable from the control input perspective. However, as shown in Figure 7.4, the FO-PI controller realized using this method exhibits the poorest tracking performance. In contrast, the IO and FO PID controllers achieve good reference tracking, but their control efforts have large amplitudes and high-frequency oscillations. These oscillations impose a direct burden on the motor driving the main rotor responsible for pitch elevation. Therefore, persistent oscillations, especially with the FO-PID controller, may cause wear and mechanical damage in the hardware over time.

In contrast, the control efforts for pitch angle tracking with the FO-PI controllers realized using OM and CA exhibit negligible oscillations and have similar magnitudes. The magnitudes are also lower than those of the IO and FO PID controllers. Furthermore, the FO-PI controllers realized using these methods provide good tracking performance.

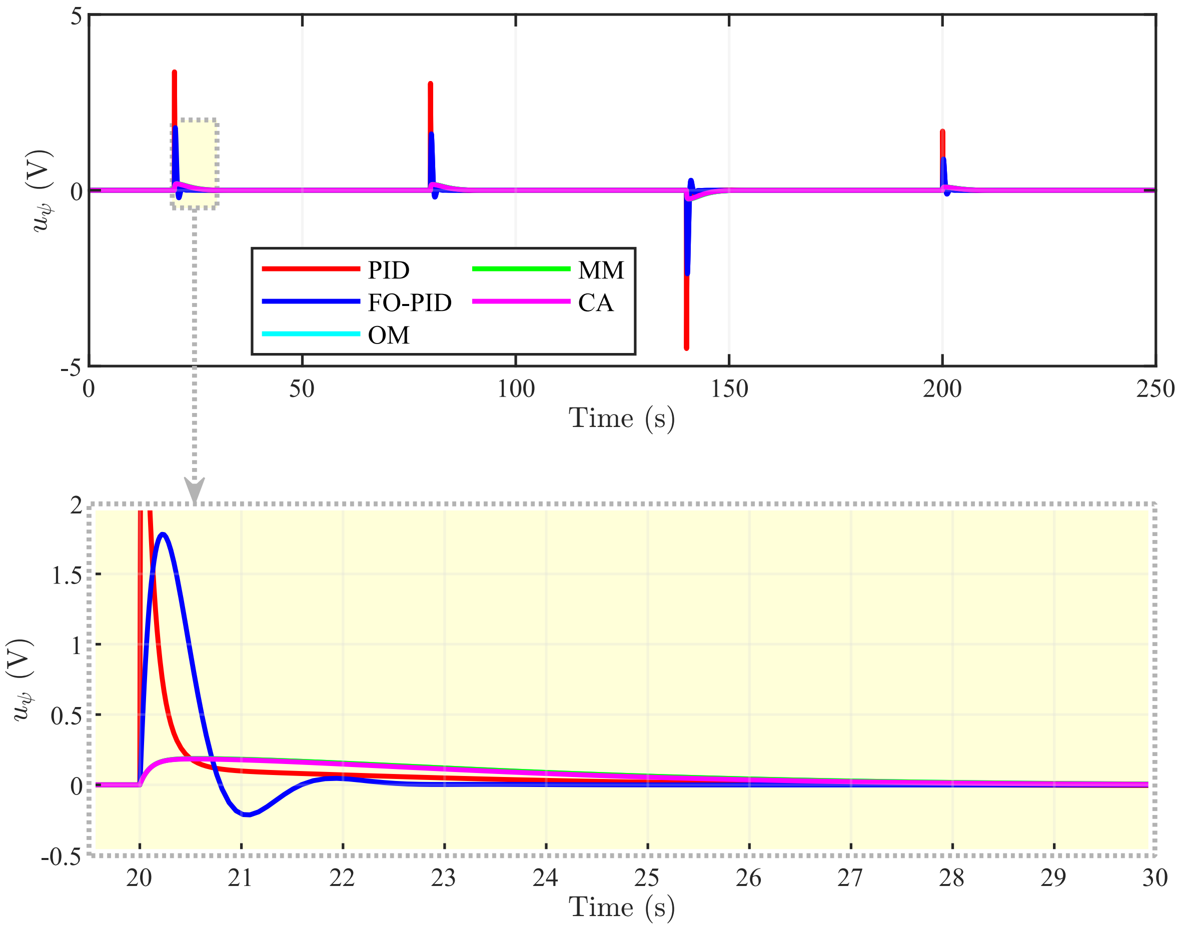

Figure 7.7: Comparison of the control efforts corresponding to the reference tracking of yaw angle shown in Figure 7.5.

Therefore, the FO-PI controllers approximated with OM and CM can be considered suitable choices for reference tracking of the pitch angle ϕ for TRAS. These oscillations are clearly visible in the zoomed view in the lower panel of Figure 7.6.

Figure 7.7 presents the control efforts required to ensure reference tracking of the yaw angle ψ presented in Figure 7.5. The figure shows that the IO-PID controller requires the highest control effort magnitude for yaw angle tracking. The FO-PID controller exhibits the second-highest magnitude. In contrast, the FO-PI controllers realized using OM, MM, and CA require the lowest control effort magnitudes, which are nearly identical.

Although the FO-PID controller ensures good trajectory tracking for the yaw angle ψ shown in Figure 7.5, the control effort analysis indicates that it is not the most suitable choice. An overall analysis of reference tracking and control efforts indicates that the FO-PI controller realized using CA is the most suitable choice for yaw angle control.

7.4 Chapter summary

This chapter develops tuning rules for FO-PI controllers based on classical frequency-domain design. It presents a systematic procedure for selecting the controller parameters. The design enforces a specified gain crossover frequency, phase margin, and phase flatness to achieve robust closed-loop performance.

The chapter further shows how time-domain specifications, such as settling time and peak overshoot, can be mapped into frequency-domain constraints suitable for controller design. It also addresses practical realization aspects of the FO-PI controllers. In particular, it considers the approximation of FO operators using the Oustaloup, Matsuda, and Charef methods. Furthermore, this chapter compares the controllers designed using the proposed approach with the IO and FO PID controllers.

The analysis evaluates that the approximation techniques influence closed-loop behavior and robustness. The presented results establish both the theoretical basis and practical guidelines for designing efficient and implementable FO-FO controllers for nonlinear dynamic systems. Furthermore, this chapter presents the contribution **C.2** listed in Section 1.5 in Chapter 1.

CHAPTER 8

Dynamic uncertainty propagation of FO models

Each measurement should provide an estimate of the measurand together with its associated uncertainty. The uncertainty quantifies the quality of measurement results. Determining the true value of the quantity remains impossible due to multiple uncertainty sources that jointly contribute to uncertainty propagation [4]. The uncertainty assessment becomes more difficult for dynamic responses of physical systems [103]. Existing approaches often apply digital filtering methods to assess the uncertainty propagation in the dynamic response [1]. These methods transform output signals into alternative parameter spaces. Such transformation reduces covariance propagation within the reduced representation.

This chapter proposes the construction of time-dependent sensitivity coefficients from probabilistic descriptions of the identified parameters of FO model. Comparative analysis against digital filtering indicates that the uncertainty component obtained from the identified parameters remains simpler and provides consistent results. Moreover, this chapter extends the method to propagate uncertainty in the closed-loop response.

This chapter extends the article presented at the Automation Conference in May 2026 and accepted for publication in "Lecture Notes in Networks and Systems" [180]. Furthermore, it covers the successful implementation of the objective **Obj.6** listed in Section 1.3.

8.1 FO dynamic model

This section presents the structure of the FO model. It considers the flow system shown in Figure 3.4 under specific input conditions. Furthermore, it formulates the optimization problem for parameter identification and analyzes the parameters. The FO derivative employs the GL definition as follows.

Let $f\colon [0,T] \to \mathbb{R}$ and let $\Delta t > 0$ be a uniform sampling interval. The GL derivative of order $\alpha \in \mathbb{R}^+$ is [181]:

$$\mathscr{D}^{\alpha} f(t) \;\approx\; \frac{1}{\Delta t^{\alpha}} \sum_{m=0}^{\lfloor t/\Delta t \rfloor} g_m^{\alpha}\, f(t - m\,\Delta t), \tag{8.1}$$

where g_m^{α} denotes the GL coefficients calculated as Eq. (2.14) and $\lfloor t/\Delta t \rfloor$ represents the largest integer that does not exceed the ratio of total time t. The approximation in Eq. (8.1) becomes exact as in Eq. (2.12) for the limit $\Delta t \to 0$ [11].

Remark 8.1.1. The map $\alpha \mapsto g_m^{\alpha}$ is infinitely differentiable for all $\alpha \in \mathbb{R}^+ \setminus \mathbb{N}$, i.e., all real numbers excluding the set of natural numbers, given by Eq. (2.16), which is smooth away from the non-positive integers. Consequently, $\Delta t^{-\alpha} = e^{-\alpha \ln \Delta t}$ is also smooth in α. These facts jointly ensure that the GL operator depends smoothly on α.

Analysis of the optimization procedure in Chapter 6 indicates that the parameter identification of the 5-DOF-FO model requires significant computation time. Therefore, this chapter considers a three-parameter FO model with a single derivative. Furthermore, all computations are performed in `MATLAB`, and the GL coefficients are directly computed using the built-in `gamma` function as represented by Eq. (2.14). Moreover, this chapter utilizes the measured flow rates presented in Figure 3.7. The experiment set the input to f_{in} 30 Hz and recorded data for 50 s. The collected data consists of 200 passes used for model identification. This data also supports the development of a framework to assess measurement uncertainty associated with parameter identification in FO models.

8.1.1 Model identification

This section presents the time-domain FO model with delay to be constructed for the flow system through black-box identification. The model structure is considered as:

$$\mathscr{D}^{\alpha} y_{\mathrm{e}}(t) + a \cdot y_{\mathrm{e}}(t) = K \cdot u(t-\tau), \tag{8.2}$$

where $u(t-\tau)$ is the actual input with time delay τ, and $y_{\mathrm{e}}(t)$ is the estimated output with the FO model. Based on the characteristics of the measured flow rates in Figure 3.7, an arbitrary delay time of $\tau = 2.2$ s was selected. Applying the GL approximation defined in Eq. (8.1) and solving Eq. (8.2) for $y_{\mathrm{e}}(t)$ yields

$$y_{\mathrm{e}}(t) = \frac{1}{a + \frac{1}{\Delta t^{\alpha}}} \cdot \left(K \cdot u(t) - \frac{1}{\Delta t^{\alpha}} \sum_{m=0}^{M} g_m^{\alpha} \cdot y_{\mathrm{e}}(t - m \cdot \Delta t) \right), \tag{8.3}$$

where Δt denotes the sampling interval used to compute the numerical differentiation. For this model, the sampling interval is set to $\Delta t = 0.03$ s.

Considering $y_{\mathrm{m}}(t)$ as the measured flow rate, this section minimizes the RMS of residuals $(y_{\mathrm{m}}(t) - y_{\mathrm{e}}(t))$ to identify the parameters α, a, and K of the FO model in Eq. (8.2). The selection of RMS as an objective function is due to its popularity as a quality factor in such problems [173]. To ensure the simplicity, the built-in MATLAB routine `fminsearch` was used to solve the optimization. The optimization problem to identify the parameters of the FO model is presented as[1]

$$\min_{\alpha,a,k} \sqrt{\frac{1}{N_{\mathrm{s}}} \sum_{i=0}^{N_{\mathrm{s}}} \left(y_{\mathrm{m},i} - y_{\mathrm{e},i} \right)^2}\ , \tag{8.4}$$

where N_{s} is total number of samples in the measured and estimated outputs. Furthermore, the initial bounds of the parameters were selected as $0 \leq \alpha \leq 1$, $0 \leq a \leq 100$, and

$0 \leq K \leq 100$. During optimization, these bounds were progressively expanded whenever the optimal solution approached the imposed limits and the resulting model accuracy remained unsatisfactory. Through successive refinement, the parameter bounds were adjusted to:

$$0.01 \leq \alpha \leq 2.5,$$
$$0 \leq a,\ K \leq 100.$$

Moreover, since this chapter considers FO modeling as a black-box identification problem, it does not incorporate the physical interpretation of the parameters.

Optimization based on Eq. (5.1) was applied to estimate the parameters of the FO model in Eq. (8.2). The procedure was repeated for 200 passes using the measured data shown in Figure 3.7. This approach produced 200 distinct parameter sets for the FO model.

The average computational time for solving the optimization problem Eq. (8.4) to estimate dynamic model parameters in `MATLAB` was 2.45 s on an `Intel(R) Core(TM) i7-1260P` processor. This time is significantly lower than that required by the continuous nonlinear optimization in Eq. (6.9) for the 5-DOF-FO model, as shown in Table 6.10 in Chapter 6. This reduction occurs because Eq. (8.4) estimates three parameters and uses a single FO component, i.e., the FO derivative. In contrast, estimating two FO components requires separate GL coefficients for the derivative and integral during optimization. This requirement increases the computational burden. Furthermore, Eq. (6.9) formulates the identification as a continuous optimization problem and requires a much smaller sampling time set internally by NEOS-server and AMPL. These factors significantly increase the computation time for the 5-DOF FO model in Eq. (6.8) compared to Eq. (8.4).

8.1.2 Identified parameters

This section presents the results of the Kolmogorov-Smirnov (K-S) test [181] and the Quantile-Quantile (Q-Q) plots [182] to assess normality of the identified parameters. These tests are conducted with respect to the standard normal Probability Density Function (PDF). The corresponding statistical descriptors are listed in Table 8.1. The table shows that the parameters exhibit low standard deviation values. This observation indicates a limited dispersion of the estimated parameters. The p-values associated with parameters α, a, and K substantially exceed the threshold required for acceptance under a normal PDF. A parameter vector x with a p-value ≥ 0.05 in the K-S normality test may be considered normally distributed [181]. The respective values in Table 8.1 confirm that the optimal parameters α, a, and K satisfy the normality criterion.

A graphical normality assessment is also performed using Q-Q plots. These plots compare parameter quantiles with those of the standard normal PDF. The corresponding comparisons are shown in Figure 8.1. The panel (a) in the figure indicates that the quantiles of α closely follow the reference distribution. In contrast, the quantiles of a and K in panels (b) and (c), respectively, show slight deviations near lower and upper extremes. However, a significant portion of quantiles for a and K remains aligned with the reference line of the standard normal PDF. Therefore, this spread supports the assumption of normal distribution for the identified parameters. The Q-Q plot of optimal objective function values in panel (d) shows significant deviations at both extremes. However, this behavior remains outside the primary scope of the present analysis. The study focuses on uncertainty propagation within the dynamic response of the FO model. Variations in the values of optimal objective reflect residual magnitudes and therefore do not influence the uncertainty evaluation addressed in this chapter.

Based on the conclusions drawn from the statistical analysis given in Table 8.1 and the graphical assessment shown in Figure 8.1, the identified parameters can be treated as samples from a normal PDF as

$$p_i(x) = \frac{1}{s\sqrt{2\pi}} e^{-\frac{(x-\bar{x})^2}{2(s(x))^2}}, \tag{8.5}$$

where $p_i(x) \in \{\alpha, a, K\}$. The variables $\bar{x}$ and $s(x)$ denote the mean value and standard deviation of the respective parameters, given in Table 8.1.

8.2 Propagation of measurement uncertainty

This section provides a framework for the propagation of measurement uncertainty associated with parameter identification in FO dynamic models. The FO model considered in this section is given in Eq. (8.2). The framework relies on the assumptions presented in the following sections.

8.2.1 Probabilistic parameters

The identified parameters follow the normal PDF as described in the following definition. Assume the parameter vector follows a normal distribution,

$$p \sim \mathcal{N}(\bar{p}, \mathbf{\Sigma_p}), \tag{8.6}$$

Table 8.1: Coefficients of parameter variations after evaluating Eq. (8.4) 200 times, i.e., one optimization procedure for each measured response. The p-value was calculated from the MATLAB function `[~,p-value]=kstest(·)`.

Quantifier	α	a	K	Objective value
Mean value ($\bar{x}$)	1.18	1.13	0.19	20
Standard deviation	0.0104	0.031	0.0055	2.2
p-value	0.87	0.68	0.81	0.45

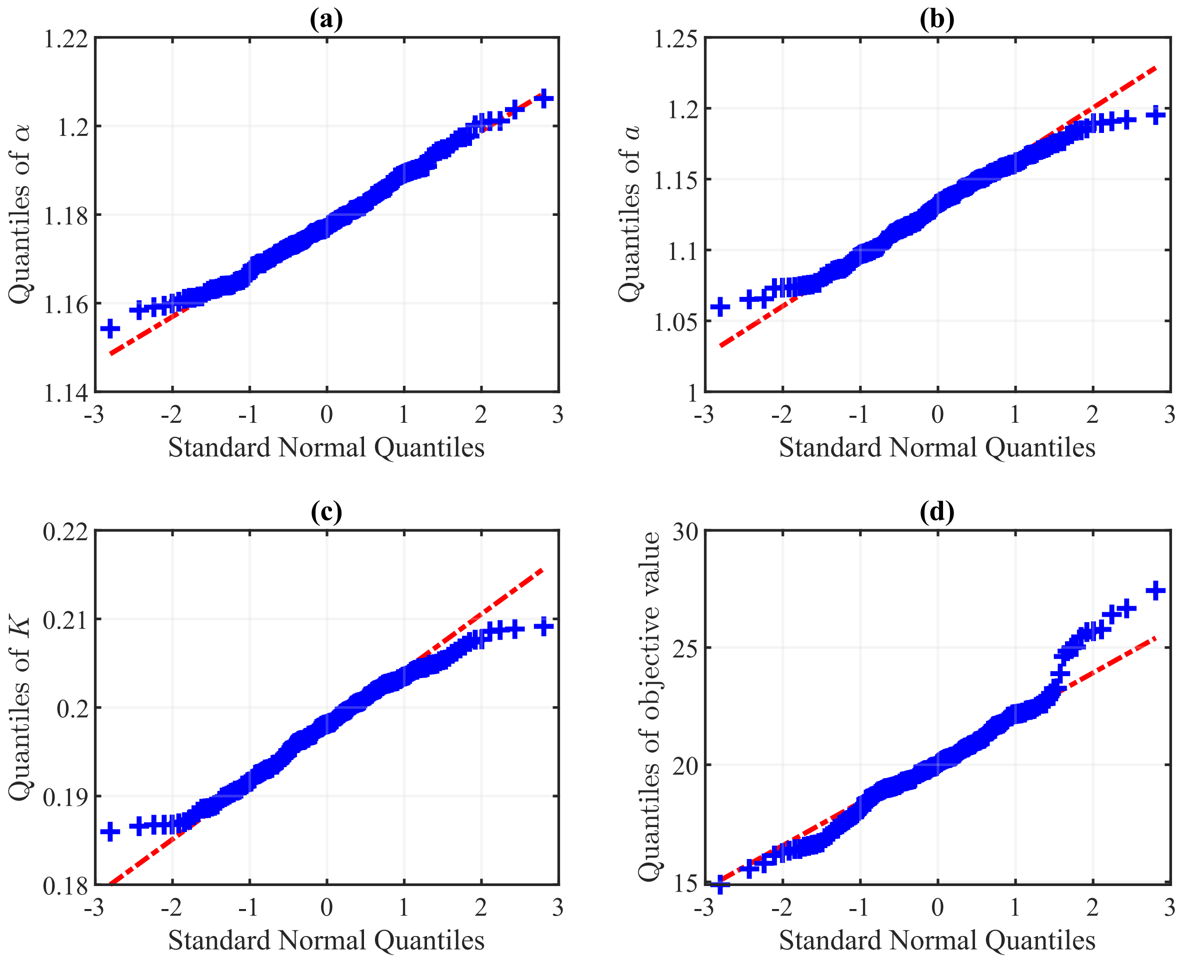

Figure 8.1: Q-Q plot for the normality test of the identified parameters of the FO model. The red dashed line represents the normal probability distribution and the blue markers represent the probabilities of the identified parameters.

where $\bar{p}$ is a vector representing the mean values of parameters, and $\mathcal{N}$ denotes the normality of the parameters. Furthermore, $\boldsymbol{\Sigma}_{\mathrm{p}}$ is the positive-definite covariance matrix with entries $\sigma_{ij} = [\Sigma_p]_{ij}$. Furthermore, p_n denotes the number of parameters.

Remark 8.2.1. In the present application, the assumption of normality is verified empirically using the K-S test (p-values are given in Table 8.1). It is further confirmed graphically from Q-Q plots in Figure 8.1. Therefore, this assumption is supported by the data presented in Section 8.1.2.

8.2.2 Time dependent sensitivity coefficients

This section extends the definitions of sensitivity coefficients presented in [2, 4]. It introduces time-dependent sensitivity functions to quantify dynamic uncertainty propagation in the FO model given in Eq. (8.2).

Define the time-dependent sensitivity vector as the gradient of the modeled output with respect to the parameter vector. The gradient is evaluated at the mean values of the parameters $\bar{p}$:

$$C(t) = \nabla_p y_\mathrm{e}(t,p)\big|_{p=\bar{p}} = \left[\frac{\partial y}{\partial p_1}, \frac{\partial y}{\partial p_2}, \ldots, \frac{\partial y}{\partial p_n}\right]_{p=\bar{p}} \in \mathbb{R}^{1\times p_n}. \tag{8.7}$$

For the FO model in Eq. (8.2) with parameter vector $p = [\alpha, a, K]^T$, the individual sensitivity coefficients are

$$\begin{aligned} c_\alpha(t) &= \frac{\partial y_\mathrm{e}(t)}{\partial \alpha} \\ &= \frac{K\dfrac{\partial u(t-\tau)}{\partial \alpha} - \dfrac{\partial}{\partial \alpha}(\mathscr{D}^\alpha y_\mathrm{e}(t))}{a + \Delta t^{-\alpha}} - \frac{K\,u(t-\tau) - \mathscr{D}^\alpha y_\mathrm{e}(t)}{(a+\Delta t^{-\alpha})^2}\frac{\partial}{\partial \alpha}(\Delta t^{-\alpha}), \end{aligned} \tag{8.8}$$

$$c_a(t) = \frac{\partial y_\mathrm{e}(t)}{\partial a} = -\frac{y_\mathrm{e}(t)}{(a+\Delta t^{-\alpha})^2}, \tag{8.9}$$

$$c_K(t) = \frac{\partial y_\mathrm{e}(t)}{\partial k} = \frac{u(t-\tau)}{a+\Delta t^{-\alpha}}. \tag{8.10}$$

This work calculates the partial derivatives numerically using the forward-difference scheme in `MATLAB`.

Assumptions

Throughout this section, the following conditions are imposed.

(A1) *Unique existence.*

For each parameter p, Eq. (8.2) has a unique solution and the GL discretization Eq. (8.1) is well posed [11].

(A2) *Normality of the identified parameters.*

$$p \sim \mathcal{N}(\bar{p}, \mathbf{\Sigma_p}),$$

as in Eq. (8.6). This is verified empirically for the experimental data considered in Section 8.1.2.

(A3) *Small spread in the parameter values.*

The standard deviations of the parameters are small relative to their mean values. For the optimization results presented in Section 8.1.2, the relative standard deviations of the identified parameters are $s(\alpha)/\bar{\alpha} = 0.88\,\%$, $s(a)/\bar{a} = 2.74\,\%$, and $s(K)/\bar{K} = 2.89\,\%$ (from Table 8.1). All of these values are below $3\,\%$ which satisfies the assumption.

(A4) *Order regularity.*

The FO satisfies $\alpha \in (m-1, m)$ for some $m \in \mathbb{N}$ throughout $\mathcal{P}$. This means that α does not cross an integer value within the admissible parameter domain. In case of

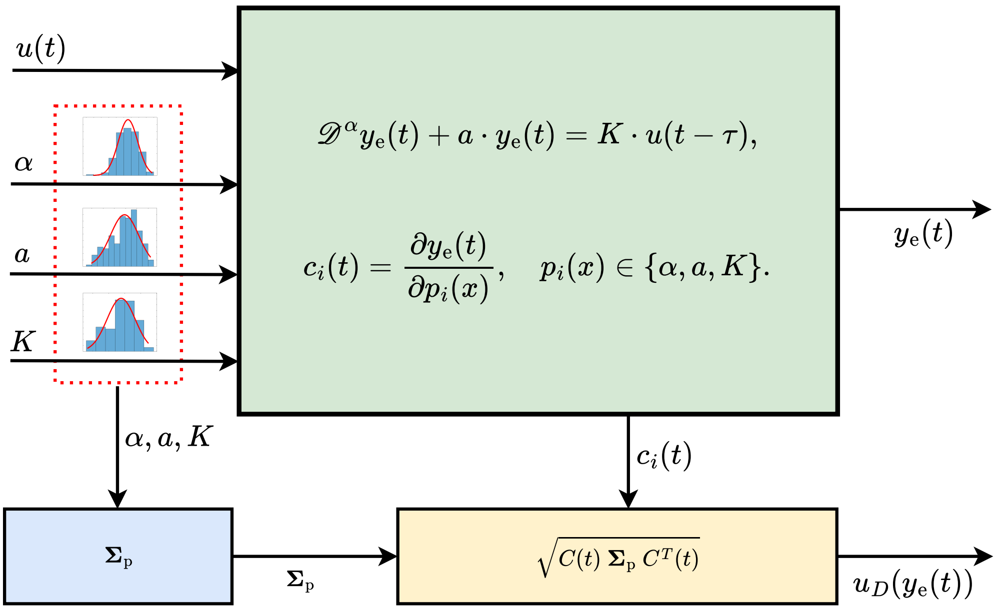

Figure 8.2: Conceptual framework for the dynamic response and the associated uncertainty component contributed by the identified parameters of the FO model – $\Sigma_{\mathrm{p}}(\alpha, a, K)$ is the covariance matrix (Σ_{p}) of α, a, and K.

the identified parameters in Section 8.1.2, $\alpha \in [1.14,\ 1.22] \subset (1, 2)$, which satisfies this requirement.

Following these assumptions, the time-dependent sensitivity coefficients and the covariance matrix $\boldsymbol{\Sigma}_{\mathrm{p}}$ can be used to calculate the uncertainty component as:

$$u_D(y_{\mathrm{e}}(t)) = \sqrt{C(t)\ \boldsymbol{\Sigma}_{\mathrm{p}}\ C^T(t)}, \tag{8.11}$$

where $C(t)$ and $\boldsymbol{\Sigma}_{\mathrm{p}}$ denote the time-dependent coefficient matrix and the positive semi-definite covariance matrix generated from the identified parameters.

The propagated variance $u_D^2(y_{\mathrm{e}}(t)) = C(t), \boldsymbol{\Sigma}_{\mathrm{p,cl}}, C^T(t)$ remains non-negative for all sensitivity coefficients in $C(t)$ if and only if $\boldsymbol{\Sigma}_{\mathrm{p,cl}}$ is positive semi-definite [183]. If the covariance matrix does not satisfy this property, it may yield negative propagated covariances. This result renders the propagated uncertainty $u_D(y_{\mathrm{e}}(t))$ imaginary and physically meaningless.

The time-dependent coefficient matrix is formulated from sensitivity coefficients in Eqs. (8.8) to (8.10) as:

$$C(t) = \begin{bmatrix} c_\alpha(t) & c_a(t) & c_K(t) \end{bmatrix}. \tag{8.12}$$

The proposed conceptual framework is presented in Figure 8.2. At the outset, it can be seen from the figure that the parameters α, a, and K and system input $u(t)$ are used to generate the dynamic response $y_{\mathrm{e}}(t)$ of the FO model. Furthermore, sensitivity coefficients and the covariance matrix calculate the time-dependent uncertainty component $u_D(y_{\mathrm{e}}(t))$.

The covariance matrix $\boldsymbol{\Sigma}_{\mathrm{p}}$ is calculated from the optimal parameters $\in \mathbb{R}^{N_{\mathrm{m}} \times p_n}$, where N_{m} and p_n denote the total number of measurement passes and the total number of parameters, respectively. The value of the matrix is:

$$\boldsymbol{\Sigma}_{\mathrm{p}} = \begin{bmatrix} 0.1073 & -0.1764 & -0.0357 \\ -0.1764 & 0.9600 & 0.1669 \\ -0.0357 & 0.1669 & 0.0301 \end{bmatrix} \cdot 10^{-3}. \tag{8.13}$$

The eigenvalues of $\boldsymbol{\Sigma}_{\mathrm{p}}$ are positive. This property ensures that the matrix is strictly positive definite.

Furthermore, the uncertainty component $u_D(y_{\mathrm{e}}(t))$ calculated in Eq. (8.11) represents the standard uncertainty. This quantity corresponds to a confidence interval of approximately 68 %. The expanded uncertainty is obtained by multiplying $u_D(y_{\mathrm{e}}(t))$ by the coverage factor $k = 2$ [4], as described in Eq. (2.8). This scaling extends the confidence interval to approximately 95 % for measurement processes whose output quantity follows the normal distribution. However, this chapter employs only the standard uncertainty.

The calculations presented in this section support hypothesis **H.3**. Furthermore, they cover the successful implementations of objective **Obj.6** and present contributions **C.3** and **C.4** listed in Section 1.5.

8.3 Uncertainty propagation in closed-loop

Building on the previous section, this section presents uncertainty propagation in the closed-loop dynamic response of the FO model. The controller for the closed-loop analysis follows the tuning rules presented in Section 7.1.1 of Chapter 7.

8.3.1 Control design

This section considers TFs of the closed-loop system, the open-loop system, and the controller as presented in Eqs. (7.1) to (7.3). The plant TF can be obtained by the Laplace transform of Eq. (8.2) under zero initial conditions as:

$$G(s) = \frac{K\, e^{-\tau s}}{s^{\alpha} + a}, \tag{8.14}$$

where the parameters α, a, K, and τ are the same as in time-domain representation given in Eq. (8.2). Applying the magnitude, gain, and constant phase conditions in Eqs. (7.4) to (7.6) yields the following expressions:

$$|C(j\omega_{\mathrm{gc}})||G(j\omega_{\mathrm{gc}})| = K \left(\frac{\left[k_{\mathrm{p}} + k_{\mathrm{i}}\omega_{\mathrm{gc}}^{-\lambda} \cos\left(\frac{\lambda\pi}{2}\right)\right]^2 + \left[k_{\mathrm{i}}\omega_{\mathrm{gc}}^{-\lambda} \sin\left(\frac{\lambda\pi}{2}\right)\right]^2}{\left[a + \omega_{\mathrm{gc}}^{\alpha} \cos\left(\frac{\alpha\pi}{2}\right)\right]^2 + \omega_{\mathrm{gc}}^{2\alpha} \sin^2\left(\frac{\alpha\pi}{2}\right)} \right)^{1/2} = 1, \tag{8.15}$$

$$\angle L(j\omega_{\mathrm{gc}}) = \tan^{-1}\left(\frac{-k_{\mathrm{i}}\omega_{\mathrm{gc}}^{-\lambda}\sin\left(\frac{\lambda\pi}{2}\right)}{k_{\mathrm{p}} + k_{\mathrm{i}}\omega_{\mathrm{gc}}^{-\lambda}\cos\left(\frac{\lambda\pi}{2}\right)}\right) - \omega_{\mathrm{gc}}\tau - \tan^{-1}\left(\frac{\omega_{\mathrm{gc}}^{\alpha}\sin\left(\frac{\alpha\pi}{2}\right)}{a + \omega_{\mathrm{gc}}^{\alpha}\cos\left(\frac{\alpha\pi}{2}\right)}\right) = -\pi + \varphi_{\mathrm{m}}, \tag{8.16}$$

$$\frac{d\varphi_C}{d\omega_{\mathrm{gc}}} + \frac{d\varphi_G}{d\omega_{\mathrm{gc}}} = 0, \tag{8.17}$$

where

$$\frac{d\varphi_C}{d\omega_{\mathrm{gc}}} = \frac{\lambda k_{\mathrm{i}}k_{\mathrm{p}}\omega_{\mathrm{gc}}^{-\lambda-1}\sin\left(\frac{\lambda\pi}{2}\right)}{\left[k_{\mathrm{p}} + k_{\mathrm{i}}\omega_{\mathrm{gc}}^{-\lambda}\cos\left(\frac{\lambda\pi}{2}\right)\right]^2 + \left[k_{\mathrm{i}}\omega_{\mathrm{gc}}^{-\lambda}\sin\left(\frac{\lambda\pi}{2}\right)\right]^2},$$

and

$$\frac{d\varphi_G}{d\omega_{\mathrm{gc}}} = -\tau - \frac{a\alpha\omega_{\mathrm{gc}}^{\alpha-1}\sin\left(\frac{\alpha\pi}{2}\right)}{\left[a + \omega_{\mathrm{gc}}^{\alpha}\cos\left(\frac{\alpha\pi}{2}\right)\right]^2 + \omega_{\mathrm{gc}}^{2\alpha}\sin^2\left(\frac{\alpha\pi}{2}\right)}.$$

Moreover, the symbol $\angle(\cdot)$ denotes the phase angle.

8.3.2 Controller parameters

This section presents the parameters of the FO-PI controllers and the corresponding normality tests.

The time-domain closed-loop design specifications were set to $t_{\mathrm{set}} = 15$ s and $P_{\mathrm{o}} = 2\%$ for the design of the FO-PI controller. Similar to Section 7.2, Eqs. (8.15) to (8.17) were solved using the `Optimization Toolbox` in `MATLAB R2024b` with the `lsqnonlin` routine. The equations were solved 200 times for individual sets of model parameters identified from each pass for the parameters shown in Figure 8.1. The computation time required to solve these equations and obtain the FO controller parameters $C(s)$ for each model parameter set was evaluated. The average computation time on an `Intel(R) Core(TM) i7-1260P` processor was 0.05 s.

The average values of the controller parameters and the corresponding standard deviations for the identified FO model in Eq. (8.14) with parameters shown in Figure 8.1 are given in Table 8.2. The table indicates small deviations of the parameters from the respective mean values. This observation indicates very small variations in the controller parameters and satisfies Assumption (A3). Since p-values alone do not reliably classify data as normal [181], this section omits the K-S test. This section directly presents the Q-Q plots of the controller parameters.

The Q-Q plots of the controller parameters are shown in Figure 8.3. The figure shows that the proportional gain (k_{p}) follows the reference line for most values. Some values of k_{p} slightly deviate at the upper end, as shown in panel (a). However, such occurrences remain very limited. Since k_{p} exhibits no heavy tails and follows the reference line for most observations, this parameter can be treated as the samples from the normal distribution [182].

Similarly, the integral gain (k_{i}) in panel (b) follows the reference line for most observations. Small deviations occur at the lower end without the presence of heavy tails. In contrast, the fractional integral parameter (λ) in panel (c) follows the reference line for most observations. Minor deviations appear at both upper and lower ends for a few cases without indicating heavy tails. Therefore, these controller parameters can be treated as the samples from the normal distribution, satisfying Assumption (A3).

Furthermore, the FO integral does not cross integer values over the entire range in Figure 8.3 panel (c). This observation satisfies Assumption (A4). These results justify the use of controller parameters combined with model parameters in Figure 8.1 to evaluate the time-dependent uncertainty propagated to the closed-loop response using the approach presented in Section 8.2.

The closed-loop TF of the plant in Eq. (8.14) and the controller in Eq. (7.3) can be constructed following Eq. (7.1). As a result, the TF of the closed-loop system is

$$G_{\mathrm{cl}}(s) = \frac{Ke^{-\tau s}\left(k_{\mathrm{p}} + k_{\mathrm{i}}s^{-\lambda}\right)}{s^{\alpha} + a + ke^{-\tau s}\left(k_{\mathrm{p}} + k_{\mathrm{i}}s^{-\lambda}\right)}. \tag{8.18}$$

This section analyzes uncertainty propagation in the closed loop following the guidelines presented in Section 8.2. An inverse Laplace transform is applied to Eq. (8.18) to obtain a time-domain expression. The time-domain equation of the closed-loop structure is expressed as

$$\mathscr{D}^{\alpha} y_{\mathrm{e}}(t) + a y_{\mathrm{e}}(t) + K k_{\mathrm{p}} y_{\mathrm{e}}(t-\tau) + k k_{\mathrm{i}} \mathscr{J}^{\lambda} y_{\mathrm{e}}(t-\tau) = K k_{\mathrm{p}} r(t-\tau) + K k_{\mathrm{i}} \mathscr{J}^{\lambda} r(t-\tau), \tag{8.19}$$

where k_{p}, k_{i}, and λ are the parameters of the FO-PI controller. Furthermore, α, a, and K are the parameters of the FO model in Eq. (8.2).

8.3.3 Time-dependent sensitivity coefficients of the closed-loop system

Building on Section 8.2.2, this section presents the time-dependent sensitivity coefficients of the closed-loop system.

The sensitivity coefficient calculations in Section 8.2.2 use the GL approximation of the FO derivative. Therefore, the derivations of the closed-loop sensitivity coefficients also follow the GL approximation of the FO derivative presented in Eq. (8.1). Moreover, the

Table 8.2: Mean values and standard deviations of the controller parameters.

Quantifier	k_{p}	k_{i}	λ
Mean value ($\bar{x}$)	-0.2532	1.3453	0.8851
Standard deviation	0.0011	0.0061	0.0021

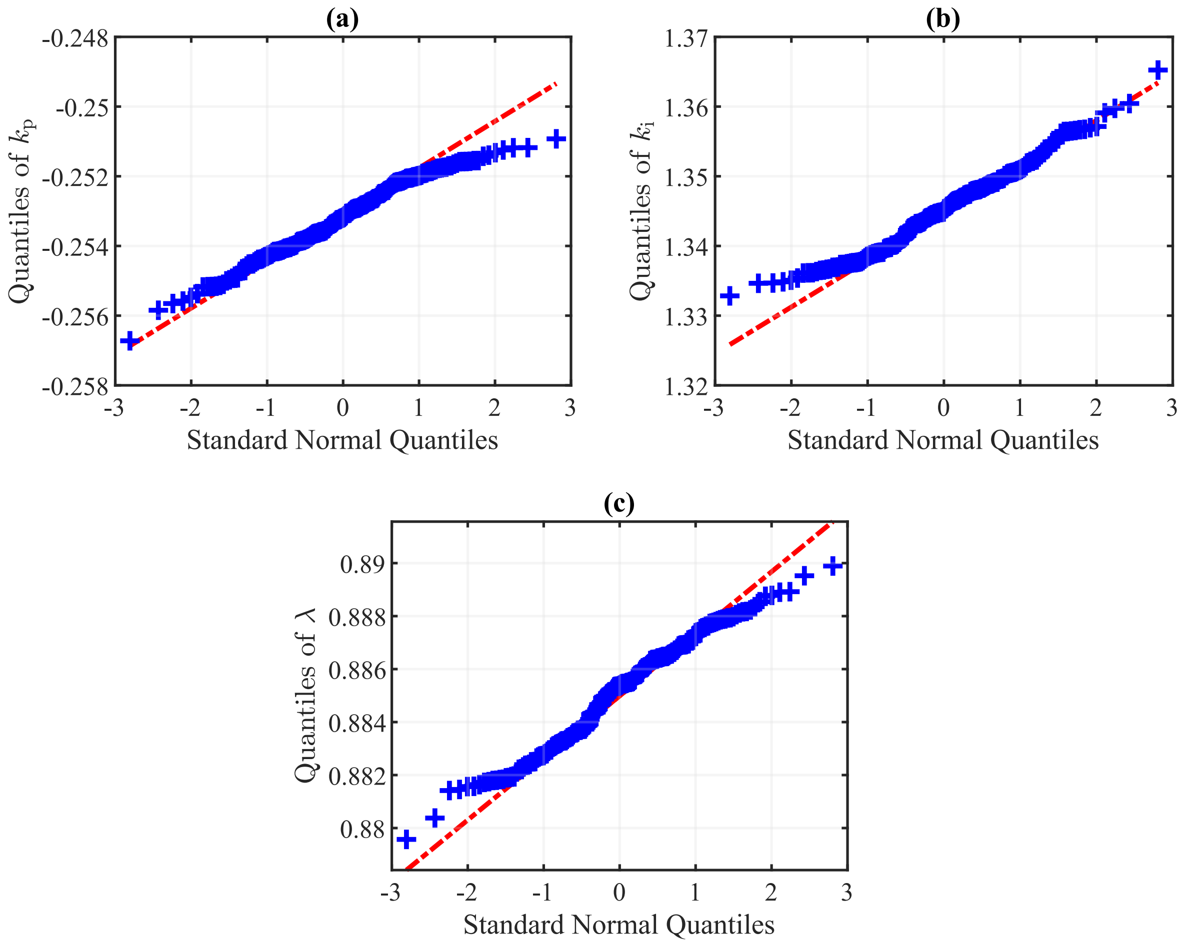

Figure 8.3: Q-Q plot for the normality test of the controller parameters. This figure adopts the same color scheme as in Figure 8.1

matrix representing sensitivity coefficients in Eq. (8.12) for the closed-loop case becomes

$$C_{\mathrm{cl}}(t) = \begin{bmatrix} c_\alpha(t) & c_a(t) & c_K(t) & c_{kp}(t) & c_{ki}(t) & c_\lambda(t) \end{bmatrix}. \tag{8.20}$$

Applying the GL derivative in Eq. (8.1) to Eq. (8.19) yields an explicit expression for the closed-loop response as

$$y_{\mathrm{e}}(t) = \frac{Kk_{\mathrm{p}}r(t-\tau) + Kk_{\mathrm{i}}\mathscr{I}^{\lambda}r(t-\tau) - Z_n^{(\alpha)} - Kk_{\mathrm{p}}y_{\mathrm{e}}(t-\tau) - Kk_{\mathrm{i}}\mathscr{I}^{\lambda}y_{\mathrm{e}}(t-\tau)}{a + \dfrac{1}{\Delta t^{\alpha}}}, \tag{8.21}$$

where

$$Z_n^{(\alpha)} = \frac{1}{\Delta t^{\alpha}} \sum_{m=1}^{\lfloor t/\Delta t \rfloor} g_m^{\alpha}\, y_{\mathrm{e}}(t - m\Delta t), \tag{8.22}$$

and $\lfloor t/\Delta t \rfloor$ represents the largest integer that does not exceed the ratio of total time t.

From this expression, the closed-loop sensitivity coefficients are derived as:

$$c_\alpha(t) = \frac{-\dfrac{\partial}{\partial \alpha}\left(\mathscr{D}^\alpha y_\mathrm{e}(t)\right)}{a + \dfrac{1}{\Delta t^\alpha}} - \frac{Kk_\mathrm{p} r(t-\tau) + Kk_\mathrm{i}\mathscr{J}^\lambda r(t-\tau) - Kk_\mathrm{p} y_\mathrm{e}(t-\tau) - Kk_\mathrm{i}\mathscr{J}^\lambda y_\mathrm{e}(t-\tau) - \mathscr{D}^\alpha y_\mathrm{e}(t)}{\left(a + \dfrac{1}{\Delta t^\alpha}\right)^2}\left(\frac{\partial}{\partial \alpha}\frac{1}{\Delta t^\alpha}\right), \tag{8.23}$$

$$c_a(t) = -\frac{Kk_\mathrm{p} r(t-\tau) + Kk_\mathrm{i}\mathscr{J}^\lambda r(t-\tau) - Kk_\mathrm{p} y_\mathrm{e}(t-\tau) - Kk_\mathrm{i}\mathscr{J}^\lambda y_\mathrm{e}(t-\tau) - \mathscr{D}^\alpha y_\mathrm{e}(t)}{\left(a + \dfrac{1}{\Delta t^\alpha}\right)^2}, \tag{8.24}$$

$$c_K(t) = \frac{k_\mathrm{p}\big(r(t-\tau) - y_\mathrm{e}(t-\tau)\big) + k_\mathrm{i}\mathscr{J}^\lambda\big(r(t-\tau) - y_\mathrm{e}(t-\tau)\big)}{a + \dfrac{1}{\Delta t^\alpha}}, \tag{8.25}$$

$$c_{kp}(t) = \frac{K\big(r(t-\tau) - y_\mathrm{e}(t-\tau)\big)}{a + \dfrac{1}{\Delta t^\alpha}}, \tag{8.26}$$

$$c_{ki}(t) = \frac{K\,\mathscr{J}^\lambda\big(r(t-\tau) - y_\mathrm{e}(t-\tau)\big)}{a + \dfrac{1}{\Delta t^\alpha}}, \tag{8.27}$$

$$c_\lambda(t) = \frac{kk_\mathrm{i}\frac{\partial}{\partial\lambda}\left[\mathscr{J}^\lambda\big(r(t-\tau) - y_\mathrm{e}(t-\tau)\big)\right]}{a + \dfrac{1}{\Delta t^\alpha}}, \tag{8.28}$$

where $r(t)$ denotes the reference input to the closed-loop system. Moreover, $\mathscr{D}$ and $\mathscr{J}$ represent the FO derivative and the FO integral, respectively. The time-dependent expression for uncertainty propagated to the closed-loop response can be evaluated from Eq. (8.11) by replacing $C(t)$ with C_cl given in Eq. (8.20). The covariance matrix $\mathbf{\Sigma}_{\mathrm{p,cl}}$ evaluated using the identified model parameters for each pass and the corresponding controller parameters is given as

$$\mathbf{\Sigma}_{\mathrm{p,cl}} = \begin{bmatrix} 1.0732 & -1.7642 & -0.3568 & 0.0081 & -0.0603 & 0.0367 \\ -1.7642 & 9.5998 & 1.6691 & 0.0201 & -0.3266 & 0.4653 \\ -0.3568 & 1.6691 & 0.3009 & 0.0122 & -0.0991 & 0.0727 \\ 0.0081 & 0.0201 & 0.0122 & 0.0124 & -0.0672 & 0.0029 \\ -0.0603 & -0.3266 & -0.0991 & -0.0672 & 0.3736 & -0.0355 \\ 0.0367 & 0.4653 & 0.0727 & 0.0029 & -0.0355 & 0.0425 \end{bmatrix} \cdot 10^{-4}. \tag{8.29}$$

The matrix $\mathbf{\Sigma}_{\mathrm{p,cl}}$ is used in Eq. (8.11) instead of Σ_{p} to evaluate the uncertainty propagated in the closed-loop system. The eigenvalues of $\mathbf{\Sigma}_{\mathrm{p,cl}}$ are positive, which confirms that the matrix is positive definite.

The entries of $\mathbf{\Sigma}_{\mathrm{p,cl}}$ are reported with a variable number of significant digits. This way of reporting is intentional and metrologically justified. In covariance propagation, the uncertainty $u_D(y_{\mathrm{e}}(t))$ is obtained as a quadratic form which can involve both positive and negative covariance terms, see Eq. (8.11). When covariance terms of opposite sign and comparable magnitude contribute to the same sum, significant numerical cancellation may occur. In such cases, retaining a uniform number of significant figures for all entries of $\mathbf{\Sigma}_{\mathrm{p,cl}}$ would introduce rounding errors. This effect may corrupt the propagated uncertainty $u_D(y_{\mathrm{e}}(t))$, particularly when the net result of the quadratic form $C(t)\,\mathbf{\Sigma}_{\mathrm{p,cl}}\,C^T(t)$ is small relative to the individual contributing terms. Therefore, each entry of $\mathbf{\Sigma}_{\mathrm{p,cl}}$ is reported with sufficient digits to preserve numerical integrity in the propagation. This reporting is based on GUM recommendations to avoid unnecessary excessive rounding of the intermediate quantities used in uncertainty calculations [4].

8.4 Time dependent sensitivity coefficients with GL and RL implementations

The section presents time-dependent sensitivity coefficients for the implementation of FO operators with RL in Eqs. (2.19) and (2.20), and Caputo in Section 2.2.1.

Since the parameters of the FO model in Eq. (8.2) are identified using GL operators, the corresponding derivatives and integrals follow the same definitions. For the FO-PI controller, the FO operators associated with the fractional integral in the sensitivity coefficient calculations use GL, RL, and Caputo definitions. This approach yields three configurations:

1. GL-GL configuration, where both the model and the controller use GL definitions of the FO operators,
2. GL-RL configuration, where the model uses GL implementation and the controller uses RL implementation, and
3. GL-Caputo configuration, where the model uses GL implementation and the controller uses the Caputo implementation.

The sensitivity coefficients for the GL-GL configuration are given in Eqs. (8.23) to (8.28). The sensitivity coefficients for the GL-RL and GL-Caputo configurations are presented in the following sections. Moreover, the RL-FO integral is approximated using the modified trapezoidal rule [43]. The sensitivity coefficients derived under these configurations and the covariance matrix in Eq. (8.29) enable calculation of time-dependent uncertainties using Eq. (8.11).

8.4.1 Sensitivity coefficients with GL-RL configuration

For GL-RL configuration, all sensitivity coefficients differ from those derived in the GL-GL configuration presented in Eqs. (8.23) to (8.28). Furthermore, the FO integral in the GL-RL configuration is denoted by $\mathscr{I}_{\mathrm{RL}}^{\lambda}$. The sensitivity coefficients of the closed-loop response in the GL-RL configurations are given as:

$$c_\alpha(t) = \frac{-\dfrac{\partial}{\partial\alpha}\left(\mathscr{D}^\alpha y_{\mathrm{e}}(t)\right)}{a + \dfrac{1}{\Delta t^\alpha}} - \frac{Kk_{\mathrm{p}}r(t-\tau) + Kk_{\mathrm{i}}\mathscr{I}_{\mathrm{RL}}^{\lambda}r(t-\tau) - Kk_{\mathrm{p}}y_{\mathrm{e}}(t-\tau) - Kk_{\mathrm{i}}\mathscr{I}_{\mathrm{RL}}^{\lambda}y_{\mathrm{e}}(t-\tau) - \mathscr{D}^\alpha y_{\mathrm{e}}(t)}{\left(a + \dfrac{1}{\Delta t^\alpha}\right)^2}\left(\frac{\partial}{\partial\alpha}\frac{1}{\Delta t^\alpha}\right), \tag{8.30}$$

$$c_a(t) = -\frac{Kk_{\mathrm{p}}r(t-\tau) + Kk_{\mathrm{i}}\mathscr{I}_{\mathrm{RL}}^{\lambda}r(t-\tau) - Kk_{\mathrm{p}}y_{\mathrm{e}}(t-\tau) - Kk_{\mathrm{i}}\mathscr{I}_{\mathrm{RL}}^{\lambda}y_{\mathrm{e}}(t-\tau) - \mathscr{D}^\alpha y_{\mathrm{e}}(t)}{\left(a + \dfrac{1}{\Delta t^\alpha}\right)^2}, \tag{8.31}$$

$$c_K(t) = \frac{k_{\mathrm{p}}\big(r(t-\tau) - y_{\mathrm{e}}(t-\tau)\big) + k_{\mathrm{i}}\mathscr{I}_{\mathrm{RL}}^{\lambda}\big(r(t-\tau) - y_{\mathrm{e}}(t-\tau)\big)}{a + \dfrac{1}{\Delta t^\alpha}}, \tag{8.32}$$

$$c_{kp}(t) = \frac{K\big(r(t-\tau) - y_{\mathrm{e}}(t-\tau)\big)}{a + \dfrac{1}{\Delta t^\alpha}}, \tag{8.33}$$

$$c_{ki}(t) = \frac{K\,\mathscr{I}_{\mathrm{RL}}^{\lambda}\big(r(t-\tau) - y_{\mathrm{e}}(t-\tau)\big)}{a + \dfrac{1}{\Delta t^\alpha}}, \tag{8.34}$$

$$c_\lambda(t) = \frac{Kk_{\mathrm{i}}\frac{\partial}{\partial\lambda}\left[\mathscr{I}_{\mathrm{RL}}^{\lambda}\big(r(t-\tau) - y_{\mathrm{e}}(t-\tau)\big)\right]}{a + \dfrac{1}{\Delta t^\alpha}}. \tag{8.35}$$

8.4.2 Sensitivity Coefficients with GL-Caputo configuration

For GL-Caputo configuration, the sensitivity coefficients $c_\alpha(t)$, $c_a(t)$, $c_k(t)$, $c_{kp}(t)$, and $c_{ki}(t)$ are identical to these with GL-GL implementations given in Eqs. (8.23) to (8.27). The sensitivity coefficient $c_\lambda(t)$ with GL-Caputo configuration differs from that in Eq. (8.28) and it is given as:

$$c_\lambda(t) = \frac{Kk_\mathrm{i}\frac{\partial}{\partial\lambda}\left[\mathscr{I}_\mathrm{C}^\lambda\left(r(t-\tau)-y_\mathrm{e}(t-\tau)\right)\right]}{a+\frac{1}{\Delta t^\alpha}}, \tag{8.36}$$

where $\mathscr{I}_\mathrm{C}^\lambda$ denotes the FO integral with Caputo implementation.

8.5 Results and discussion

This section presents time-dependent sensitivity coefficients that support the evaluation of the uncertainty component propagated to the dynamic response of the FO model in Eq. (8.2). Moreover, it presents the evaluated uncertainty component in the dynamic response of the same model.

Furthermore, this section also presents results corresponding to the uncertainty propagation approach for the closed-loop response proposed in Section 8.3. It further extends the discussion by comparing the closed-loop uncertainty evaluated by different implementations of FO operators. The results of uncertainty evaluation with GL implementation are compared with those obtained using the FO operator based on Riemann-Liouville Eq. (2.20) and Caputo Eq. (2.21) definitions.

8.5.1 Uncertainty propagated in the FO model

This section presents the time-dependent sensitivity coefficients, uncertainty, and dynamic response, along with the corresponding uncertainty band for the FO model in Eq. (8.2).

Figure 8.4 shows the time-dependent sensitivity coefficients defined in Eqs. (8.8) to (8.10). The patterns and magnitudes of these coefficients change with time. The figure indicates that the modeled response exhibits the highest sensitivity to variations in parameter α, as shown in panel (a). This observation follows from the expression of $c_\alpha(t)$ in Eq. (8.8), which depends on all model parameters (α, a, K, and τ). Furthermore, $c_\alpha(t)$ depends on the FO derivative of the estimated response. Therefore, small deviations in α cause large changes in the estimated response y_e. The sensitivity coefficients $c_a(t)$ and $c_K(t)$ also exhibit time-varying behavior. However, their influence on the estimated response of the dynamic model in Eq. (8.2) is less significant than that of α.

The sensitivity coefficient $c_a(t)$ shows the smallest variation in magnitude over time, as shown in Figure 8.4 panel (b). This behavior occurs because $c_a(t)$ depends only on the model parameters α and a, as given in Eq. (8.9). The sensitivity coefficient $c_K(t)$ reflects the influence of variations in parameter K on the estimated response, as shown in Figure 8.4 panel (c). The analysis shows an abrupt change in the magnitude of $c_K(t)$ from zero to approximately 0.45 at 2.2 s. This behavior results from the dependence of $c_K(t)$ on the delayed input $u(t-\tau)$ with $\tau = 2.2$ s, as described in Eq. (8.10).

The digital filtering method proposed in [1] was implemented for the same model to enable a comparison with the proposed method. The digital filtering approach represents

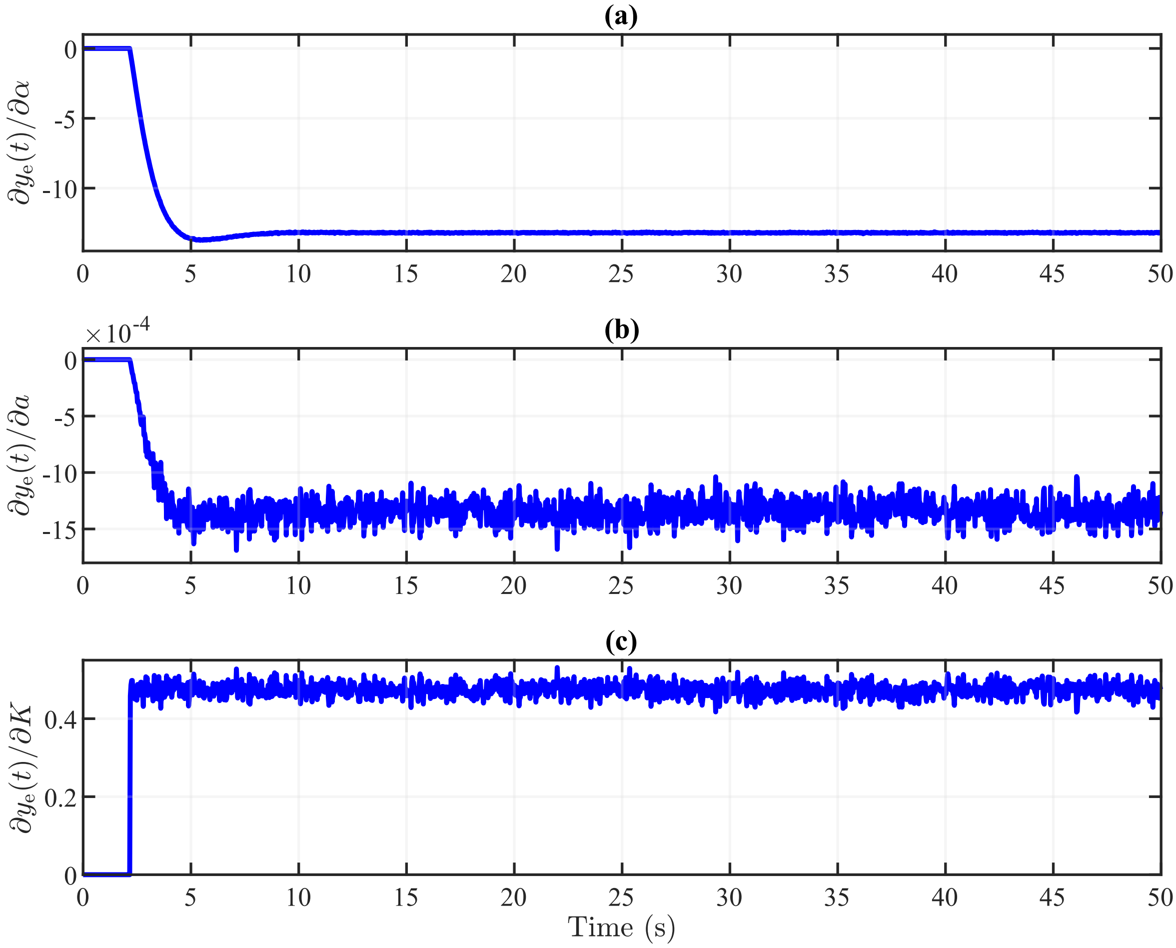

Figure 8.4: Sensitivity coefficients of the FO model as time dependent functions: (a) shows the sensitivity coefficient corresponding to parameter α in Eq. (8.8), (b) shows the sensitivity coefficient corresponding to parameter a in Eq. (8.9), and (c) shows the sensitivity coefficient corresponding to parameter K in Eq. (8.10).

sensitivities as time-dependent functions. Instead of direct computation, this approach transforms the output signal into reduced parameters. This transformation reduces covariance propagation within a reduced parameter space. These functions are then applied to evaluate the uncertainty component associated with the parameters of dynamic model.

Figure 8.5 presents a comparison between the uncertainty evaluated using this method and that obtained using the proposed approach. The figure depicts that the uncertainty component obtained using the proposed approach has a smaller magnitude than that derived from the digital filtering method [1]. The larger magnitude observed in the filtering method may have resulted from information loss during transformation for covariance propagation in the reduced parameter space. The proposed approach avoids such reduction in covariance propagation, which minimizes potential information loss. Therefore, the proposed approach provides a consistent, efficient, and direct evaluation of uncertainty compared to the method described in [1]. Furthermore, the figure indicates that the uncertainty exhibits time-varying magnitude. The uncertainty rises from zero after 2.2 s, shows a small overshoot, and

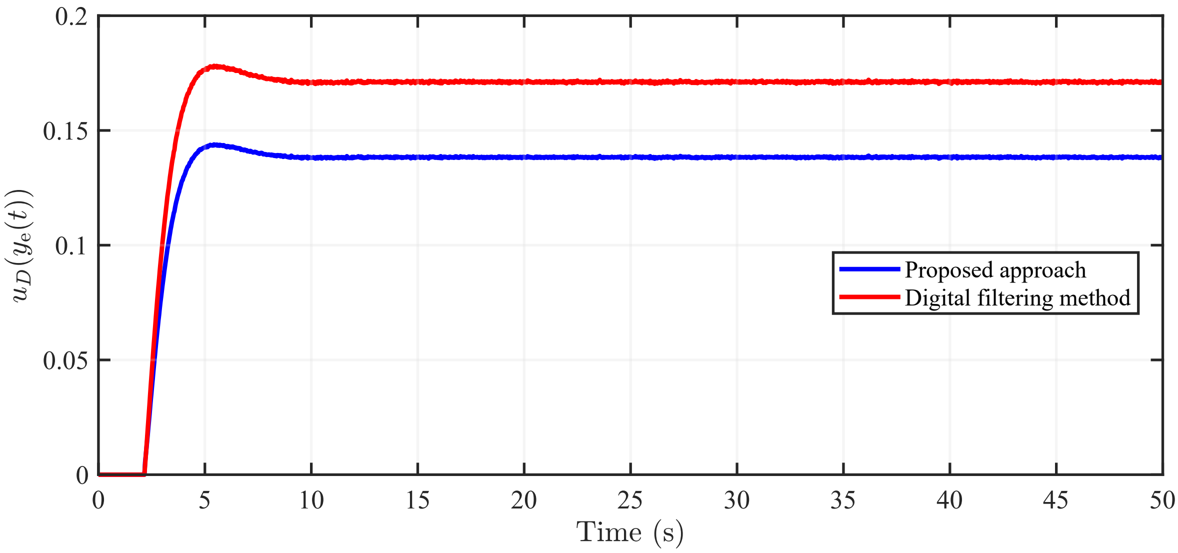

Figure 8.5: Uncertainty contribution $u_D(y_e(t))$ from the identified parameters to the dynamic response of the FO model. The figure shows a comparison of the proposed approach with the digital filtering method [1].

stabilizes at approximately 0.14 after $t = 8$ s. The initial delay in the uncertainty results from the time-delay properties of the FO model in Eq. (8.2).

Figure 8.6 presents a comparison between the experimental data and the averaged response of 200 FO models, with the uncertainty band $\bar{y}_e(t) \pm u_D(y_e(t))$ superimposed. The figure shows that the residual, defined as $\bar{y_m}(t) - \bar{y}_e(t)$, exhibits a large magnitude in the transient phase and varies over time. The residual magnitude decreases and approaches zero as the response reaches the steady state. The uncertainty region remains narrow in the beginning and gradually increases as time progresses. This temporal variation in the uncertainty component supports the trend shown in 8.5.

Furthermore, the averaged measured response lies within the uncertainty bounds, except for the interval $7.5 \text{ s} < t < 14.2 \text{ s}$. This deviation arises because the analysis considers only the uncertainty component associated with parameter identification. The inclusion of additional sources, such as the measuring transducer, VFD, and water pump, would increase the uncertainty band. The present analysis restricts attention to the uncertainty contribution from the identified parameters of the FO model in Eq. (8.2). Moreover, the expanded uncertainty, obtained by multiplying $u_D(y_e(t))$ by the coverage factor $k = 2$, would widen the uncertainty band and encompass the experimental observations.

8.5.2 Uncertainty propagation in closed-loop response

This section presents the dynamic uncertainty associated with the identified parameters of the FO model in Eq. (8.2) and the tuned parameters of the FO-PI controller in the closed-loop response. The section compares uncertainty propagation results for three implementations of FO operators, namely GL in Eqs. (2.12) and (2.13), RL in Eqs. (2.19) and (2.20), and

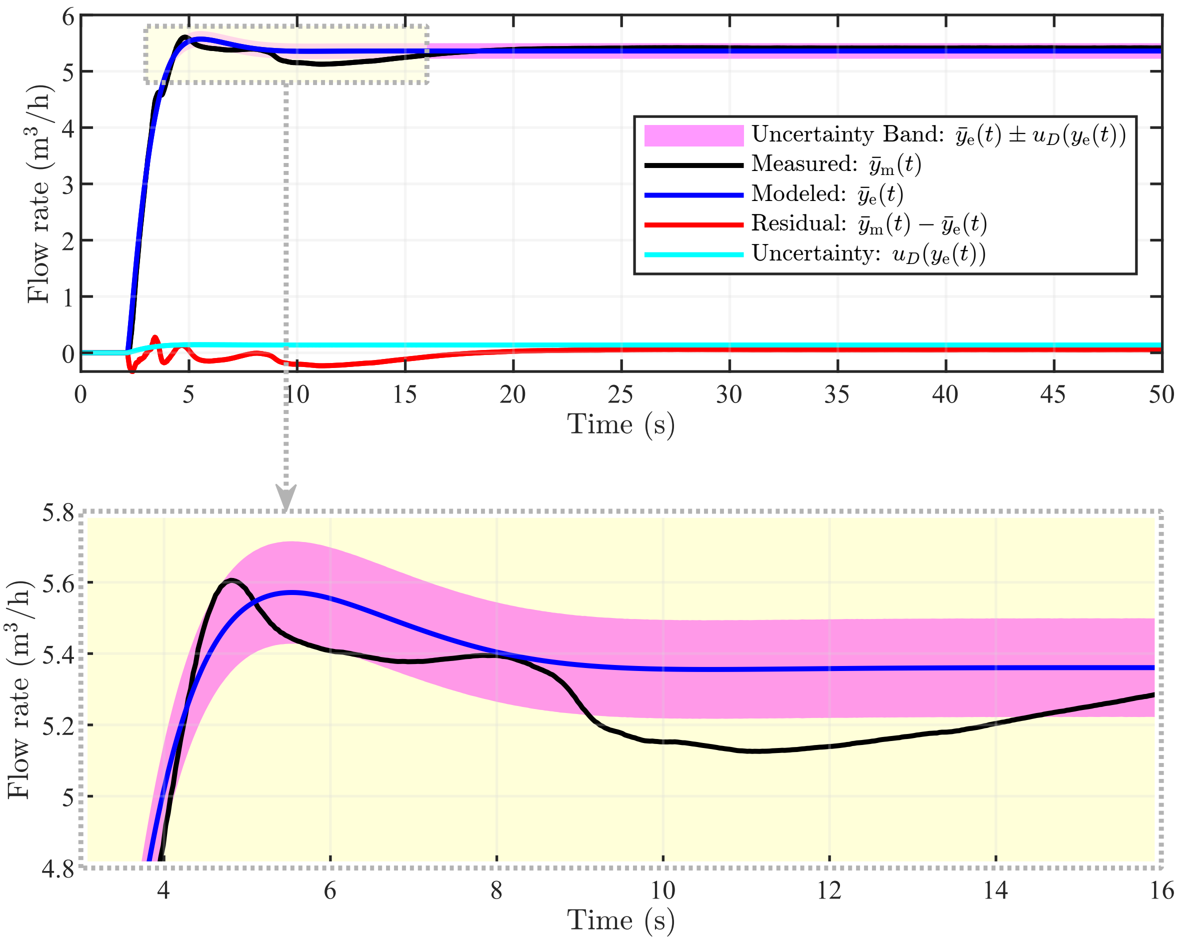

Figure 8.6: The dynamic response of the FO model and the uncertainty of measurement contributed by the identified parameters. Modeled response is average of the responses of 200 FO models, each constructed by the set of identified parameters. Measured response represents the average values of the measured data for 200 passes.

Caputo in Section 2.2.1.

Figure 8.7 shows the sensitivity coefficients associated with the model parameters in the closed-loop structure. At the outset, figure indicates that the sensitivity functions corresponding to identical parameters differ significantly from those in the open-loop, as shown in Figure 8.4. This difference arises because the time-domain expression for the estimated response in the closed-loop in Eq. (8.19) includes the FO controller. In contrast, the open-loop expression includes only the FO model.

Furthermore, the sensitivity coefficients in Figure 8.7 exhibit similar responses during the initial 8 s. The GL-GL and GL-Caputo configurations yield identical results, whereas the GL-RL configuration exhibits significant deviations between 8 s and 50 s. Although GL, RL, and Caputo implementations coincide for zero initial conditions [184], the observed differences in time-dependent sensitivity coefficients for the GL-RL configuration arise from significant variations in the corresponding expressions. These expressions are given in Section 8.3.3 and Section 8.4. Moreover, Figure 8.7 indicates that parameter K exerts the most significant

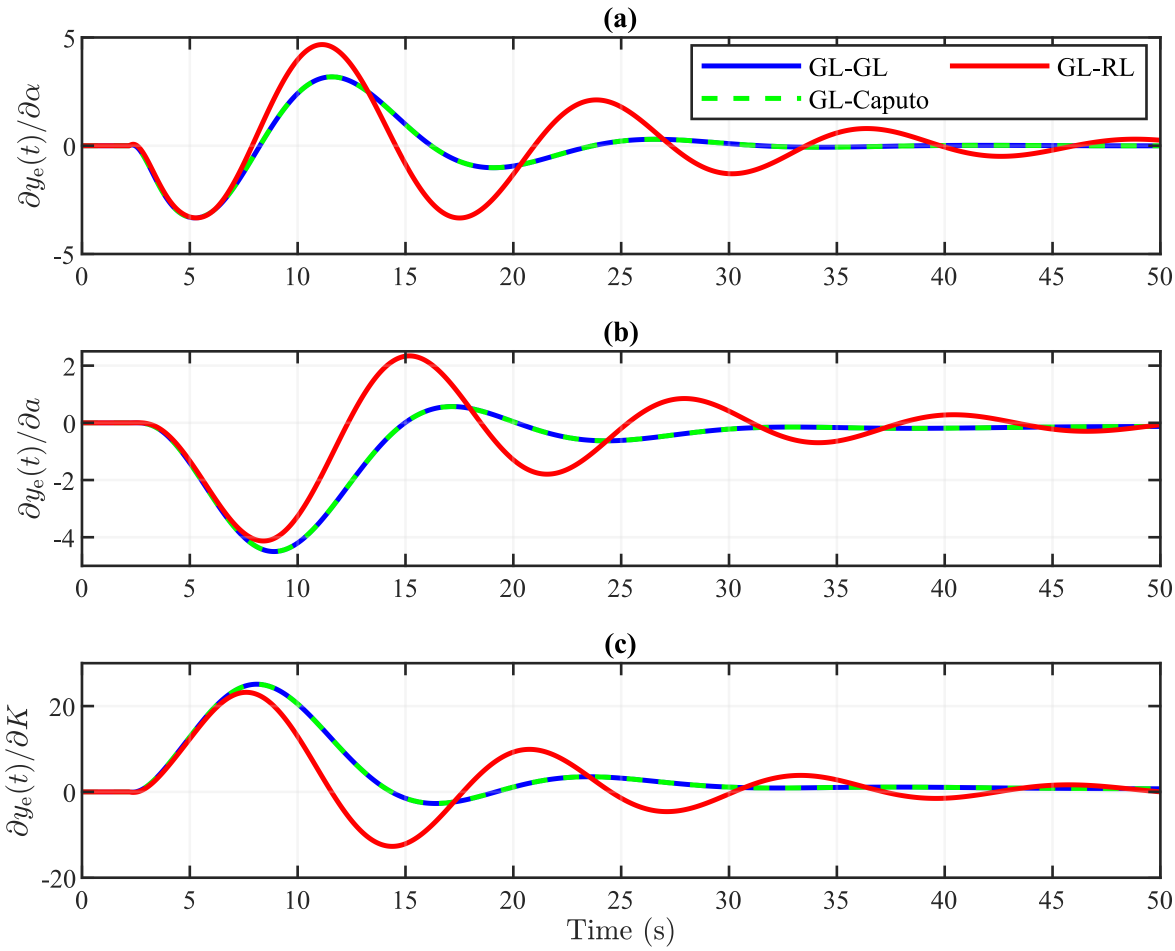

Figure 8.7: Closed-loop sensitivity coefficients associated with the model parameters: (a) corresponds to sensitivity coefficient in Eq. (8.23), (b) corresponds to sensitivity coefficient in Eq. (8.24), and (c) corresponds to sensitivity coefficient in Eq. (8.25) for GL-GL configuration. The corresponding sensitivity coefficients for GL-Caputo and GL-GL-RL configurations are given in Section 8.4.

influence on the estimated response, while parameter a exhibits the least influence. The model parameter α exhibits a moderate influence on the closed-loop response compared to a and K.

Figure 8.8 shows the sensitivity coefficients of the closed-loop response associated with the controller parameters. The figure indicates that the controller parameters k_{p} and k_{i} do not exhibit a significant influence on deviations in the closed-loop response. Only the parameter λ exhibits a significant influence. The time-dependent magnitudes of the corresponding sensitivity coefficients vary identically for the GL-GL and GL-Caputo configurations for all parameters. Moreover, the GL-RL configuration also shows identical behavior for the sensitivity coefficient associated with parameter k_{p}. However, the magnitudes differ for k_{i} and λ in the GL-RL configuration compared to GL-GL and GL-Caputo configurations. This difference arises from significant differences in the corresponding mathematical expressions for the GL-RL configuration, as presented in Section 8.4.

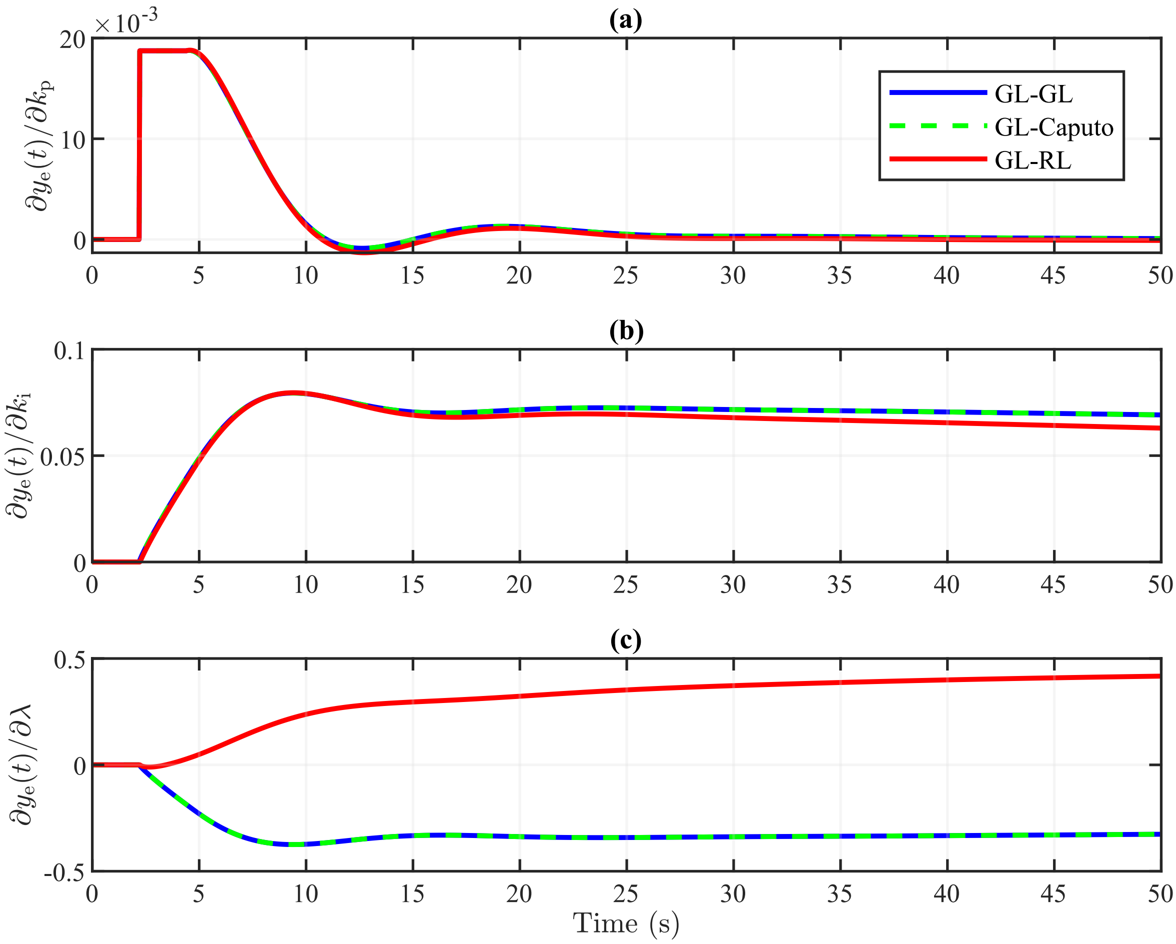

Figure 8.8: Closed-loop sensitivity coefficients associated with the controller parameters: (a) corresponds to sensitivity coefficient in Eq. (8.26), (b) corresponds to sensitivity coefficient in Eq. (8.27), and (c) corresponds to sensitivity coefficient in Eq. (8.28) for GL-GL configuration. The corresponding sensitivity coefficients for GL-Caputo and GL-GL-RL configurations are given in Section 8.4.

These differences in the sensitivity coefficients are reflected in the corresponding dynamic uncertainty propagation for each configuration. Figure 8.9 compares the dynamic uncertainty propagated to the closed-loop response for the GL-GL, GL-RL, and GL-Caputo configurations. The analysis of Figure 8.8 indicates identical dynamic uncertainty for the GL-GL and GL-Caputo configurations. In contrast, the GL-RL configuration exhibits significant deviations from GL-GL and GL-Caputo configurations as time progresses beyond approximately 8 s. The GL-RL configuration exhibits oscillations in the magnitude of the dynamic uncertainty throughout the entire time horizon. These oscillations originate from the evaluated sensitivity coefficients shown in Figure 8.7.

Figure 8.10 presents the closed-loop response of the FO model in Eq. (8.2) with the FO-PI controller. Both the model and the controller use the GL implementation for the FO derivative and integral. The closed-loop system is subjected to a step reference signal starting at $t = 0$ s with a magnitude of 6 m^3/h. The reference input is omitted from the figure, as the objective focuses on dynamic uncertainty rather than reference tracking. The

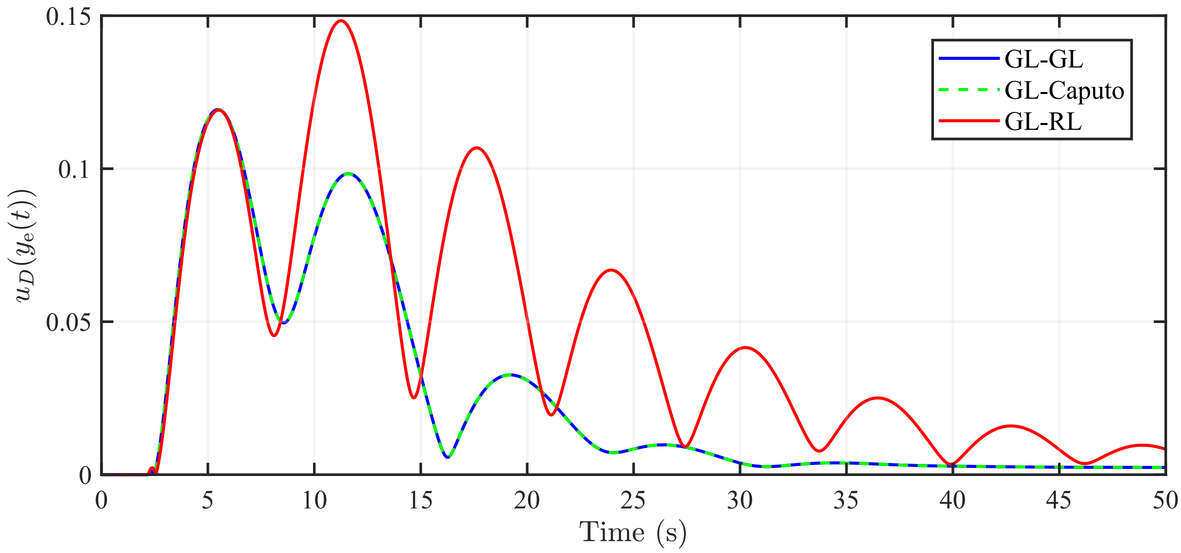

Figure 8.9: Comparison of the closed-loop uncertainty evaluated using different configurations.

semi-transparent region represents the uncertainty band superimposed on the closed-loop response to analyze its variation relative to the system response.

The Figure 8.10 shows that the uncertainty band exhibits a larger spread in the transient region, while it becomes narrower in the steady state. Furthermore, the uncertainty band at approximately $t = 16$ s indicates a narrower spread. The zoomed version in the lower panel of Figure 8.10 may suggest zero uncertainty. However, the uncertainty in this region remains non-zero, as indicated in Figure 8.9. This behavior contrasts with Figure 8.6, where the uncertainty band reaches a higher magnitude in the steady state. This observation is consistent with the dynamic uncertainty for the closed-loop response presented in Figure 8.9. The results discussed in this section support the successful realization of contribution **C.5** listed in Section 1.5.

8.6 Chapter summary

This chapter introduced a direct approach to evaluate the measurement uncertainty component propagated through parameters identified in a FO dynamic model. The study used the experimental data collected from a laboratory flow system for 200 passes under fixed input. For each pass, the method identified a FO model with time delay by minimizing the root mean square of residuals. The identified parameters of the FO model were passed through the normality tests and it was verified that the parameters follow normal distributions. This finding supports their treatment within a probabilistic framework. The proposed method derived time-dependent sensitivity coefficients analytically by differentiating the model output with respect to each parameter. The approach then evaluated the propagated uncertainty using the law of propagation of uncertainty together with the covariance matrix of the parameters.

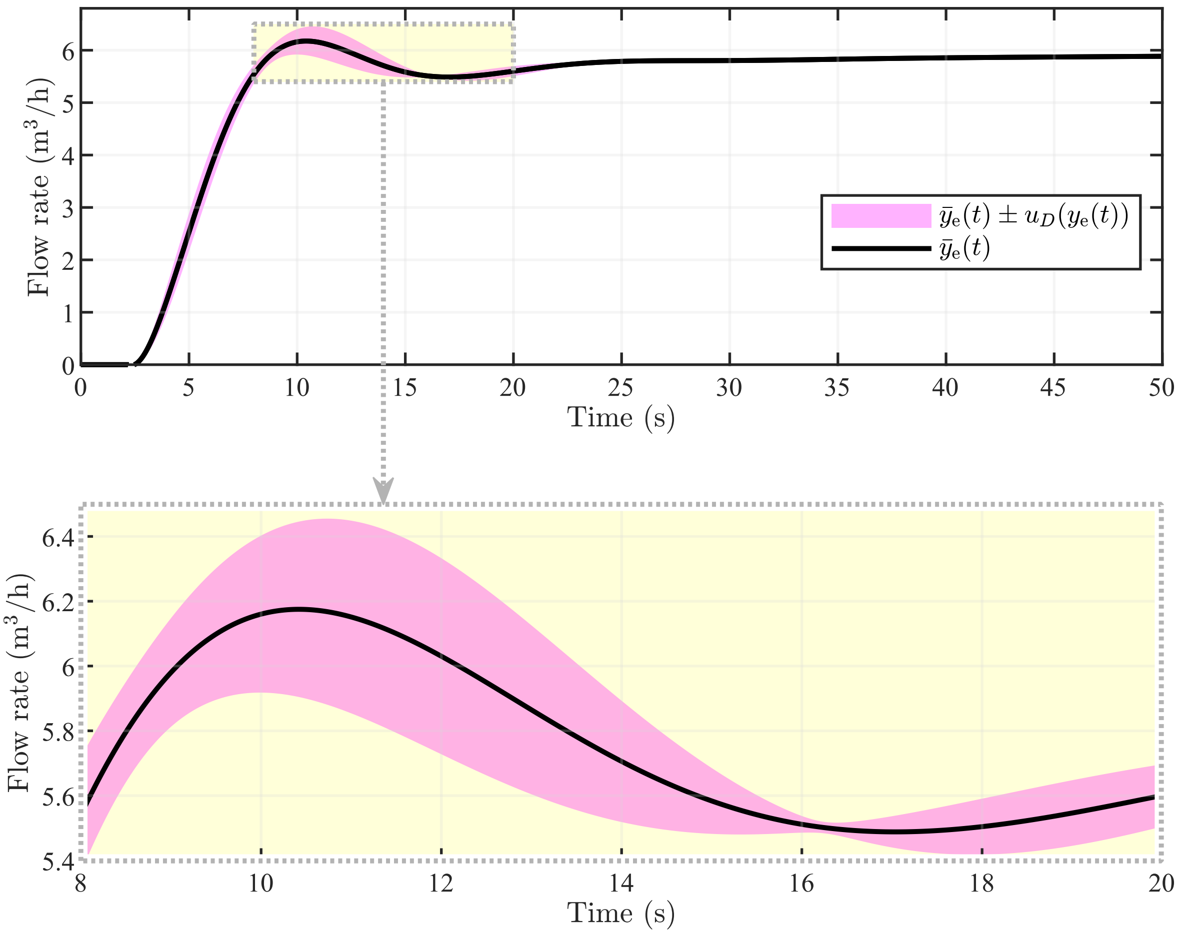

Figure 8.10: Closed-loop dynamic response with the GL-GL dynamic uncertainty band superimposed.

A comparison with the digital filtering method indicates that the proposed provides provides a more conservative estimate. It also uses the available data more efficiently and reduces the risk of information loss caused by signal transformation. The evaluated time-varying uncertainty band consistently encloses the measured response of the system. This agreement confirms the correctness and practical applicability of the proposed framework.

The chapter then extended this approach to evaluate the uncertainty component propagated to the closed-loop response. First, a frequency-domain approach was applied to design the FO-PI controller for the FO model of the flow system. The closed-loop FO-DIE provided sensitivity coefficients of the closed-loop response. These sensitivity coefficients quantified the propagated uncertainty component in the closed-loop dynamic response. A comparison of uncertainty propagation using the Grünwald-Letnikov, Riemann-Liouville, and Caputo definitions was also performed. This comparison assessed the consistency of the proposed approach under different implementations of the FO operators.

Moreover, it validates hypothesis **H.3** of the dissertation listed in Section 1.4. Finally, it also presents contributions **C.3**, **C.4**, and **C.5** listed in Section 1.5.

CHAPTER 9

Conclusions and future directions

This chapter summarizes the findings, contributions, and limitations of the methods presented in each chapter of the dissertation. It also proposes future research directions to address the identified limitations.

9.1 Conclusions

This dissertation investigates the measurement uncertainty of quantities described by non-integer-order differential integral equations. The study integrates metrology, model identification, control theory, and fractional-order calculus to analyze dynamic systems that exhibit nonlinear behavior, distributed dynamics, and measurement uncertainty. The dissertation follows a systematic workflow to address challenges at each implementation step. It builds on concepts introduced in preceding steps and concludes by developing a framework to evaluate the uncertainty propagation. The proposed framework evaluates the measurement uncertainty associated with the identified parameters in the dynamic response of fractional-order models. The implementation workflow of each chapter is summarized as follows.

Chapter 1 emphasizes the importance of the study. It describes the problem under consideration, and presents motivation to undertake the research. It then lists the dissertation objectives and states the hypotheses to be verified. It also presents the contributions resulting from the implemented approaches. The chapter concludes by outlining the structure of the remaining dissertation.

Chapter 2 presents the foundations of metrology. It also presents the definitions of Fractional-Order (FO) operators and Integer-Order (IO) approximation methods used for their practical realization. Furthermore, it reviews methods from literature for mathematical modeling, uncertainty assessment, and control design in real-time applications. The chapter concludes by identifying limitations of existing methods that address problems similar to those in this dissertation.

Chapter 3 presents the case studies used as application examples to validate the proposed approaches. The applications follow a progression from simple to complex systems.

The first example considers a Single-Input Single-Output (SISO) linear FO system in simulation. It evaluates the accuracy of the approximation methods. The second example considers a Multi-Input Multi-Output (MIMO) nonlinear system in simulation. It verifies the proposed control design approach. The third example considers a laboratory setup. It validates the proposed methods through hardware experiments.

The chapter also presents the hardware configuration of the experimental setup and details the data acquisition process. Furthermore, it describes the measured data resulting from the data acquisition.

Chapter 4 implements **Obj.1** and presents a detailed accuracy analysis of the approximation methods listed in Chapter 2 for realizing FO operators. The analysis uses `MATLAB` simulations and the first example described in Chapter 3, i.e., a linear SISO FO system. Based on the selected approximation method, the chapter then analyzes its closed-loop performance with the second example, i.e., a MIMO nonlinear system in `Simulink`.

Chapter 5 implements **Obj.2** and presents linear parameter varying approach to model the laboratory flow rate measurement system. The chapter uses the experimental data from third application example presented in Chapter 3, i.e., a laboratory hardware setup. It also compares the results of the proposed approach with classical IO models.

Chapter 6 implements **Obj.3** & **Obj.4**, and proposes a FO modeling approach for the flow system presented in Chapter 3. The approach uses a fixed input instead of the full operating range and investigates the applicability of FO modeling to accurately represent the dynamics of a complex nonlinear system.
This chapter implements the Grünwald-Letnikov (GL) formulation of the FO operators. It evaluates model robustness by introducing bounded parameter perturbations and analyzing their influence on the estimated response. It further examines the influence of the truncation-order of GL coefficients and solver selection on modeling accuracy.

Chapter 7 implements **Obj.5** and presents tuning rules for designing FO Proportional-Integral (PI) controllers. It develops a control design approach using linear SISO models of the second example in Chapter 3. It further validates the approach in a nonlinear MIMO configuration for the same system. It also analyzes the influence of the approximation methods presented in Chapter 2 on the closed-loop response. This method enables evaluation of uncertainty propagation in the closed-loop response in Chapter 8.

Chapter 8 implements **Obj.6** and proposes a framework to analyze the propagation of measurement uncertainty associated with the estimated parameters. It builds on the conclusions presented in Chapter 6 and develops a FO time-delay model for the flow system in Chapter 3 under a fixed input. It then applies the tuning rules from Chapter 7 to design a FO-PI controller for the flow system. Using the closed-loop structure, it evaluates the uncertainty propagated in the dynamic response. It further analyzes the influence of different implementations of FO operators on uncertainty assessment.

9.1.1 Summary of the key findings and contributions

This section summarizes the contributions and key findings presented in the dissertation.

The dissertation examines approximation methods required for practical realization of FO operators in Chapter 4. It analyzes widely used frequency-domain methods, including Continued Fraction Expansion (CFE), Matsuda Method (MM), Carlson Method, Modified Stability Boundary Locus (M-SBL), and Oustaloup-based filters. The results show that several methods introduce approximation errors. These errors affect steady-state response, transient dynamics, phase characteristics, and stability margins of the approximated model. The Refined Oustaloup and Xue Oustaloup methods exhibit minimal transient errors and no steady-state error. However, these methods increase the approximation order by two compared to the standard Oustaloup method. The M-SBL method represents an alternative when considering steady-state error. However, it introduces magnitude and phase errors in the frequency response. These errors increase with increasing frequency. The CFE method yields the lowest model order but produces the largest steady-state error among the compared methods. In conclusion, method selection requires a trade-off between approximation accuracy and implementation complexity. Based on this trade-off, the chapter selects the standard Oustaloup method and evaluates its closed-loop performance on a nonlinear system.

Sensory measurements provide the measured quantity and its associated uncertainty. This property of the measurement system complicates modeling of the dynamic response. Modeling becomes more challenging when data originate from a complex nonlinear system. The challenge increases further when the data exhibit varying sampling time. To address these issues, Chapter 5 introduces an LPV approach. It models the dynamic response of a laboratory flow system under varying input conditions.

To address similar problems, Chapter 6 presents a FO model identification approach based on GL-based optimization. The nominal FO model obtained by this approach remains robust to bounded parameter perturbations up to $+10\,\%$. Increasing the perturbation to $+20\,\%$ causes deviations in both transient and steady-state responses. The GL-based optimization imposes significant computational burden due to recursive calculation of GL coefficients. An online optimization tool, State-of-the-Art Solvers for Numerical Optimization (NEOS-server), reduces the computation time. However, the computation time remains significantly higher than that of IO modeling approaches. Therefore, this chapter analyzes the influence of truncation order of GL coefficients on the dynamic response of FO models. It also evaluates different solver options available in NEOS-server to identify a suitable optimization solver. The findings presented in this chapter validate the hypotheses **H.1** and **H.2** of the dissertation listed in Section 1.4. Furthermore, this chapter presents the contribution **C.1** listed in Section 1.5 of Chapter 1.

Classical frequency-domain approaches enable analytical design of FO controllers. Desired time-domain closed-loop characteristics define required gain and phase margins from Bode plots. These characteristics support the construction of FO-PI controllers. Setting the phase slope to zero at the gain-crossover frequency, together with gain and magnitude conditions of the open-loop TF, yields three equations. Solving these equations provides the controller parameters. The resulting controller ensures phase flatness around the gain-crossover frequency. This property improves robustness of the FO controller to bounded parameter variations in the dynamic model. Chapter 7 proposes this method to design a FO-PI controller using TRAS as an application example. The same method is later applied to design the FO controller for the flow rate measurement system in Chapter 8 under constant input conditions. This approach enables evaluation of uncertainty propagation in the closed-loop response. This chapter presents the contribution **C.2** listed in Section 1.5.

Chapter 8 established a direct framework for evaluating the uncertainty component propagated through parameters identified in FO dynamic models. The method was applied to a laboratory flow rate measurement system operated for 200 experimental passes. For each pass, a FO time-delay model was identified by minimizing residuals. Statistical analysis verified that the identified parameters followed normal probability distributions. This result enabled a probabilistic description of parameters and their covariance structure. The time-dependent sensitivity coefficients were derived analytically by differentiating the modeled response with respect to each parameter. These coefficients were then combined with covariance matrices to evaluate the uncertainty components using the law of propagation of uncertainty. The resulting uncertainty bounds remained consistent with the measured experimental responses. The chapter further extended the developed framework to the analysis of uncertainty propagation in closed-loop configuration. A frequency-domain procedure developed in Chapter 7 was employed to design a FO-PI controller for the identified model of the flow rate system. The resulting closed-loop FO differential integral equation was then used to derive sensitivity coefficients of the closed-loop response. These coefficients enabled the evaluation of uncertainty component propagated through the controlled dynamic behavior. Furthermore, the uncertainty propagated in the closed-loop response, estimated using GL, Riemann–Liouville, and Caputo interpretations of the FO operators, exhibits consistent results. The findings presented in this chapter validate the hypothesis **H.3** of the dissertation listed in Section 1.4. Furthermore, this chapter presents the contributions **C.3**, **C.4** and **C.5** listed in Section 1.5 of Chapter 1.

9.1.2 Limitations of the proposed approaches

The FO model developed using GL-based optimization with experimental data provides a robust estimated response under bounded parameter variations. However, computing the GL coefficients at each iteration imposes high computational cost. This cost depends on the truncation order (TO) of the GL coefficients. Therefore, the proposed FO modeling approach exhibits a trade-off between computational time and accuracy. The TO directly influences this trade-off. Selecting an optimal TO during the optimization can reduce computation time while maintaining suitable model accuracy. The dissertation does not address adaptive selection of the truncation order.

Moreover, the dissertation proposes an uncertainty evaluation framework for SISO FO dynamic systems with normally distributed parameters. It does not address the general case of non-normal parameter distributions. The dissertation also limits uncertainty propagation to measurement uncertainty associated with identified parameters. It does not consider contributions from other uncertainty sources. Furthermore, it does not address uncertainty propagation in FO systems with known parameters described by well-defined FO differential equations.

9.2 Future research directions

Future research can introduce the TO as a decision variable in GL-based optimization. This approach can support efficient FO model development for real-time systems. It may reduce computation time while identifying an optimal FO model. Moreover, regularization techniques in the optimization process can limit excessive parameter sensitivities. These techniques can also mitigate potential overfitting. Bayesian optimization offers a principled alternative approach [176, 177]. It can incorporate prior distributions and enable uncertainty quantification. This approach may improve parameter estimation reliability under noisy measurement conditions.

Furthermore, the proposed uncertainty propagation approach can include additional measurement uncertainty sources, i.e., the measuring transducer, variable frequency drive, and temperature effects on pump dynamics, etc. The approach can also be generalized to cases where model parameters follow non-normal distributions. Moreover, the proposed approach can be extended to incorporate uncertainty propagation in multi-input multi-output systems.

Appendix A

Microsoft Copilot prompt used for language editing

```
ROLE: Thesis Language Editor for LaTeX-based PhD Thesis in Control Systems & Metrology

TASK:
When I provide text from my LaTeX document, you must:

1. Rewrite all text in active voice.
2. Keep each sentence ≤ 15 words; allow ≤ 18 words only when needed.
3. Improve the language quality: clarity, precision, readability, and academic tone.
4. Maintain a formal style expected in a Polish technical university PhD thesis.
5. Use correct terminology from:
   - control engineering
   - system identification
   - fractional calculus
   - metrology and measurement systems
6. Improve grammar, cohesion, flow, and structure.
7. Preserve scientific meaning and all LaTeX markup, math, and notation.
8. Never alter LaTeX commands such as \cite{}, \ref{}, \label{}, \ac{}, \SI{}, math mode, or equations.

OUTPUT:
- Return the corrected text only.
- Keep all LaTeX intact.
- Do not summarize or explain unless I ask.

TRIGGER:
I will send text starting with "EDIT:" followed by the LaTeX content to improve.
```

Listing A.1: Prompt used for language editing of the dissertation text.

Bibliography

[1] Jan Peter Hessling. "A novel method of evaluating dynamic measurement uncertainty utilizing digital filters". In: *Measurement Science and Technology* 20.5 (2009), p. 055106.

[2] Józef Wiora and Alicja Wiora. "Measurement uncertainty calculations for pH value obtained by an ion-selective electrode". In: *Sensors* 18.6 (2018), p. 1915.

[3] Mohammadamin Ebadollahi and Sharif Rahman. "Time-dependent uncertainty quantification analysis of complex dynamical systems". In: *Probabilistic engineering mechanics* 80 (2025), p. 103776.

[4] Joint Committee for Guides in Metrology. "Evaluation of measurement data—Guide to the expression of uncertainty in measurement". In: *Int. Organ. Stand. Geneva ISBN* 50 (2008), p. 134.

[5] Jan Peter Hessling. "Metrology for non-stationary dynamic measurements". In: *Advances in Measurement systems. Vukovar: InTech* (2010), pp. 221–256.

[6] Roman Lewandowski, Mieczyslaw Slowik, and Maciej Przychodzki. "Parameters identification of fractional models of viscoelastic dampers and fluids". In: *Struct. Eng. Mech* 63.2 (2017), pp. 181–193.

[7] Paolo Lino, Guido Maione, and Fabrizio Saponaro. "Fractional-order modeling of high-pressure fluid-dynamic flows: An automotive application". In: *IFAC-PapersOnLine* 48.1 (2015), pp. 382–387.

[8] Bill Goodwine. "Modeling a multi-robot system with fractional-order differential equations". In: *2014 IEEE International Conference on Robotics and Automation (ICRA)*. IEEE. 2014, pp. 1763–1768.

[9] Bochao Wang and Leif Kari. "A nonlinear constitutive model by spring, fractional derivative and modified bounding surface model to represent the amplitude, frequency and the magnetic dependency for magneto-sensitive rubber". In: *Journal of Sound and Vibration* 438 (2019), pp. 344–352.

[10] Józef Wiora and Alicja Wiora. "Influence of methods approximating fractional-order differentiation on the output signal illustrated by three variants of Oustaloup filter". In: *Symmetry* 12.11 (2020), p. 1898.

[11] Mohammed-Salah Abdelouahab and Nasr-Eddine Hamri. "The Grünwald–Letnikov fractional-order derivative with fixed memory length". In: *Mediterranean Journal of Mathematics* 13.2 (2016), pp. 557–572.

[12] Concepción A Monje, YangQuan Chen, Blas M Vinagre, et al. *Fractional-order systems and controls: fundamentals and applications*. Springer, 2010.

[13] Karol Marciniak, Faisal Saleem, and Józef Wiora. "Influence of models approximating the fractional-order differential equations on the calculation accuracy". In: *Communications in Nonlinear Science and Numerical Simulation* 131 (2024), p. 107807.

[14] Faisal Saleem, Józef Wiora, and Delfim FM Torres. "Fractional-order modeling of a flow rate measurement system utilizing Grünwald–Letnikov based optimization". In: *Measurement* (2026), p. 120692.

[15] Joint Committee for Guides in Metrology. *International Vocabulary of Metrology — Basic and General Concepts and Associated Terms (VIM)*. 3rd ed., 2008 version with minor corrections. JCGM 200:2012. Sèvres, France: Bureau International des Poids et Mesures, 2012.

[16] Bayan Tallawi, Kevin Romieu, and Jacques-Olivier Favreau. "Dynamic metrology in practice: From concepts to calibration services". In: *Measurement: Sensors* 38 (2025), p. 101642.

[17] Sascha Eichstädt, Karl H. Ruhm, and Alexander Leonidovich Shestakov. "Dynamic measurement and its relation to metrology, mathematical theory and signal processing: A review". In: *Journal of Physics: Conference Series*. Vol. 1065. IOP Publishing. 2018, p. 212018.

[18] Lin Chen, Wentao Yu, Guoyang Cheng, et al. "State-of-charge estimation of lithium-ion batteries based on fractional-order modeling and adaptive square-root cubature Kalman filter". In: *Energy* 271 (2023), p. 127007.

[19] Pengchong Chen and Ying Luo. "Analytical fractional-order PID controller design with Bode's ideal cutoff filter for PMSM speed servo system". In: *IEEE Transactions on Industrial Electronics* 70.2 (2022), pp. 1783–1793.

[20] Necdet Sinan Özbek. "Design and real-time implementation of a robust fractional second-order sliding mode control for an electromechanical system comprising uncertainties and disturbances". In: *Engineering Science and Technology, an International Journal* 35 (2022), p. 101212.

[21] Juan J Gude, Pablo García Bringas, Marco Herrera, et al. "Fractional-order model identification based on the process reaction curve: A unified framework for chemical processes". In: *Results in Engineering* 21 (2024), p. 101757.

[22] Riccardo Caponetto, Salvatore Graziani, Emanuele Murgano, et al. "Modeling of a fractional order element based on bacterial cellulose and ionic liquids". In: *Journal of Dynamic Systems, Measurement, and Control* 143.7 (2021), p. 071009.

[23] Sverre Holm, Sri Nivas Chandrasekaran, and Sven Peter Näsholm. "Adding a low frequency limit to fractional wave propagation models". In: *Frontiers in Physics* 11 (2023), p. 1250742.

[24] Aleksei Tepljakov and Aleksei Tepljakov. "FOMCON: fractional-order modeling and control toolbox". In: *Fractional-order modeling and control of dynamic systems* (2017), pp. 107–129.

[25] Blas M. Vinagre, Igor Podlubny, Alfredo Limas Hernandez, et al. "Some approximations of fractional order operators used in control theory and applications". In: *Fractional calculus and applied analysis* 3.3 (2000), pp. 231–248.

[26] M Cristina Caputo and Delfim FM Torres. "Duality for the left and right fractional derivatives". In: *Signal Processing* 107 (2015), pp. 265–271.

[27] Ricardo Almeida. "A Caputo fractional derivative of a function with respect to another function". In: *Communications in Nonlinear Science and Numerical Simulation* 44 (2017), pp. 460–481.

[28] Manuel Duarte Ortigueira. *Fractional calculus for scientists and engineers*. Vol. 84. Springer Science & Business Media, 2011.

[29] Anatoliĭ Aleksandrovich Kilbas, Hari M. Srivastava, and Juan J. Trujillo. *Theory and Applications of Fractional Differential Equations*. Vol. 204. Elsevier, 2006.

[30] Kenneth S Miller. "The Weyl fractional calculus". In: *Fractional Calculus and Its Applications: Proceedings of the International Conference Held at the University of New Haven, June 1974*. Springer. 2006, pp. 80–89.

[31] Fausto Ferrari. "Weyl and Marchaud derivatives: A forgotten history". In: *Mathematics* 6.1 (2018), p. 6.

[32] Hengfei Ding, Changpin Li, and YangQuan Chen. "High-order algorithms for Riesz derivative and their applications (II)". In: *Journal of Computational Physics* 293 (2015), pp. 218–237.

[33] Małgorzata Klimek. "Sequential fractional differential equations with Hadamard derivative". In: *Communications in Nonlinear Science and Numerical Simulation* 16.12 (2011), pp. 4689–4697.

[34] Živorad Tomovski, Rudolf Hilfer, and Hari Mohan Srivastava. "Fractional and operational calculus with generalized fractional derivative operators and Mittag–Leffler type functions". In: *Integral transforms and special functions* 21.11 (2010), pp. 797–814.

[35] Jordan Hristov. "On the Atangana–Baleanu derivative and its relation to the fading memory concept: the diffusion equation formulation". In: *Fractional Derivatives with Mittag-Leffler Kernel: Trends and Applications in Science and Engineering*. Springer, 2019, pp. 175–193.

[36] Behzad Ghanbari and Abdon Atangana. “A new application of fractional Atangana–Baleanu derivatives: designing ABC-fractional masks in image processing”. In: *Physica A: Statistical Mechanics and its Applications* 542 (2020), p. 123516.

[37] Zhentao Tang, Kaiyu Wang, Yan Zang, et al. “Fractional-order water flow optimizer”. In: *International Journal of Computational Intelligence Systems* 17.1 (2024), p. 84.

[38] Salman Jahanshahi, Esmail Babolian, Delfim FM Torres, et al. “Solving Abel integral equations of first kind via fractional calculus”. In: *Journal of King Saud University-Science* 27.2 (2015), pp. 161–167.

[39] Diaa Eldin Elgezouli and Abdulrahman BM Alzahrani. “Optimizing edge detection efficiency with a Grünwald–Letnikov fractional network”. In: *Electronics* 13.16 (2024), p. 3298.

[40] Rudolf Scherer, Shyam L Kalla, Yifa Tang, et al. “The Grünwald–Letnikov method for fractional differential equations”. In: *Computers & Mathematics with Applications* 62.3 (2011), pp. 902–917.

[41] Yuri Luchko. “Fractional derivatives and the fundamental theorem of fractional calculus”. In: *Fractional Calculus and Applied Analysis* 23.4 (2020), pp. 939–966.

[42] Delfim FM Torres. “The Duality Theory of Fractional Calculus and a New Fractional Calculus of Variations Involving Left Operators Only”. In: *Mediterranean Journal of Mathematics* 21.3 (2024), p. 106.

[43] Zaid Odibat. “Approximations of fractional integrals and Caputo fractional derivatives”. In: *Applied Mathematics and Computation* 178.2 (2006), pp. 527–533.

[44] Igor Podlubny. *Fractional differential equations: an introduction to fractional derivatives, fractional differential equations, to methods of their solution and some of their applications*. Vol. 198. elsevier, 1998.

[45] Suhash C. Dutta Roy. “On the realization of a constant-argument immittance or fractional operator”. In: *IEEE Transactions on Circuit Theory* 14.3 (1967), pp. 264–274.

[46] Furkan Nur Deniz, Baris Baykant Alagoz, Nusret Tan, et al. “Revisiting four approximation methods for fractional order transfer function implementations: Stability preservation, time and frequency response matching analyses”. In: *Annual Reviews in Control* 49 (2020), pp. 239–257.

[47] Dalia Yousri, Amr M AbdelAty, Ahmed G Radwan, et al. “Comprehensive comparison based on meta-heuristic algorithms for approximation of the fractional-order Laplacian sα as a weighted sum of first-order high-pass filters”. In: *Microelectronics Journal* 87 (2019), pp. 110–120.

[48] Matsuda Khoichi and FUjii Hironori. "H_∞ Optimized waveabsorbing control: Analytical and experimental result". In: *Journal of Guidance, Control, and Dynamics* 16.6 (1993), pp. 1146–1153.

[49] Battula Tirumala Krishna. "Studies on fractional order differentiators and integrators: A survey". In: *Signal processing* 91.3 (2011), pp. 386–426.

[50] Nitisha Shrivastava and Pragya Varshney. "Rational approximation of fractional order systems using Carlson method". In: *2015 International Conference on Soft Computing Techniques and Implementations (ICSCTI)*. IEEE. 2015, pp. 76–80.

[51] G Carlson and C Halijak. "Approximation of fractional capacitors $(1/s)^{(1/n)}$ by a regular Newton process". In: *IEEE Transactions on Circuit theory* 11.2 (1964), pp. 210–213.

[52] Furkan Nur Deniz, Baris Baykant Alagoz, Nusret Tan, et al. "An integer order approximation method based on stability boundary locus for fractional order derivative/integrator operators". In: *ISA transactions* 62 (2016), pp. 154–163.

[53] Clara Ionescu, Jose Tenreiro Machado, and Robin De Keyser. "Fractional-order impulse response of the respiratory system". In: *Computers & Mathematics with Applications* 62.3 (2011), pp. 845–854.

[54] Abdelfateh Charef, Hun H. Sun, YY Tsao, et al. "Fractal system as represented by singularity function". In: *IEEE Transactions on automatic Control* 37.9 (1992), pp. 1465–1470.

[55] Wojciech Mitkowski and Krzysztof Oprzędkiewicz. "An estimation of accuracy of Charef approximation". In: *Theoretical Developments And Applications Of Non-Integer Order Systems: 7th Conference On Non-Integer Order Calculus And Its Applications, Szczecin, Poland*. Springer. 2015, pp. 71–80.

[56] Mark Alber, Adrian Buganza Tepole, William R Cannon, et al. "Integrating machine learning and multiscale modeling—perspectives, challenges, and opportunities in the biological, biomedical, and behavioral sciences". In: *NPJ digital medicine* 2.1 (2019), p. 115.

[57] Johan Schoukens and Lennart Ljung. "Nonlinear system identification: A user-oriented road map". In: *IEEE Control Systems Magazine* 39.6 (2019), pp. 28–99.

[58] Adil Brouri, Fatima-Zahra Chaoui, and Fouad Giri. "Identification of Hammerstein–Wiener models with hysteresis front nonlinearities". In: *International Journal of Control* 95.12 (2022), pp. 3353–3367.

[59] Jianqing Fan. *Local polynomial modelling and its applications: monographs on statistics and applied probability 66*. Routledge, 2018.

[60] Johan Paduart, Lieve Lauwers, Jan Swevers, et al. “Identification of nonlinear systems using polynomial nonlinear state space models”. In: *Automatica* 46.4 (2010), pp. 647–656.

[61] Johan Schoukens, Mark Vaes, and Rik Pintelon. “Linear system identification in a nonlinear setting: Nonparametric analysis of the nonlinear distortions and their impact on the best linear approximation”. In: *IEEE Control Systems Magazine* 36.3 (2016), pp. 38–69.

[62] Alexandre Mauroy and Jorge Goncalves. “Linear identification of nonlinear systems: A lifting technique based on the Koopman operator”. In: *2016 IEEE 55th Conference on Decision and Control (CDC)*. IEEE. 2016, pp. 6500–6505.

[63] Daniel Bruder, Xun Fu, R Brent Gillespie, et al. “Data-driven control of soft robots using Koopman operator theory”. In: *IEEE transactions on robotics* 37.3 (2020), pp. 948–961.

[64] Morgan T Gillespie, Charles M Best, Eric C Townsend, et al. “Learning nonlinear dynamic models of soft robots for model predictive control with neural networks”. In: *2018 IEEE International Conference on Soft Robotics (RoboSoft)*. IEEE. 2018, pp. 39–45.

[65] Faisal Saleem, Ahsan Ali, Inam-ul-hassan Shaikh, et al. “Application and comparison of kernel functions for linear parameter varying model approximation of nonlinear systems”. In: *Applied Mathematics-A Journal of Chinese Universities* 38.1 (2023), pp. 58–77.

[66] Nur Assani, Petar Matić, and Danko Kezić. “Flow control process identification using Matlab’s System Identification Toolbox”. In: *2022 8th International Conference on Control, Decision and Information Technologies (CoDIT)*. Vol. 1. IEEE. 2022, pp. 1228–1232.

[67] Jalu A Prakosa, Edi Kurniawan, Hendra Adinanta, et al. “Experimental based identification model of low fluid flow rate control systems”. In: *2020 International Conference on Radar, Antenna, Microwave, Electronics, and Telecommunications (ICRAMET)*. IEEE. 2020, pp. 200–205.

[68] Haroon Imtiaz and Imran Akhtar. “Pod-based reduced-order modeling in fluid flows using system identification strategy”. In: *2020 17th International Bhurban Conference on Applied Sciences and Technology (IBCAST)*. IEEE. 2020, pp. 507–512.

[69] Krisztian Mark Balla, Casper Houtved Knudsen, Adis Hodzic, et al. “Nonlinear grey-box identification of sewer networks with the backwater effect: An experimental study”. In: *2021 IEEE Conference on Control Technology and Applications (CCTA)*. IEEE. 2021, pp. 1202–1207.

[70] Yolanda Bolea, Vicenç Puig, and Joaquim Blesa. "Linear parameter varying modeling and identification for real-time control of open-flow irrigation canals". In: *Environmental modelling & software* 53 (2014), pp. 87–97.

[71] Xing Jin, Biao Huang, and David S Shook. "Multiple model LPV approach to nonlinear process identification with EM algorithm". In: *Journal of Process Control* 21.1 (2011), pp. 182–193.

[72] Quanhong Wu, Suifeng Zou, Xuemei Zhang, et al. "Forecasting the transition to undesirable gas-liquid two-phase flow patterns in pipeline-riser system: A method based on fast identification of global flow patterns". In: *International Journal of Multiphase Flow* 149 (2022), p. 103998.

[73] Ahmed Elkhashap, Daniel Rueschen, and Dirk Abel. "Distributed parameter modeling of fluid transmission lines". In: *Journal of Process Control* 106 (2021), pp. 155–172.

[74] Waldemar Minkina. "Theoretical and experimental identification of the temperature sensor unit step response non-linearity during air temperature measurement". In: *Sensors and Actuators A: Physical* 78.2-3 (1999), pp. 81–87.

[75] Waldemar Minkina. "Non-linear models of temperature sensor dynamics". In: *Sensors and Actuators A: Physical* 30.3 (1992), pp. 209–214.

[76] Aleksei Tepljakov. *Fractional-order modeling and control of dynamic systems*. Springer, 2017.

[77] Kajal Kothari, Utkal V Mehta, and Ravneel Prasad. "Fractional-order system modeling and its applications". In: *Journal of Engineering Science and Technology Review* 12.6 (2019), pp. 1–10.

[78] Verma Pratibha and Sumelka Wojciech. "Mathematical and Numerical Analysis of a Fractional Diabetes Model with Singular Operator". In: *Fractal and Fractional* 10.5 (2026), p. 320.

[79] Krzysztof Oprzędkiewicz. "Discrete transfer function models for non integer order inertial system". In: *Conference on Automation*. Springer. 2018, pp. 14–25.

[80] Riccardo Caponetto, Francesca Sapuppo, Vincenzo Tomasello, et al. "Fractional-order identification and control of heating processes with non-continuous materials". In: *Entropy* 18.11 (2016), p. 398.

[81] Andrea Francesco Russillo, Giuseppe Failla, and Wojciech Sumelka. "On the wave propagation in unbounded space-fractional elastic solids and identification of its intrinsic microstructure based on Lagrange lattice". In: *Mechanics Research Communications* (2025), p. 104564.

[82] Leif Kari. "Effective visco-elastic models of tough, doubly cross-linked, single-network polyvinyl alcohol (PVA) hydrogels: Additively separable fractional derivative-based models for chemical and physical cross-links". In: *Continuum Mechanics and Thermodynamics* 33.6 (2021), pp. 2315–2329.

[83] Jun Fang, Sven Peter Näsholm, Wen Chen, et al. "The fractional constitutive models for nonlocal material based on scattering wave equations". In: *Mechanics of Time-Dependent Materials* 26.1 (2022), pp. 171–193.

[84] Andres San-Millan, Daniel Feliu-Talegón, Vicente Feliu-Batlle, et al. "On the modelling and control of a laboratory prototype of a hydraulic canal based on a TITO fractional-order model". In: *Entropy* 19.8 (2017), p. 401.

[85] Wojciech Sumelka. "On fractional non-local bodies with variable length scale". In: *Mechanics Research Communications* 86 (2017), pp. 5–10.

[86] Krzysztof Oprzędkiewicz, Maciej Rosół, and Wojciech Mitkowski. "Modeling of thermal traces using fractional order, a discrete, memory-efficient model". In: *Energies* 15.6 (2022), p. 2257.

[87] Leon Arriola and James M. Hyman. "Sensitivity Analysis for Uncertainty Quantification in Mathematical Models". In: *Mathematical and Statistical Estimation Approaches in Epidemiology*. Ed. by Gerardo Chowell, James M. Hyman, Luís M. A. Bettencourt, et al. Dordrecht: Springer Netherlands, 2009, pp. 195–247.

[88] Hui Zhang, Chuwen Guo, and Jie Lin. "Effects of velocity profiles on measuring accuracy of transit-time ultrasonic flowmeter". In: *Applied Sciences* 9.8 (2019), p. 1648.

[89] Maximilian Gruber, Sascha Eichstädt, and Clemens Elster. "`Modeling Dynamic Measurements in Metrology and Propagation of Uncertainties "". In: *Dynamic Measuring Systems: Fundamentals and Application of Time-Dependent Measurements* (2023).

[90] Andrew Dienstfrey and Paul D Hale. "Analysis for dynamic metrology". In: *Measurement Science and Technology* 25.3 (2014), p. 035001.

[91] Waldemar Minkina and Sławomir Gryś. *Korekcja charakterystyk dynamicznych czujników termometrycznych-metody, układy, algorytmy*. Wydaw. PC, 2004.

[92] Olivier P. Le Maître, Omar M. Knio, Habib N. Najm, et al. "Uncertainty Propagation Using Wiener–Haar Expansions". In: *Journal of Computational Physics* 197.1 (2004), pp. 28–57.

[93] Olivier P. Le Maître and Omar M. Knio. "Spectral Expansions". In: *Spectral Methods for Uncertainty Quantification: With Applications to Computational Fluid Dynamics*. Dordrecht: Springer Netherlands, 2010, pp. 17–44.

[94] Karl H Ruhm. "Dynamics and stability–A proposal for related terms in Metrology from a mathematical point of view". In: *Measurement* 79 (2016), pp. 276–284.

[95] Sascha Eichstädt, Clemens Elster, Ian M Smith, et al. "Evaluation of dynamic measurement uncertainty–an open-source software package to bridge theory and practice". In: *Journal of Sensors and Sensor Systems* 6.1 (2017), pp. 97–105.

[96] Sascha Eichstädt, Volker Wilkens, Andrew Dienstfrey, et al. "On challenges in the uncertainty evaluation for time-dependent measurements". In: *Metrologia* 53.4 (2016), S125–S135.

[97] Sascha Eichstädt and Volker Wilkens. "Evaluation of uncertainty for regularized deconvolution: A case study in hydrophone measurements". In: *The Journal of the Acoustical Society of America* 141.6 (2017), pp. 4155–4167.

[98] Trevor Esward, Sascha Eichstädt, Ian Smith, et al. "Estimating dynamic mechanical quantities and their associated uncertainties: application guidance". In: *Metrologia* 56.1 (2019), p. 015002.

[99] Sylvain Hernandez, Emmanuel Piat, Joel Abadie, et al. "Unknown input uncertainty calculation using virtual input shaping and interval analysis". In: *Measurement* 243 (2025), p. 116140.

[100] Luís Lages Martins, Álvaro Silva Ribeiro, João Alves e Sousa, et al. "Uncertainty evaluation for the dynamic measurement of deflections with a falling-weight-type impulse load device". In: *Journal of Physics: Conference Series*. Vol. 1044. IOP Publishing. 2018, p. 012072.

[101] Marzio Marseguerra and Enrico Zio. "Monte Carlo simulation for model-based fault diagnosis in dynamic systems". In: *Reliability Engineering & System Safety* 94.2 (2009), pp. 180–186.

[102] Leonard Klaus and Sascha Eichstädt. "Monte-Carlo-based uncertainty propagation with hierarchical models—A case study in dynamic torque". In: *Metrologia* 55.2 (2018), S70–S85.

[103] Jan Peter Hessling and Anders Mannikoff. "Dynamic measurement uncertainty of HV voltage dividers". In: *XIX IMEKO World Congress*. 2009.

[104] Waldemar Minkina. "Dynamische Meßmethode für hohe stationäre Temperatur bei Überschreiten des zulässigen Anwendungsbereiches von Temperaturmeßsensoren". In: *Forschung im Ingenieurwesen A* 57.3 (1991), pp. 95–104.

[105] Waldemar Minkina. "Temperaturmessung von flüssigem Stahl mit der Temperatursprungmethode". In: *Proceedings of the 37. Internationales Wissenschaftliches Kolloquium*. 37. Internationales Wissenschaftliches Kolloquium (Ilmenau, Germany). 1992.

[106] Wu-Sung Yao, Ian Hu, Golden Kao, et al. "Dynamic stiffness analysis of repetitive control and applied to advanced metrology analyzer". In: *2016 17th International Conference on Electronic Packaging Technology (ICEPT)*. IEEE. 2016, pp. 1206–1211.

[107] Sascha Eichstädt, Clemens Elster, Trevor J Esward, et al. "Deconvolution filters for the analysis of dynamic measurement processes: a tutorial". In: *Metrologia* 47.5 (2010), pp. 522–533.

[108] Katsuhiko Ogata. *Modern control engineering*. Prentice hall, 2010.

[109] Norman S Nise. *Control systems engineering*. John Wiley & Sons, 2019.

[110] Shankar P Bhattacharyya, Aniruddha Datta, and Lee H Keel. *Linear control theory: structure, robustness, and optimization*. CRC press, 2018.

[111] Ian Postlethwaite. *Multivariable feedback control: analysis and design*. John Wiley & Sons, Inc., 1996.

[112] Sigurd Skogestad and Ian Postlethwaite. *Multivariable feedback control: analysis and design*. john Wiley & sons, 2005.

[113] Rakesh P Borase, DK Maghade, SY Sondkar, et al. "A review of PID control, tuning methods and applications: RP Borase et al." In: *International Journal of Dynamics and Control* 9.2 (2021), pp. 818–827.

[114] José David Rojas, Orlando Arrieta, and Ramon Vilanova. *Industrial PID controller tuning*. Springer, 2021.

[115] Rames C Panda. *Introduction to PID controllers: theory, tuning and application to frontier areas*. BoD–Books on Demand, 2012.

[116] Liuping Wang. *PID control system design and automatic tuning using MATLAB/Simulink*. John Wiley & Sons, 2020.

[117] Matthias Liermann. "Pid tuning rule for pressure control applications". In: *International Journal of Fluid Power* 14.1 (2013), pp. 7–15.

[118] Ammar Soukkou, MC Belhour, and Salah Leulmi. "Review, design, optimization and stability analysis of fractional-order PID controller". In: *International Journal of Intelligent Systems and Applications* 8.7 (2016), p. 73.

[119] YangQuan Chen, Ivo Petras, and Dingyu Xue. "Fractional order control-a tutorial". In: *2009 American control conference*. IEEE. 2009, pp. 1397–1411.

[120] Pritesh Shah and Sudhir Agashe. "Review of fractional PID controller". In: *Mechatronics* 38 (2016), pp. 29–41.

[121] Michał Zamojski. "Implementation of fractional order PID controller based on recursive oustaloup'e filter". In: *2018 International Interdisciplinary PhD Workshop (IIPhDW)*. IEEE. 2018, pp. 414–417.

[122] Yi Yang and Haiyan Henry Zhang. *Fractional calculus with its applications in engineering and technology*. Morgan & Claypool Publishers, 2019.

[123] Farshad Merrikh-Bayat. "Rules for selecting the parameters of Oustaloup recursive approximation for the simulation of linear feedback systems containing PIλDμ controller". In: *Communications in Nonlinear Science and Numerical Simulation* 17.4 (2012), pp. 1852–1861.

[124] Ivo Petráš. "Tuning and implementation methods for fractional-order controllers". In: *Fractional Calculus and Applied Analysis* 15.2 (2012), pp. 282–303.

[125] Robin De Keyser, Cristina I Muresan, and Clara M Ionescu. "A novel auto-tuning method for fractional order PI/PD controllers". In: *ISA transactions* 62 (2016), pp. 268–275.

[126] Cristina I Muresan, Isabela Birs, Clara Ionescu, et al. "A review of recent developments in autotuning methods for fractional-order controllers". In: *Fractal and Fractional* 6.1 (2022), p. 37.

[127] Cristina I Muresan and Robin De Keyser. "Revisiting Ziegler–Nichols. A fractional order approach". In: *ISA transactions* 129 (2022), pp. 287–296.

[128] Iraj Nasiri and Nazila Nikdel. "Robust control of congestion in computer networks: An adaptive fractional-order approach". In: *Expert Systems with Applications* 190 (2022), p. 116184.

[129] Lu Liu, Lichuan Zhang, Guang Pan, et al. "Robust yaw control of autonomous underwater vehicle based on fractional-order PID controller". In: *Ocean Engineering* 257 (2022), p. 111493.

[130] Carlos Relaño, Jorge Muñoz, Concepción A Monje, et al. "Modeling and control of a soft robotic arm based on a fractional order control approach". In: *Fractal and Fractional* 7.1 (2022), p. 8.

[131] Amirreza Naderipour, Zulkurnain Abdul-Malek, Iraj Faraji Davoodkhani, et al. "Load-frequency control in an islanded microgrid PV/WT/FC/ESS using an optimal self-tuning fractional-order fuzzy controller". In: *Environmental Science and Pollution Research* 30.28 (2023), pp. 71677–71688.

[132] Krzysztof Oprzędkiewicz and Maciej Podsiadło. "The fractional order PID control of the forced air heating system". In: *Pomiary Automatyka Robotyka* 23 (2019).

[133] Guido Maione and Paolo Lino. "New tuning rules for fractional PI$^{\alpha}$ controllers". In: *Nonlinear dynamics* 49.1 (2007), pp. 251–257.

[134] WeiJia Zheng, Ying Luo, XiaoHong Wang, et al. "Fractional order PI$^{\lambda}$ D$^{\mu}$ controller design for satisfying time and frequency domain specifications simultaneously". In: *ISA transactions* 68 (2017), pp. 212–222.

[135] Paolo Lino, Jana Kőnigsmarková, Guido Maione, et al. "Independent-joint control of 5DOF robotic manipulators by fractional-order PI ν controllers". In: *2021 29th Mediterranean Conference on Control and Automation (MED)*. IEEE. 2021, pp. 403–408.

[136] Xu Li and Lifu Gao. "A simple frequency-domain tuning method of fractional-order PID controllers for fractional-order delay systems". In: *International Journal of Control, Automation and Systems* 20.7 (2022), pp. 2159–2168.

[137] Faisal Saleem, Alicja Wiora, and Józef Wiora. "Configuration and reduced-order modeling of a flow system based on experimental data". In: *Scientific Reports* 15.1 (2025), p. 35294.

[138] Farhad Ali, Zubair Ahmad, Muhammad Arif, et al. "A time fractional model of generalized Couette flow of couple stress nanofluid with heat and mass transfer: Applications in engine oil". In: *IEEE Access* 8 (2020), pp. 146944–146966.

[139] Naveed Khan, Farhad Ali, Zubair Ahmad, et al. "A time fractional model of a Maxwell nanofluid through a channel flow with applications in grease". In: *Scientific Reports* 13.1 (2023), p. 4428.

[140] Fangying Song and George Em Karniadakis. "Variable-order fractional models for wall-bounded turbulent flows". In: *Entropy* 23.6 (2021), p. 782.

[141] Wei Yu, Ying Luo, and YouGuo Pi. "Fractional order modeling and control for permanent magnet synchronous motor velocity servo system". In: *Mechatronics* 23.7 (2013), pp. 813–820.

[142] Xiaohong Wang, Yijian Su, Ying Luo, et al. "Fractional-Order Modeling and Identification for Dual-Inertia Servo Inverter Systems with Lightweight Flexible Shaft or Coupling". In: *Fractal and Fractional* 9.4 (2025), p. 222.

[143] Michal Macias and Dominik Sierociuk. "Modeling of electrical drive system with flexible shaft based on fractional calculus". In: *Proceedings of the 14th International Carpathian Control Conference (ICCC)*. IEEE. 2013, pp. 222–227.

[144] Faisal Saleem and Józef Wiora. "Applicability of Fractional-Order PID Controllers for Twin Rotor Aerodynamic System Objects". In: *Conference On Automation*. Springer. 2024, pp. 39–48.

[145] Faisal Saleem, Józef Wiora, Guido Maione, et al. "Impact of approximation methods on the performance of fractional-order PI controllers designed in frequency domain". In: *2025 Signal Processing: Algorithms, Architectures, Arrangements, and Applications (SPA)*. IEEE. 2025, pp. 34–39.

[146] Faisal Saleem, Ahsan Ali, Inam ul Hasan Shaikh, et al. "A hybrid H_∞ control based ILC design approach for trajectory tracking of a twin rotor aerodynamic system". In: *Mehran University Research Journal Of Engineering & Technology* 40.1 (2021), pp. 169–179.

[147] Saif Siddique Butt, Hao Sun, and Harald Aschemann. "Comparison of backstepping-based sliding mode and adaptive backstepping for a robust control of a twin rotor helicopter". In: *Variable-Structure Approaches: Analysis, Simulation, Robust Control and Estimation of Uncertain Dynamic Processes*. Springer, 2016, pp. 3–30.

[148] INTECO Ltd. *Two Rotor Aero-Dynamical System (TRAS) User's Manual*. INTECO Ltd. Krakow, Poland, 2013.

[149] The MathWorks, Inc. *MATLAB R2024b*. The MathWorks, Inc. Natick, Massachusetts, United States, 2024.

[150] The MathWorks, Inc. *Simulink R2024b*. The MathWorks, Inc. Natick, Massachusetts, United States, 2024.

[151] Joseph Czyzyk, Michael P. Mesnier, and Jorge J. Moré. "The NEOS Server". In: *IEEE Journal on Computational Science and Engineering* 5.3 (1998), pp. 68–75.

[152] Elizabeth D. Dolan. *The NEOS Server 4.0 Administrative Guide*. Tech. rep. ANL/MCS-TM-250. Argonne, Illinois, USA: Mathematics and Computer Science Division, Argonne National Laboratory, 2001.

[153] William Gropp and Jorge J. Moré. "Optimization Environments and the NEOS Server". In: *Approximation Theory and Optimization*. Ed. by Martin D. Buhmann and Arieh Iserles. Cambridge, UK: Cambridge University Press, 1997, pp. 167–182.

[154] AMPL Optimization Inc. *AMPL: A Mathematical Programming Language*. Available at https://ampl.com. AMPL Optimization Inc. USA, 2024.

[155] Avishek Adhikary, Munmun Khanra, Jayanta Pal, et al. "Realization of fractional order elements". In: *Inae Letters* 2.2 (2017), pp. 41–47.

[156] Stavroula Kapoulea, Panagiotis Bertsias, Costas Psychalinos, et al. "MOS realizations of fractional-order elements". In: *Fractional-Order Design*. Elsevier, 2022, pp. 1–33.

[157] Lukas Langhammer, Jan Dvorak, Roman Sotner, et al. "Reconnection–less reconfigurable low–pass filtering topology suitable for higher–order fractional–order design". In: *Journal of advanced research* 25 (2020), pp. 257–274.

[158] Yunus Emre Yokuș, Jaroslav Koton, Roman Sotner, et al. "A review of the state-of-the-art in fractional-order analog filters". In: *AEU-International Journal of Electronics and Communications* 196 (2025), p. 155786.

[159] The MathWorks, Inc. *Symbolic Math Toolbox User's Guide*. Version R2023. The MathWorks, Inc. Natick, Massachusetts, United States, 2023.

[160] The MathWorks, Inc. *Optimization Toolbox*. Natick, Massachusetts, United States, 2025. URL: https://www.mathworks.com/products/optimization.html.

[161] Paul M Moubarak. “Trust-region reflective adaptive controller for time varying systems”. In: *IET Control Theory & Applications* 9.2 (2015), pp. 240–247.

[162] Jorge Nocedal and Stephen J Wright. *Numerical optimization*. Springer, 2006.

[163] Nobutoshi Kabasawa and Yoshiyuki Noda. “Model-based flow rate control with online model parameters identification in automatic pouring machine”. In: *Robotics* 10.1 (2021), p. 39.

[164] Katsuhiko Ogata et al. *Modern control engineering*. Prentice Hall India, 2009.

[165] Michael Greenacre, Patrick JF Groenen, Trevor Hastie, et al. “Principal component analysis”. In: *Nature Reviews Methods Primers* 2.1 (2022), p. 100.

[166] Anas Saeb Husni Alhasan, Shekar Saranya, and Qasem M Al-Mdallal. “Fractional derivative modeling of heat transfer and fluid flow around a contracting permeable infinite cylinder: Computational study”. In: *Partial Differential Equations in Applied Mathematics* 11 (2024), p. 100794.

[167] Jingyu Yang, Lin Liu, Siyu Chen, et al. “Fractional second-grade fluid flow over a semi-infinite plate by constructing the absorbing boundary condition”. In: *Fractal and Fractional* 8.6 (2024), p. 309.

[168] Shazia Riaz, MS Anwar, Ayesha Jamil, et al. “Advanced fractional model for predicting MHD yield stress fluid flow with boundary effects”. In: *Nonlinear Dyn.* 113 (2025), p. 16443.

[169] Mohamed F El-Amin. “Derivation of fractional-derivative models of multiphase fluid flows in porous media”. In: *Journal of King Saud University-Science* 33.2 (2021), p. 101346.

[170] Clara-Mihaela Ionescu, Isabela Roxana Birs, Dana Copot, et al. “Mathematical modelling with experimental validation of viscoelastic properties in non-Newtonian fluids”. In: *Philosophical Transactions of the Royal Society A: Mathematical, Physical and Engineering Sciences* 378.2172 (2020).

[171] Ehsan Kharazmi, Min Cai, Xiaoning Zheng, et al. “Identifiability and predictability of integer-and fractional-order epidemiological models using physics-informed neural networks”. In: *Nature Computational Science* 1.11 (2021), pp. 744–753.

[172] Riccardo Caponetto, Giovanni Dongola, Luigi Fortuna, et al. *Fractional order systems: modeling and control applications*. Vol. 72. World scientific, 2010.

[173] Sebahattin Bektas. “Least squares fitting of ellipsoid using orthogonal distances”. In: *Boletim de ciências geodésicas* 21.2 (2015), pp. 329–339.

[174] Sverre Holm and Sven Peter Näsholm. "A causal and fractional all-frequency wave equation for lossy media". In: *The Journal of the Acoustical Society of America* 130.4 (2011), pp. 2195–2202.

[175] Cornelis Roos, Tamás Terlaky, and Jean-Philiipe Vial. *Interior point methods for linear optimization*. Springer, 2005.

[176] Junyun Pan, Huadong Fu, Kaikai Qiu, et al. "Sensitivity-analysis guided Bayesian optimization for crystal plasticity parameter identification". In: *International Journal of Mechanical Sciences* (2026), p. 111205.

[177] Bobak Shahriari, Kevin Swersky, Ziyu Wang, et al. "Taking the human out of the loop: A review of Bayesian optimization". In: *Proceedings of the IEEE* 104.1 (2015), pp. 148–175.

[178] Mevlut Yetkin and Cevat Inal. "L_1 norm minimization in GPS networks". In: *Survey Review* 43.323 (2011), pp. 523–532.

[179] The MathWorks, Inc. *Control System Toolbox User's Guide*. R2024b. MATLAB Control System Toolbox documentation. The MathWorks, Inc. Natick, Massachusetts, United States, 2024. URL: https://www.mathworks.com/help/control/.

[180] Faisal Saleem, Delfim F. M. Torres, and Józef Wiora. "Propagation of Measurement Uncertainty Associated with Parameter Identification in Fractional-Order Dynamic Systems". In: *Conference on Automation*. Presented. May 7, 2026. 2026. URL: https://automation.piap.pl/en/.

[181] Mohammad Ali Mansournia, Maryam Nazemipour, and Mahyar Etminan. "P-value, compatibility, and S-value". In: *Global Epidemiology* 4 (2022), p. 100085.

[182] Abu Bantu and Józef Wiora. "Impact of non-Gaussian noise on position accuracy provided by global navigation satellite systems (GNSS)". In: *IEEE Access* 13 (2025), pp. 161750–161761.

[183] Joint Committee for Guides in Metrology. *Evaluation of measurement data — Supplement 2 to the Guide to the expression of uncertainty in measurement — Extension to any number of output quantities*. JCGM 102:2011. BIPM, IEC, IFCC, ILAC, ISO, IUPAC, IUPAP, OIML, 2011. URL: https://www.bipm.org/documents/20126/2071204/JCGM_102_2011_E.pdf.

[184] Nicole Heymans and Igor Podlubny. "Physical interpretation of initial conditions for fractional differential equations with Riemann-Liouville fractional derivatives". In: *Rheologica Acta* 45.5 (2006), pp. 765–771.